

Declaration of Originality

I, Craig Justin Pregalato, declare that this thesis is my own work and contains no material that has been accepted for the award of any other degree or diploma in any university or other institution. To the best of my knowledge, this thesis contains no material previously published or written by another person, except where due reference is made in the text of the thesis.

Craig Justin Pregalato, 2 May 2003

Flow-Induced Vibrations Of A Tethered Sphere

This thesis is submitted in fulfillment of
the requirements for the degree of Doctor of Philosophy

By
Craig Justin Pregnalato
BE (Mechanical – Honours)

May 2003

Department of Mechanical Engineering
Monash University

Abstract

The flow-induced vibrations of a tethered sphere are investigated numerically and experimentally. Numerical techniques based on spectral/spectral-element methods are used to examine the dynamics of the sphere for mass ratios in the range $0.082 < M^* < 0.8$, and for tether lengths ranging from $L^* = 5$ to $L^* = 10$. In addition, experiments at laminar flow conditions are performed and good agreement is obtained with the numerical results.

The computations reveal that large-amplitude oscillations occur over a wide range of reduced velocity. Furthermore, the amplitudes of these oscillations are found to be strongly dependent on the mass ratio, whereas the frequencies of oscillation are relatively independent of the mass ratio. For harmonic oscillations, the drag coefficient is found to increase substantially from that of a non-oscillating sphere.

Four modes of vibration are known for a tethered sphere, the last three of which are reproduced in this study. The first mode is proposed to occur only at higher Reynolds numbers, ie. when the flow is turbulent. Visualizations of the vortex structures suggest that the mechanisms causing the large-amplitude Mode II and III vibrations result from the vortex shedding frequency being modulated by the oscillation frequency. The Mode IV response, which occurs only for the highest mass ratios investigated, is speculated to occur either via a subharmonic resonance (a type of instability-induced excitation) or a movement-induced excitation.

The existence of a critical mass for the tethered sphere system is proposed. Moreover, a neutrally buoyant tethered sphere ($M^* = 1$) is investigated for the first time computationally, the dynamics of which, to the author's knowledge, are largely unexplored.

Acknowledgements

I would like to express my gratitude to my supervisors, Professor Kerry Hourigan and Associate Professor Mark Thompson, for their continual guidance and support throughout the duration of my PhD candidature. In particular, I would like to thank Kerry for his enthusiasm and suggestions that led to numerous investigations, and Mark for his painstaking efforts in developing the computational techniques.

In addition, thank you to the dedicated staff of the Mechanical Engineering workshop, for their professionalism and efficiency in assisting with the experimental apparatus.

I am also grateful to my colleagues and friends in the Department with whom I have shared many experiences. Above all, I would like to thank my office mates, Kris Ryan and Greg Sheard, for the many hours of discussion and amusement that made life at Monash endurable.

I would also like to acknowledge the financial assistance in the form of a Monash Departmental Scholarship and Postgraduate Travel Grant. The resources provided by the Australian Partnership for Advanced Computing and the Victorian Partnership for Advanced Computing are also gratefully acknowledged.

Last but by no means least, I would like to express my deepest thanks and appreciation to my family, and especially to my best friend and companion Dawn, for making me smile through all the hard times and whose honesty and kindness continue to inspire me.

Publications

Pregalato, C.J. 2001 High-performance computing in bluff body flows (Poster presentation). *HPC Asia 2001*, Gold Coast, QLD, Australia.

Pregalato, C.J., Thompson, M.C. & Hourigan, K. 2001 Three-dimensional simulations of the flow past a rotating sphere. *Melbourne Graduate Fluid Mech. Conf.*, Melbourne, VIC, Australia.

Pregalato, C.J., Thompson, M.C. & Hourigan, K. 2001 Flow transition in the wake of a rotating sphere. *Proc. of 14th Australasian Fluid Mech. Conf.* (ed. B. Dally), Adelaide, SA, Australia.

Pregalato, C.J., Ryan, K., Thompson, M.C. & Hourigan, K. 2002 Numerical simulations of the flow-induced vibrations of tethered bluff bodies. *Proc. of IMECE 2002: 5th Int. Symp. on FSI, AE, FIV & N*, New Orleans, LA, USA.

Pregalato, C.J., Thompson, M.C. & Hourigan, K. 2002 DNS of the flow-induced vibrations of a tethered sphere. *APS DFD02*. November 24 – 26, Dallas TX, USA.

Pregalato, C.J., Thompson, M.C. & Hourigan, K. 2002 Flow transitions in the wake of a streamwise-rotating sphere. *Proc. of BBVIV 3* (eds. K. Hourigan, T. Leweke, M.C. Thompson, C.H.K. Williamson), Port Douglas, QLD, Australia.

Pregalato, C.J., Thompson, M.C. & Hourigan, K. 2002 Forces and wake transitions in the flow past a rotating sphere. *Phys. Fluids* (submitted).

Ryan, K., Pregalato, C.J., Thompson, M.C. & Hourigan, K. 2003 Flow-induced vibrations of a tethered circular cylinder. *J. Fluids Struct.* (to appear).

The following papers are in preparation.

Pregalato, C.J., Thompson, M.C. & Hourigan, K. The flow-induced vibrations of a tethered sphere. *J. Fluid Mech.*

Pregalato, C.J., Thompson, M.C. & Hourigan, K. Vortex-induced vibrations of a sphere at low Reynolds numbers. *J. Fluids Struct.*

Pregalato, C.J., Thompson, M.C. & Hourigan, K. Dynamics of a neutrally buoyant tethered sphere. *Phys. Rev. Lett.*

Nomenclature

α	non-dimensional numerical parameter similar to the Froude number
α_0	first coefficient of Adams-Bashforth predictors
α_1	second coefficient of Adams-Bashforth predictors
α_2	third coefficient of Adams-Bashforth predictors
A	cross-sectional area; amplitude of oscillation
\mathbf{A}	acceleration of the body
A^*	normalized amplitude of oscillation
B	net buoyancy force of the body
β	non-dimensional numerical parameter similar to the mass ratio
β_0	first coefficient of Adams-Moulton correctors
β_1	second coefficient of Adams-Moulton correctors
β_2	third coefficient of Adams-Moulton correctors
C_a	added mass coefficient
C_d	drag coefficient, also known as C_x
C_d'	root-mean-square drag coefficient
C_l	lateral force coefficient, also known as C_y
C_l'	root-mean-square lateral force coefficient
C_s	transverse force coefficient, also known as C_z
C_s'	root-mean-square transverse force coefficient
δ	boundary layer thickness
$d\mathbf{x}$	integral vector length element
$d\varphi$	integral azimuthal angle element
D	body diameter
ε	relaxation parameter
f	oscillation frequency
f_n	natural frequency of vibration
f_{vo}	vortex shedding frequency
f^*	normalized oscillation frequency
F_d	drag force
F_y	lateral force
F_z	transverse force
F_{tol}	force tolerance

Fr	Froude number
g	gravitational acceleration
γ	non-dimensional numerical parameter similar to the body acceleration
J	order of the numerical integration scheme employed
k	number of physical Fourier planes
L	tether length
\mathbf{L}	linear vector operator
L^*	normalized tether length
L_N	Legendre polynomial of degree N
λ	constant in the Helmholtz equation; eigenvalues of the $\mathcal{S}^2 + \mathcal{Q}^2$ tensor
m	mass of the sphere; also denotes an azimuthal mode
M^*	mass ratio
n	present time instant
\mathbf{n}	outward unit normal vector
\mathbf{N}	nonlinear vector operator
p	pressure; order of the polynomial interpolants
p'	inertial pressure
ρ	density of the fluid
ρ_s	density of the body
r	radial coordinate
R	radius of the body
Re	Reynolds number
S_{ij}	rate-of-strain tensor
S_n	normalized natural frequency of vibration
St	Strouhal number
t	time
T	tension in the tether; period of oscillation
Δt	infinitesimal time interval
Δt^*	non-dimensional time
\mathbf{u}	velocity vector field, composed of (u, v, w)
u_{tol}	velocity tolerance
\mathbf{u}_B	velocity vector of the body
\mathbf{u}'	inertial velocity vector
$\hat{\mathbf{u}}$	first intermediate velocity field
$\hat{\hat{\mathbf{u}}}$	second intermediate velocity field
U	freestream (asymptotic) velocity

U^*	reduced velocity
V	volume of the body
ν	kinematic viscosity of the fluid
$\boldsymbol{\omega}$	vorticity vector
\boldsymbol{x}	displacement vector field, composed of (x, y, z)
\boldsymbol{x}_B	displacement vector of the body
\boldsymbol{x}'	inertial spatial vector
$\ddot{\boldsymbol{x}}$	acceleration vector of the body
$\boldsymbol{\Omega}$	normalized angular velocity of the body
$\boldsymbol{\Omega}^*$	angular velocity of the body
$\boldsymbol{\Omega}_{ij}$	rate-of-rotation tensor
θ	mean layover angle; also a polar coordinate
φ	azimuthal coordinate
∇	gradient operator
\bullet	dot product operator
\times	curl operator

Contents

1	Introduction and Background Research	1
1.1	Flow past stationary spheres.....	2
1.1.1.	Early experimental work.....	3
1.1.2.	Recent experimental techniques and results	5
1.1.3.	Numerical simulations	6
1.1.4.	Theoretical approaches and stability analysis.....	11
1.2	Flow past rotating spheres	13
1.2.1.	Early experimental and numerical work	13
1.2.2.	Recent results: non-streamwise sphere rotations	14
1.2.3.	Recent results: streamwise sphere rotations.....	15
1.3	Vortex-induced vibration.....	15
1.3.1.	Classical studies and early experimental work	16
1.3.2.	Recent numerical and experimental studies.....	17
1.4	Flow past a tethered sphere	19
1.4.1.	Tethered spheres in oscillatory flows.....	19
1.4.2.	Tethered spheres in uniform flows.....	20
1.4.3.	Scope of the present investigation	22
2	Methodology and Mesh Independence	25
2.1	Problem formulation and governing equations of the tethered sphere	26
2.2	Time-advancement of governing equations.....	29
2.3	Spatial-discretization: the spectral/spectral-element method	33
2.4	Differences between experimental and numerical simulations	37
2.5	Numerical flow visualization techniques.....	39

2.5.1.	Vorticity	40
2.5.2.	Complex eigenvalues of $\nabla\mathbf{u}$	41
2.5.3.	The second invariant of $\nabla\mathbf{u}$	42
2.5.4.	Negative λ_2	42
2.6	Mesh independence: stationary sphere	43
2.6.1.	$Re = 300$	44
2.6.2.	$Re = 500$	48
2.7	Tethered sphere: dependence on ε and the convergence criteria	51
2.8	Experimental equipment and setup.....	54
3	Stationary Sphere	56
3.1	Axisymmetric flow	57
3.1.1.	Separation angle, length, vortex location and drag coefficient	57
3.1.2.	Pressure and vorticity fields.....	59
3.2	Steady asymmetric flow	62
3.2.1.	Transition to planar symmetry	62
3.2.2.	Drag and lift coefficients.....	63
3.2.3.	Streamlines.....	64
3.2.4.	Pressure and vorticity fields.....	64
3.2.5.	Visualization of vortex structures	67
3.3	Unsteady planar-symmetric flow.....	69
3.3.1.	Transition to unsteadiness.....	69
3.3.2.	Drag and lift coefficients, Strouhal number.....	69
3.3.3.	Streamlines.....	72
3.3.4.	Pressure and vorticity fields.....	75
3.3.5.	Vortex shedding mechanism.....	79
3.3.6.	Visualization of vortex structures	79
3.4	Unsteady asymmetric flow: $Re \leq 500$	81

3.4.1.	Transition to asymmetry	81
3.4.2.	Drag and lift forces, Strouhal number.....	82
3.4.3.	Analysis of fluid forces.....	83
3.4.4.	Visualization of vortex structures	88
4	Rotating Sphere	89
4.1	Introduction and parameter range.....	89
4.2	Non-streamwise sphere rotations.....	92
4.2.1.	Drag and lift coefficients.....	92
4.2.2.	Streamlines, pressure and vorticity fields	94
4.2.3.	Vortex shedding frequencies and vortex structures	98
4.2.4.	Critical Reynolds numbers.....	98
4.3	Streamwise sphere rotations	100
4.3.1.	Drag coefficients.....	101
4.3.2.	Vortex structures.....	103
4.3.3.	The “frozen” vortex structure	103
4.3.4.	Higher Reynolds number simulations.....	105
4.3.5.	Dynamics of the frozen vortex.....	106
4.3.6.	Critical Reynolds numbers.....	110
5	Tethered Sphere	111
5.1	Calculation of the natural frequency.....	112
5.2	Experimental results at low Reynolds numbers.....	114
5.2.1.	Time traces of the sphere response	114
5.2.2.	Oscillation amplitudes.....	116
5.2.3.	Frequency response.....	117
5.2.4.	Comparisons with the numerical simulations	117
5.3	Very low mass ratios	120
5.3.1.	Mean layover angles	120

5.3.2.	Oscillation amplitudes.....	122
5.3.3.	Force coefficient behaviour	125
5.3.4.	Frequency response.....	127
5.3.5.	Oscillation time traces.....	129
5.4	High mass ratios	131
5.4.1.	Mean layover angles	133
5.4.2.	Oscillation amplitudes.....	134
5.4.3.	Force coefficient behaviour	137
5.4.4.	Frequency response.....	139
5.4.5.	Effect of changing L^*	143
5.5	Putting the results together: suitability of the reduced velocity.....	144
5.6	The neutrally buoyant tethered sphere: $M^* = 1$	147
5.6.1.	Amplitudes of oscillation.....	148
5.6.2.	Force coefficient behaviour	150
5.6.3.	Frequency response.....	152
5.6.4.	Trajectories of sphere motion	154
5.7	Mode I response	156
5.8	Mode II response	159
5.8.1.	Sphere displacement and forces, $U^* = 5$	161
5.8.2.	Pressure fields	162
5.8.3.	Visualization of vortex structures	164
5.8.4.	Sphere displacement and forces, $U^* = 10$	168
5.8.5.	Pressure fields	169
5.8.6.	Visualization of vortex structures	172
5.8.7.	Dynamics of the Mode II response	175
5.9	Mode III response.....	176
5.9.1.	Sphere displacement and forces.....	177

5.9.2.	Pressure fields	180
5.9.3.	Visualization of vortex structures	181
5.9.4.	Dynamics of the Mode III response	185
5.10	Mode IV response.....	186
5.11	Existence of a critical mass ratio	189
5.12	Further work	190
6	Summary/Conclusion	192
6.1	Computational procedure and methodology.....	192
6.1.1.	Discretization and solution procedure.....	193
6.1.2.	DNS and experimental differences	193
6.1.3.	Numerical flow visualization techniques	194
6.1.4.	Mesh independence.....	194
6.1.5.	Relaxation parameter and convergence criteria	195
6.2	Stationary sphere	195
6.2.1.	Steady, axisymmetric flow.....	195
6.2.2.	Steady, planar-symmetric flow	197
6.2.3.	Unsteady, planar-symmetric flow	197
6.2.4.	Unsteady, asymmetric flow.....	198
6.3	Rotating sphere.....	198
6.3.1.	Non-streamwise sphere rotations	199
6.3.2.	Streamwise sphere rotations.....	199
6.3.3.	The “frozen” vortex structure	200
6.3.4.	Critical Reynolds numbers.....	200
6.4	Tethered sphere	201
6.4.1.	Experimental results at low Reynolds numbers	201
6.4.2.	Mean layover angles	202
6.4.3.	Oscillation amplitudes.....	204

6.4.4. Drag coefficients	205
6.4.5. Frequency response.....	206
6.4.6. Neutrally buoyant tethered sphere	207
6.4.7. Mode I response	208
6.4.8. Mode II response.....	209
6.4.9. Mode III response	210
6.4.10. Mode IV response	213
6.4.11. Existence of a critical mass ratio.....	214

References

215

Addendum

A statement is made in the abstract and conclusions that the frequency of oscillation is relatively independent of the mass ratio. However, this statement is based solely on the two mass ratios investigated and any perceived generalization to other mass ratios is unintentional. Experimental observations show that the frequency of oscillation is a strong function of mass ratio, especially for $M^* < 1$. It is perhaps a coincidence that the numerical results show a similar frequency response for the two mass ratios, or possibly there is a strong Reynolds number effect between the experiments and the simulations.

Chapter 1

Introduction and Background Research

The flow-induced vibration of structures is an important problem in many fields of engineering. Oscillations of a structure induced by vortex shedding may yield amplitudes as large as 1.5 to 2 diameters (Bearman 1984); in addition, any other bodies in the wake may be forced into oscillation. It is well known that some bodies can extract energy from a fluid stream and sustain oscillations, e.g. galloping. A well-documented example is the spectacular collapse of the Tacoma-Narrows Bridge in November 1940, which was a result of the inadequate understanding of the aerodynamic forces acting on bluff bodies that cause them to vibrate.

Knowledge of the instantaneous fluid forces (ie. drag and lift) is crucial in understanding flow-induced vibration phenomena. As a result, much recent research has been devoted to deducing the unsteady fluid forces on elastically vibrating structures. Novel techniques of estimating these fluid forces have been introduced by Gharib *et al.* (2000) & Hover *et al.* (1998), among others. However, precise measurements also need to be made regarding the wake structure in order to gain a real understanding of this phenomenon. This is accomplished in most detail through direct numerical simulations.

To the author's knowledge, the present work represents the first direct numerical simulations of the flow-induced vibrations of a tethered sphere. Indeed, although empirical models have been derived and used quite successfully for tethered structures affected by waves, the conceptually simple case of a tethered sphere subjected to a uniform flow has received little attention experimentally, and

practically no attention at all numerically, despite its significance in the offshore engineering and marine industries. It is to this end that we focus for the present study.

This chapter provides the reader with a brief background on the topics of interest in the present study. In particular, we focus on four relevant areas with increasing degree of complexity: the flow past stationary spheres; the flow past rotating spheres; vortex-induced vibrations; and finally, the flow past a tethered sphere. The background research is presented in chronological order. In each of the four areas of interest, in our opinion, only the most noteworthy investigations are reported. As a result, what follows is an extensive (but by no means exhaustive) summary on the appropriate research to the present.

1.1 Flow past stationary spheres

The flow of an incompressible, viscous fluid past a stationary sphere may be viewed as one of the simplest cases of bluff body flows. Its two-dimensional counterpart, the circular cylinder, has been studied extensively for decades and recent computations and experiments have shed much light on its wake vortex dynamics. On the other hand, much less is known concerning the flow past a fixed sphere, presumably because of the fully three-dimensional nature of the problem. However, the last ten years has seen a surge in research regarding spheres which is a direct result of increasing computer power and modern three-dimensional numerical algorithms.

Reynolds number Re	Wake characteristics
$Re < 24$	Laminar, axisymmetric, attached to sphere.
$24 < Re < 212$	Axisymmetric, steady, separated.
$212 < Re < 275$	Non-axisymmetric, steady, planar-symmetric, “double thread” wake vortex formation.
$275 < Re < 420$	Non-axisymmetric, unsteady, planar-symmetric, periodic vortex shedding in the form of vortex loops or hairpin vortices.
$420 < Re < 480$	Planar symmetry is lost, shedding direction oscillates intermittently.
$480 < Re < 650$	Vortex shedding pattern becomes irregular.
$650 < Re < 800$	Separated cylindrical vortex sheet pulsates, vortex tubes begin to be periodically shed in accordance with the pulsation.
$800 < Re < 3000$	Hairpin vortices become turbulent with alternate fluctuations, both high- and low-mode Strouhal numbers coexist.

Table 1 Wake characteristics for the range of Re investigated in the present study.

The wake of a fixed sphere consists of many regimes, encountered as the Reynolds number is increased. Here, the Reynolds number Re is based on the freestream velocity U , the diameter of the sphere d and the fluid kinematic viscosity ν . Table 1 summarises the characteristics of these regimes as well as the Reynolds numbers at which they occur for the range of Re investigated in the present study.

1.1.1 Early experimental work

Before any systematic study of the vortex shedding characteristics of the flow past a sphere was undertaken, the problem was essentially a classic one with an extensive literature. Before the advent of high performance computing enabled numerical solutions to become straightforward, early researchers were primarily concerned with analytical solutions (and in particular the drag coefficient) of the steady, incompressible axisymmetric flow past a sphere in a uniform stream. Stokes (1851) provided the first such treatment of the problem. However, obtaining higher order approximations beyond the first term given by Stokes (1851) proved to be difficult because expansions in terms of the Reynolds number in the vicinity of the sphere are not valid at large distances from the sphere. Proudman & Pearson (1957) tackled this problem by calculating the “outer” flow and matching the solution to the “inner” flow using matched asymptotic expansions. Their work was greatly extended by Chester & Breach (1969) to continue the analysis as far as the term of order $R^3 \log R$. However, they conclude that the expansion is only of practical value in the limited range $0 < Re < 0.5$.

Taneda (1956) was among the first to experimentally investigate the wake of a sphere at Reynolds numbers up to 300. He found that the critical Reynolds number for which the permanent vortex ring forms occurs at approximately $Re = 24$. This value was obtained by plotting the normalized vortex formation length against the logarithm of Re and extrapolating to the limit as the formation length approaches zero. Also, as previously mentioned, the relationship between the vortex formation length and Reynolds number is linear when plotted against the *logarithm* of Re , however, for a circular cylinder the relationship is linear when plotted against Re itself. This is evidence of the differences in wake formation between a sphere (3-dimensional) and a cylinder (2-dimensional).

Magarvey & Bishop (1961a,b) looked at wake configurations observed in liquid-liquid systems. Photographs were obtained of wake patterns behind the drops falling at terminal velocity through water. For Reynolds numbers less than 200, it was found that a vortex sheet separated the wake from the main flow and closed at some distance downstream. Furthermore, the wake liquid leaked into the main flow at this point of closure. As Re was increased, the vortex sheet did not close and a periodic

shedding of vortices began to appear. By analysing stereo pairs of photographs, the vortex rings were found to be formed by a simple cycle of build-up and release.

The formation and structure of vortices characteristic of sphere wakes were examined in a follow-up paper by Magarvey & MacLachy (1965). They realized that a stable three-dimensional wake based on ring elements appears to have no theoretical foundation, and hence the only theoretically possible cyclic configuration of the sphere wake consists of a procession of equally spaced vortex loops. The process by which vorticity is transferred to the region immediately downstream of the sphere and discharged into the stream was deduced from photographic sequences obtained with a calibrated moving-picture camera.

Roos & Willmarth (1971) investigated the drag on spheres and disks for Reynolds numbers from 5 to 100,000. They found that the drag on a sphere or disk translating at constant speed is not significantly affected by vortex shedding in the wake. Furthermore, the sphere $C_D - Re$ data did not provide any indication of the Reynolds number at which wake unsteadiness commences, ie. the data did not show any “jump” or “bend” to mark the onset of wake fluctuations. Also, the minimum Reynolds number for unsteadiness was found to be $Re = 290$.

Vortex shedding from spheres was studied in the Reynolds number range $400 < Re < 5 \times 10^6$ by Achenbach (1974) using hot-wire measurements. A water channel was used for the low Reynolds number experiments whereas a wind tunnel was used for the higher Re . Two distinct modes of vortex shedding were observed: a shear layer mode, dominant for $400 < Re < 6000$ and characterized by a Strouhal number that increases with Reynolds number, and a second mode dominant between Reynolds numbers of 6000 and 3×10^5 , which is distinguished by an approximately constant and well-defined Strouhal number. The rolling up of the separating shear layer was observed in the water channel and at $Re = 400$, the resultant vortex sheet began to form loops, which were periodically released from the sphere at a Strouhal frequency (based on sphere diameter and inflow velocity) of approximately $St \approx 0.16$. The position of the rolling up of the vortex sheet creeps closer to the sphere with increasing Reynolds number. For example, at $Re = 400$ the length of the discontinuity sheet was 1.5 diameters, whereas at $Re = 3000$, the length was only 0.5 diameters. However, no description could satisfactorily explain the Strouhal number change by one order of magnitude when the lower critical Re was exceeded.

The steady wake behind a sphere was studied experimentally by Nakamura (1976). After being dipped in dyed water, the sphere was released and its motion recorded with a strobe and camera. Nakamura deduced that at $Re = 7.3$ and above, the flow was separated and exhibited a toroidal vortex (or recirculation eddy) in the immediate wake, since no dyed water may be contained in the fluid which passes over the surface of the sphere and the created recirculating fluid with dyed water only makes the closed wake region visible. Furthermore, this toroidal vortex remains axisymmetric

up to $Re = 190$, after which the wake was deformed. However, these results are questionable since the mass of the fluid contents in the spherical shells was free to move about, potentially affecting the sphere's motion and its subsequent wake development.

1.1.2 Recent experimental techniques and results

A description of the natural frequencies in the wake behind a sphere was undertaken by Kim & Durbin (1988) in the range $500 < Re < 60,000$. Their measurements showed two dominant modes of unsteadiness to exist, one associated with the small-scale instability of the separating shear layer and the other with the large-scale instability of the wake. For Re less than a few thousand, previous researchers (eg. Achenbach (1974)) described the vortex shedding Strouhal number as increasing with increasing Re , whereas it is seems that it is actually the instability frequency that was being described. In this range, it was found that the vortex shedding Strouhal number is practically independent of the Reynolds number. The higher frequency was detected only in the region of the wake immediately downstream of the sphere, but the low frequency could be observed in a much larger region. At Reynolds numbers less than 800, the higher frequency was not observed.

Measurements of Strouhal numbers in the Reynolds number range $300 < Re < 40,000$ were obtained by Sakamoto & Haniu (1990) using hot-wire techniques. Strouhal frequencies were determined by power spectrum analysis of the fluctuating velocity in the wake behind the sphere. It was found that when the Reynolds number exceeds approximately 300, hairpin-shaped vortices begin to be periodically shed from the sphere. For $Re > 800$, two distinct modes of unsteadiness were observed which are associated with the small-scale instability of the separating shear layer and the large-scale instability of the wake, in agreement with Kim & Durbin (1988). Also, it was demonstrated that the higher frequency was detected only in the immediate downstream vicinity of the sphere at these higher Re . Moreover, a number of regions were identified concerning the changes in Strouhal number as the Reynolds number is increased. These regions are summarised in Table 1.

Experiments to investigate the formation mechanism and shedding frequency of vortices from a sphere in a uniform shear flow were conducted by Sakamoto & Haniu (1995). The Reynolds numbers considered ranged from 200 to 3000, and computer graphics image processing was utilised to examine the structure of the vortex shedding. The formation mechanism and configuration of a vortex detached from a sphere in a uniform flow, as described by Sakamoto & Haniu (1990), were found to be exactly the same as in the case of a uniform *shear* flow. Three instability modes are described: an axisymmetric pulsation of the recirculating zone with vortex shedding, an axisymmetric vortex shedding associated with the shear at the periphery of the recirculating zone, and a spiral mode related to a rotation of the separation line. For $Re > 300$, the first instability is

excited and vortex shedding occurs. When $Re > 800$, the second instability is excited and the two modes are simultaneously present but unlocked. Although they do not substantially affect the wake structure, they were found to affect the vortex shedding frequency mode.

The transition to turbulence in the wake of a sphere was investigated experimentally by Ormières & Provansal (1999). By changing slightly the angle of inclination of the supporting rod, they were able to observe a change in the orientation of the plane of symmetry. The transition to unsteadiness was observed at a Reynolds number of $Re = 280$. Above $Re = 360$, the velocity fluctuations were irregular and their spectrum exhibited a low frequency part. Near the threshold the variation was linear, in agreement with the Landau model (see Landau & Lifshitz (1987)) which describes the transition from steady to periodic flow as a supercritical bifurcation. Also, the location in the maximum of amplitude along the streamwise direction varied with the Reynolds number, from $[4.5d, 5.5d]$ near the threshold to $[4d, 4.5d]$ at $Re = 360$. Experimental visualizations of the flow structures in the wake of the sphere within this unsteady, planar-symmetric regime are shown in Figure 1.1.1.

1.1.3 Numerical simulations

Over the past two decades, direct numerical simulations have contributed much to the understanding of the wake states and flow structures observed in the wake of a sphere. Tomboulides *et al.* (1993) used a spectral element/spectral method to calculate the flow past a sphere for Reynolds numbers up to 1000 using DNS and $Re = 20,000$ using LES. The singularities introduced by the polar coordinate transformation were removed before applying the variational projection by multiplying the Fourier form of the governing equations by r , the radius of the sphere. They found that the flow past a sphere is axisymmetric up to a Reynolds number of approximately 212. Furthermore, results of wake length and separation angle followed an approximately logarithmic relationship with the Reynolds number, as previously observed by Taneda (1956). At this Reynolds number of 212, the flow was found to undergo a transition to three-dimensionality through a *regular* bifurcation, with the most unstable mode being the $m = 1$ mode with zero frequency associated with it. As Re was increased, the flow reached a three-dimensional steady-state solution, corresponding to the “double thread” wake observed by previous researchers. The second transition that leads to a time-dependent solution was found to occur within the range $250 < Re < 285$, which was again due to the $m = 1$ mode. In contrast to the first transition, the second transition was through a *Hopf* bifurcation, and the flow settled to a time-periodic final state with a Strouhal number of $St = 0.136$ at a Reynolds number of $Re = 300$. It was also found that the planar symmetry which was observed at $Re = 300$ was not preserved at $Re = 500$. At a Reynolds number of 500, a lower frequency was found which was

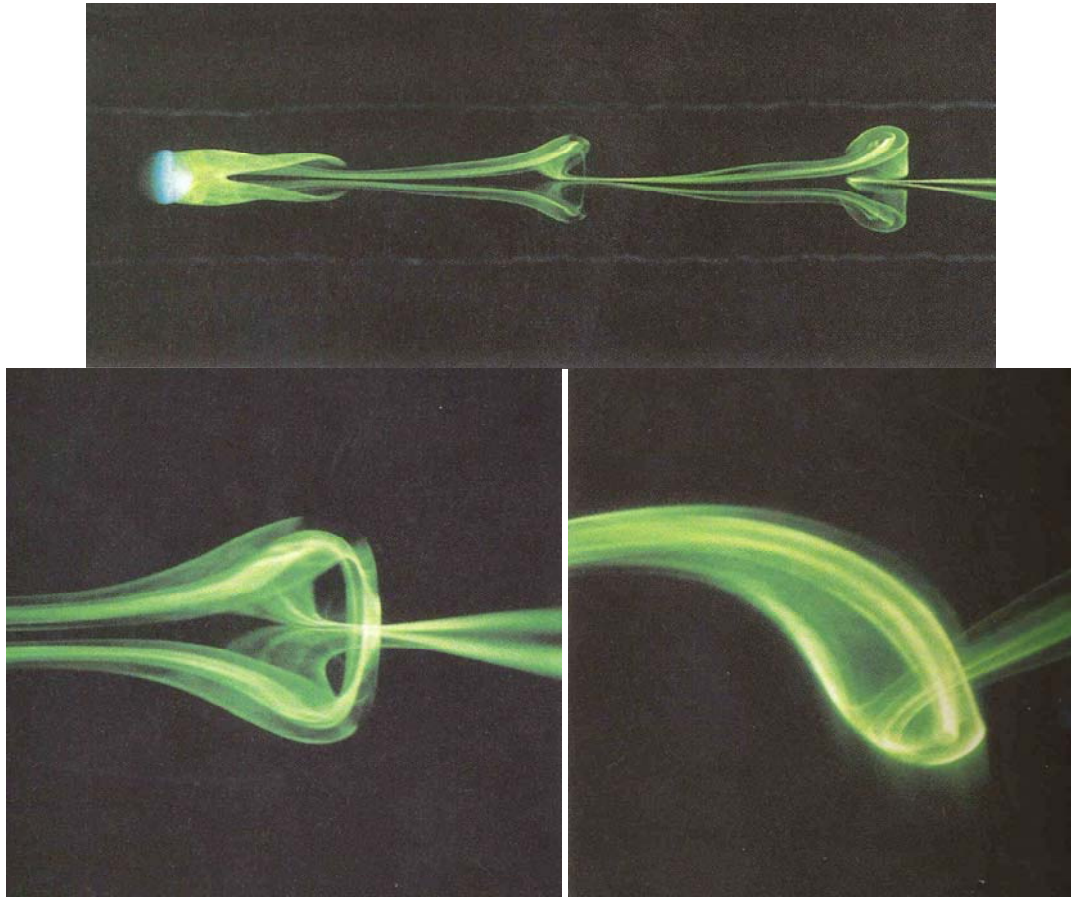


Figure 1.1.1. Experimental visualizations of the hairpin vortices in the wake of a sphere, $Re = 320$ (from Leweke *et al.* (1999)).

responsible for the irregular rotation of the separation point azimuthally around the rear part of the sphere. The value of this lower frequency was $St = 0.045$, whereas the Strouhal number associated with the vortex shedding was $St = 0.176$. A direct numerical simulation performed at $Re = 1000$ revealed the presence of small-scale structures in the flow, whose origin is the Kelvin-Helmholtz-like instability of the separating cylindrical shear layer. These small scales eventually rendered the wake turbulent and at $Re = 1000$, a Strouhal number of $St = 0.202$ was observed. Again, less prominent frequencies were observed, and the second frequency associated with the instability of the shear layer tended to increase with Re (or equivalently with decreasing shear layer thickness) since the shear layer becomes unstable to smaller wavelengths.

Mittal (1999a) used a Fourier-Chebyshev spectral collocation method to simulate flow past prolate spheroids. For a stationary sphere, his simulations showed a transition to non-axisymmetry at a Reynolds number of about 210. Furthermore, a transition to unsteadiness was observed at a Reynolds number between 250 and 350. However, no simulations were performed within this range to investigate the Reynolds at which this process precisely occurs. It was also found that at a Reynolds number of 500, the vortex loops being shed off the rear of the sphere did not have any

preferred orientation, and a reorganization of these vortex loops into vortex rings occurred in the downstream region of the wake, as reported by Magarvey & Bishop (1961).

To explore the planar symmetry in the unsteady wake of a sphere, Mittal (1999b) used the same method as Mittal (1999a) and focused on a Reynolds number of 350, which lies in the middle of the range where planar symmetry is indicated by experiments. The results indicate that at this particular Reynolds number investigated, the vortices are formed at exactly the same location in every shedding cycle. Also, in contrast to the cylinder wake where the maximum lift is comparable to the drag, for the sphere it is an order of magnitude lower than the drag. Furthermore, the drag force for the sphere oscillates at the shedding frequency whereas for the cylinder it oscillates at twice the shedding frequency due to the two counter-rotating vortices shed in the cylinder wake. It was found that planar symmetry was lost in the range $350 < Re < 375$, although the cycle-to-cycle variations in the vortex formation angle were small. However, at $Re = 425$, large cycle-to-cycle variations were observed, and hence the tendency of experiments to identify the loss of planar symmetry for $Re > 420$ may be due to the inability of the experiments to detect the small cycle-to-cycle variations of the vortex formation angle.

Although much research has been devoted to the flow past a stationary sphere, little has been achieved regarding the transitions to asymmetry and unsteadiness. Johnson & Patel (1999) analysed the flow past a sphere for Reynolds numbers up to 300. At $Re > 210$, asymmetric flow was observed and at $Re = 300$, unsteadiness was observed. They find that in the steady asymmetric regime, the pressure minimum in the region of the lower focus of the toroidal vortex is lower than that in the upper focus. This azimuthal pressure gradient propagates through the core of the toroidal vortex inducing flow along the vortex axis, resulting in a breakdown of axial symmetry. Hence, it appears that the unsteadiness of the axisymmetric flow is connected to the generation of a ring of low pressure in the wake. Also, the radially inward motion of the high-pressure side of the vortex serves to entrain free-stream fluid into the recirculating region, thereby opening up the previously closed separated wake. The transition to unsteadiness is similarly illustrated. For steady flow, the flow out of the centre of the upper focus generates a stable focus (radially inward flow) and attains equilibrium, ie. the azimuthal pressure-driven flow is sufficiently maintained by the entrainment of fluid into the upper focus. However, for unsteady flow, the Reynolds number is high enough that the upper focus does not reach an equilibrium state and continues to grow, entraining fluid from its own side of the sphere. The strength of circulation of the upper focus increases to a point where it changes from a stable focus to an unstable focus and its radial motion is against its own pressure gradient. The increased reversed flow impinging upon the upper separated flow generates a pressure maximum which appears to push the strengthened upper side of the vortex away from the sphere, thereby “shedding” the vortex, although not completely, into the wake. Finally, after the convection of the upper side of the vortex, a strong shear layer is left at the interface of the separated flow and

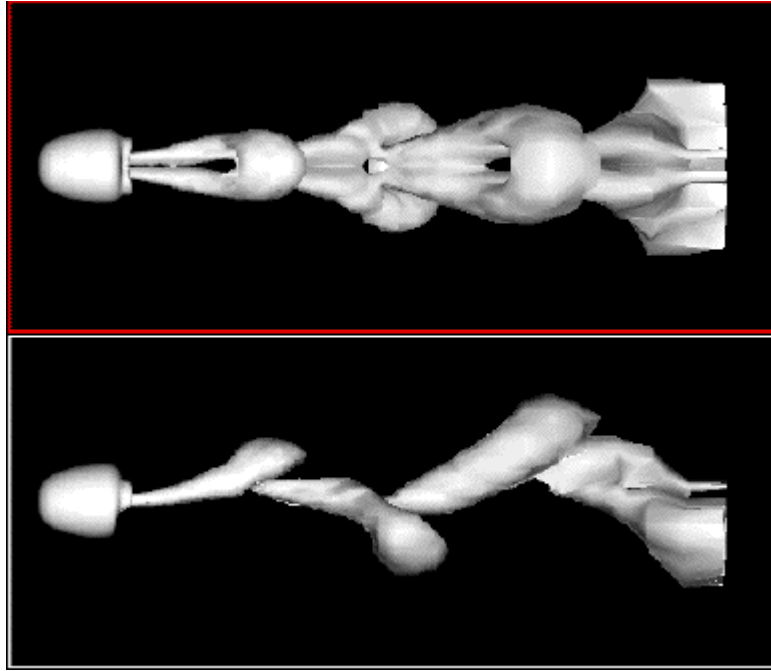


Figure 1.1.2. Numerical visualizations of the hairpin vortices in the wake of a sphere, $Re = 300$ (from Johnson & Patel (1999)).

the reversed flow passing through the centre of the wake. This shear layer quickly rolls up to produce a new upper focus, and the process starts over. Numerical visualizations of the hairpin vortices in the wake of the sphere are shown in Figure 1.1.2.

The turbulent flow over a sphere was investigated by Constantinescu & Squires (2000) using Large Eddy Simulations (LES) and Detached Eddy Simulations (DES), a technique based on a hybrid LES/RANS approach developed by Spalart *et al.* (1997). The advantage of considering a DES approach lies in the fact that near solid boundaries the standard Spalart *et al.* (1997) model is recovered, and the flow is predicted from the Reynolds-averaged equations. Far from walls, the length scale redefinition draws down the eddy viscosity and allows instabilities to develop as in classical LES. This method allowed the accurate prediction of boundary layer separation with transition to turbulence occurring shortly downstream in the detached shear layers. Furthermore, the subgrid models remained dormant in the sphere boundary layers as well as in the non-turbulent regions outside the sphere wake. This unique approach enabled Reynolds numbers up to $Re = 10,000$ to be studied, with the possibility of higher Reynolds numbers and massively separated flows in the near future.

A mixed spectral element/Fourier spectral method was used by Tomboulides & Orszag (2000) to understand the physical mechanisms of the transition to turbulence for incompressible flow past a sphere. They found that the flow undergoes a transition to three-dimensionality through a *regular* bifurcation at approximately $Re = 212$, with the most unstable mode being the $m = 1$ mode with zero

frequency associated with it, in agreement with Natarajan & Acrivos (1993). It should be noted that many of the results presented in this paper were reported in Tomboulides *et al.* (1993). As also observed by Ormières & Provansal (1999), the fluctuation energy first grows downstream and then decays, which they point out may indicate the existence of a convectively unstable mode which becomes absolutely unstable after the second critical Re is reached. Direct numerical simulations at $Re = 1000$ revealed that small scales were present in the flow field and their origin is a Kelvin-Helmholtz-like instability of the cylindrical shear layer that results from the separation of the boundary layer on the sphere. At this Re , lower frequencies of the same order as that at $Re = 500$ were observed, and the small scales associated with the shear-layer instability caused a rapid distortion of the large-scale vortex structures and eventually rendered the wake turbulent.

A similar spectral/spectral-element approach was employed by Ghidersa & Dušek (2000) to investigate the primary and secondary instabilities of the sphere wake. The reason for choosing this particular numerical approach was because the azimuthal spectral modes coincided with the nonlinear modes of the instability. After the first transition to planar symmetry, it was discovered that for a strong perturbation only one “thread” would be present in the wake. However, for a weak perturbation a “double thread” wake was observed, where the two counter-rotating vortices of the linear perturbation were strong enough to appear in spite of the presence of the (axisymmetric) base flow. The fundamental $m = 1$ mode was the most important; the higher-order modes were found to be practically irrelevant. The Reynolds number at which transition occurred was $Re_1 = 212$. For the secondary (Hopf) bifurcation, the critical Reynolds number was found to be $272.3 < Re_2 < 275$, taking into account any mesh inaccuracies and error estimates. At a Reynolds number of $Re = 300$, a Strouhal number of $St = 0.135$ was determined. The superposition of the $m = 0$ and $m = 1$ modes was analyzed to provide an explanation for the difference in the one-sided hairpin vortices observed in flow visualizations and the spatial picture of alternately shed hairpin vortices (for example, Johnson & Patel (1999)). Although the first two transitions were the primary focus of this study, the authors note that the method presented demonstrates the possibility of investigating the whole transition to turbulence.

Thompson *et al.* (2001) investigated the symmetry-breaking transitions of the wake of a sphere as it changes from laminar to turbulent. The principal aim of the study was to determine whether the transitions were subcritical or supercritical, ie. if they were hysteretic or not. This was carried out by assuming that the transitions behaved according to the Landau model:

$$\frac{dA}{dt} = (a_R + ia_I)A - l_R(1 + ic) |A|^2 A,$$

where A represents the global perturbation amplitude of some quantity from the base flow. The coefficient of the linear term on the right hand side represents the growth rate coefficient in the

linear regime, and changes from negative to positive through the transition and hence determines the stability of the system. Furthermore, the transition is supercritical if the coefficient of the cubic term is positive. For the first transition, it was found that the growth rate coefficient became positive at $Re_1 = 212$, close to predictions from linear stability analysis by Natarajan & Acrivos (1993) and other direct numerical simulations. Similarly, the second transition occurred at a critical Reynolds number of $Re_2 = 272$. Both of these transitions were found to be supercritical (or non-hysteretic). The transition process after the first critical Reynolds number was also examined by looking at the development of streamwise vorticity. Below Re_1 , rings of fluid passing close to the surface of the sphere maintain their axes parallel to the streamwise axis. Above Re_1 , these rings tilt which result in the conversion of azimuthal vorticity into streamwise vorticity that is then convected downstream into the wake.

Mittal *et al.* (2002) recently examined the symmetry properties of the transitional sphere wake for Reynolds numbers in the range $500 < Re < 1000$. The near-wake symmetry was explored through the phase plane plot of the two side force coefficients, C_y and C_z . For Reynolds numbers of 500 and 650, a preferred orientation of the side force was discerned, but not for $Re = 1000$. However, with increasing Re the preference for any particular orientation diminished, and the time-averaged near wake tended to become more axisymmetric. For all of the Reynolds numbers investigated, flow visualizations indicated that the vortex loops and rings have a preferred orientation in the wake. Furthermore, there was no significant change in the apparent plane of symmetry with streamwise distance, suggesting that the preferred direction associated with the formation of vortex loops in the near wake is also maintained in the downstream wake region.

1.1.4 Theoretical approaches and stability analysis

Monkewitz (1988a) investigated the stability of a family of axisymmetric wake profiles in the range of Reynolds numbers where vortex shedding from bodies of revolution is observed. The absolute or convective nature of the instability was then investigated using the Briggs-Bers criterion by determining the temporal growth rate of the dominant discrete mode at the location of the impulse source. For $Re = Re_{cA}$, the absolute growth rate $\text{Im}[\omega^0]$ is zero; for $Re > Re_{cA}$, one finds absolute instability; and for $Re < Re_{cA}$, there is a convective instability or stable flow. The minimum Re_{cA} was found to strongly depend on the normalized velocity ratio: for example, for zero centreline velocity $Re_{cA} = 820$, and for a reversed flow on the centreline of 5% of the freestream velocity $Re_{cA} = 59$. On the other hand, the shape parameter N at which the minimum Re_{cA} was observed was found to be quite insensitive to the velocity ratio and had a value of approximately $N \approx 3$. For zero or near-zero centreline velocities, the critical Reynolds number at which the wake becomes convectively unstable

was found to be of $O(10)$, then the occurrence of local absolute instability at an Re_{cA} of $O(10^2 - 10^3)$, depending on the amount of reverse flow. These results confirm physical intuition that reverse flow promotes absolute instability, ie. enhances the growth of disturbances that travel upstream.

Kim & Pearlstein (1990) report results of a linear stability analysis of the axisymmetric base flow of a fixed sphere. The spectral method used is a modification of a technique which employs a fourth-order stream function formulation of the governing equations for steady axisymmetric flow in spherical coordinates, used previously for Reynolds numbers up to $Re = 10$. Moreover, with certain modifications, this procedure was used for Reynolds numbers up to 200. Based on this approach, it was found that disturbances with azimuthal wavenumber $m = 1$ become unstable at $Re \approx 175.1$. The imaginary part of the associated (neutral) eigenvalue was $\Omega \approx 0.300$, corresponding to a *Hopf* bifurcation. The resulting flow field was unsteady and indicated that the onset of instability occurs via oscillatory disturbances. However, this result does not agree well with the abundance of experimental and numerical evidence that indicates that the first transition occurs through a *regular* bifurcation at $Re \approx 210$. On the other hand, Kim & Pearlstein (1990) believe that their results are valid in light of the fact that the experimental determination of the first critical Reynolds number is complicated by noting that the wake oscillations have a very low frequency.

Due to the lack of consensus regarding the nature of the first instability of the flow past a sphere, Natarajan & Acrivos (1993) numerically computed the details of this transition using a Galerkin finite element method. After accurately calculating the axisymmetric base flow, it was found that as Re increased from small values, the two leading eigenvalues were seen to move toward the imaginary axis. The crossing first occurred for the real eigenvalue at $Re_1 = 210$, which represents a *regular* bifurcation point on the branch of base flows. This resulted in a flow field that was no longer axisymmetric. Also, the other leading complex eigenvalue crossed the imaginary axis at $Re_2 = 277.5$, which represents a *Hopf* bifurcation point on the now-unstable branch of base flows. At Re_1 , the variation of the unstable eigenvector was primarily in the near-eddy region of the axisymmetric base flow, whereas for Re_2 , the variations had a spatially periodic downstream structure that is characteristic of an oscillatory wake instability, as is the case of flow past a cylinder. The first unstable mode was found to be nonaxisymmetric with $m = 1$, in agreement with Kim & Pearlstein (1990). However, the value of the critical Reynolds number at which this transition takes place varies significantly; Natarajan & Acrivos (1993) attribute this apparent inconsistency to the complicated nature of the numerical problem as well as the different computational approaches used in these studies.

A stationary sphere in a nominally steady, incompressible flow experiences unsteady lift and drag, with vortex shedding at large Reynolds numbers predominantly at a Strouhal number of approximately 0.2. An experimental and theoretical investigation was made by Howe *et al.* (2001),

who modelled the influence of the coherent vortex structures in the near wake as a succession of randomly orientated vortex rings. These vortex rings were interconnected by pairs of oppositely rotating vortices, and shed at quasi-periodic intervals at a Strouhal number ~ 0.19 . It is well known that at high Re , coherent wake structures of this kind must be rapidly dissipated by turbulence diffusion. For $St > 1$, the force spectrum was found to be governed by the initial stages of formation of the ring, and is therefore essentially independent of the shape of the fully formed vortex. For smaller St , the predictions were more strongly influenced by hypotheses regarding the orientation and statistics of vortex rings.

1.2 Flow past rotating spheres

Rotating spheres are found in many industries, yet very little research has been undertaken concerning the changes in flow topology as the Reynolds number and angular rotation are varied. For example, the trajectories of golf balls (and baseballs, etc.) are highly dependent on the amount of spin on the ball, which affects the ball's lift and drag characteristics. Furthermore, particle-laden and suspension flows are widely encountered in production, and therefore it is of great practical interest to investigate particle motion in designing manufacturing equipment. The present study aims to explore the impact of rotation on the transition (or critical) Reynolds numbers for a sphere rotating about the streamwise and non-streamwise axes respectively.

1.2.1 Early experimental and numerical work

For Reynolds numbers of the order of 10^5 , it was realised relatively early that a sphere rotating about the streamwise axis showed a marked influence of rotation on drag. Schlichting (1979) summarizes these early works and presents data of the drag coefficient in terms of Re , as well as highlighting the effect of (streamwise) rotary motion on the position of the line of laminar separation. When Ω has attained the value of 5, the line of separation will have moved by about 10° in the upstream direction, compared with a sphere at rest. The reason for this is that the centrifugal forces acting on the fluid particles rotating with the sphere in its boundary layer have the same effect as an additional pressure gradient directed towards the plane of the equator.

The Magnus (or Robins) effect on rotating spheres was investigated by Barkla & Auchterlonie (1971) by measuring the precession of a simple pendulum. The lift coefficient was calculated by measuring the angle of the pendulum to the vertical and the increase of period $\delta\tau$ for Reynolds numbers between 1500 and 3000. They observed that the lift coefficients rise less rapidly at first,

with increasing spin, but continue to rise to higher values, tending towards proportionality to the rate of spin.

Another experimental measurement of the Magnus force was performed by Tsuji *et al.* (1985). The motivation for their experiments was to get fundamental data which is necessary to calculate the motion of particles conveyed pneumatically in a pipeline. Their measurements indicate that in the Reynolds number range $550 < Re < 1600$ and nondimensional angular velocity $\Omega < 0.7$, the lift coefficient may be approximated by $C_L = (0.4 \pm 0.1)\Omega$, obtained empirically by comparing measurements of the range of flight of the sphere with the solution of its equation of motion. They also found that the drag coefficient was virtually unaffected by rotation.

Watts & Ferrer (1987) measured the lateral force on a spinning baseball in a subsonic wind tunnel. They found that the lift coefficient for rough spheres is a function of the ratio $\pi D\omega/V$ and is at most a weak function of the Reynolds number, which appears to be more consistent with the Kutta-Zhukovskii theorem than do previous results, even though this theorem is strictly applicable only to two-dimensional inviscid flows. Note that the Kutta-Zhukovskii theorem states that the lift force should be proportional to ωV , meaning the lift coefficient should be directly proportional to $\pi D\omega/V$. Furthermore, the orientation of the seams of the baseball had little effect on the lift force.

1.2.2 Recent results: non-streamwise sphere rotations

More recent experimental data has been acquired by Oesterlé & Bui Dinh (1998) over the Reynolds number range $10 < Re < 140$ and (dimensionless) sphere rotation rates varying from $1 < \Omega < 6$. This particular parameter space was chosen principally to obtain measurements that may be compared to the theoretical results of Rubinow & Keller (1961) who used matched asymptotic expansions. They found that the lift coefficient increases with increasing rotation rate and decreases with increasing Reynolds number. Moreover, the results suggest that the influence of Ω vanishes for Re greater than 100. Despite the scatter in the experimental results, an expression was proposed to estimate the lift coefficient in the form $C_L \approx 0.45 + (2\Omega - 0.45)\exp(-0.075\Omega^{0.4}Re^{0.7})$. Although providing a useful correlation, this equation does not support rotation rates less than unity, and may be used primarily to supplement existing results.

More applicable to the present study is the computations performed on a rotating sphere in a linear shear flow by Kurose & Komori (1999), with the parameter range $1 < Re < 500$ and $0 < \Omega < 0.25$. A finite difference scheme based on the marker-and-cell method was used to calculate the drag and lift forces on the sphere. Based on simulations performed at particular Reynolds numbers and rotation rates, an approximate expression for the lift coefficient was obtained as $C_L = K\Omega$, where the value of

K depends on the Reynolds number and is listed as K_2 in Table 3 of their paper. The drag coefficient was found to increase with increasing rotation rate, and the lift coefficient approached a constant value for $Re > 200$ for a given rotational speed. This asymptotic value of C_L increased with increasing Ω , as did the Strouhal number, St . However, no attempt was made to explain these trends as details regarding the structure of the wake were not thoroughly examined.

1.2.3 Recent results: streamwise sphere rotations

Wang *et al.* (2001) were among the first to characterize the flow states resulting from the rotation of a sphere about the streamwise axis. They investigated Reynolds numbers of $Re = 200, 250$ and 300 , and rotation rates of $0.025 < \Omega < 1$. At $Re = 200$, it was found that the wake remained axisymmetric for rotation rates up to $\Omega = 0.25$. For $Re = 250$, the flow structures rotated about the streamwise axis at a certain angular velocity without deformation of its shape. Finally, for higher Reynolds numbers ($Re = 300$), they found that the rotating frequency of the vortex structures in the near wake of the sphere was nearly independent of the Reynolds number.

Recently, laminar flow past a rotating sphere was investigated numerically by Kim & Choi (2002) at Reynolds numbers of $100, 250$ and 300 and rotation rates of $0 < \Omega < 1$. Like Wang *et al.* (2001), the rotations investigated were parallel to the streamwise axis. At $Re = 100$, the vortical structures in the wake were axisymmetric for all Ω and became stronger in the streamwise direction with increasing Ω . For $Re = 250$, at low rotation rates ($\Omega < 0.3$) one tail of the double thread vortex became stronger and the other weaker. This effect was more pronounced at $\Omega = 0.3$, at which one tail disappeared completely. However, for $\Omega \geq 0.5$ the tail reappeared and the two tails were twisted together in a complex pattern for higher rotation rates. For $\Omega \leq 0.3$, the vortical structure was “frozen” (ie. rotated without temporal variation in its shape and strength, as first observed by Wang *et al.* (2001)) and the lift and side forces were sinusoidal in time, but the magnitudes of the drag, lift and side forces were constant in time. For $Re = 300$ and low rotational speeds, the flows became unsteady asymmetric. At this Reynolds number, frozen flows were obtained at $\Omega = 0.5$ and 0.6 .

1.3 **Vortex-induced vibration**

The vast field of vortex-induced vibration (VIV) has seen much activity over the last few decades because of its importance in many engineering applications. VIV is a potential problem affecting many types of offshore structures, including production and drilling risers, conductors, pipelines, moorings, tethers of tension leg platforms, spar platforms and the members of jacket structures

(Ziada & Staubli (2000)). Because of these problems in the marine sector, much research has been devoted to analysing the vortex-induced vibrations of a circular cylinder. Indeed, many books are devoted to this topic, and the reader is referred to the texts by Blevins (1994) and Naudascher & Rockwell (1994) as an introduction to the field. The following is a summary of recent research that is applicable to the current study.

1.3.1 Classical studies and early experimental work

Long flexible cables are commonly used in engineering applications, for example, in suspension bridges and electrical power transmission lines. For a stationary circular cylinder, the vortex shedding frequency f_{vs} matches the Strouhal frequency f_s . As the vortex shedding frequency approaches the natural frequency of a given flexible circular cylinder, a resonant response tends to develop in which amplitudes can be of the order of $1D$ as the vortex shedding frequency locks-in to the cylinder frequency, where D is the diameter of the body. This synchronization is part of a nonlinear phenomenon featuring a hysteresis loop, as pointed out by the early studies of Feng (1968) and Bishop & Hassan (1964).

This hysteresis loop was originally thought to occur due to nonlinear spring or damping behaviour. However, an experimental investigation of the vortex-induced oscillations of a long flexible circular cylinder was carried out by Brika & Laneville (1993), who found that the hysteresis loop is indeed a fluid mechanic phenomenon. It is characterized by two branches, with each branch associated with a particular vortex shedding mode and delimited by a discontinuity featuring a jump to the other branch. The upper branch is associated with the von Kármán type wake or the 2S mode of vortex shedding. The lower branch of the hysteresis loop is associated with a 2P mode in which two vortices of opposite sign are shed from each side of the cylinder in every vibration cycle. For flow velocities less than the lower critical velocity (where a 2P \rightarrow 2S mode jump occurs), the cylinder oscillation amplitude grows as it is released from rest towards a first stationary amplitude and then bifurcates towards a secondary stationary amplitude. The amplitudes of the bifurcation occurrence coincide with the critical curve separating the 2S mode and 2P mode regions. This bifurcation is accompanied by a sudden change of the phase angle between the fluid excitation and the cylinder displacement.

It is well known that shear flows around bluff bodies are sensitive to periodic excitation such as a sound wave with the specific frequency related to the convective instability of the shear layers. As a result, the vortex-induced vibrations can be suppressed by stimulating the separated shear layers around the body by an acoustic excitation with the frequency of the transition waves. Hiejima *et al.* (1997) investigated such a problem by applying a periodic velocity excitation at two locations on he

surface of a circular cylinder. They found that the excitation with the transition wave frequency, which is the most unstable and can grow into the strong fluctuation in the shear layer around the cylinder, is the most effective in changing the flow characteristics around the cylinder and the characteristics of the vortex-induced vibrations. In these simulations, the cylinder oscillated because of the periodic vortex shedding behind the cylinder, and therefore the characteristics of the vortex-induced vibrations were altered by the change of the vortex shedding frequency behind the cylinder. However, the effect of periodic excitation for larger amplitude vibrations needs to be addressed.

1.3.2 Recent numerical and experimental studies

An example of a fluid-elastic problem is the vortex-induced vibration of a cable. Newman & Karniadakis (1997) present DNS results of the flow-induced vibrations of an infinitely long flexible cable at Reynolds numbers $Re = 100$ and $Re = 200$, in which the flow was analysed when the cable was both unconstrained and constrained to move transversely only. The cable vibration wavelength varied from $L/d = 6.3$ to 201.1. For the constrained case, both a standing wave and travelling wave vibration response was observed over several shedding periods. However, the travelling wave response prevailed over longer time periods. For the unconstrained cable, only the travelling wave response was observed, which in general is the preferred response. Furthermore, the vibration response was found to be quite sensitive to the tension (or phase speed) in the cable. At $Re = 100$, the maximum amplitude response was approximately 0.7 diameters, whereas for $Re = 200$ it was about one diameter. It should be noted that primarily lock-in states were considered: no attempt was made to determine the boundaries of the lock-in regions for freely moving cables, though it has been demonstrated that even a small variation in the diameter of an oscillating cylinder can change the lock-in region, creating subharmonic responses at the lower end of the lock-in boundary.

Returning now to the problem of VIV for a circular cylinder, two distinct types of amplitude response are observed depending on the mass-damping parameter. At high mass-damping, two branches are observed known as the initial and lower branches (eg. Feng (1968), Brika & Laneville (1993)). However, for low mass-damping, three branches are found (initial, upper and lower), as shown in Figure 1.3.1. Khalak & Williamson (1999) summarized the features of this low mass-damping regime. They found that a five-fold increase in the maximum drag, a seven-fold increase in the R.M.S. lift and a fluctuating drag of 102 times that for a stationary cylinder could be expected. The transition from the initial to the upper branch was found to be hysteretic. In contrast, the transition from the upper to the lower branch was rather different, and the system switched between these branches intermittently and seemed only weakly “locked” onto one or the other mode over a narrow reduced velocity range. Both the mode transitions were associated with jumps in amplitude

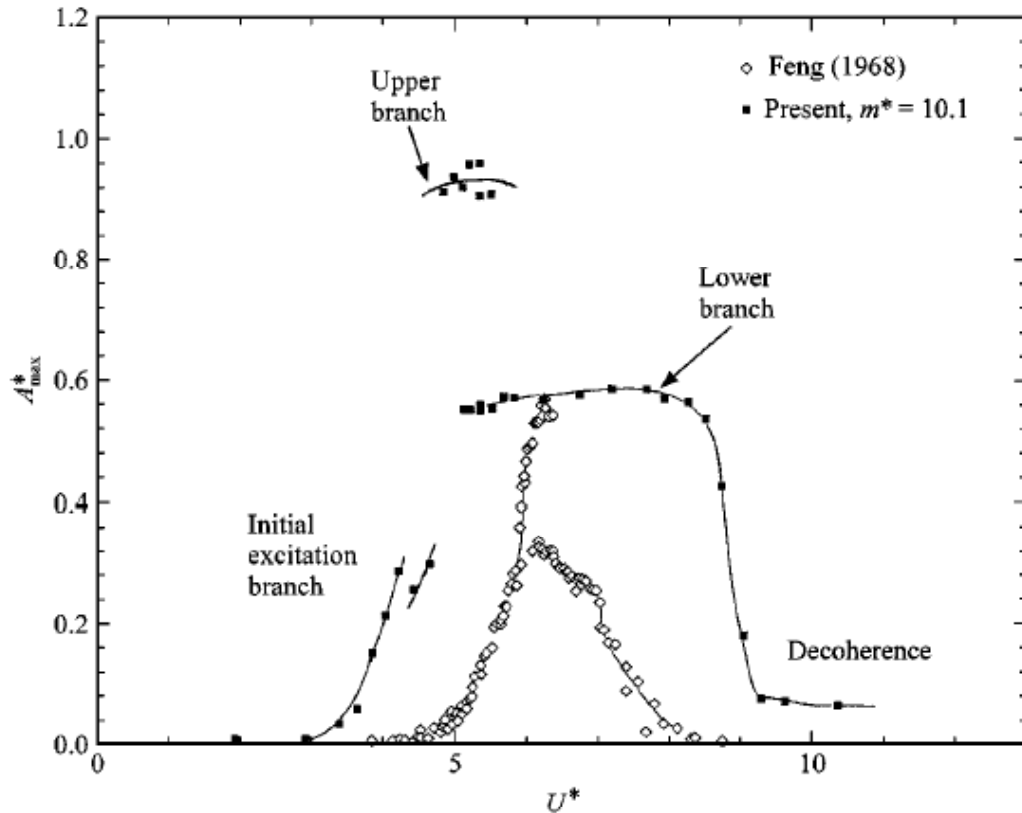


Figure 1.3.1. Amplitude response of a hydroelastically mounted cylinder with the mass-damping parameter equal to 0.013 (from Khalak & Williamson (1999)).

and frequency, but the 180° jump in phase angle was found only when the flow jumped between the upper and lower branches. The initial branch corresponded to a 2S mode of vortex shedding, whereas the lower branch corresponded to a 2P mode: the data was insufficient to clarify the vortex shedding mode for the upper branch. Finally, an excellent collapse of data for a set of response amplitude plots was observed when using the actual oscillation frequency f rather than the still-water natural frequency f_n to form a normalized velocity U^*/f^* (also known as a “true” reduced velocity in recent studies).

The disparity in the transitions between the initial, upper and lower branches was made clear by Govardhan & Williamson (2000). By decomposing the fluid force into its “potential” and “vortex” components, they found that there was no clear jump in “vortex phase” at the upper-lower branch transition, but between the initial and upper branches there was a phase jump in the “vortex force.” There are thus two phase jumps: a large jump in the *vortex* phase (but a minute jump in *total* phase) at the initial-upper transition, associated with a switch in timing of vortex shedding in which the response frequency passes through $f^*_{water} = 1.0$; and a large jump in the *total* phase (but a minute jump in *vortex* phase) at the upper-lower transition, which is *not* associated with a switch in timing of the shedding and in which the response frequency passes through $f^*_{vacuum} = 1.0$. Both large phase

jumps have a magnitude of π . Furthermore, for low mass-damping, when mass ratios fall below $m^*_{crit} = 0.54$, the lower branch cannot be reached and ceases to exist. As a result, the upper branch will continue indefinitely and the synchronization regime will extend to infinity. The high strain rate region between neighbouring vortices lies within a vorticity concentration for the 2P mode, but in between vorticity concentrations for the 2S mode. This internal intense strain rate for the 2P mode splits the vortex apart to form two separate vortices. Both 2P modes in the upper and lower branches are steady-state periodic modes.

The flow-induced vibration response of a flexibly mounted cylinder with attached wires is significantly altered, even far away from lock-in, as observed by Hover *et al.* (2001). They found that for a stationary cylinder in crossflow, small trip wires at $\pm 70^\circ$ from the mean stagnation point can significantly reduce the drag and lift characteristics for $Re > 2 \times 10^4$. For forced oscillations, the lift amplitude and phase curves as functions of reduced velocity retained some of the main features observed in smooth cylinders, although these features were generally shifted to higher frequencies for a given amplitude of motion. For free vibrations, the wires introduced an earlier mode transition that occurred at lower U^* , and corresponded to an early lock-in to the structural mode. The maximum response was moderately reduced for the cylinder with wires and for $U^* > 6$, the response was largely eliminated by the wires. Furthermore, the amplitude response of the flexibly mounted cylinder with wires was sensitive to bias in the angle of the oncoming stream.

1.4 Flow past a tethered sphere

Research involving tethered spheres has experienced somewhat of a resurgence in recent years. Applications to ocean mooring systems have necessarily resulted in deterministic models based on approximate theoretical analyses. These studies usually involved the response of ocean-mooring systems excited by finite-amplitude waves. However, the response of (submerged) structures exposed to a uniform flow, despite its apparent simplicity, has received very little attention. It is this issue to which we address the following question: does a tethered sphere vibrate in a uniform flow, and if so what are the mechanisms causing these vibrations.

1.4.1 Tethered spheres in oscillatory flows

The vast majority of work on tethered spheres were concerned with the action of surface waves on tethered buoyant structures. For example, the investigations of Harleman & Shapiro (1961) and Shi-Igai & Kono (1969) employed empirically obtained drag and inertia coefficients for use in

Morison's equation. Consequently, because the waves represented harmonic forcing functions, the tethered sphere was found to vibrate vigorously. However, the coupling of the wave motion and the dynamics of the sphere resulted in complicated equations of motion from which it is difficult to understand the underlying physics.

Gottlieb (1997) investigated a nonlinear, small-body mooring configuration excited by finite-amplitude waves and restrained by a massless elastic tether. A Lagrangian approach was formulated in which the stability of periodic motion was determined numerically using Floquet analysis and revealed a bifurcation structure including ultrasubharmonic and quasi-periodic responses. The hydrodynamic dissipation mechanism was found to control stability thresholds, whereas the convective terms enhanced the onset of secondary resonances culminating in chaotic motion. Consequently, excitation by finite-amplitude waves may generate a complex transfer of energy between the modes of motion for wave frequencies that are integer multiples of the system natural frequencies.

This work was extended by Gottlieb & Perlin (1998) in which the nonlinear large-amplitude period-doubling response of a submerged tethered sphere excited by finite-amplitude waves was investigated. Experiments were performed in a gravity-wave/air-sea interaction laboratory, and compared to a theoretical model previously derived by Gottlieb (1997). The theoretical model successfully captured the dominant period-doubling topology whereas a standard Morison-based formulation does not. The latter exhibits pure external excitation while the period-doubling threshold was found to be governed by the parametric excitation induced by the nonlinear convective terms. These results shed light on the magnitude of the nonlinear wave-excited drag force which cannot be estimated using coefficients estimated from simple periodic motion.

1.4.2 Tethered spheres in uniform flows

Returning now to the question at the beginning of this section, Williamson & Govardhan (1997) found that a tethered sphere does indeed vibrate in a uniform flow. In particular, they found that it will oscillate vigorously at a transverse saturation amplitude of close to two diameters peak-to-peak. This transverse oscillation frequency was at half the frequency of the in-line oscillations, although the natural frequencies of both the in-line and transverse motions were the same. In the Reynolds number range of their experiments ($Re < 12 \times 10^3$), the response amplitude was a function of the flow velocity. However, they found that a more suitable parameter on which to gauge the response is the reduced velocity, U^* . Furthermore, the normalized amplitude was reasonably independent of the mass ratio or tether length ratio, except insofar as these groups influence the value of the natural frequency. However, conclusions regarding the synchronization of natural and vortex formation

frequencies were lacking due to the large scatter in the literature of the vortex formation frequency in the wake of a sphere.

Govardhan & Williamson (1997) went on to find that the saturation RMS response value increases with mass ratio. Also, the maximum amplitude was approximately 1.1 diameters, regardless of the mass ratio (a Mode II response). It was also found that the vortex shedding frequency (for a stationary sphere) crossed the natural frequency for the tethered sphere at the same reduced velocity $U^* \approx 5$, at which the local peak in the RMS response occurred. This suggests that the local peak in the RMS response is caused by a resonance between the natural frequency of the tethered body and the wake vortex shedding frequency, as one might expect, and is known as a Mode I response. For high mass ratios (typically $M^* > 1$), the oscillation frequency at large reduced velocity tended toward the natural frequency. However, it is interesting to note that the oscillation frequency for lower mass ratios ($M^* < 1$) at high U^* did not correspond to either the natural frequency or the vortex shedding frequency for a stationary sphere. In addition, unless one takes into account the tendency of a tethered sphere to vibrate, an increase in the drag of the order of 90% is to be expected.

Up to now, spheres of low mass ratio have been studied (primarily in water channel facilities). However, a wide range of mass ratios and reduced velocities may be examined by performing experiments in a wind tunnel. Jauvtis *et al.* (2001) focused on mass ratios between $M^* = 80$ and $M^* = 940$ and reduced velocities in the range $0 < U^* < 300$. For the sphere of mass ratio 80, they found a new mode of vibration (which they define as Mode III) and which extends over a broad regime of U^* from 20 to 40. Because of the high mass ratios involved, the oscillation frequency remained very close to the natural frequency of the tethered sphere, whereas low M^* yielded oscillation frequencies higher than, and depart significantly from, the natural frequency (Govardhan & Williamson (1997)). This mode cannot be explained as the classical lock-in effect, since between 3 and 8 cycles of vortex shedding occurs for each cycle of sphere motion. Although no explanation is given here, they note that there must exist vortex dynamics which are repeatable in each cycle, and which give rise to the fluid forcing component that is synchronized with the body motion. For reduced velocities beyond the regime for Mode III, another vibration mode was discovered that grew in amplitude and persisted to the limit of flow speed in the wind tunnel. The sphere dynamics of this “Mode IV” were characterized by intermittent bursts of large-amplitude vibration, in contrast to the periodic vibrations of Modes I-III. In addition, despite these intermittent bursts, the vibration frequency of this mode remained very close to the natural frequency throughout the range of up to at least $U^* = 300$. With the vortex shedding frequency between 40 and 50 times the oscillation frequency, the vortex shedding cannot be responsible for these large vibrations, and the origin of these transient bursts remains unknown. The amplitudes and the periodic nature of these oscillations for these modes are shown in Figure 1.4.1.

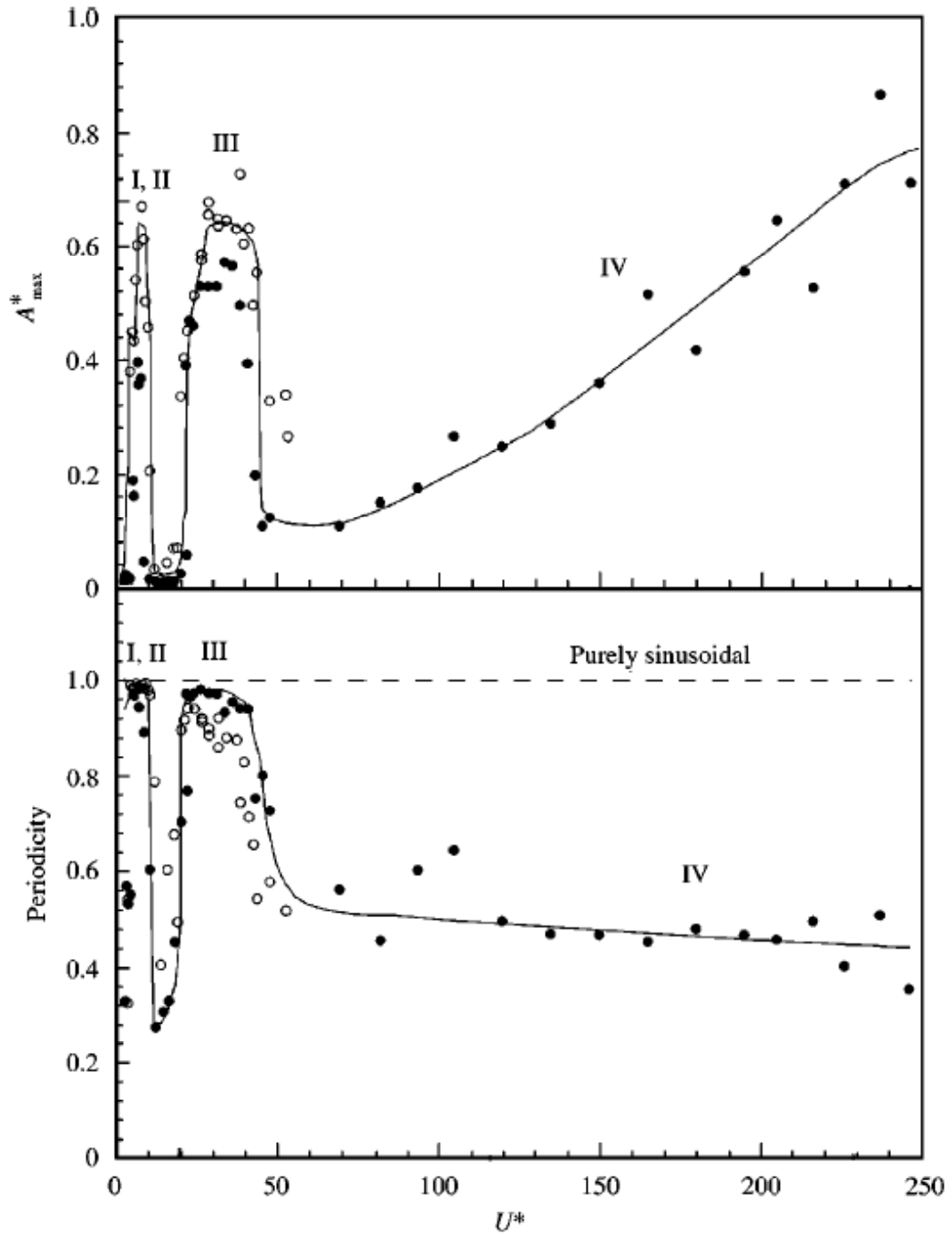


Figure 1.4.1. Amplitude response and periodicity ($\sqrt{2}y_{rms}/y_{max}$) for a tethered sphere, showing that the Mode IV response is not sinusoidal (from Jauvtis *et al.* (2001)).

1.5 Scope of the present investigation

In light of the comprehensive background information provided above, we are now able to present the scope of the present investigation. We first note the major limitation experienced by Govardhan

& Williamson (1997) and Williamson & Govardhan (1997): the ability to explore high reduced velocities is limited by the experimental arrangements. This was overcome to some extent by Jauvtis *et al.* (2001) by changing the focus from water tunnels to wind tunnels, albeit by investigating very high mass ratios ($M^* = O(100)$). This enabled reduced velocities up to $U^* = 300$ to be explored, and as a result, four distinct modes of sphere response were observed, two of which were observed for low mass ratios ($M^* = O(1)$).

This problem is also overcome numerically, simply because the range of Froude numbers (and hence reduced velocities) that is possible to investigate is infinite, as will be shown in Chapter 2. We observe that for the case of the flow-induced vibrations of a tethered sphere, the mass ratio is perhaps the most important parameter, and accordingly we choose to look at two distinct mass ratios: $M^* = O(0.1)$ and $M^* = O(1)$. For the $M^* = O(1)$ case, the tether length is also varied from $L^* = 5$ up to $L^* = 10$, in order to investigate to what extent the changes in the tether length affect the sphere response. Like Jauvtis *et al.* (2001), we examine higher reduced velocities, and undertake a detailed analysis into the flow physics with the intention of describing and characterizing the resultant motion of the tethered sphere. In addition, we present results for the first time of the theoretically important case of a neutrally buoyant tethered sphere, $M^* = 1$.

This thesis is organized as follows. In Chapter 2, we present the methods used to investigate the motions of a tethered sphere in a uniform flow. Derivations of the governing equations of motion for the sphere are performed in §2.1, and the procedure for time integration of these equations is shown in §2.2. In §2.3, we briefly discuss the spectral element method and its applications in unsteady flows, followed by the major differences in the numerical and experimental simulations in §2.4. We also examine a few visualization techniques presently used to elucidate vortical structures in complex flows (§2.5). Mesh independence is verified for a stationary sphere in §2.6 for Reynolds numbers of $Re = 300$ and $Re = 500$. Finally, the effect of the convergence criteria and the relaxation parameter is presented for a tethered sphere in §2.7 and the experimental method and setup is explained in §2.8.

A discussion of the results commences in Chapter 3. We first look at a stationary sphere in Chapter 3 and examine the flow structures observed at particular Reynolds numbers up to $Re = 500$. These results are then used as a basis of comparison to analyze the effect of sphere rotation as presented in Chapter 4. In particular, we examine in detail the outcomes of low-velocity rotations about the non-streamwise (§4.2) and streamwise (§4.3) axes respectively. We then proceed to study the flow-induced vibrations of a three-dimensional tethered sphere. We present findings in relation to the topic of this thesis, namely the flow-induced vibrations of a tethered sphere in Chapter 5, and look at a range of mass ratios and tether lengths, with the aim of examining the underlying physical mechanisms generating the observed motions.

In Chapter 6, we briefly summarize the results found in Chapters 3 - 5 for the four cases examined. Finally, a full list of references is presented at the end of the thesis.

Chapter 2

Methodology and Mesh Independence

The flow-induced vibration of a tethered sphere when immersed in a uniform flow is a problem that has been investigated recently by experimental techniques exclusively. This study aims to investigate the dynamics of a tethered sphere computationally, which will be of great practical use to the ocean engineering industry. Furthermore, direct numerical simulations are employed without any turbulence or sub-grid scale models and, as a result, only laminar flow is under consideration, whereas the experiments described in the previous chapter were performed in turbulent flow conditions. The use of DNS enables the accurate evaluation of pressure, velocity and other flow variables of interest, in contrast to experimental techniques that do not provide as much insight to the flow physics.

Since the geometry is axisymmetric, we employ a spectral-element discretization for the plane of symmetry. A Fourier expansion is used in the azimuth to extend the model to three dimensions. This chapter describes the implementation of this numerical procedure. In addition, tests are performed to verify the accuracy of the method as well as mesh independence. Furthermore, present techniques of vortex visualization are discussed and the experimental procedure used to analyze the response of the tethered sphere at low Reynolds numbers is outlined in the final section.

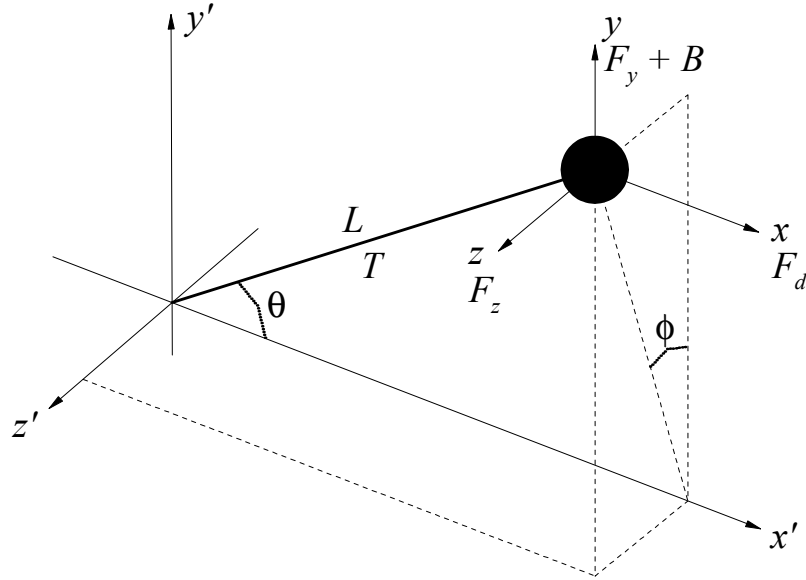


Figure 2.1.1. The problem geometry and coordinate system.

2.1 Problem formulation and governing equations of the tethered sphere

We examine the flow-induced vibrations of a tethered sphere using a spectral-element/spectral numerical method. The problem geometry and coordinate system is shown in Figure 2.1.1. The forces acting on the sphere are of three types: a *structural* force T (the tension in the tether); a *buoyancy* force B ; and the *fluid* forces F_d , F_y and F_z , which denote the components of the fluid forces acting in the x -, y -, and z -directions respectively. We make only one assumption: the tether is presumed to be inextensible, ie. there is no radial movement along the tether axis. This assumption turns out to be a very good one, as Williamson (private communication, 2002) points out that experimentally there appears to be very little movement in the radial direction.

A free-body diagram of the sphere shows that the tension in the tether is linked to the buoyancy and fluid forces by the relation

$$T = F_d \cos \theta + (F_y + B) \sin \theta \cos \phi + F_z \sin \theta \sin \phi . \quad (2.1.1)$$

We now invoke Newton's 2nd Law of Motion to relate the acceleration of the sphere in terms of the forces acting on it as

$$m\ddot{x} = F_d - T \cos \theta \quad (2.1.2)$$

$$m\ddot{y} = (F_y + B) - T \sin \theta \cos \phi \quad (2.1.3)$$

$$m\ddot{z} = F_z - T \sin \theta \sin \phi. \quad (2.1.4)$$

In order to avoid repetition, we will now work with only the x -component equation of motion, Equation (2.1.2). We then substitute Equation (2.1.1) into Equation (2.1.2) and collect like terms to yield

$$m\ddot{x} = F_d \sin^2 \theta - \left\{ (F_y + B) \cos \phi + F_z \sin \phi \right\} \sin \theta \cos \theta. \quad (2.1.5)$$

Equation (2.1.5) is in dimensional form, so the non-dimensional forms of the fluid forces and buoyancy are used (see nomenclature) to obtain

$$\ddot{x} = \left(\frac{\rho}{\rho_s} \right) \left(\frac{U^2 A}{2V} \right) \left[C_d \sin \theta - \left\{ \left(C_y + \left(1 - \frac{\rho_s}{\rho} \right) \frac{2gV}{U^2 A} \right) \cos \phi + C_z \sin \phi \right\} \cos \theta \right] \sin \theta. \quad (2.1.6)$$

Figure 2.1.1 is used to relate the polar coordinates in Equation (2.1.6) to Cartesian coordinates. The acceleration of the sphere thus becomes:

$$\ddot{x} = \left(\frac{\rho}{\rho_s} \right) \left(\frac{U^2 A}{2VL^2} \right) \left[(L^2 - x^2) C_d - \left\{ \left(C_y + \left(1 - \frac{\rho_s}{\rho} \right) \frac{2gV}{U^2 A} \right) y + C_z z \right\} x \right]. \quad (2.1.7)$$

Finally, the governing parameters in Equation (2.1.7) are defined as follows:

$$M^* = \frac{m_s}{m_f} \equiv \frac{\rho_s}{\rho} \quad (2.1.8)$$

$$\alpha = \frac{2gV}{U^2 A} \equiv \frac{4}{3} \frac{1}{Fr^2} \quad (2.1.9)$$

$$\gamma = \frac{U^2 A}{2V} \equiv \frac{3}{4} \frac{U^2}{D}. \quad (2.1.10)$$

Note that Equations (2.1.8) and (2.1.9) define non-dimensional parameters, whereas γ defined in Equation (2.1.10) has units of acceleration.

Substitution of the above parameters into Equation (2.1.7) results in the following equations of motion for the tethered sphere, where the y - and z -components are included for completeness:

$$\frac{\ddot{x}}{\gamma} = \frac{1}{M^*} \left[\left(1 - \left(\frac{x}{L} \right)^2 \right) C_d - \left\{ \left(C_y + (1 - M^*) \alpha \right) \frac{y}{L} + C_z \frac{z}{L} \right\} \frac{x}{L} \right] \quad (2.1.11)$$

$$\frac{\ddot{y}}{\gamma} = \frac{1}{M^*} \left[\left(1 - \left(\frac{y}{L} \right)^2 \right) \left(C_y + (1 - M^*) \alpha \right) - \left\{ C_d \frac{x}{L} + C_z \frac{z}{L} \right\} \frac{y}{L} \right] \quad (2.1.12)$$

$$\frac{\ddot{z}}{\gamma} = \frac{1}{M^*} \left[\left(1 - \left(\frac{z}{L} \right)^2 \right) C_z - \left\{ C_d \frac{x}{L} + (C_y + (1 - M^*)\alpha) \frac{y}{L} \right\} \frac{z}{L} \right]. \quad (2.1.13)$$

It is apparent from the form of Equations (2.1.11), (2.1.12) and (2.1.13) that the dynamics of the tethered sphere are described by a set of coupled, nonlinear equations. Thus, the solutions of these equations are best tackled with a predictor-corrector technique.

Solving fluid-structure interaction problems generally involves the use of deforming and/or moving computational domains. The arbitrary Lagrangian-Eulerian (ALE) formulation has been used successfully in the past for spectral discretizations involving flow-induced vibrations (see, for example, Warburton & Karniadakis (1996)). However, for the tethered sphere problem the difficulty of using a deforming mesh is avoided by attaching the reference frame to the sphere. Using Figure 2.1.1, this mapping is given by the following transformation:

$$x = x' + X(t) \quad (2.1.14)$$

$$y = y' + Y(t) \quad (2.1.15)$$

$$z = z' + Z(t), \quad (2.1.16)$$

where

$$X(t) = L \cos \theta(t) \quad (2.1.17)$$

$$Y(t) = L \sin \theta(t) \cos \phi(t) \quad (2.1.18)$$

$$Z(t) = L \sin \theta(t) \sin \phi(t). \quad (2.1.19)$$

Similarly, the velocity and pressure fields are transformed as follows:

$$\mathbf{u} = \mathbf{u}' + \frac{\partial \mathbf{X}}{\partial t} \quad (2.1.20)$$

$$p = p' \quad (2.1.21)$$

where $\mathbf{X} = (X, Y, Z)(t)$.

Equations (2.1.14) - (2.1.16) provide the relationship between an inertial coordinate system (denoted by a prime) and the non-inertial coordinate system attached to the sphere. The equations for the tethered sphere ((2.1.11) - (2.1.13)) and the fluid (to be discussed in §2.3) are solved in the non-inertial coordinate system and, for the purposes of presenting the results, are transformed back to the original coordinate system using Equations (2.1.14) - (2.1.16).

2.2 Time-advancement of governing equations

The equations governing the motion of the fluid are the unsteady, viscous, incompressible Navier-Stokes and continuity equations:

$$\frac{\partial \mathbf{u}}{\partial t} = -\frac{1}{\rho} \nabla p + \nu \mathbf{L}(\mathbf{u}) + \mathbf{N}(\mathbf{u}) - \mathbf{A}(\mathbf{X}, \mathbf{u}, p) \quad (2.2.1)$$

$$\nabla \cdot \mathbf{u} = 0, \quad (2.2.2)$$

written here in the reference frame of the sphere, where $\mathbf{u} = \mathbf{u}(z, r, \theta, t) = (u, v, w)(t)$ is the velocity field, $\mathbf{N}(\mathbf{u})$ represents nonlinear advection terms and $\mathbf{A}(\mathbf{X}, \mathbf{u}, p)$ is an additional acceleration introduced by the transformation (2.1.14) - (2.1.16) and is equivalent to the acceleration of the body. The variables z , r , θ , and t are the axial, radial, azimuthal and time coordinates and u , v , w are the velocity components in the axial, radial and azimuthal directions. The nonlinear operator in Equation (2.2.1) is defined as:

$$\mathbf{N}(\mathbf{u}) = -(\mathbf{u} \cdot \nabla) \mathbf{u}. \quad (2.2.3)$$

Also, the linear operator $\mathbf{L}(\mathbf{u})$ in Equation (2.2.1) is defined as

$$\mathbf{L}(\mathbf{u}) \equiv \nabla^2 \mathbf{u} = \nabla(\nabla \cdot \mathbf{u}) - \nabla \times (\nabla \times \mathbf{u}). \quad (2.2.4)$$

Because splitting methods generally result in inconsistent boundary conditions, splitting errors result which appear in the form of boundary layers in the velocity-divergence field (Karniadakis & Henderson (1998)). To minimize these splitting errors, we use a time-splitting algorithm developed by Karniadakis *et al.* (1991) that introduces a new pressure boundary condition. This reduces the thickness of the divergence boundary layers to $O(\nu \Delta t)^J$, where J is the order of the time-integration scheme employed. The advantage of this scheme is that it reduces the coupled system of Equations (2.2.1) and (2.2.2) into a set of separately solvable equations for the pressure and velocity, which is crucial in high-resolution computations for flows in complex geometries (Karniadakis (1990)).

Using this scheme, the velocity and pressure fields are propagated over a time interval Δt to determine the fields \mathbf{u}^{n+1} , p^{n+1} in three substeps. However, given the initial displacement of the sphere, we first predict the velocity of the sphere (\mathbf{u}_B) and its displacement (\mathbf{x}_B) at the new time instant ($n + 1$). For the first time through the loop, this is given by:

$$\mathbf{u}_B^{(n+1)*} = 3\mathbf{u}_B^{(n)} - 3\mathbf{u}_B^{(n-1)} + \mathbf{u}_B^{(n-2)} \quad (2.2.5)$$

$$\mathbf{x}_B^{(n+1)*} = \mathbf{x}_B^{(n)} + \frac{5\mathbf{u}_B^{(n+1)*} + 8\mathbf{u}_B^{(n)} - \mathbf{u}_B^{(n-1)}}{12} \Delta t. \quad (2.2.6)$$

Note that Equation (2.2.5) is just quadratic extrapolation from known values at the previous timesteps.

With these new estimates of the displacement and velocity of the sphere, we proceed to solve the fluid equations (2.2.1) - (2.2.4). The first substep involves solving the convective (nonlinear) terms for an intermediate velocity field $\hat{\mathbf{u}}$ as follows:

$$\frac{\hat{\mathbf{u}} - \mathbf{u}^{(n)}}{\Delta t} = N(\mathbf{u}) - \left[\frac{\mathbf{u}_B^{(n+1)} - \mathbf{u}_B^{(n)}}{\Delta t} \right], \quad (2.2.7)$$

where the term in brackets is the acceleration of the sphere $\mathbf{A}(\mathbf{X}, \mathbf{u}, p)$. For the first time through the loop, Equation (2.2.7) is solved using a third-order Adams-Bashforth scheme. For subsequent iterations, we use a third-order Adams-Moulton method. The solution of Equation (2.2.7) is then given by:

$$\hat{\mathbf{u}}^{(n+1)} = \mathbf{u}^{(n)} + \Delta t \sum_{q=0}^{J-1} \alpha_q N^{(n-q)} - \left(\mathbf{u}_B^{(n+1)} - \mathbf{u}_B^{(n)} \right) \quad (2.2.8)$$

for the first time through the loop and

$$\hat{\mathbf{u}}^{(n+1)} = \mathbf{u}^{(n)} + \Delta t \sum_{q=0}^{J-1} \beta_q N^{(n+1-q)} - \left(\mathbf{u}_B^{(n+1)} - \mathbf{u}_B^{(n)} \right) \quad (2.2.9)$$

for subsequent iterations, where the constants α_q, β_q are the Adams-Bashforth and Adams-Moulton coefficients respectively and are compiled in Table 2.2.1 for schemes of order J (see Chapra & Canale (1998) or Gear (1973)).

J	α_0	α_1	α_2	β_0	β_1	β_2
1	1					
2	3/2	-1/2		1/2	1/2	
3	23/12	-16/12	5/12	5/12	8/12	-1/12

Table 2.2.1. Coefficients for Adams-Bashforth predictors and Adams-Moulton correctors.

The second substep involves solving the equation for the pressure, namely:

$$\frac{1}{\Delta t} (\hat{\mathbf{u}} - \hat{\mathbf{u}}) = -\nabla \bar{p}^{(n+1/2)}, \quad (2.2.10)$$

where $\hat{\mathbf{u}}$ is a second intermediate velocity field. By taking the divergence of Equation (2.2.10) and imposing the continuity constraint that the second intermediate velocity field be divergence-free, a Poisson equation for the pressure is obtained:

$$\nabla^2 \bar{p} - \frac{1}{\Delta t} \nabla \cdot \hat{\mathbf{u}} = 0. \quad (2.2.11)$$

Equation (2.2.11) must be solved together with the appropriate Neumann pressure boundary condition on the surface of the sphere given by

$$\frac{\partial \bar{p}^{(n+1/2)}}{\partial n} = \mathbf{n} \cdot \sum_{q=0}^{J-1} \beta_q \left[N(\mathbf{u}^{n-q}) - \nu \nabla \times \nabla \times \mathbf{u}^{n-q} \right] \text{ on } \Gamma, \quad (2.2.12)$$

where \mathbf{n} is the unit normal to the boundary Γ . Equation (2.2.12) is evaluated using information from the previous time steps, and the rotational form of the viscous term reduces splitting errors at prescribed velocity boundaries to the same order as the time-stepping. At solid or moving walls (ie. the surface of the sphere), the Dirichlet boundary conditions $\bar{\mathbf{u}}_0$ for the fluid velocities are set to match the prescribed wall velocities as given by

$$\mathbf{u}^{(n+1)} = \bar{\mathbf{u}}_0. \quad (2.2.13)$$

The third and final substep involves solving for the diffusion terms as follows:

$$\frac{\mathbf{u}^{(n+1)} - \hat{\mathbf{u}}}{\Delta t} = \nu \mathbf{L}(\mathbf{u}) \quad (2.2.14)$$

This is performed implicitly using a Crank-Nicolson method that is second-order accurate in both space and time, together with a theta scheme modification (see Canuto *et al.* (1988)). This requires the velocity of the reference frame at the boundaries that comes from the current best estimate of $\mathbf{u}_B^{(n+1)}$.

Karniadakis *et al.* (1991) demonstrate that the above scheme produces time-differencing errors in the velocity field that are one order smaller in Δt than the corresponding error in the boundary divergence. In particular, a time-treatment of first-order for Equation (2.2.12) can expect to produce second-order results in the velocity field. Note that higher-order accurate treatments are generally less stable and require reduced timesteps.

We now have estimates of the fluid velocities and pressures at the $(n + 1)$ step. We then use these to calculate the components of the fluid force coefficients acting on the body, ie. the drag, lateral and side force coefficients. The motion (acceleration) of the sphere is then calculated using Equations (2.1.11) - (2.1.13).

The next step is then to update or correct the velocity and displacement of the sphere. For the first time through the loop, these corrections are given by:

$$\mathbf{u}_B^{(n+1)*} = \mathbf{u}_B^{(n)} + \frac{25\ddot{\mathbf{x}}^{(n+1)} - 2\ddot{\mathbf{x}}^{(n)} + \ddot{\mathbf{x}}^{(n-1)}}{24} \Delta t \quad (2.2.15)$$

$$\mathbf{x}_B^{(n+1)*} = \mathbf{x}_B^{(n)} + \frac{5\mathbf{u}_B^{(n+1)*} + 8\mathbf{u}_B^{(n)} - \mathbf{u}_B^{(n-1)}}{12} \Delta t. \quad (2.2.16)$$

For subsequent iterations, the corrections are given as:

$$\mathbf{u}_B^{(n+1)**} = \mathbf{u}_B^{(n)} + \frac{25\ddot{\mathbf{x}}^{(n+1)*} - 2\ddot{\mathbf{x}}^{(n)} + \ddot{\mathbf{x}}^{(n-1)}}{24} \Delta t \quad (2.2.17)$$

$$\mathbf{u}_B^{(n+1)'} = \mathbf{u}_B^{(n+1)*} + \varepsilon \left(\mathbf{u}_B^{(n+1)**} - \mathbf{u}_B^{\{n+1\}*} \right) \quad (2.2.18)$$

$$\mathbf{x}_B^{(n+1)**} = \mathbf{x}_B^{(n)} + \frac{5\mathbf{u}_B^{(n+1)'} + 8\mathbf{u}_B^{(n)} - \mathbf{u}_B^{(n-1)}}{12} \Delta t. \quad (2.2.19)$$

In Equation (2.2.18), we improve the convergence characteristics by employing underrelaxation, in which ε is the relaxation parameter. The underrelaxation parameter was introduced after extensive testing without it found that for some parameter combinations, the method was unstable except for very small timesteps. The introduction of underrelaxation improves the convergence quality considerably. The choice of an optimal value for ε is highly problem-specific and, because we are solving a very large system of PDEs that arise when modeling continuous variations of variables, the efficiency introduced by a wise choice of ε can be extremely important (Chapra & Canale (1998)). This will be further discussed in §2.7.

The local truncation errors introduced by the approximations are typically of the order (Δt^3) for both the third-order Adams-Bashforth predictors and the Adams-Moulton correctors used in the present method, although overall the combined problem is second-order accurate. Even though the errors are small, the position of the sphere drifts away from the surface defined by the tether, although only marginally over a single time step. However, when considering the long time traces that are needed for accurate determinations of oscillation amplitudes and frequencies for example, this position drifting is no longer insignificant. Accordingly, for the present simulations the position of the sphere $\mathbf{x}_B^{(n+1)**}$ is projected onto the surface defined by the tether and, for consistency, the velocity of the sphere is also projected. This stabilizes the scheme without affecting the accuracy.

Finally, convergence of the system is monitored by three convergence criteria. These are represented by the following formulae:

$$\frac{\Delta \mathbf{u}_B}{|\mathbf{u}_B|} < u_{tol} \quad (2.2.20)$$

$$\frac{(\Delta \mathbf{u})_{\max}}{\mathbf{u}_{\max}} < u_{tol} \quad (2.2.21)$$

$$\frac{\Delta \mathbf{F}_B}{\mathbf{F}_B} < F_{tol}. \quad (2.2.22)$$

Equation (2.2.20) states that the normalized change in the velocity of the sphere between iterations must be less than some tolerance u_{tol} , whereas Equation (2.2.21) asserts that the normalized maximum change in the velocity field between iterations must be less than the tolerance u_{tol} at any point in the entire domain. The last convergence criterion ensures that the normalized change in the force of the body between iterations is less than some tolerance F_{tol} . For all of the simulations, the values of u_{tol} and F_{tol} were kept at 0.0001 and 0.01 respectively. If these criteria are not met, then the process restarts at the first substep, ie. the solution of Equation (2.2.7). However, if Equations (2.2.20) - (2.2.22) are satisfied, then we continue to the next step.

2.3 Spatial-discretization: the spectral/spectral-element method

Over the past few decades, three dominant grid-based classes of techniques for solving the Navier-Stokes equations have emerged. These are the finite-difference, finite-element and spectral methods. Recently, the spectral-element method, developed by Anthony Patera and co-workers in the early 1980's, has become one of the most widely used computational tools applied to fundamental flow problems where high accuracy is important. This is mainly because the spectral-element method combines the generality of finite-element methods with the accuracy of spectral methods in a more flexible ratio than is found in either technique alone (Patera (1984)). As a result, complex problems may be studied that yield highly accurate results.

The first unsteady and three-dimensional simulations of flow past a sphere were conducted by Tomboulides *et al.* (1993a). Like the present study, they used a spectral-element discretization in the z - r plane and analysed the flow in φ in its Fourier components because of the inherent periodicity of 2π in the azimuthal direction. Similar spectral-element/spectral methods for axisymmetric geometries in cylindrical coordinates have been employed by Tomboulides (1992), Tomboulides *et al.* (1993b), Ghidersa & Dusek (2000), Thompson *et al.* (2001) and Blackburn & Lopez (2002), to name but a few.

We start by considering the flow past a sphere in cylindrical coordinates z , r and φ , with the origin located at the centre of the sphere. The z -axis is parallel to the asymptotic flow velocity U , r is the distance to the z -axis and φ is the azimuthal angle. Having discussed the semi-discrete formulation in §2.2, we now turn to the spatial discretization of Equations (2.2.1) - (2.2.4). As previously mentioned, due to the homogeneity in the azimuthal direction, the velocity field can be decomposed using a Fourier series expansion in φ by

$$u(z, r, \phi, t) = \sum_{m=0}^{M-1} u_m(z, r, t) e^{im\phi}, \quad (2.3.1)$$

where the two-dimensional complex Fourier modes \mathbf{u}_m are defined as

$$\mathbf{u}_m(z, r, t) = \frac{1}{2\pi} \int_0^{2\pi} \mathbf{u}(z, r, \phi, t) e^{-ik\phi} d\phi \quad (2.3.2)$$

and m is an integer wavenumber. Substitution of Equation (2.3.1) into the governing Equations (2.2.1) - (2.2.2) results in the following transformed equations

$$\frac{\partial u_m}{\partial t} + \mathfrak{S}_m [N(\mathbf{u})]_z = -\frac{1}{\rho} \frac{\partial p_m}{\partial z} + v \left(\nabla_{rz}^2 - \frac{m^2}{r^2} \right) u_m \quad (2.3.3)$$

$$\frac{\partial v_m}{\partial t} + \mathfrak{S}_m [N(\mathbf{u})]_r = -\frac{1}{\rho} \frac{\partial p_m}{\partial r} + v \left(\nabla_{rz}^2 - \frac{m^2+1}{r^2} \right) v_m - v \frac{2im}{r^2} w_m \quad (2.3.4)$$

$$\frac{\partial w_m}{\partial t} + \mathfrak{S}_m [N(\mathbf{u})]_\phi = -\frac{1}{\rho} \frac{im}{r} p_m + v \left(\nabla_{rz}^2 - \frac{m^2+1}{r^2} \right) w_m + v \frac{2im}{r^2} v_m, \quad (2.3.5)$$

where \mathfrak{S}_m refers to a Fourier transform in ϕ , and we have used the following definitions for the gradient and Laplacian

$$\nabla_m = \left(\frac{\partial}{\partial z}, \frac{\partial}{\partial r}, \frac{im}{r} \right) \quad (2.3.6)$$

$$\nabla_m^2 = \frac{\partial^2}{\partial z^2} + \frac{1}{r} \frac{\partial}{\partial r} \left(r \frac{\partial}{\partial r} \right) - \frac{m^2}{r^2} = \nabla_{rz}^2 - \frac{m^2}{r^2}. \quad (2.3.7)$$

It is evident in Equations (2.3.4) - (2.3.5) that there is a strong coupling in the linear terms. Following Orszag (1974), and Tomboulides & Orszag (2000), to decouple these equations we introduce the following change of variables

$$\tilde{v}_m = v_m + iw_m \quad (2.3.8)$$

$$\tilde{w}_m = v_m - iw_m. \quad (2.3.9)$$

Equations (2.3.3) - (2.3.5) then reduce to the uncoupled set

$$\frac{\partial u_m}{\partial t} + \mathfrak{S}_m [N(\mathbf{u})]_z = -\frac{1}{\rho} \frac{\partial p_m}{\partial z} + v \left(\nabla_{rz}^2 - \frac{m^2}{r^2} \right) u_m \quad (2.3.10)$$

$$\frac{\partial \tilde{v}_m}{\partial t} + \tilde{\mathfrak{S}}_m [N(\mathbf{u})]_r = -\frac{1}{\rho} \left(\frac{\partial}{\partial r} - \frac{m}{r} \right) p_m + v \left(\nabla_{rz}^2 - \frac{(m+1)^2}{r^2} \right) \tilde{v}_m \quad (2.3.11)$$

$$\frac{\partial \tilde{w}_m}{\partial t} + \tilde{\mathfrak{S}}_m [N(\mathbf{u})]_\phi = -\frac{1}{\rho} \left(\frac{\partial}{\partial r} + \frac{m}{r} \right) p_m + v \left(\nabla_{rz}^2 - \frac{(m-1)^2}{r^2} \right) \tilde{w}_m, \quad (2.3.12)$$

where

$$\tilde{\mathfrak{S}}_m [N(\mathbf{u})]_r = \mathfrak{S}_m [N(\mathbf{u})]_r + i\mathfrak{S}_m [N(\mathbf{u})]_\phi \quad (2.3.13)$$

$$\tilde{\mathfrak{S}}_m [N(\mathbf{u})]_\phi = \mathfrak{S}_m [N(\mathbf{u})]_\phi - i\mathfrak{S}_m [N(\mathbf{u})]_r. \quad (2.3.14)$$

In practice, we keep only the positive wavenumber half of the spectrum ($m \geq 0$), as the modes possess the symmetry $\mathbf{u}_{-m} = \mathbf{u}_m$. For reasons of efficiency, the z -derivative terms in Equations (2.3.10) - (2.3.12) are computed in Fourier space, whereas the nonlinear products are computed in physical space (Karniadakis (1989)). In other words, the nonlinear substep of the timestepping scheme is performed in physical space, and the second and third substeps are performed in Fourier space.

The time-integration of Equations (2.3.10) - (2.3.12) (as discussed in the previous section) results in a set of Helmholtz-like equations for the velocity and pressure modes. The spatial discretization of these equations in the z - r plane is accomplished using two-dimensional spectral elements, as described in detail in Maday & Patera (1989) and reviewed here for completeness. We break the computational domain up into K elements, called ‘‘spectral elements,’’ where each element is given by $\Omega^k = [a^k, b^k]$. The dependent and independent variables in each spectral element are approximated by tensor-product polynomial expansions of order N . The Helmholtz equations are of the form

$$\frac{1}{r} \frac{\partial}{\partial r} \left(r \frac{\partial}{\partial r} u_m \right) - \frac{m^2}{r^2} u_m - \lambda^2 u_m = g, \quad (2.3.15)$$

where u_m is either a velocity or pressure Fourier mode, and the constant λ^2 is equal to zero for the pressure and $\gamma_0/(v\Delta t)$ for the velocity equations (where γ_0 is a coefficient associated with the order of the time-stepping used). To simplify the notation, Equation (2.3.15) may be written as

$$(\nabla^2 - \lambda^2)\phi = g, \quad (2.3.16)$$

subject to Dirichlet or Neumann boundary conditions on $\partial\Omega$.

The variational statement equivalent to Equation (2.3.16) is well documented in the finite-element literature (see Gresho & Sani (2000)). However, numerically we work with the weighted residual approximation resulting from Equation (2.3.16), so that the problem is thus: Find $\phi \in H_0^1(\Omega)$ such that

$$\int_{\Omega} \nabla \psi \cdot \nabla \phi \, d\mathbf{x} + \lambda^2 \int_{\Omega} \psi \phi \, d\mathbf{x} = - \int_{\Omega} \psi g \, d\mathbf{x}, \quad (2.3.17)$$

where $\psi \in H_0^1(\Omega)$ and $H_0^1(\Omega)$ is the Sobolev space for which all functions vanish at the boundary $\partial\Omega$. The spectral element discretization corresponds to numerical quadrature of the variational

statement (Equation (2.3.17)) restricted to the discrete space X_h , which is defined in terms of the parameters K and N . We perform Gauss-Lobatto-Legendre quadrature and select appropriate Gauss-Lobatto points ξ_{pq}^k and corresponding weights $\rho_{pq} = \rho_p \rho_q$, after which Equation (2.3.17) becomes

$$\begin{aligned} & \sum_{k=1}^K \sum_{p=0}^N \sum_{q=0}^N \rho_{pq} J_{pq}^k [\nabla \psi \cdot \nabla \phi]_{\xi_{pq}^k} + \lambda^2 \sum_{k=1}^K \sum_{p=0}^N \sum_{q=0}^N \rho_{pq} J_{pq}^k [\psi \phi]_{\xi_{pq}^k} \\ & = - \sum_{k=1}^K \sum_{p=0}^N \sum_{q=0}^N \rho_{pq} J_{pq}^k [\psi g]_{\xi_{pq}^k} \end{aligned} \quad (2.3.18)$$

where J_{pq}^k is the Jacobian of the transformation from global to local coordinates. The next step is to choose a suitable basis which reflects the structure of the piecewise smooth space X_h (Karniadakis (1990)). We use Lagrange polynomials that provide accuracy of order N for the solution over that particular domain and are given by

$$\phi_i(\xi) = - \frac{(1-\xi^2)L'_N(\xi)}{N(N+1)L_N(\xi_i)(\xi-\xi_i)}. \quad (2.3.19)$$

These polynomials are known as the Gauss-Lobatto-Legendre (GLL) interpolants. The chosen nodes ξ_i are the solutions of the equation

$$(1-\xi^2)L'_N(\xi) = 0, \quad (2.3.20)$$

where $L_N(\xi)$ is the Legendre polynomial of degree N . Singular Sturm-Liouville theory (see Gottlieb & Orszag (1977)) states that the expansion of any smooth function using the GLL interpolants converges exponentially fast, which is an important reason for choosing this basis.

For the present formulation, the GLL interpolants are used in all elements in the entire domain. This departs somewhat from the method employed by Tomboulides (1992), who used Lagrange interpolants based on zeroes of Jacobi (0,1) polynomials in the elements adjacent to the axis of symmetry and GLL interpolants in the rest of the elements. In the present approach, the singular terms in Equations (2.3.10) - (2.3.12) are set equal to zero at the axis. As pointed out by Blackburn & Lopez (2002), for modal variables other than u_0 , \tilde{w}_1 and p_0 , this is equivalent to assuming that values go toward zero faster than r^2 as $r \rightarrow 0$. This retains the efficiency of standard spectral-element techniques as well as preserving spectral convergence for typical axisymmetric problems (see Gerritsma & Phillips (2000)).

Having selected the basis, the dependent and independent variables are expanded in terms of tensor products as

$$(\mathbf{x}, \mathbf{u}, \phi)^k = (\mathbf{x}_{mn}^k, \mathbf{u}_{mn}^k, \phi_{mn}^k) h_m(r_1) h_n(r_2), \quad (2.3.21)$$

where (r_1, r_2) defines a local coordinate system. The functions (2.3.21) are then inserted into (2.3.18) and the test functions ψ_{mn} chosen (which are non-vanishing at only one global node) to arrive at the discrete elemental equations for the Helmholtz operator, given by

$$\left(A_{ijmn}^k - \lambda^2 \hat{B}_{ijmn}^k \right) \phi_{mn}^k = \hat{B}_{ijmn}^k \mathbf{g}_{mn}^k, \quad (2.3.22)$$

where A_{ijmn}^k is the stiffness matrix and \hat{B}_{ijmn}^k is the mass matrix, both of which are defined in Karniadakis (1989). To complete the development, direct stiffness summation is applied to Equation (2.3.22) in order to construct a global assembly of the elemental equations. The advantage of the procedure outlined above is that the separate elliptic equations for the pressure and velocity can be efficiently and robustly solved directly, using direct inversion of the linear matrix problems, that only needs to be performed once at the start of the timestepping. Following this, the pressure and diffusion substeps are efficiently tackled using only matrix multiplications.

2.4 Differences between experimental and numerical simulations

The work of Govardhan & Williamson (1997), Williamson & Govardhan (1997) and Jauvtis *et al.* (2001) highlights the differences involved when performing experiments and running numerical simulations. The problem arises in the need to characterize the motion of the sphere in terms of a suitable parameter. Govardhan & Williamson (1997) realized that scaling their data against the Reynolds number did not provide much insight, but when they scaled against the reduced velocity, a lot more information was made available. This is not surprising, since the reduced velocity (which is the inverse of the system natural frequency) has been used extensively in vortex-induced vibration problems (see Chapter 1).

However, a range of reduced velocity is obtained experimentally by increasing the flow velocity U . This has the undesirable side-effect (numerically speaking) of also increasing the Reynolds number Re . For example, in the experiments of Williamson & Govardhan (1997), a reduced velocity range of approximately $1 < U^* < 9$ was investigated for a mass ratio of $M^* = 0.082$. This corresponded to a Reynolds number range of approximately $750 < Re < 13000$. For a mass ratio of $M^* = 0.76$ (Govardhan & Williamson (1997)), a reduced velocity range of $1 < U^* < 22$ was made possible, corresponding to a Reynolds number range of roughly $1000 < Re < 14000$. Furthermore, Jauvtis *et al.* (2001) investigated mass ratios up to $M^* = 940$, which represented a reduced velocity range of roughly $3 < U^* < 250$. However, the corresponding Reynolds number range was not identified.

Nonetheless, in all cases Reynolds numbers typically of $O(10^3 - 10^4)$ were obtained. This differs greatly from the Reynolds numbers used numerically in the present study, which are typically an order of magnitude smaller. Moreover, the vortex dynamics in the near wake at the Reynolds numbers observed experimentally are essentially inviscid, with the effects of viscosity reduced to setting the boundary layer thickness at separation. Without knowing the precise effect of the Reynolds number, it is impossible to determine *a priori* if similar modes of response will be observed numerically, where the effects of viscosity are more pronounced.

As previously mentioned, a range of reduced velocity is obtained by increasing the flow velocity (and hence Re) experimentally. When performing the computations, however, it is desirable to keep the Reynolds number fixed at a suitable value. This is because if one increases the Reynolds number numerically, smaller scales are gradually introduced as the flow undergoes transition to turbulence. In order to accurately capture these small scales, a finer mesh density is required, which translates to much higher computational overheads. The question is thus whether it is possible to obtain a range of reduced velocities without increasing the Reynolds number.

Thankfully, the answer is yes. The expression for the natural frequency of the tethered sphere system is given by Williamson & Govardhan (1997) as

$$S_n \approx \left(\frac{1}{2\pi} \right) \frac{1}{Fr\sqrt{L^*}} \sqrt{\frac{1-M^*}{C_a + M^*}}, \quad (2.4.1)$$

where C_a is the added mass coefficient for a sphere and is equal to 0.5. The reduced velocity U^* is defined as the inverse of Equation (2.4.1). For any given numerical simulation or experiment performed, the mass ratio and tether length are kept constant. It is apparent then, that the reduced velocity is altered by varying the Froude number Fr , defined as

$$Fr = \frac{U}{\sqrt{gD}}, \quad (2.4.2)$$

where g is the (constant) gravitational acceleration. Evidently, g cannot be altered experimentally, so the only easy way to vary Fr experimentally is to vary the flow velocity U . However, it makes more sense computationally to vary Fr by varying g rather than U . This results in a wide range of reduced velocity U^* , while the Reynolds number is kept constant at some desirable value that is high enough so that the wake is fully three-dimensional and well developed but not fully turbulent. One could also vary U and D in combination, although experimentalists prefer just a single sphere. Furthermore, it is conceivably possible to numerically investigate reduced velocities up to $U^* = \infty$, whereas the range of U^* experimentally is limited to the speeds attainable in the flow facility.

To some, the idea of changing g may seem absurd. On the other hand, as noted by Govardhan & Williamson (1997), over the entire range of Reynolds number (and U^*) in their experiments, they

found that the vibrational response of the tethered sphere was essentially *independent* of the Reynolds number, but was a strong function of the reduced velocity. As a result, it is expected that similar large-amplitude oscillations will occur numerically although the Reynolds number is much smaller.

The next question is, what Reynolds number should be used for the numerical simulations? Due to the high costs of computational time, Re should be restricted to the laminar flow regime. Because the experimental conditions dictate that the flow is highly unsteady and aperiodic, the same conditions should be observed numerically. This means that the (numerical) Reynolds number should be greater than approximately $Re = 375$ (Mittal (1999b)), corresponding to the Reynolds number at which planar symmetry is lost. Furthermore, to avoid the appearance of small scales in the flow, the Reynolds number should be less than approximately $Re = 800$ (Tomboulides & Orszag (2000)). Thus, the most reasonable Reynolds numbers lie in the range $375 < Re < 800$. For all the simulations and results for the tethered sphere presented in Chapter 5, a Reynolds number of $Re = 500$ was chosen unless otherwise noted.

Also note that on the related problem of a cylinder undergoing vortex-induced vibration, Blackburn *et al.* (2000) found that two-dimensional direct numerical simulations at a Reynolds number of $Re = 556$ (corresponding to a reduced velocity of $U^* = 5$) were inadequate for predicting the full nature of the response envelope and of the vortex shedding mechanics. However, three-dimensional simulations revealed computationally for the first time the existence of the 2P shedding mode, and the response amplitudes, although somewhat smaller than the corresponding experimental results at the same Reynolds number, were similar and imitated the experimentally observed behaviour quite well.

In addition, the large-scale vortex dynamics that are observed in the wake of a stationary sphere for Re in the tens of thousands are fundamentally the same as those observed in the unsteady aperiodic regime ($Re > 375$), as indicated by Sakamoto & Haniu (1995). In conclusion then, we expect numerically to obtain large-amplitude oscillations for the tethered sphere at a Reynolds number of $Re = 500$, although whether or not the four distinct modes of vibration observed experimentally will also be captured numerically is still a matter for debate.

2.5 Numerical flow visualization techniques

There are a number of flow visualization techniques that are used by numericists to visualize vortex structures for laminar and turbulent flows. However, in order to identify vortical regions in complex flows, it is first necessary to define what exactly is a vortex. This simple question still lacks an

accepted answer. The definitions in §§2.5.1 – 4 for identifying vortex structures are the most widely accepted classifications used today.

Lamb (1945) defined a vortex simply as the fluid contained within a vortex tube. This uncomplicated definition, however, does not apply to wall bounded flows, such as the laminar flow through a pipe in which there exists a vortex tube but obviously no vortex. Similarly, local pressure minima, pathlines and streamlines (Lugt (1979)) have been used intuitively to identify vortical regions. In order to clarify the debate, Jeong & Hussain (1995) have summarised the current techniques and have proposed the following requirements for a *vortex core* (since the size of a vortex in a viscous fluid depends on the identifier's threshold selected):

- (1) A vortex core must have a net vorticity (and hence circulation). Thus, potential flow regions are excluded from vortex cores.
- (2) The geometry of the identified vortex core should be Galilean invariant, ie. independent of the frame of reference.

Unfortunately, the above requirements do not result in a unique identification scheme. The following identification methods all satisfy the above requirements and are compared in order to obtain an identification scheme that is best suited for the unsteady viscous flow past bluff bodies.

2.5.1 Vorticity

The vorticity magnitude ($|\boldsymbol{\omega}|$) has been used for decades to elucidate coherent structures and recently to identify vortex cores (see, for example, Hussain & Hayakawa (1987)). For the present purposes, however, this approach may not be very satisfactory because ($|\boldsymbol{\omega}|$) does not properly identify vortex cores in a shear flow, especially if the background shear is comparable to the vorticity magnitude. In the fore-mentioned case of laminar flow through a pipe, the maximum vorticity magnitude occurs immediately near the wall, and is characterized by shear, although there are by no means any swirling motions. The same may be said of the dynamics of coherent structures in near-wall turbulence (Schoppa & Hussain (2000)). Although these examples concern bounded flows, even in free shear flows the use of the vorticity magnitude as a vortex core identification scheme may prove potentially difficult. For example, Virk *et al.* (1994) investigated an axisymmetric vortex with a strong axial variation in vorticity, and found that a vorticity magnitude surface may terminate along the vortex axis (indicating segmented vortices) although there is only one continuous vortex column. However, note that for the present problem the background is not a shear flow.

For bluff body flows (especially circular cylinders), both experiments and numerical simulations have relied on visualizing the vortex structures using the vorticity magnitude. Williamson (1996) investigated the wake of a cylinder experimentally and visualized different modes of vortex shedding (namely modes A & B) in addition to the Kármán vortex street. Numerical visualizations of the vorticity magnitude by Thompson *et al.* (1996) clearly illuminated the same vortex structures. In the unsteady wake of a sphere, however, contours of the vorticity magnitude may not correctly identify the vortices, since the “vortical structures” visualized experimentally may be sole artefacts of dye propagation and may not necessarily correspond to “true” vortex structures, as pointed out by Thompson (private communication, 2003).

2.5.2 Complex eigenvalues of $\nabla\mathbf{u}$

Chong *et al.* (1990) extended the work of Perry & Chong (1987) by studying three-dimensional flow fields from the point of view of the topology of three-dimensional critical points, ie. in a reference frame moving with the velocity of that point. The velocity gradient tensor u_{ij} (or equivalently $\nabla\mathbf{u}$) may be decomposed into a symmetric and antisymmetric component, known as the rate-of-strain and rate-of-rotation tensors respectively, given by $S_{ij} = (u_{ij} + u_{ji})/2$ and $\Omega_{ij} = (u_{ij} - u_{ji})/2$. The eigenvalues σ can be determined by solving the characteristic equation

$$\sigma^3 - P\sigma^2 + Q\sigma - R = 0, \quad (2.5.1)$$

where the invariants P , Q and R are defined as

$$P = S_{ii} \equiv u_{i,i} = 0 \quad (2.5.2)$$

$$Q = \frac{1}{2}(S_{ii}^2 - S_{ij}S_{ji} - R_{ij}R_{ji}) \equiv -\frac{1}{2}u_{i,j}u_{j,i} \quad (2.5.3)$$

$$R = \frac{1}{3}(P^3 - 3PQ + S_{ij}S_{jk}S_{ki} + 3R_{ij}R_{jk}S_{ki}) \equiv \det[u_{i,j}]. \quad (2.5.4)$$

In Equations (2.5.2) and (2.5.3), the incompressibility constraint has been imposed, ie. $u_{i,i} = 0$. Chong *et al.* (1990) propose that a vortex core is a region where the eigenvalues σ are complex, which implies that the local streamline pattern is closed or spirals in a reference frame moving with the point. Complex eigenvalues occur when the discriminant Δ is positive, ie.

$$\Delta = \left(\frac{1}{3}Q\right)^3 + \left(\frac{1}{2}R\right)^2 > 0. \quad (2.5.5)$$

In other words, whether or not a region of vorticity appears as a “vortex” depends on the local rate-of-strain field induced by motions outside of the region of interest. However, the above definition of a vortex core is inadequate when considering coherent structures with core dynamics that exhibit helical vortex lines and strong axial flow (see Melander & Hussain (1993)), and especially for the

proper identification of vortices with non-uniform core sizes. This definition is also not suitable for mixing layers and evolving jets.

2.5.3 The second invariant of $\nabla\mathbf{u}$

Hunt *et al.* (1988) defined an “eddy” as a region with positive second invariant of $\nabla\mathbf{u}$, with the additional constraint that the pressure be lower than the ambient. The second invariant Q is defined in Equation (2.5.3), and represents the local balance between shear strain rate and vorticity magnitude. As shown by Jeong & Hussain (1995), Q vanishes at solid boundaries (as does Δ), unlike the vorticity magnitude. As a result, vortex identification schemes based on Q and Δ do not suffer from the problems associated with the vorticity magnitude, which does not properly represent vortical structures near a wall (see §2.5.1).

Although the definitions based on Q and Δ produce results that are similar in many situations, the inadequacy of the definition based on Q becomes obvious when considering, for example, a conically symmetric vortex, as in the previous section. However, unlike the Δ definition that predicts two separate vortical regions, the Q definition predicts a single vortical region with a narrow hollow core along the axis of the vortex, which is clearly wrong owing to the almost solid-body rotation of the fluid particles along the vortex axis. For most practical cases, the Q definition may be insufficient when considering vortices that are subjected to a strong external strain field.

2.5.4 Negative λ_2

The inconsistencies between the existence of a pressure minimum and a vortex core described at the start of §2.5 arise due to two effects: unsteady straining and viscous effects. By discarding these effects, Jeong & Hussain (1995) proposed a new identification criterion that is based on the Hessian ($p_{,ij}$) of the pressure, which contains information on local pressure extrema. By taking the gradient of the Navier-Stokes equations, the acceleration gradient tensor $a_{i,j}$ (like the velocity gradient tensor) may be decomposed into a symmetric and antisymmetric component as follows:

$$a_{i,j} = \left[\frac{DS_{ij}}{Dt} + \Omega_{ik}\Omega_{kj} + S_{ik}S_{kj} \right] + \left[\frac{D\Omega_{ij}}{Dt} + \Omega_{ik}S_{kj} + S_{ik}\Omega_{kj} \right]. \quad (2.5.6)$$

The second term in brackets in Equation (2.5.6) is antisymmetric and is the well-known vorticity transport equation, whereas the first term in brackets is symmetric and is given by

$$\frac{DS_{ij}}{Dt} - \nu S_{ij,kk} + \Omega_{ik}\Omega_{kj} + S_{ik}S_{kj} = -\frac{1}{\rho} p_{,ij}. \quad (2.5.7)$$

As stated above, the first two terms in Equation (2.5.7) represent unsteady irrotational straining and viscous effects respectively which, when discarded, should provide a better indication for the existence of a vortex. Furthermore, the occurrence of a local pressure minimum in a plane requires two positive eigenvalues of the tensor $p_{,ij}$. Thus, only the third and fourth terms in Equation (2.5.7) determine the existence of a local pressure minimum due to vortical motion. A vortex core is then defined as a connected region with two negative eigenvalues of $\mathbf{S}^2 + \mathbf{\Omega}^2$. With λ_1, λ_2 and λ_3 being the eigenvalues and $\lambda_1 \geq \lambda_2 \geq \lambda_3$, this definition is equivalent to the requirement that $\lambda_2 < 0$ within the vortex core. Jeong & Hussain (1995) investigated a wide variety of flows where the vortex geometry is intuitively clear. They found that for all of the cases examined, the definition based on λ_2 proved to be superior.

To summarize, the vorticity magnitude definition does not have an a priori defined level, so that the identification of vortex boundaries are ambiguous. The definition based on Δ tends to overestimate the size of vortex cores, resulting in noisy boundaries (especially for DNS data). The Q definition, although often producing results similar to that of λ_2 , may be inadequate when vortices are subject to a strong external strain field. On the other hand, the definition based on λ_2 has been used very successfully in the visualization of vortex structures in bluff body flows, especially for spheres (see Johnson & Patel (1999)). As a result, for all flow visualizations presented in this thesis, the vortex identification scheme proposed by Jeong & Hussain (1995) based on λ_2 has been used unless otherwise noted.

2.6 Mesh independence: stationary sphere

A detailed grid resolution study was performed to verify the suitability of the mesh used for all of the simulations of the flow past a stationary sphere. An initial mesh was used which was known to yield acceptable results (see Thompson *et al.* (2001)) and was scrutinized according to the following method.

Two Reynolds numbers were chosen to measure mesh independence: $Re = 300$ and $Re = 500$. The former was selected to yield results that may be compared to both experimental and numerical data by previous investigators (see Chapter 1). Furthermore, at this Reynolds number of $Re = 300$, the flow past a sphere is known to be unsteady and characterized by the presence of periodically shed vortices. However, some of the results presented in Chapter 3 are computed at a Reynolds number of 500 and, as a result, mesh independence needs to be addressed at this extent.

The resolution of the grid was increased by two methods: increasing the order of the polynomial interpolants (p -refinement); and increasing the number of elements in the domain (h -refinement).

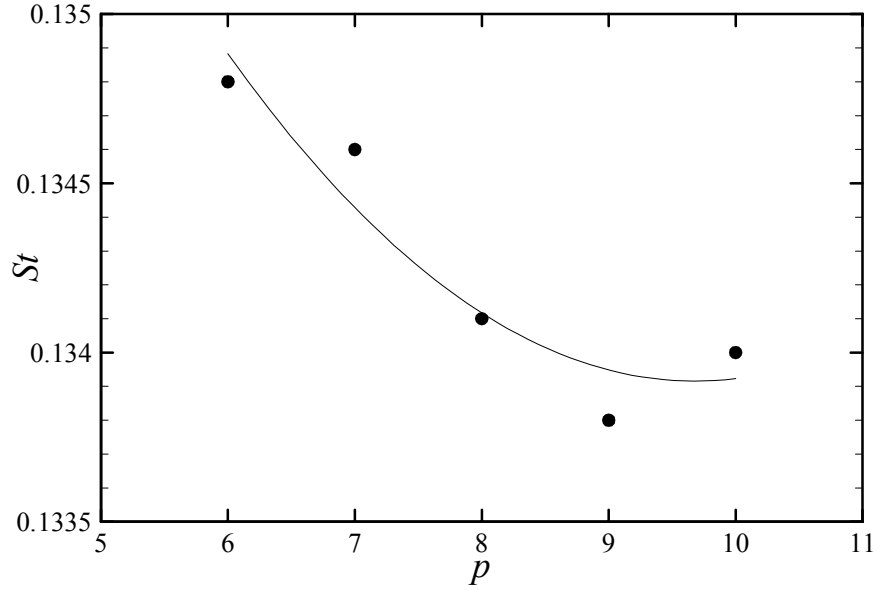


Figure 2.6.1. Variation of the Strouhal number with the order of the polynomial interpolants.

The former is more suited to spectral element methods, due to the exponential convergence inherent in spectral techniques. However, in order to allow for a “cleaner” visualization of the vortex structures in the wake of the sphere, more elements were added to the original mesh. Furthermore, the size of the elements immediately adjacent to the sphere surface was reduced, in order to capture more completely the reduced thickness of the boundary layer at $Re = 500$. Given these adjustments, a p -refinement study was then conducted to obtain the particular value of p that was most suitable for the present applications.

2.6.1 $Re = 300$

At a Reynolds number of $Re = 300$, drag and lift forces were computed, along with calculated vortex shedding frequencies expressed in terms of the Strouhal number St , for values of p in the range $6 < p < 10$. These measurements are compared with those of selected and accepted previous results, namely: Johnson & Patel (1999), Tomboulides & Orszag (2000), Ormieres & Provansal (1999), Sakamoto & Haniu (1995), Sakamoto & Haniu (1990), and finally Roos & Willmarth (1971). As another convergence criterion, velocity fluctuations for the $m = 1$ azimuthal mode were measured in the near wake at a point 1 diameter downstream of the sphere and 0.5 diameter above the wake centreline. The percentage difference (PD) in the solution between the case of interest (p) and the highest resolved simulation ($p = 10$) is used as the primary indicator of mesh independence. For $PD < 1\%$, we find that adequate resolution is obtained.

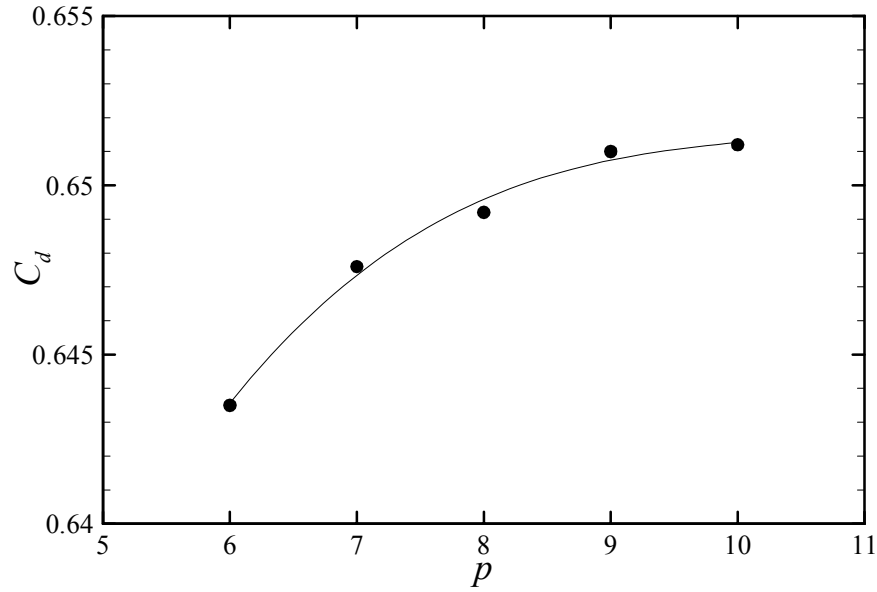


Figure 2.6.2. Variation of the drag coefficient with the order of the polynomial interpolants.

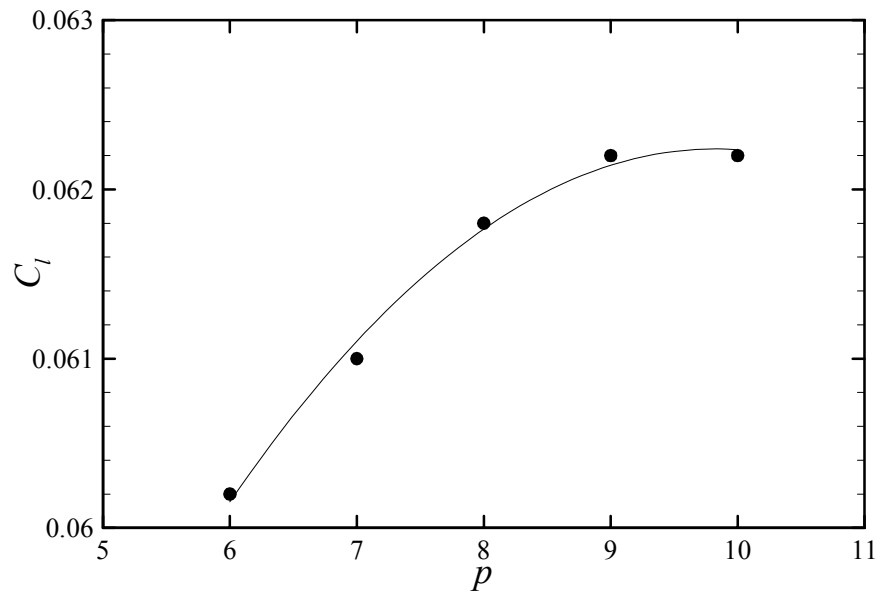


Figure 2.6.3. Variation of the lift coefficient with the order of the polynomial interpolants.

Figure 2.6.1 shows the results of the mesh independence study for the vortex shedding Strouhal frequency. The percentage difference (PD) in the Strouhal number (between the present value and the St for the highest resolved case, ie. $p = 10$) behaves as follows: for $p = 6$, PD = 0.6%; for $p = 7$, PD = 0.4%; for $p = 8$, PD = 0.07%; and for $p = 9$, PD = 0.1%. For all cases, it is evident that the effect of increasing p is marginal, and that adequate resolution is obtained for $p \geq 6$. We also note that the Strouhal number appears to be rather more sensitive to the (area) blockage ratio, as discussed shortly.

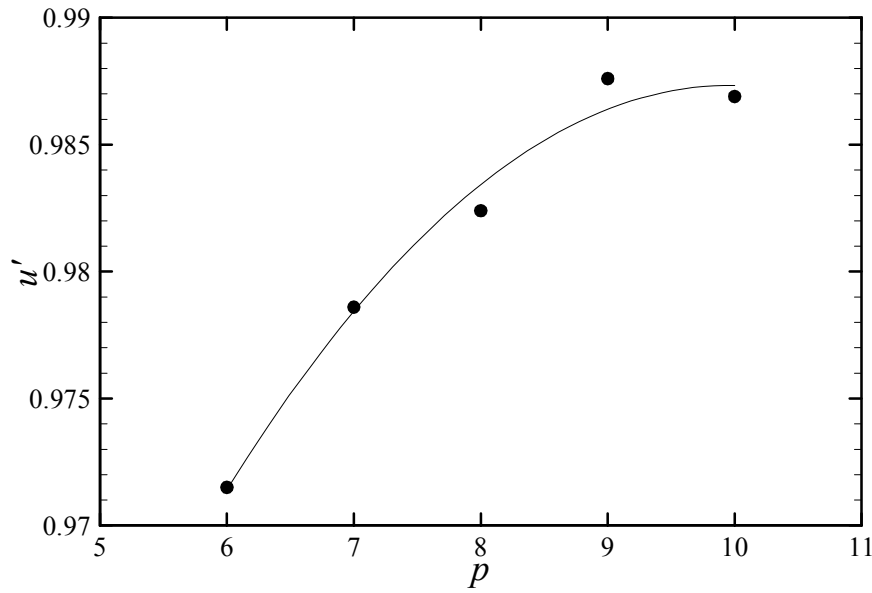


Figure 2.6.4. Variation of the streamwise fluctuating velocity component with the order of the polynomial interpolants.

Figure 2.6.2 summarizes the results of the time-averaged drag coefficient. Again, the percentage differences are: for $p = 6$, PD = 1%; for $p = 7$, PD = 0.6%; for $p = 8$, PD = 0.3%; and for $p = 9$, PD = 0.03%. Furthermore, we find that adequate resolution is obtained for $p \geq 7$.

Figure 2.6.3 depicts the results of the time-averaged lift coefficient. We find that for $p = 6$, PD = 3%; for $p = 7$, PD = 2%; for $p = 8$, PD = 0.6%; and for $p = 9$, PD = 0%. The lift coefficient is obviously more affected by increasing the resolution than the drag coefficient. In this case, we find that adequate resolution is obtained when $p \geq 8$.

Finally, measurements of the streamwise fluctuating velocity component are shown in Figure 2.6.4. For $p = 6$, PD = 2%; for $p = 7$, PD = 0.8%; for $p = 8$, PD = 0.5%; and for $p = 9$, PD = 0.07%. Clearly, adequate resolution is obtained for $p \geq 7$. It is also apparent that due to the spatial position of the point used to extract the fluctuating velocities, which is located near the separating shear layer and hence provides a measure of the velocity gradients there, the resolution in the near wake is satisfactory: this notion is confirmed when examining the smoothness of the vorticity contours, which contains jumps at element boundaries when the resolution is insufficient.

Given the measures employed in the previous paragraphs to determine the most efficient value of p to use for the simulations, we find that the most cost-effective case is obtained when $p = 8$. This is cost-effective in the sense that all scales observed in the flow for Reynolds numbers up to and including $Re = 300$ are clearly resolved, and running the simulations using $p = 8$ is much more efficient than corresponding simulation runs using $p = 9$, which only marginally increases the

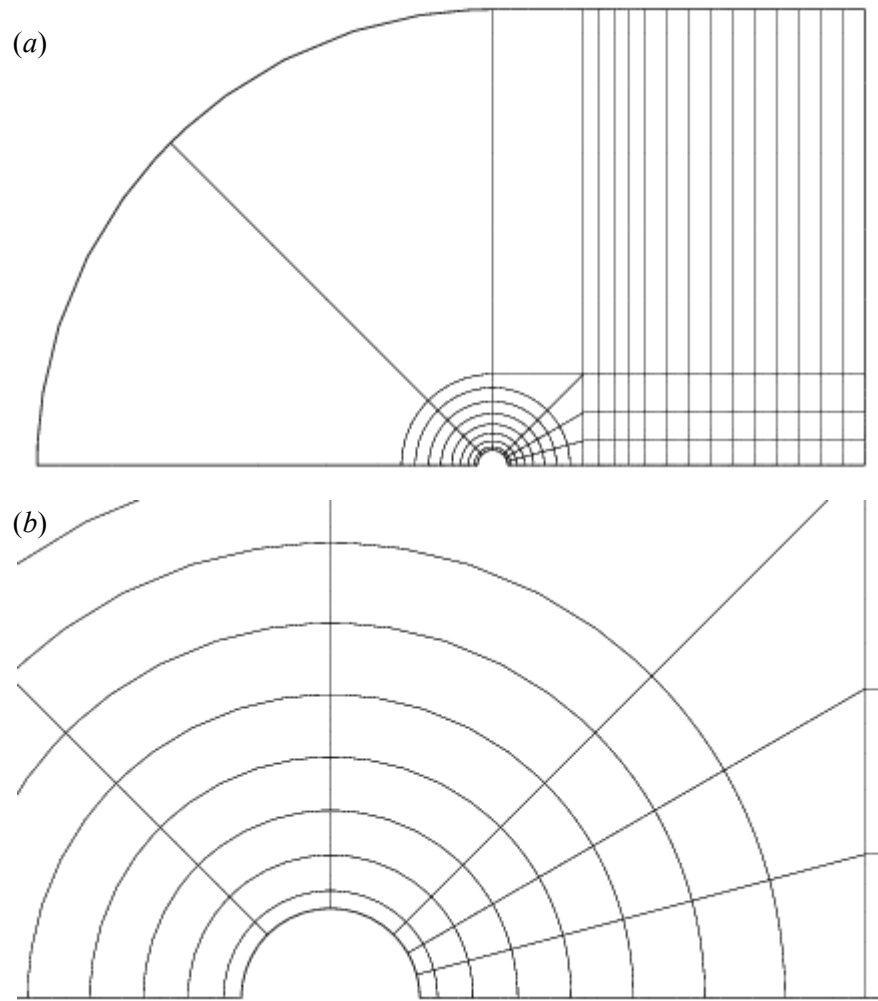


Figure 2.6.5. Mesh used for the stationary and rotating sphere simulations: (a) macro-elements in the entire domain; (b) close-up of the macro-elements around the sphere.

resolution properties. For these reasons, all simulations up to and including Reynolds numbers of $Re = 300$ were simulated using $p = 8$ as the order of the Lagrange polynomial interpolants. The mesh used for these simulations is shown in Figure 2.6.5.

Using $p = 8$ as the basis of the interpolating polynomials, we can now compare the values of C_d , C_l , and St to previous measurements and calculations by other authors, namely those cited at the beginning of this chapter. Table 2.6.1 shows the results of this comparison.

Reference	C_d	C_l	St
Present simulations	0.6492	0.0656	0.134
Tomboulides & Orszag (2000)	0.6714	n/a	0.136
Johnson & Patel (1999)	0.6560	0.0690	0.137
Ormieres & Provansal (1999)	n/a	n/a	0.122
Sakamoto & Haniu (1990)	n/a	n/a	0.15 – 0.18
Sakamoto & Haniu (1995)	n/a	n/a	0.125
Roos & Willmarth (1971)	0.6290	n/a	n/a

Table 2.6.1. Comparison of different flow quantities against previous research.

For all of the variables employed in the comparison in Table 2.6.1, it is clear that the results from the present simulation match those from previous authors, especially those of Tomboulides & Orszag (2000) and Johnson & Patel (1999) who employed computational techniques. The experimental results of Ormieres & Provansal (1999) and Sakamoto & Haniu (1995) yield lower values of St , whereas the results of Sakamoto & Haniu (1990) and Roos & Willmarth (1971) yield higher values of the Strouhal number, as expected, probably because of the perturbations introduced by the support structures of the sphere and the errors in measuring the vortex shedding frequency.

The effects of blockage were also analyzed by halving the radial and inlet extent of the domain, as well as doubling the extent. The values of C_d , C_l and St were all less than 0.1% different to that observed in the present simulations in Table 2.6.1, and hence are not depicted here. Furthermore, changing the outlet extent of the domain to 20D and 40D resulted in negligible difference in all flow quantities.

2.6.2 $Re = 500$

An additional mesh independence study was performed at a Reynolds number of $Re = 500$, primarily because this is the Reynolds number that was chosen for the tethered sphere calculations. In hindsight, although excellent results were obtained for the stationary sphere and the rotating sphere, it appears that the original mesh used for the stationary and rotating sphere simulations for Reynolds numbers up to $Re = 500$ may be unsuitable for the tethered sphere simulations. This is solely due to the motion of the tethered sphere, since the flow variables in the immediate vicinity of the object need to be highly resolved in order to capture the accelerating movements.

The mesh used for the stationary and rotating sphere computations was greatly altered to incorporate the accelerating motion of the tethered sphere. The number of elements around the sphere was increased, in order to resolve the deforming and developing boundary layer on the sphere surface.

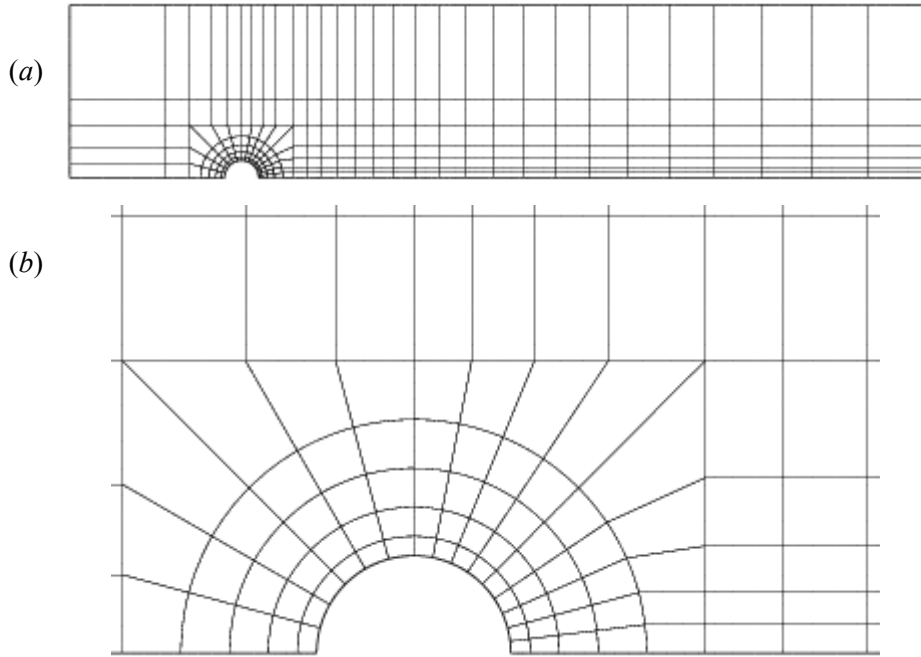


Figure 2.6.6. Mesh used for the tethered sphere simulations: (a) macro-elements in the entire domain; (b) close-up of the macro-elements around the sphere.

The radial and inlet extent of the domain were also decreased to $5D$ for computational efficiency, since it was shown in the previous section that halving the extent produced negligible error. Furthermore, perturbations due to the sphere decay away from the sphere at a rate proportional to $1/r^3$, where r is the distance from the centre of the sphere, as shown by Batchelor (1967). This means that, according to potential theory, at the inlet and radial extent the velocity is less than 0.1% different from the freestream velocity. As a final reworking of the original mesh, it was decided to increase the extent of the outlet to $20D$, simply to capture a minimum of three-to-four vortical structures being shed into the wake. This aids in understanding the vortex dynamics of the wake and hence in determining the origins for the motion of the sphere.

A Reynolds number of 500 was chosen because this is well within the vortex shedding regime for a stationary sphere. The large-scale vortex structures at this Reynolds number are sufficiently strong enough to appreciably affect the motion of the sphere, and the planar symmetry observed at lower Reynolds numbers is not observed at $Re = 500$. Because the flow is unsteady and asymmetric, we expect to qualitatively observe similar behaviour at these low Reynolds numbers to that of higher Reynolds numbers commonly used in experiments cf. Williamson & Govardhan (1997), Govardhan & Williamson (1997), Jauvtis *et al.* (2000). In other words, although the amplitudes of oscillation are likely to be dissimilar, the small-scale structures observed for $Re > 800$ are expected to not substantially affect the vortex shedding characteristics of the flow. The macro-elements for the mesh used for these simulations are shown in Figure 2.6.6.

Also apparent in Figure 2.6.6 is the increased resolution in the immediate vicinity of the sphere. The size of the elements adjacent to the surface of the sphere was chosen according to the boundary layer thickness for axisymmetric laminar boundary layers (Schlichting (1979)). Given these estimates of the boundary layer thickness, the required size of the elements was derived following Tomboulides & Orszag (2000) and Gottlieb & Orszag (1977) for spectral methods. The results are shown in Table 2.6.2 for select Reynolds numbers of $Re = 100, 300, 500$ and 1000 . Note that L_{req} is an estimate of the element thickness required for accurate resolution of the gradient there, and is obtained using the approximation $L_{req} \approx N^2 \delta / 8$ for a polynomial of degree 8 (Gottlieb & Orszag (1977)).

Re	100	300	500	1000
δ	0.113	0.065	0.05	0.035
L_{req}	0.69	0.40	0.31	0.21
L_{used}	0.1	0.1	0.1	0.1

Table 2.6.2. Estimated and required element thickness for accurate resolution of the boundary layer for Reynolds numbers less than $Re = 1000$.

It is apparent that the size of the elements close to the sphere surface, as well as the order of the interpolating polynomials used within the elements, is more than sufficient to accurately resolve the strong gradients generated at the surface of the sphere as well as the near wake dynamics for all the Reynolds numbers of interest in this study. Furthermore, a quick calculation shows that polynomials of degree 5 can be used for accurate resolution of the boundary layer, even for a Reynolds number of $Re = 1000$. However, for the purposes of precisely capturing the near wake vortex dynamics, as well as the evolution of the vortices as they convect into the far wake, 8th-order Lagrange interpolants were used in all elements for $Re \leq 500$.

Having gone through the intensive process of achieving an accurate (2-D) mesh, the final issue remains concerning the accuracy of the results with respect to the *azimuthal* resolution. This was examined by altering the number of physical planes (ie. double the number of Fourier modes) in the azimuthal direction. For Reynolds numbers of $Re \leq 300$, it was shown that 24 Fourier planes were sufficient to yield accurate results. The flow in this regime was found to be unsteady, although a plane of symmetry was observed in the wake (see Chapter 3). However, at a Reynolds number of $Re = 500$, the flow is known to be unsteady and asymmetric, and the variations of the vortex orientation in the azimuthal direction, as well as the smaller scales observed in the flow, need to be accurately resolved. As a result, the number of Fourier planes was increased from $k = 24$ to $k = 32$ for simulations in the range $300 \leq Re \leq 500$. For spectral element methods, this resolution is known to be sufficient (Tomboulides & Orszag (2000)). Nevertheless, to confirm the validity of this choice for

k , drag and lift coefficients were determined for $k = 24$ and $k = 32$ at a Reynolds number of $Re = 500$. Furthermore, the effect of increasing the 2-dimensional resolution was also examined by increasing p from $p = 6$ to $p = 9$ for each value of k . The results of this analysis are shown in Tables 2.6.3 – 4.

p	C_d	C_l
6	0.563	0.057
7	0.566	0.056
8	0.565	0.055
9	0.567	0.057

Table 2.6.3. Drag and lift coefficients for $k = 24$.

p	C_d	C_l
6	0.566	0.058
7	0.566	0.055
8	0.566	0.056
9	0.565	0.058

Table 2.6.4. Drag and lift coefficients for $k = 32$.

For all of the drag and lift coefficients shown in Tables 2.6.3 – 4, the simulations were run for a total non-dimensional time of $\Delta t^* = 1000$ units. For each value of p analyzed, the difference in the drag coefficient between $k = 24$ and $k = 32$ was less than 0.5%, whereas the difference in the net lift coefficient between $k = 24$ and $k = 32$ was less than 3%. However, due to the highly unsteady and aperiodic nature of the flow, a sufficiently long time trace is needed in order to obtain reasonable comparisons. Although the difference in C_l may be considered negligible, as a precaution all results presented in the following Chapters were simulated with $p = 8$ and $k = 32$.

2.7 Tethered sphere: dependence on ε and the convergence criteria

Knowing that the results are essentially independent of the mesh, we now proceed to examine the effects of altering the relaxation parameter ε . To this extent, we look at a typical tethered sphere simulation, in this case with the parameters $M^* = 0.8$ and $L^* = 10$ at two different reduced velocities, $U^* = 8$ and $U^* = 20$. The quantities chosen for evaluation of the relaxation parameter independence

are the time-averaged normalized x - and y -locations of the centre of the sphere, the root-mean-square (RMS) z -vibrational response of the sphere (since we are interested in the response of the tethered sphere in relation to ε) as well as the RMS drag coefficient. Furthermore, the average layover angle θ is also shown since this is the quantity that is the easiest to measure experimentally. In all cases, a sampling period of $\Delta t^* = 800$ time units has been used to calculate all quantities unless otherwise noted.

Relaxation parameters in the range $0.2 < \varepsilon < 0.8$ were investigated. For the tethered sphere simulations, the purpose of changing ε is to improve the convergence rate properties of the solver, rather than to improve the converged *solution*. As a result, increasing ε from 0.2 to 0.8 is not expected to significantly alter the vibrational response of the tethered sphere. The results of these simulations are shown in Table 2.7.1 for $U^* = 8$ and Table 2.7.2 for $U^* = 20$.

ε	x	y	z (RMS)	C_d	θ
0.2	0.724066	9.973752	0.732397	0.776215	85.84777
0.3	0.724069	9.973752	0.732398	0.776218	85.84776
0.4	0.724068	9.973752	0.732397	0.776217	85.84776
0.5	0.724066	9.973752	0.732394	0.776215	85.84777
0.6	0.724070	9.973752	0.732400	0.776219	85.84775
0.7	0.724066	9.973752	0.732401	0.776215	85.84777
0.8	0.723730	9.973776	0.731104	0.775853	85.84970

Table 2.7.1. Effect of changing ε for $U^* = 8$.

ε	x	y	z (RMS)	C_d	θ
0.2	3.203501	9.472992	0.481496	0.578522	71.3159
0.3	3.204034	9.472812	0.515418	0.578629	71.31268
0.4	3.200918	9.473865	0.498837	0.578002	71.33152
0.5	3.203845	9.472876	0.493002	0.578591	71.31382
0.6	3.218523	9.467899	0.529674	0.581547	71.22502
0.7	3.197304	9.475086	0.501480	0.577275	71.35338
0.8	3.210035	9.470782	0.515644	0.579836	71.27641

Table 2.7.2. Effect of changing ε for $U^* = 20$.

For a low reduced velocity of $U^* = 8$, we see that for $\varepsilon < 0.8$ the difference in all quantities measured is extremely small. For example, the x - y displacement of the sphere (and hence the corresponding layover angle θ) may be considered independent of the particular value of ε used. Similarly, the

RMS amplitude response changes by less than 0.001% for relaxation parameters in the range $0.2 < \varepsilon < 0.7$. The maximum change in the drag coefficient is even less significant: within this range of ε , C_d changes by approximately 0.0005%. However, the results for $\varepsilon = 0.8$ are slightly different, mainly because a sampling period of only $\Delta t^* = 500$ time units was used due to unexplained discrepancies in the output of the numerical data. Nevertheless, the maximum change in the x and y displacement is less than 0.05% and 0.0003% respectively, whereas the maximum change in the RMS amplitude response is less than 0.2%. Similarly, the drag coefficient experiences a maximum change of less than 0.05% and the maximum change in the mean layover angle is approximately 0.002%. For practical applications, the maximum changes in all quantities may be considered negligible over the entire range of ε investigated. This is because at this reduced velocity, as we shall see in Chapter 5, the sphere is oscillating sinusoidally and is within the Mode II regime.

For a higher reduced velocity of $U^* = 20$, the sphere is no longer locked-in to the Mode II response. As a result, the motion of the sphere and the drag acting on it are expected to vary more significantly than that observed for $U^* = 8$. That this is indeed the case is clearly seen in Table 2.7.2. For the entire range of ε investigated, the maximum change in the x and y displacements was 0.7% and 0.08% respectively, corresponding to a maximum change in the mean layover angle of roughly 0.2%. However, the maximum change in the z -vibrational response was approximately 10%, whereas the change in the drag coefficient was 0.7%. These higher discrepancies (as opposed to the results at $U^* = 8$) are due mainly to the periodic and highly non-sinusoidal nature of the oscillations, since the layover angle of the tethered sphere at this higher reduced velocity causes greater fluctuations in the fluid forces and hence the vibrational response, as will be shown in Chapter 5. Furthermore, because the response is non-sinusoidal, far longer time traces are required to measure accurate RMS oscillation amplitudes.

Finally, the results should theoretically be independent of the relaxation parameter if they are converged. Thus, it may be of use to test the results against the convergence criteria defined in Equations (2.2.20) - (2.2.22). In light of this, an investigation was performed in which the convergence criteria were decreased an order of magnitude from $u_{tol} = 0.0001$ and $F_{tol} = 0.01$ to $u_{tol} = 0.00001$ and $F_{tol} = 0.001$. This was performed for a single simulation with the parameters $M^* = 0.8$, $L^* = 10$ and $U^* = 8$ and a relaxation parameter of $\varepsilon = 0.5$. The results are depicted in Table 2.7.3.

u_{tol}/F_{tol}	x	y	z (RMS)	C_d	θ
0.0001/0.01	0.724066	9.973752	0.732394	0.776215	85.84777
0.00001/0.001	0.724070	9.973752	0.732399	0.776219	85.84775

Table 2.7.3. Effect of decreasing the convergence criteria for $U^* = 8$, $\varepsilon = 0.5$.

It is evident from Table 2.7.3 that decreasing the convergence criteria by an order of magnitude results in very little to no change in all of the measured quantities. From a practical point of view, the most important is the change in the z -vibrational response of the sphere, which changes by less than 0.0007% when the convergence criteria are decreased an order of magnitude. The minute changes in the quantities of interest are clearly not significant enough to warrant the additional computational time required for the iterations described in §2.2. In conclusion, in all of the results presented in Chapter 5, a relaxation parameter of $\varepsilon = 0.5$ was used, along with the convergence criteria of $u_{tol} = 0.0001$ and $F_{tol} = 0.01$.

2.8 Experimental equipment and setup

The results of Williamson & Govardhan (1997), Govardhan & Williamson (1997) and Jauvtis *et al.* (2001) have shown that a tethered sphere experiences large-amplitude vibrations over a wide range of reduced velocities. However, as previously mentioned, all of these experiments were performed at Reynolds numbers typically in the range $1000 < Re < 14000$. For this range of Reynolds number, the flow past a sphere is turbulent. On the other hand, for Reynolds numbers less than $Re = 800$ (ie. when the flow is laminar), it is not known whether the different modes of vibration that occur at higher Reynolds numbers are also found at these lower Reynolds numbers. In addition, it is not known if the sphere even experiences large-amplitude oscillations in this laminar flow regime. It is the aim of the present experiments to find how the response of the tethered sphere is altered by laminar flow, and in particular if the aforementioned modes of vibration exist within this regime.

These experiments are performed in the Monash FLAIR water channel. Figure 2.8.1 shows a schematic of the experimental equipment and setup. The water channel has a cross-section of 60cm by 80cm, and a maximum speed of 40 cm/s. For the present experimental simulations, the flow velocity varies from $U = 4$ cm/s to $U = 6.2$ cm/s. Since motion is observed primarily in the z -direction, a digital video camera is placed underneath the channel and used to capture the movement of the sphere as the Reynolds number (reduced velocity) is altered. This camera is mounted on 80/20 modular T-slotted aluminium frames and linear bearings to enable highly accurate positioning. Furthermore, the camera is connected to a personal computer and the corresponding displacements of the sphere are measured and analyzed using standard image-processing hardware. Similar data acquisition techniques were employed by Williamson & Govardhan (1997) in their experiments.

For the sole purpose of examining the response of a typical tethered sphere at these low Reynolds numbers, we consider a single polypropylene sphere of diameter 12.7mm, which has a mass ratio of $M^* = 0.91$. The sphere is tethered, using extremely fine superline of diameter 0.1mm, to a thin rod that traverses the water channel. This thin rod is placed at a position that is well below the free

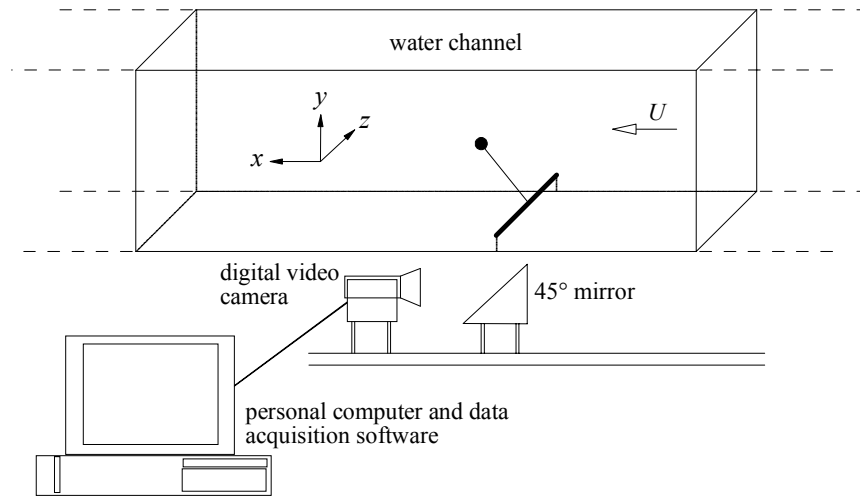


Figure 2.8.1. Schematic of the present experimental equipment and setup.

surface yet far enough from the base of the water channel so as to avoid boundary layer effects. The tethered sphere is thus free to move in all three directions.

Accurate determinations of the oscillation response are obtained by analyzing every single digital video image. The sampling rate of the video feed is 25Hz, so that a characteristic oscillation cycle contains typically 75 data points. The movement of the sphere is calculated by numerically contrasting the bright edge of the sphere surface with the surrounding dark fluid, thereby obtaining displacements that are accurate to within roughly 2 pixels. Furthermore, temporally accurate results are obtained by recording hundreds of oscillation cycles.

Chapter 3

Stationary Sphere

The flow past a stationary sphere undergoes a number of transitions as the Reynolds number increases. §1 in Chapter 1 summarizes the main wake characteristics observed, and are repeated here for conciseness (note that the ranges for the Reynolds number are only approximate):

- $Re < 24$, the wake is laminar, steady, axisymmetric and attached to the sphere;
- $24 < Re < 212$, separated flow is observed;
- $212 < Re < 275$, the wake is non-axisymmetric (or asymmetric). Planar symmetry is still maintained. “Double-thread” or “two-tailed” wake is observed;
- $275 < Re < 350$, the wake is unsteady. Periodic vortex shedding in the form of vortex loops or hairpin vortices is observed;
- $350 < Re < 375$, loss of planar symmetry. Shedding direction oscillates intermittently;
- $375 < Re < 650$, vortex shedding pattern becomes irregular;
- $650 < Re < 800$, the separated cylindrical vortex sheet pulsates and vortex tubes begin to be periodically shed in accordance with the pulsation;
- $800 < Re < 3000$, the vortex loops become turbulent with alternate fluctuations, both high- and low-mode Strouhal numbers coexist.

Four primary Reynolds numbers are considered in this section, to coincide with the major transitions that the wake experiences with increasing Re . These are Reynolds numbers of $Re = 100, 250, 300$ and 500 .

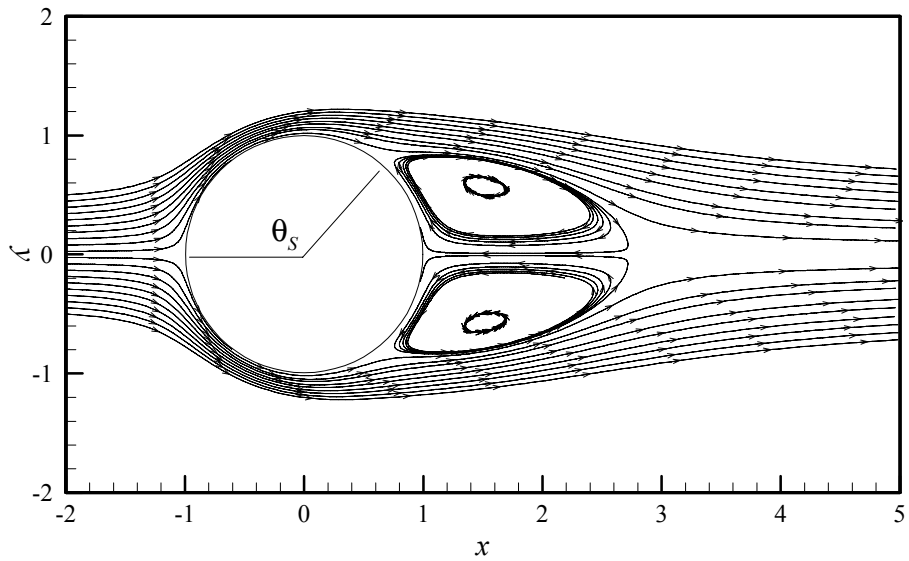


Figure 3.1.1. Computed streamlines for steady axisymmetric flow, $Re = 100$.

3.1 Steady axisymmetric flow

3.1.1 Separation angle, length, vortex location and drag coefficient

At Reynolds numbers less than $Re = 212$ (but greater than 24), the flow was found to be laminar, steady and axisymmetric. It is well known that within this regime, there exists a toroidal vortex in the immediate near wake of the sphere. This is evident in the computed streamline plot shown in Figure 3.1.1 for a Reynolds number of $Re = 100$, which shows the flow separating from the surface of the sphere at an angle θ_s from the front stagnation point and rejoining on the flow centreline at a location x_s (taken from the rear of the sphere) to form a closed separation bubble (or toroidal vortex). The angle of separation shown in Figure 3.1.1 is approximately $\theta_s = 128^\circ$, whereas the separation length is about $x_s = 0.87D$ from the rear of the sphere. These values compare well to those of Taneda (1956), Rimon & Cheng (1969), Pruppacher *et al.* (1970), Shirayama (1992), Magnaudet *et al.* (1995) and Johnson & Patel (1999), as shown in Table 3.1.1. Note that all lengths are made non-dimensional by the diameter of the sphere.

Also shown in Table 3.1.1 are comparisons of the (x, y) location of the centre of the toroidal vortex (denoted by (x_C, y_C)) and the drag coefficient, C_d . For all of the parameters shown in Table 3.1.1, the present results compare very well to those of previous authors.

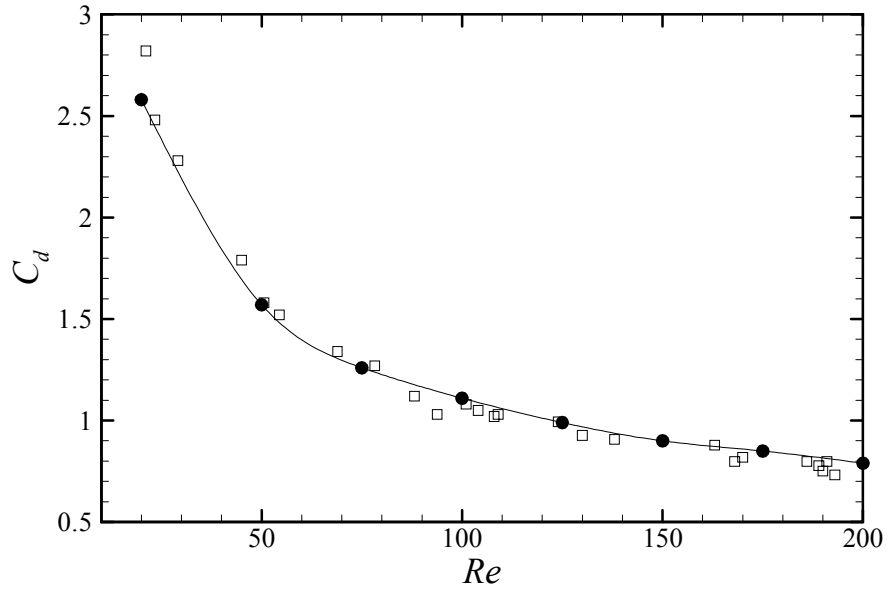


Figure 3.1.2. Drag coefficient for Reynolds numbers up to $Re = 200$: numerical results, \bullet ; experimental results (Roos & Willmarth (1971)), \square .

Author	θ_s	x_s	(x_c, y_c)	C_d
Present results	128	0.87	(0.75, 0.28)	1.09
Taneda (1956)	128	0.87	(0.75, 0.27)	n/a
Rimon & Cheng (1969)	128	0.83	n/a	1.01
Pruppacher <i>et al.</i> (1970)	128	0.95	n/a	n/a
Shirayama (1992)	127	0.84	n/a	1.10
Magnaudet <i>et al.</i> (1995)	128	0.85	n/a	1.09
Johnson & Patel (1999)	126	0.86	(0.75, 0.29)	1.11

Table 3.1.1. Comparisons of axisymmetric flow for $Re = 100$.

For all Reynolds numbers up to $Re = 212$ in this regime, the flow remains axisymmetric and topologically similar with changes only in the polar separation angle, separation length and vortex position. The drag coefficient in this steady, axisymmetric regime for Reynolds numbers up to $Re = 200$ is shown in Figure 3.1.2, where the experimental results of Roos and Willmarth (1971) are plotted for comparison. The drag curve exhibits a trend that may be approximated well by a power law model, as pointed out in Pregalato *et al.* (2002c). For all discrete values of the Reynolds number shown in Figure 3.1.2, the drag coefficient from the present simulations compare very well with the extensive measurements of Roos and Willmarth (1971).

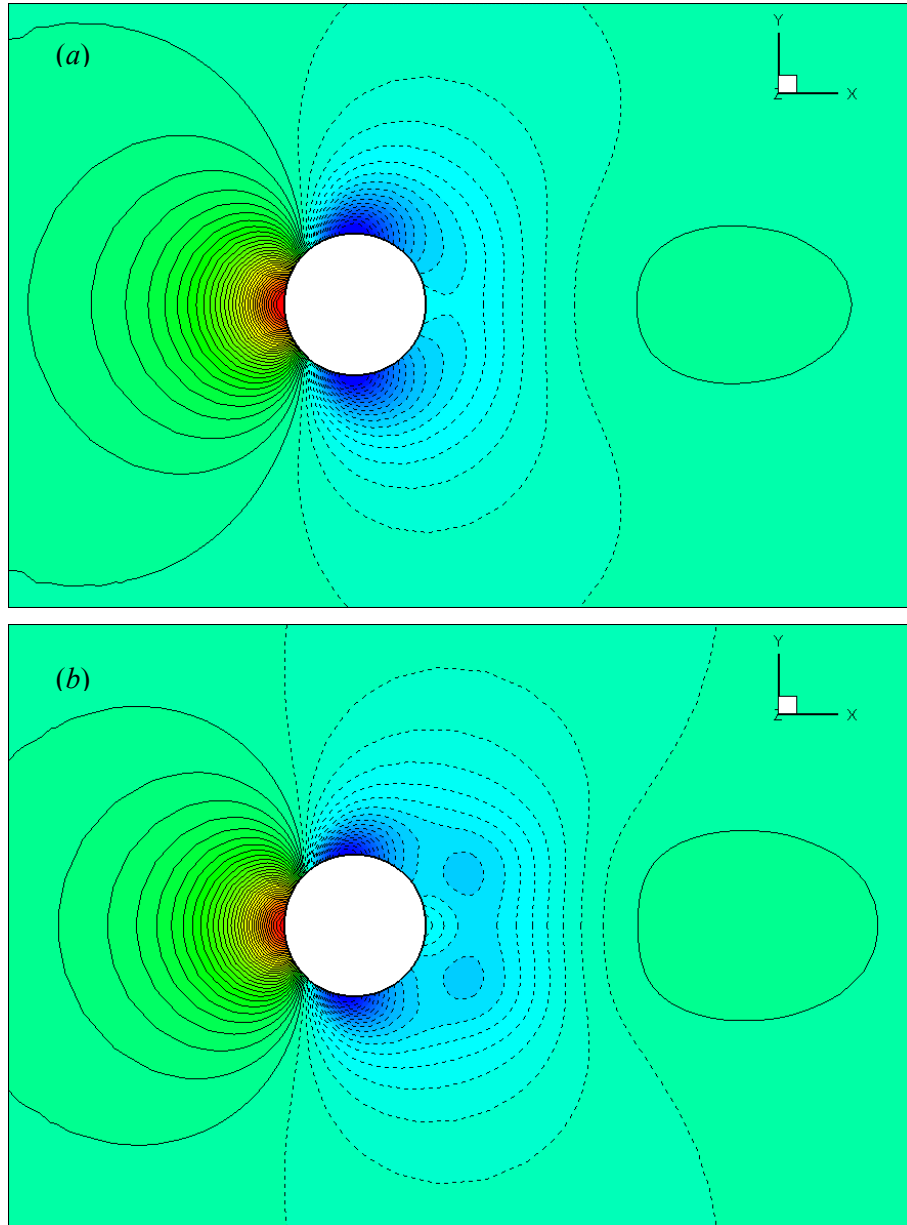


Figure 3.1.3. Pressure coefficient contours for steady axisymmetric flow: (a) $Re = 100$; (b) $Re = 200$.

3.1.2 Pressure and vorticity fields

Pressure coefficient contours, C_p (defined in the nomenclature), are shown in Figure 3.1.3 for Reynolds numbers of $Re = 100$ and $Re = 200$. Note that negative values of C_p are depicted by dashed lines. The axisymmetric pressure coefficient contours are similar at both Reynolds numbers, apart from one major difference: at $Re = 200$, a pressure minimum is observed in the wake, which is not evident in the contours at $Re = 100$. By comparing Figure 3.1.1 with the pressure coefficient contours, we find that this pressure minimum shows up as a ring of low pressure in the wake, located

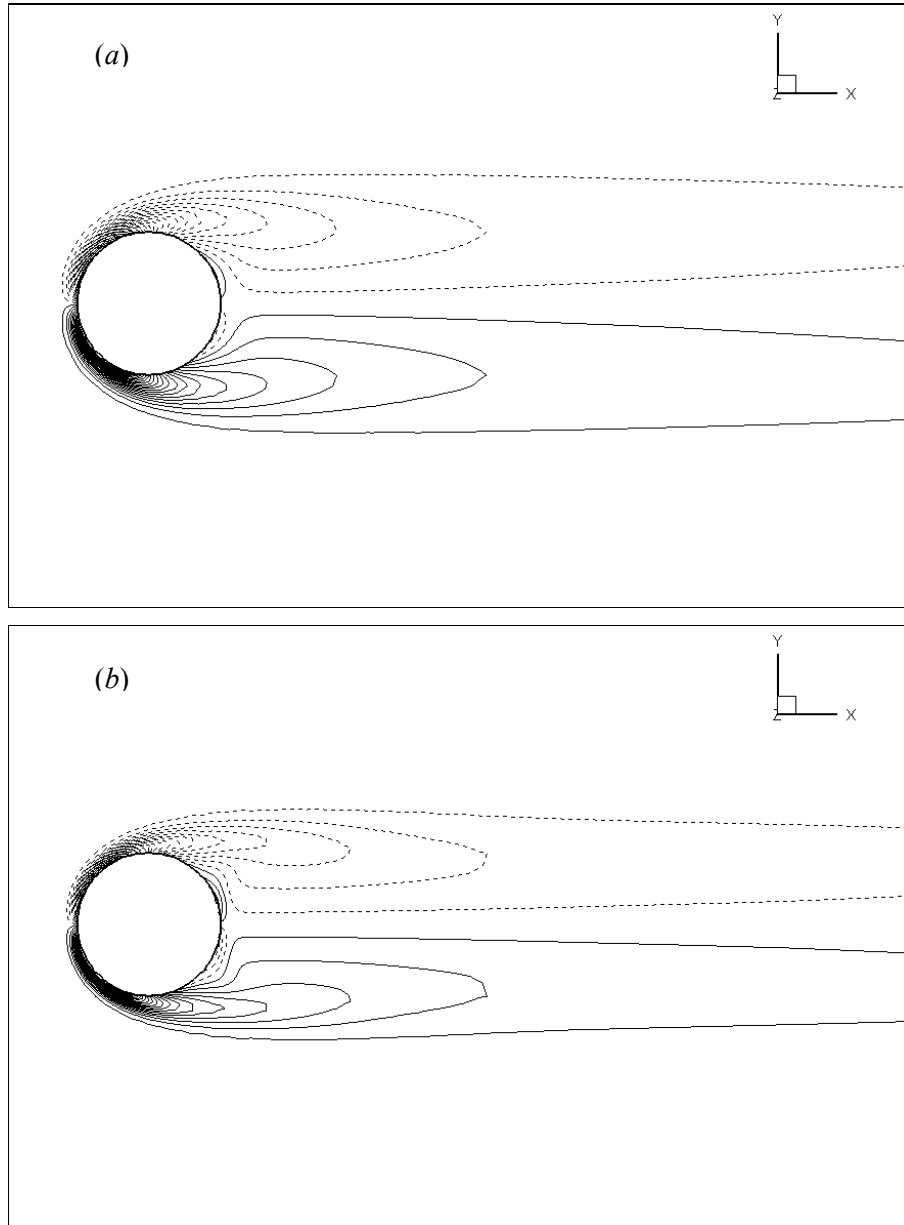


Figure 3.1.4. Azimuthal vorticity contours for steady axisymmetric flow: (a) $Re = 100$; (b) $Re = 200$.

very close to the centre of rotation of the toroidal vortex, as highlighted by the two circular contours in Figure 3.1.3b. Note that for $Re < 200$, the centrifugal force of the vortex's rotation must be balanced by viscous forces as opposed to a radial pressure gradient, as pointed out by Johnson & Patel (1999).

Azimuthal vorticity contours are depicted in Figure 3.1.4 for the same Reynolds numbers of $Re = 100$ and $Re = 200$. Again, the dashed contour lines denote negative values. Evident is the thinning of the boundary layer as the Reynolds number is increased, as well as the convection of the vorticity further downstream for higher Reynolds numbers. However, although the vorticity and pressure

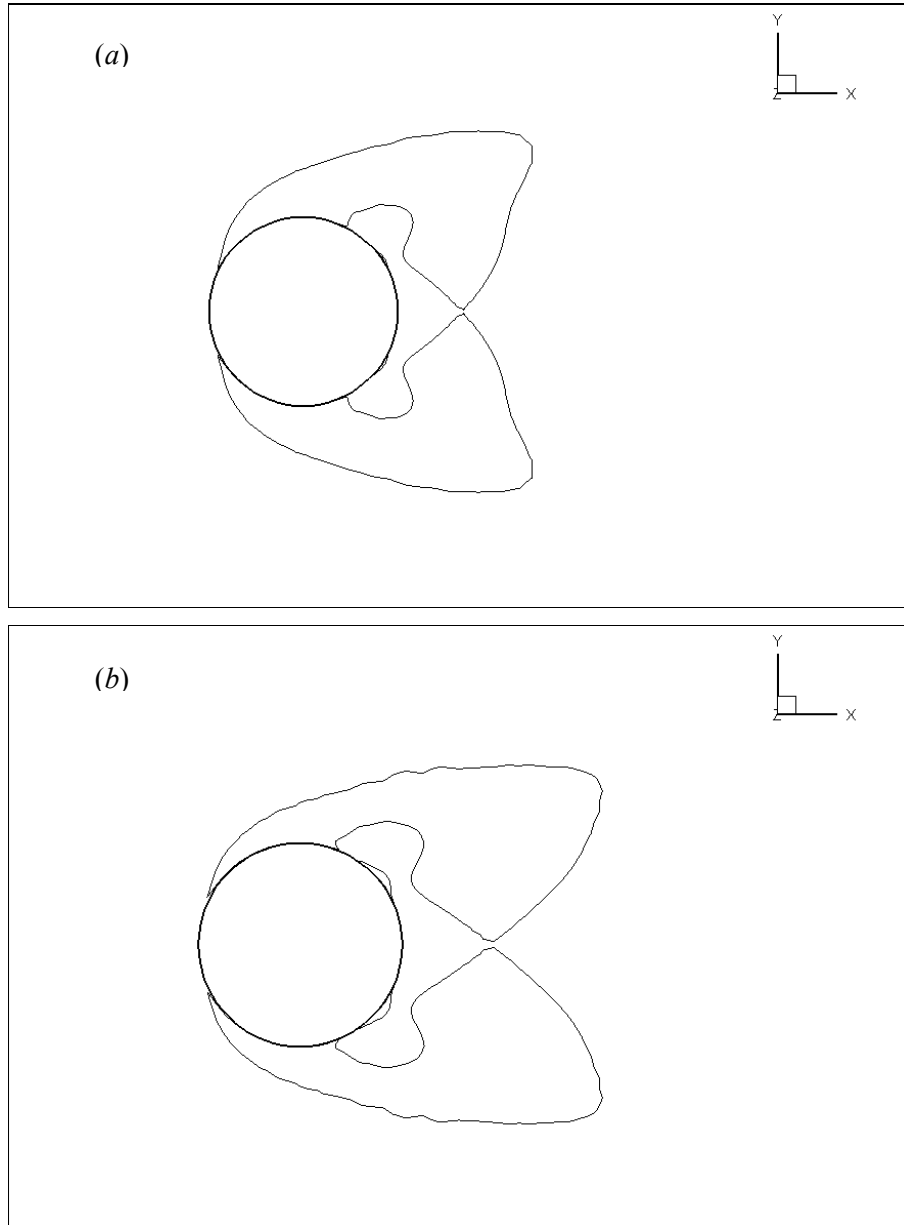


Figure 3.1.5. Vortical regions for steady axisymmetric flow as given by an isosurface of negative λ_2 (see Chapter 2): (a) $Re = 100$; (b) $Re = 200$.

plots convey information on the flow dynamics, they do not clearly convey information on the wake structure, especially at the higher Reynolds numbers to be discussed in the next sections. For example, the presence of spiraling streamlines is not evident in Figures 3.1.3 - 4. Therefore, the method of Jeong & Hussain (1995) as discussed in Chapter 2 is used to properly identify these vortical regions. The result is depicted in Figure 3.1.5 for an axisymmetric flow at Reynolds numbers of $Re = 100$ and $Re = 200$. The thinning of the boundary layer evident in Figure 3.1.4 is further revealed in Figure 3.1.5, which shows that the vortical structures are produced by the boundary layer moving over the convex surface of the sphere. Also apparent is the growth of the

vortical region at the higher Reynolds number, analogous to the growth of the toroidal vortex in Figure 3.1.1. Furthermore, it is noticeable that using the present quantitative method to visualize the vortical regions in the flow is much more advantageous than relying on streamlines, which are reference frame dependent.

3.2 Steady asymmetric flow

3.2.1 Transition to planar symmetry

The onset of asymmetry (or non-axisymmetry) is well documented in the literature. Kim & Pearlstein (1990) previously considered the numerical determination of the first instability mode for the flow past a sphere. They found that the first most unstable mode is asymmetric (non-axisymmetric) with azimuthal wavenumber $m = 1$, and report that the onset of the instability is through a Hopf bifurcation at a critical Reynolds number $Re_l = 175$. However, Natarajan & Acrivos (1993) used a linear stability analysis to find that $Re_l = 210$, in which the transition occurs through a regular bifurcation on the branch of axisymmetric base flows and the most unstable mode is the $m = 1$ mode. The discrepancy between these results appears to lie in the complicated nature of the numerical problem. Tomboulides *et al.* (1993a, b) found that the flow past a sphere undergoes a transition to three-dimensionality at approximately $Re_l = 212$ through a regular bifurcation, in which the most unstable azimuthal mode was the $m = 1$ mode, in accordance with the results of Natarajan & Acrivos (1993). Furthermore, Johnson & Patel (1999) report a critical Reynolds number, Re_l , of $210 < Re_l < 212$, by observing that the lift coefficient jumped from $C_l = 0$ at $Re = 210$ to $C_l = -2.4 \times 10^{-2}$ at $Re = 212$. Also, Ghidersa & Dušek (2000) showed that the axisymmetry gives way to planar symmetry, with the orientation of the plane of symmetry being random (determined only by the initial conditions) in the absence of any external perturbations. Finally, Thompson *et al.* (2001) used the Landau model to verify that the transition to asymmetry occurs at a critical Reynolds number $Re_l = 212$.

In light of the results briefly reported above, direct numerical solutions were performed in increments of unity for Reynolds numbers inclusive in the range $209 < Re < 213$. For each value of Re , the mean axisymmetric flow was obtained first and a random azimuthal perturbation was applied to the $m = 1$ mode, which was allowed to grow (or decay) depending on the stability of the flow at that particular Reynolds number. After the flow became statistically steady, the lift coefficient was measured for these Reynolds numbers and is shown in Figure 3.2.1. Note that for axisymmetric flows, C_l is naturally zero. It is evident in Figure 3.2.1 that for Reynolds numbers less than and equal

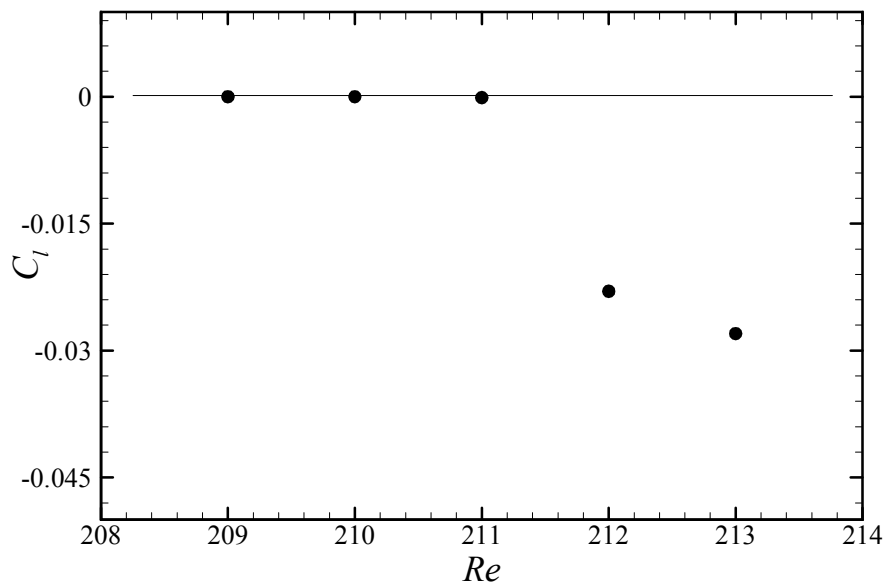


Figure 3.2.1. Lift coefficient versus Reynolds number, showing transition to three-dimensionality.

to $Re = 211$, the flow remains axisymmetric. When the Reynolds number exceeds the critical value of approximately $Re_c = 212$, the flow becomes asymmetric. Furthermore, this bifurcation is a *regular* or *supercritical* one in the sense that the transition process does not involve any hysteresis effects (Tobak & Peake (1982)).

The flow past a sphere becomes asymmetric when the Reynolds number exceeds $Re = 212$. In contrast to the axisymmetric regime, the flow becomes asymmetric with a plane of symmetry remaining in the wake. For the present simulations, the plane of symmetry was allowed to arise naturally through numerical errors inherent in any numerical solver. For the purposes of presenting the results, however, the computed flow field was rotated such that the symmetry plane coincides with the x - y plane. As mentioned at the start of the chapter, a representative Reynolds number of $Re = 250$ was chosen to yield results in this steady asymmetric regime.

3.2.2 Drag and lift coefficients

Table 3.2.1 shows the drag and lift coefficients at a Reynolds number of $Re = 250$ obtained for the present study and those found in previous research. Note that C_l is the net lift coefficient of the sphere, as defined in the nomenclature. For both the values of C_d and C_l obtained in the present study, the comparisons to previous results are excellent. The only apparent discrepancy is in the lift coefficient found by Schlichting (1979), whose value of $C_l = 0.220$ also is much greater than the

numerical results obtained by Johnson & Patel (1999), Constantinescu & Squires (2000), and Kim & Choi (2002).

Author	C_d	C_l
Present results	0.704	0.0610
Schlichting (1979)	0.70 – 0.72	0.220
Johnson & Patel (1999)	0.70	0.0620
Constantinescu & Squires (2000)	0.70	0.0617
Kim & Choi (2002)	0.702	0.060

Table 3.2.1. Comparisons of steady asymmetric flow for $Re = 250$.

3.2.3 Streamlines

The presence of a plane of symmetry is most obvious in the streamline plots shown in Figure 3.2.2. The streamlines constructed in this manner are from the global velocity components, so that the lines correspond to true three-dimensional streamlines and relate directly to what is observed experimentally using dye visualization, for example. It is also evident from the x - y symmetry-plane view in Figure 3.2.2a that the toroidal vortex has tilted, and that the size of the vortex differs in the azimuthal direction from the upper focus to the lower focus. The arrows on the streamlines also indicate that the upper focus is fed from fluid originating from upstream, whereas the lower focus actually releases fluid into the near wake. As a result, the separation bubble is no longer closed. Because of continuity, there must be fluid flowing out of the centre of the upper vortex as well as fluid flowing into the centre of the lower vortex. This flow is directly from the centre of the upper focus to the centre of the lower focus, as is clearly shown in Figure 3.2.2.

3.2.4 Pressure and vorticity fields

Pressure coefficient contours are depicted in Figure 3.2.3a for the x - y plane, and Figure 3.2.3b for the x - z plane. Also shown in Figure 3.2.3c are isocontours of C_p , depicted in an isometric view for clarity. The surface of the sphere is shaded blue, whereas the front stagnation region is green. The inconsistency of the size of the toroidal vortex in the azimuthal direction mentioned in the previous section is apparent in Figure 3.2.3c. The pressure minimum in the upper focus is clearly higher than the pressure minimum in the lower focus. This azimuthal pressure gradient drives the flow through

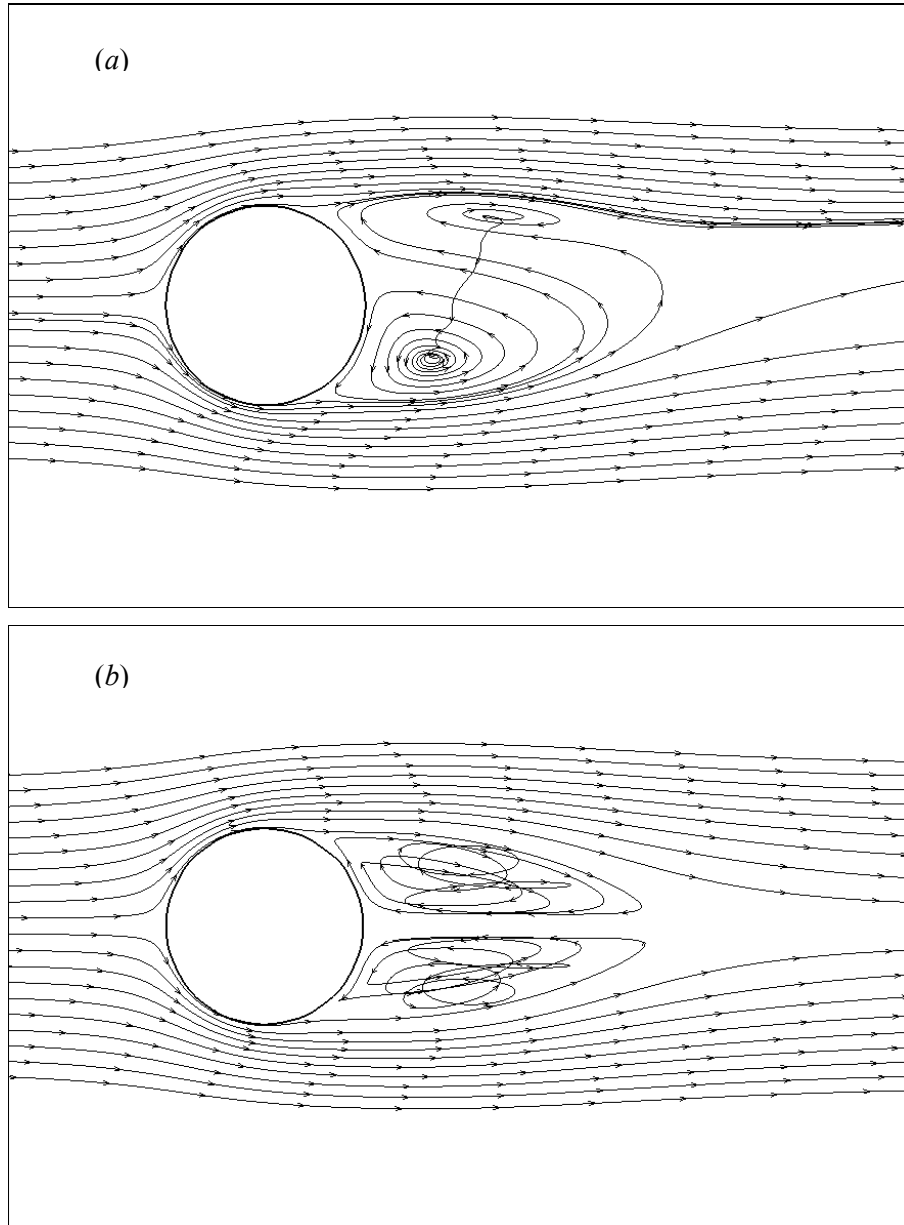


Figure 3.2.2. Three-dimensional streamlines at a Reynolds number of $Re = 250$: (a) x - y symmetry-plane; (b) x - z plane.

the core of the toroidal vortex, resulting in the flow propagating from the centre of the upper focus to the lower, as mentioned in the previous paragraph. In contrast to the axisymmetric ring of low pressure at $Re = 200$ shown in Figure 3.1.3, at a Reynolds number of $Re = 250$ the ring is seen to have tilted, in accordance with the spiraling streamlines shown in Figure 3.2.2. The tilting of this ring of low pressure after the flow has become non-axisymmetric results in the conversion of azimuthal vorticity (which was prominent before the transition) to streamwise vorticity. This streamwise vorticity, shown in Figure 3.2.4, is positive on one side of the sphere and negative on the other. As in the previous figures, negative values are depicted by dashed contour lines.

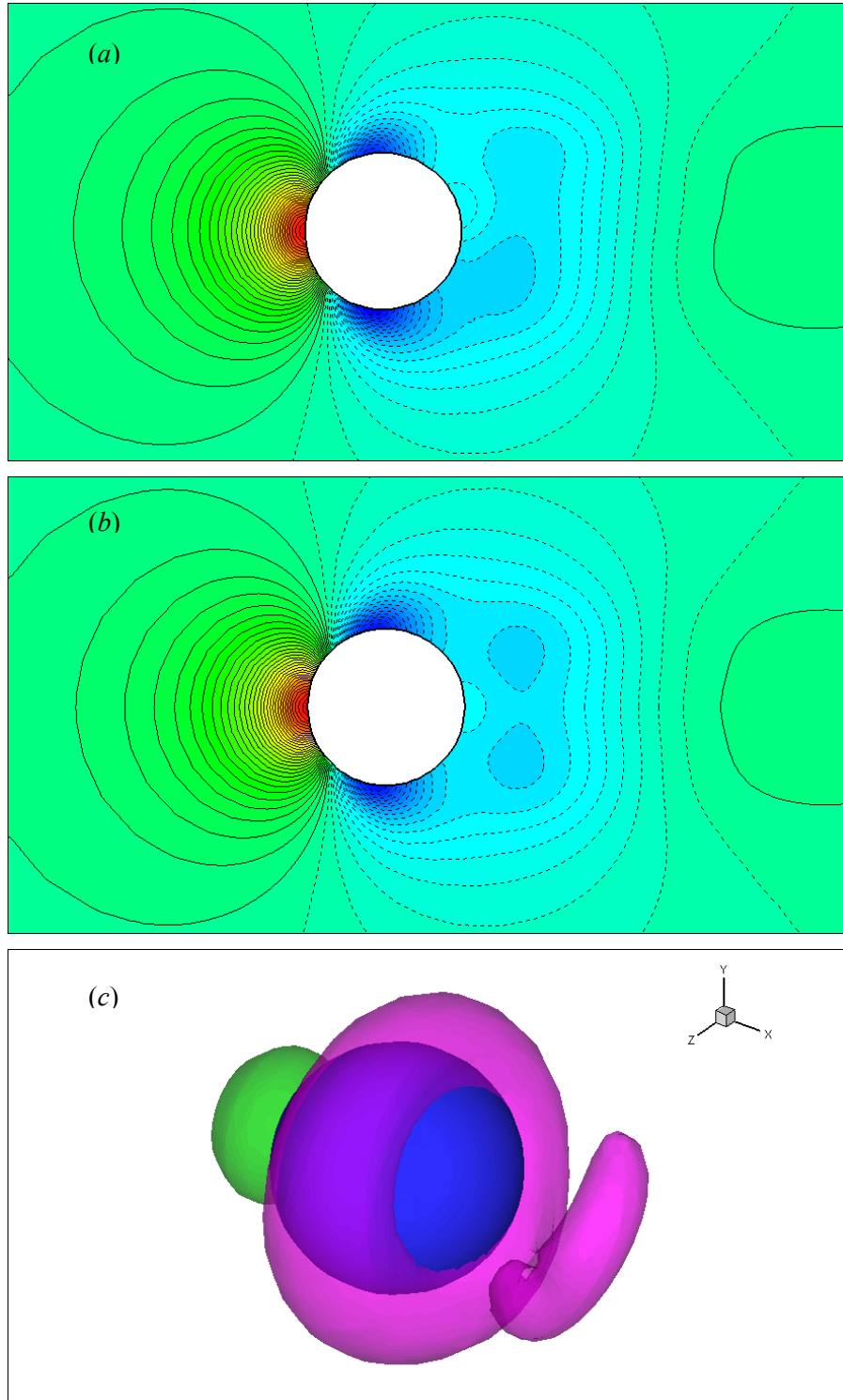


Figure 3.2.3. Pressure coefficient contours for $Re = 250$: (a) x - y plane; (b) x - z plane; (c) isocontours of the pressure coefficient showing the detached ring of low pressure in the core of the toroidal vortex. Note that the sphere is shaded blue.

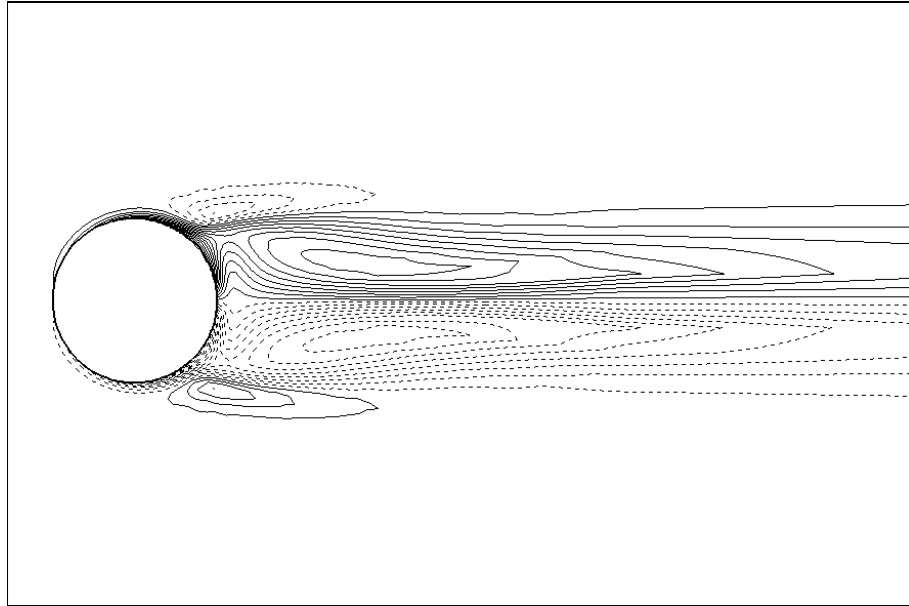


Figure 3.2.4. Streamwise vorticity contours (ω_x) in the x - z plane for steady planar-symmetric flow, $Re = 250$.

As the flow develops, this streamwise vorticity convects downstream via two tails (also known as the “double-thread” or “two-tailed” wake), with very little migration from the flow centreline.

3.2.5 Visualization of vortex structures

Experiments indicate that the two-tailed wake appears quite suddenly once the critical Reynolds number, Re_c , is reached. Visual observations of the wake in this regime are provided in Magarvey & Bishop (1961a,b), Nakamura (1976) and Ormières & Provansal (1999), to name but a few. Numerically, as in the previous section, we use the method of Jeong & Hussain (1995) to visualize the vortex structures in the wake of a sphere at a Reynolds number of $Re = 250$, shown in Figure 3.2.5. Here, and in all subsequent figures, we plot an isosurface of $-\lambda_2 = 0.1$. The isosurface has a degree of transparency associated with it in order to reveal the surface of the sphere. The plot in Figure 3.2.5 compares qualitatively very well with that of Johnson & Patel (1999), Thompson *et al.* (2001) and Kim & Choi (2002). It is noticeable that in the near wake, approximately one diameter downstream from the rear of the sphere, there is a kinking of the trailing vortex tails. Thompson *et al.* (2001) demonstrate that as the Reynolds number approaches the critical Reynolds number for transition to unsteadiness, the kinking of these trailing vortices increases, ie. the tails get closer together at this point before moving apart again. They go further to speculate that this may be associated with the transition to the periodic wake.

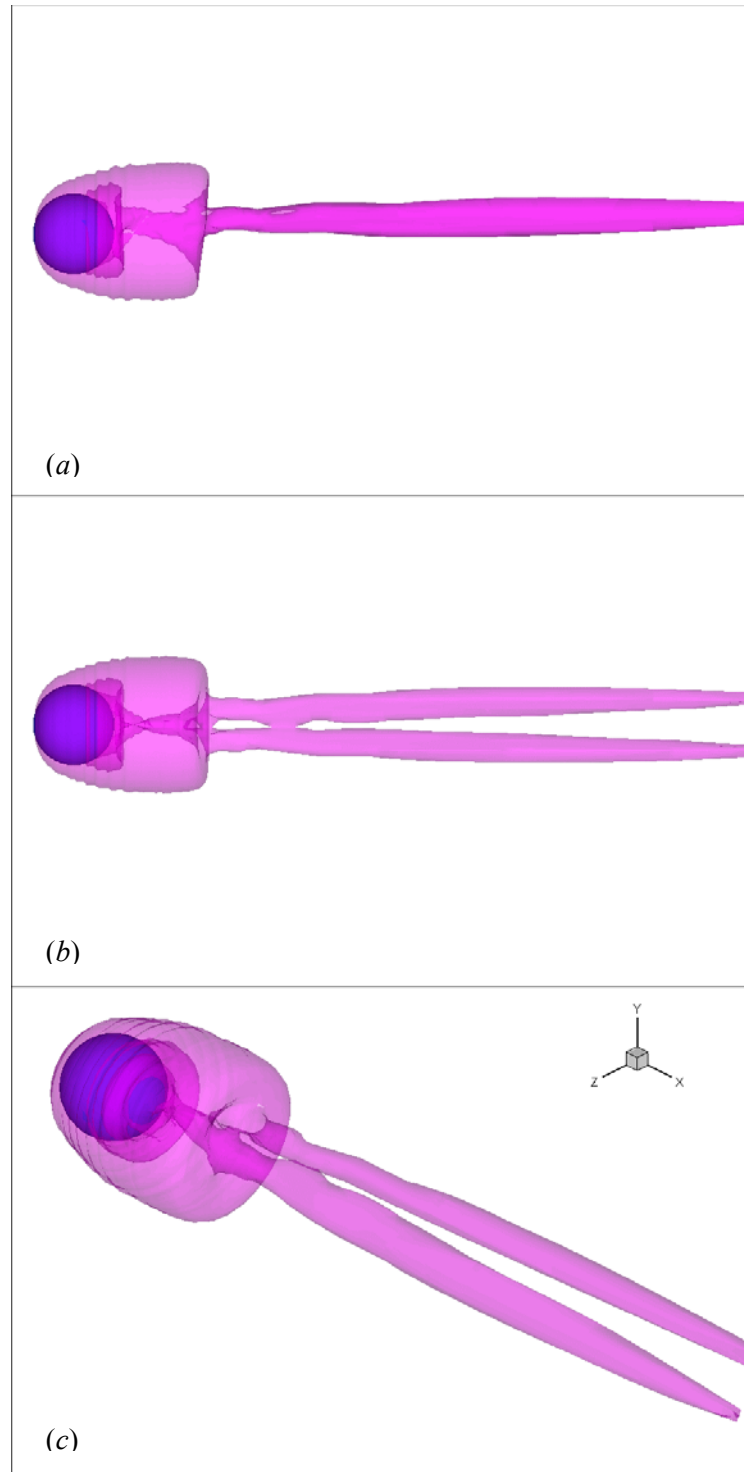


Figure 3.2.5. Visualization of vortex structures for steady planar-symmetric flow at $Re = 250$: (a) x - y plane; (b) x - z plane; (c) isometric view.

3.3 Unsteady planar-symmetric flow

When the Reynolds number is further increased to $Re_2 \approx 275$, the flow becomes unsteady with the appearance of periodic vortex shedding. This vortex shedding is represented by the occurrence of hairpin vortices or vortex loops, and the plane of symmetry that was observed in the steady flow is also preserved in this regime. This regime has received by far the most attention in the literature, with extensive measurements being made of the vortex shedding frequencies and wake structures.

3.3.1 Transition to unsteadiness

The critical Reynolds number for this transition to unsteadiness, Re_2 , is well documented from both experimental and numerical studies. Experimentally, Goldberg & Florsheim (1966) report a value of $Re_2 \approx 270$, whereas Magarvey & MacLachy (1965) give a value of 300. Wu & Faeth (1993) observed the onset of vortex shedding at $Re_2 = 280$, whereas Sakamoto & Haniu (1990) found a value of $Re_2 = 300$. The discrepancies in the values reported in experiments appear to lie in the presence of the support structures, experimental determination of the free stream (or sphere) velocity, and hence an accurate determination of the Reynolds number, among other things. On the other hand, numerical studies have reported a much narrower range of Re_2 . For example, Tomboulides & Orszag (2000) find a value in the range $270 < Re_2 < 285$ with $m = 1$ being the most unstable mode. Similarly, Natarajan & Acrivos (1993) report a value of $Re_2 = 277.5$ and $m = 1$, although their analysis is based on the axisymmetric base flow. This secondary *Hopf* bifurcation corresponds to the onset of time-dependence in the flow field. Finally, Thompson *et al.* (2001) found that $Re_2 = 272$ by linear interpolation of the growth rate for the development of the periodic mode in the complex Landau equation. Nevertheless, it is interesting to note that the appearance of vortex shedding for a sphere occurs at a Reynolds number that is considerably higher than the corresponding critical Reynolds number for flow past a cylinder which is only 49 (Williamson (1996)).

3.3.2 Drag and lift coefficients, Strouhal number

A Reynolds number of $Re = 300$ was chosen to characterize the flow features in this unsteady, planar-symmetric regime. As in §3.2, the plane of symmetry was allowed to arise naturally through numerical errors in the solver, although for the presentation of the following results the flow field was rotated so that the symmetry plane coincided with the x - y plane. We first present results of the

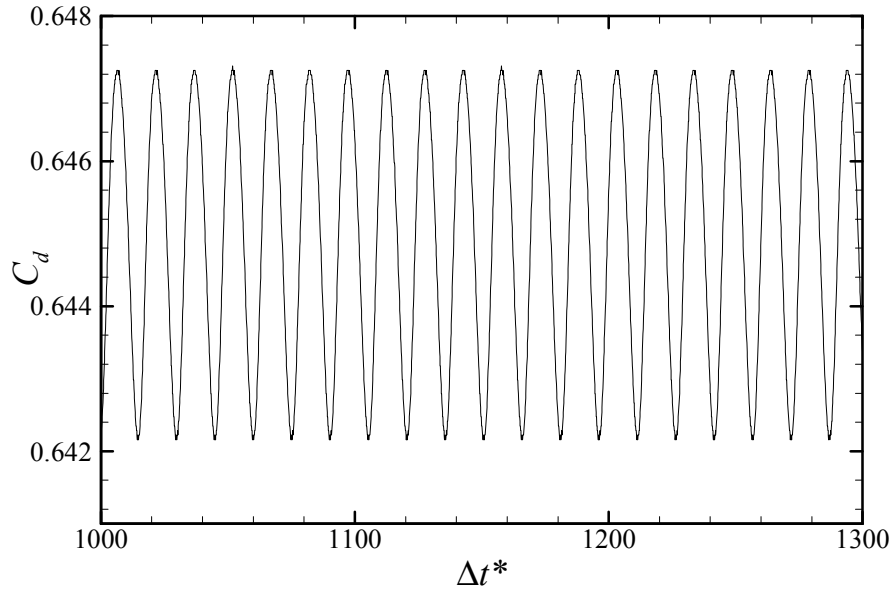


Figure 3.3.1. Sample time history of the drag coefficient for $Re = 300$.

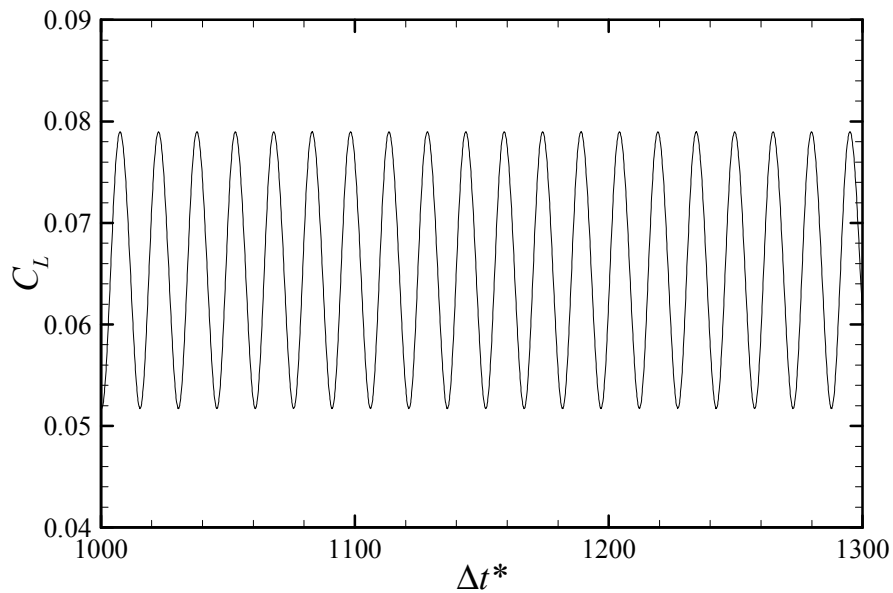


Figure 3.3.2. Sample time history of the net lift coefficient for $Re = 300$.

drag coefficient, shown in Figure 3.3.1. For these simulations at $Re = 300$, the flow was initialized with the corresponding axisymmetric solution at the same Reynolds number, along with a small perturbation in the $m = 1$ mode. The time history of C_d (and subsequent figures) was calculated for the duration of approximately 100 periods of motion, long after the flow has reached a statistically steady state, although for clarity only 20 oscillations are shown. The time-averaged drag coefficient observed in Figure 3.3.1 has a value of $C_d \approx 0.6449$, with an oscillation amplitude of 2.3×10^{-3} . This

compares well to the values of $C_d = 0.671$ with an oscillation amplitude of 2.8×10^{-3} of Tomboulides (1993), and $C_d = 0.656$ with an oscillation amplitude of 3.5×10^{-3} of Johnson & Patel (1999).

A sample time history of the net lift coefficient C_l is depicted in Figure 3.3.2. The time-averaged value of the lift coefficient is $C_l = 0.0656$, with an oscillation amplitude of 1.3×10^{-2} . Johnson & Patel (1999) found that $C_l = 0.069$ with an oscillation amplitude of 1.6×10^{-2} . Also, Constantinescu & Squires (2000) report a value of $C_l = 0.065$, although no oscillation amplitudes are conveyed. Spectral analysis of the periodic waveforms presented in Figures 3.3.1 – 2 gives a dominant frequency of $St = 0.134$, corresponding to the frequency of vortex shedding from the sphere, and a second frequency at twice the Strouhal frequency, which appears to have a greater effect on the drag rather than the lift. This value of $St = 0.134$ compares well to that of recent previous research, both experimental and numerical, as listed in Table 3.3.1.

Author	Method	St
Present results	Numerical	0.134
Tomboulides & Orszag (2000)	Numerical	0.136
Constantinescu & Squires (2000)	Numerical	0.136
Johnson & Patel (1999)	Numerical	0.137
Ormières & Provansal (1999)	Experimental	0.122
Sakamoto & Haniu (1995)	Experimental	0.124
Sakamoto & Haniu (1990)	Experimental	0.142

Table 3.3.1. Comparisons of vortex shedding Strouhal numbers.

The discrepancy in the results of Sakamoto & Haniu (1995) and (1990) lies in the fact that the results of Sakamoto & Haniu (1990) were obtained in a wind tunnel in which the free-stream velocity for $Re < 400$ was estimated using Roshko's (1956) formula based on the vortex shedding frequency from a two-dimensional circular cylinder. For all of the Strouhal numbers reported in the numerical studies in Table 3.3.1, the maximum difference in St is approximately 2%. Furthermore, the present results compare very well to the experimentally observed vortex shedding frequencies obtained by Ormières & Provansal (1999) and Sakamoto & Haniu (1990, 1995), in which the maximum difference in St in this case is approximately 6%. At first glance, one may assume that the differences may be due to blockage effects. However, as pointed out by Modi & Akutsu (1984), blockage effects are essentially negligible for blockage (area) ratios up to 11%. As previously mentioned, the presence of support structures as well as accurate determinations of the Reynolds number may contribute to the disparities.

We now proceed to describe in some detail the structure of the wake in terms of streamlines, pressure, vorticity, and the wake vortical structure. With this knowledge of the structure of the wake, it is possible to describe the vortex shedding process in this unsteady planar-symmetric regime, with the hope of extending these results to the case of a tethered sphere in a uniform flow. Furthermore, it is assumed *a priori* that the vortex shedding process at $Re = 300$ is similar to that at $Re = 500$. This will enable direct comparisons to be made with the tethered sphere results to be presented in Chapter 5.

3.3.3 Streamlines

This and the following sections aim to complement rather than replace the work performed in understanding the vortex shedding process by Sakamoto & Haniu (1990, 1995) and Shirayama (1992). In particular, we follow Johnson & Patel (1999) in noting that a complete picture of the vortex shedding process is obtained through regularly spaced snapshots of the wake. In this respect, given the Strouhal frequency of $St = 0.134$, we obtain snapshots of the flow quantities in equally spaced increments of $\varphi = T/4$, where T is the period of oscillation in Figure 3.3.2. Note that the initial temporal location of the sample period is arbitrary.

Plots of instantaneous streamlines are depicted in Figure 3.3.3. Part (a) shows contours in the x - z plane, whereas (b) shows contours in the x - y plane. The most notable difference between the two diagrams is the presence of a plane of symmetry, which coincides with the x - y plane as previously mentioned. However, this planar-symmetry is not as obvious as it is in Figure 3.2.2 because of the unsteady nature of the flow, resulting in the calculation of streamlines that have an inherent error due to the corresponding time-integration in the post-processing stage. Furthermore, the x - y plane presented in Figure 3.3.3 does not correspond *exactly* to the plane of symmetry due to post-processing difficulties. Also, the streamlines represent true three-dimensional streamlines (and hence actual particle paths), and thus provide insight into the dynamics of the wake, although the out-of-plane components are not evident in these figures. In Figure 3.3.3(a), the streamlines for $\varphi = 0$ and $\varphi = T/4$ spiral into the centre of the focus, thereby rendering the focus “stable” (Tobak & Peake (1982)). On the other hand, as time moves on, for $\varphi = T/2$ and $\varphi = 3T/4$ the streamlines spiral out of the focus, making the focus “unstable”. The presence of a stable focus may be considered analogous to the vortex being stretched, whereas the unstable focus could represent a compression of the vortex axis (Johnson & Patel (1999)).

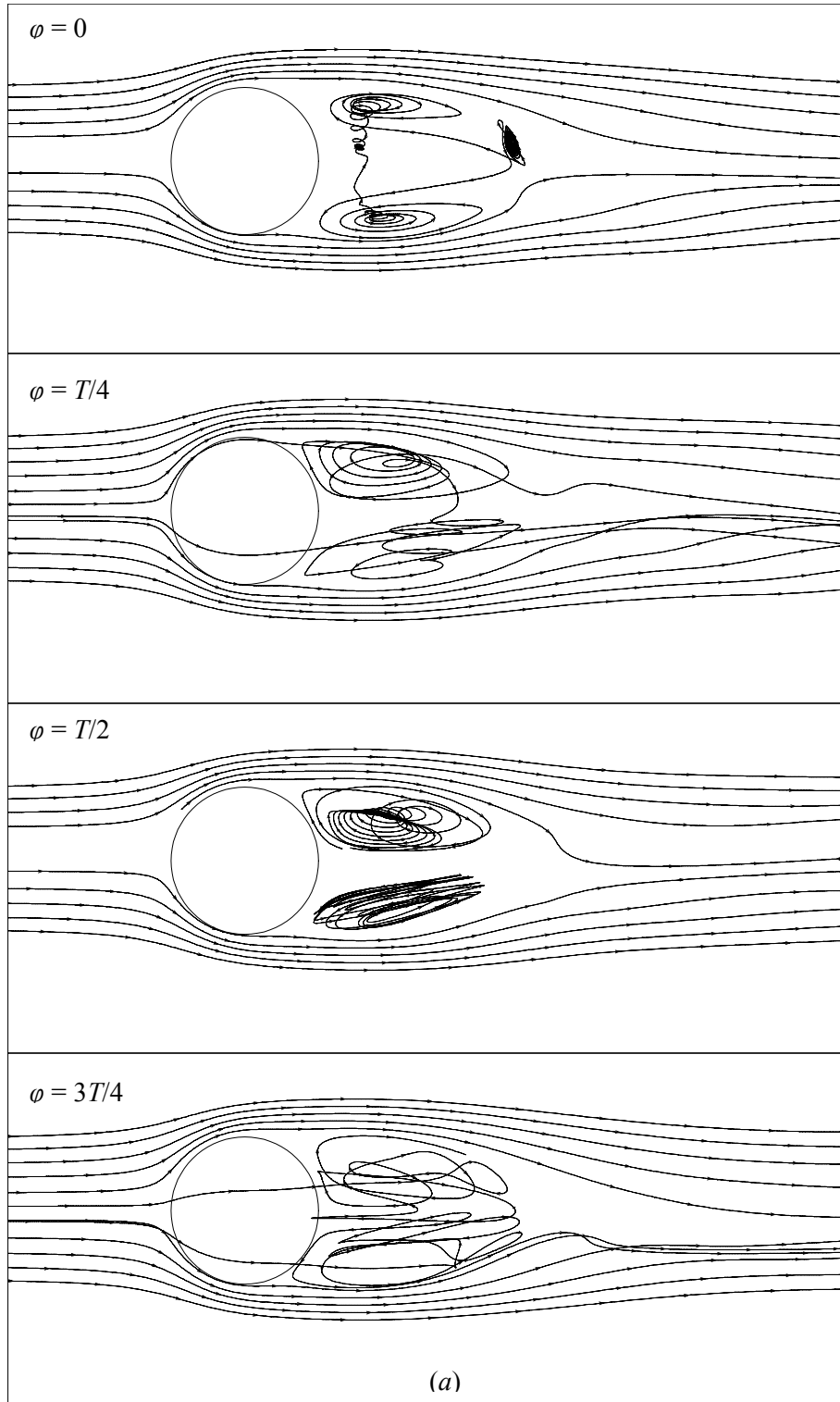


Figure 3.3.3. Instantaneous streamlines over one period of vortex shedding for $Re = 300$: (a) x - z plane; (b) x - y plane.

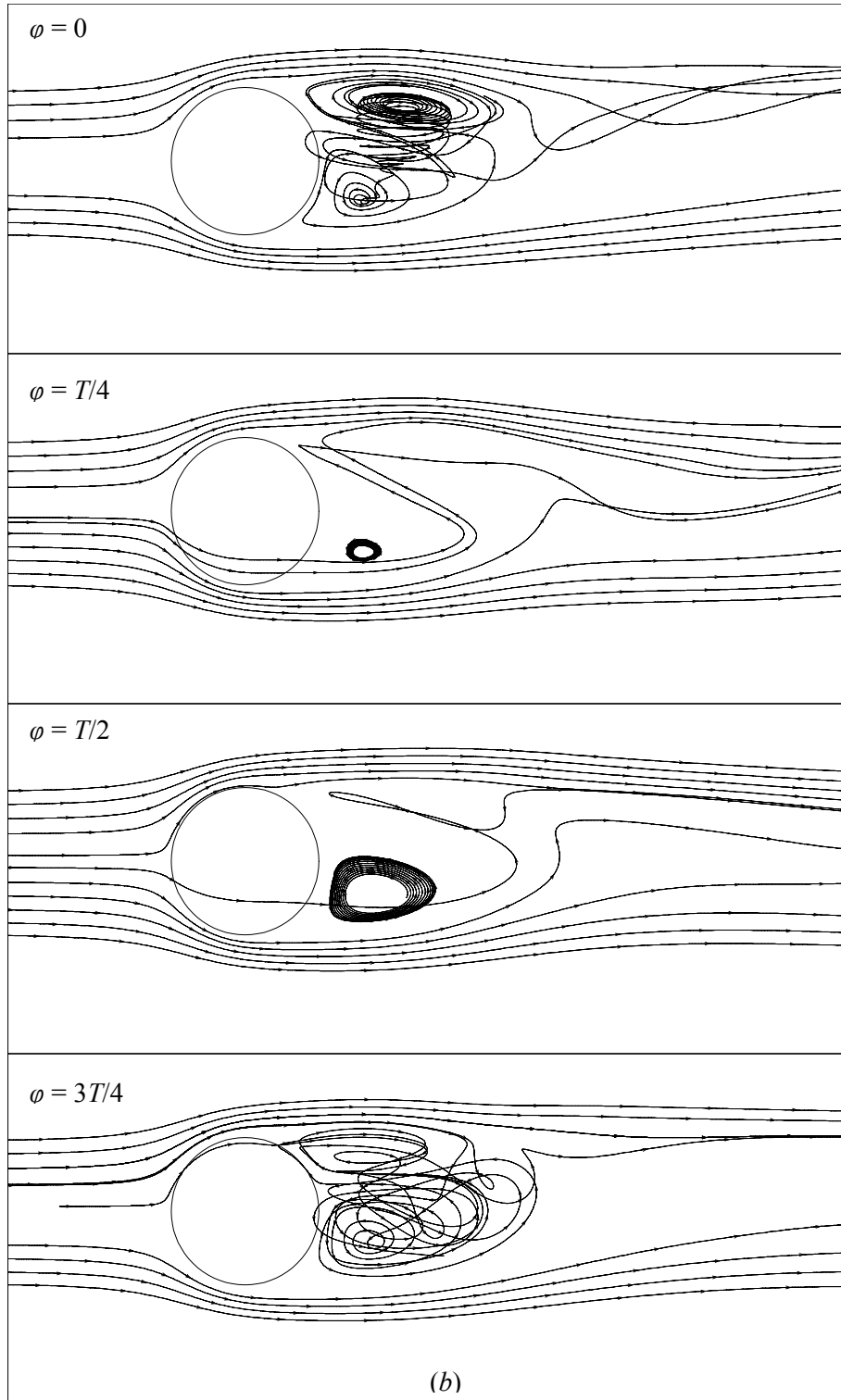


Figure 3.3.3. Continued.

In Figure 3.3.3(b), at $\varphi = 0$ there is an unstable focus in the lower half of the x - y plane. The fluid emanating from this lower focus is expelled into the near wake from above the upper (also unstable) focus, which is enclosed by a limit cycle that is fed from fluid that originates from upstream of the

sphere. Note that the upper and lower foci are not “in-line”, ie. the toroidal vortex is tilted. At $\varphi = T/4$, the toroidal vortex has tilted further and the limit cycle enclosing the upper vortex has disappeared. Also, the previously entrained fluid has been ejected around the top of the upper focus and convects downstream. Meanwhile, the lower focus has become stable and is enclosed by a limit cycle that appears to be fed from the same fluid that was previously fed into the limit cycle of the upper focus. At $\varphi = T/2$, the upper focus has convected downstream and there appears a new smaller upper focus (although more streamlines are needed to highlight its appearance) that is in-line with the lower focus, ie. the vortex has been shed. At this same instant, the lower focus has now become unstable, and in the final frame at $\varphi = 3T/4$, the upper focus has grown in strength and remains in-line with the lower focus. Furthermore, it is now fed by fluid originating from the upper upstream flow. At the completion of the period, this stable upper focus then becomes unstable at $\varphi = 0$, which appears to indicate that the limit cycle behaviour observed defines the crossing point of this transition (Johnson & Patel (1999)).

3.3.4 Pressure and vorticity fields

Contours of the pressure coefficient corresponding to the same snapshots as in Figure 3.3.3 are shown in Figure 3.3.4, where again the plane of symmetry does not coincide exactly with the x - y plane. As in §§1 and 2, dashed lines depict negative values of C_p . In Figure 3.3.4(a), at $\varphi = 0$, the axis of the toroidal vortex is clearly seen as the two closed contours of C_p . These two contours are negative, indicating a pressure minimum that is indicative of a vortex core. The pressure in the near wake increases by the time φ reaches $3T/4$. The contours in the x - y plane in Figure 3.3.4(b) provide much more information about the periodicity of the flow. At $\varphi = 0$, the pressure minimum in the core of the upper focus is evident, as is the slightly higher pressure in the core of the lower focus. There is also an apparent pressure maximum immediately upstream of the upper focus. At $\varphi = T/4$, the pressure in the core of the upper focus has increased, and the previously closed contour of higher pressure upstream of the upper focus appears to have pushed the upper focus downstream. At $\varphi = T/2$, the pressure minimum in the lower focus has intensified, and the cores of the two foci have become aligned normal to the streamwise direction. In the final panel, the intensity of the relative foci have switched from one to the other, similar to the last panel of Figure 3.3.3(b).

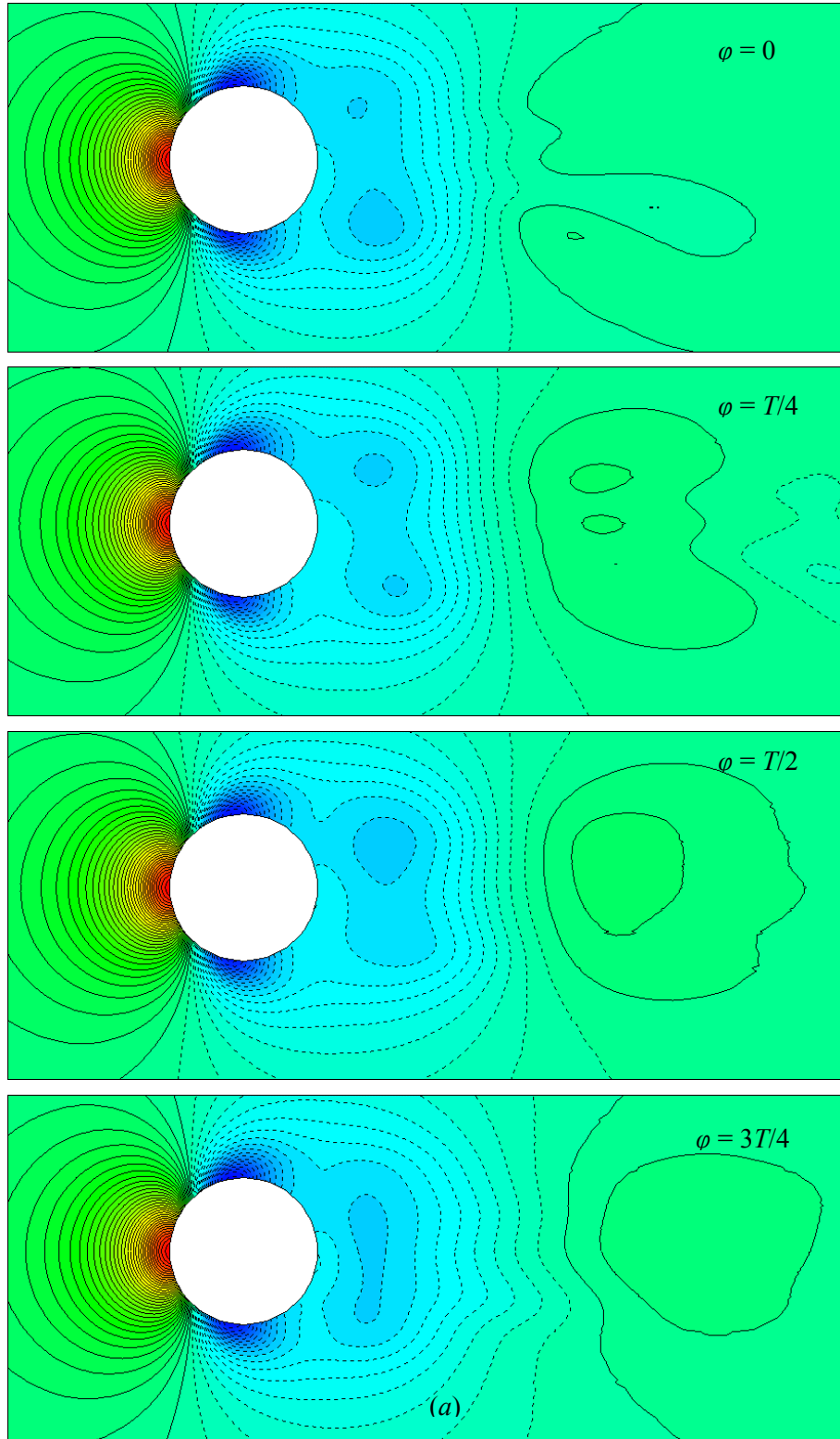


Figure 3.3.4. Instantaneous pressure coefficient contours over one period of vortex shedding for $Re = 300$: (a) x - z plane; (b) x - y plane.

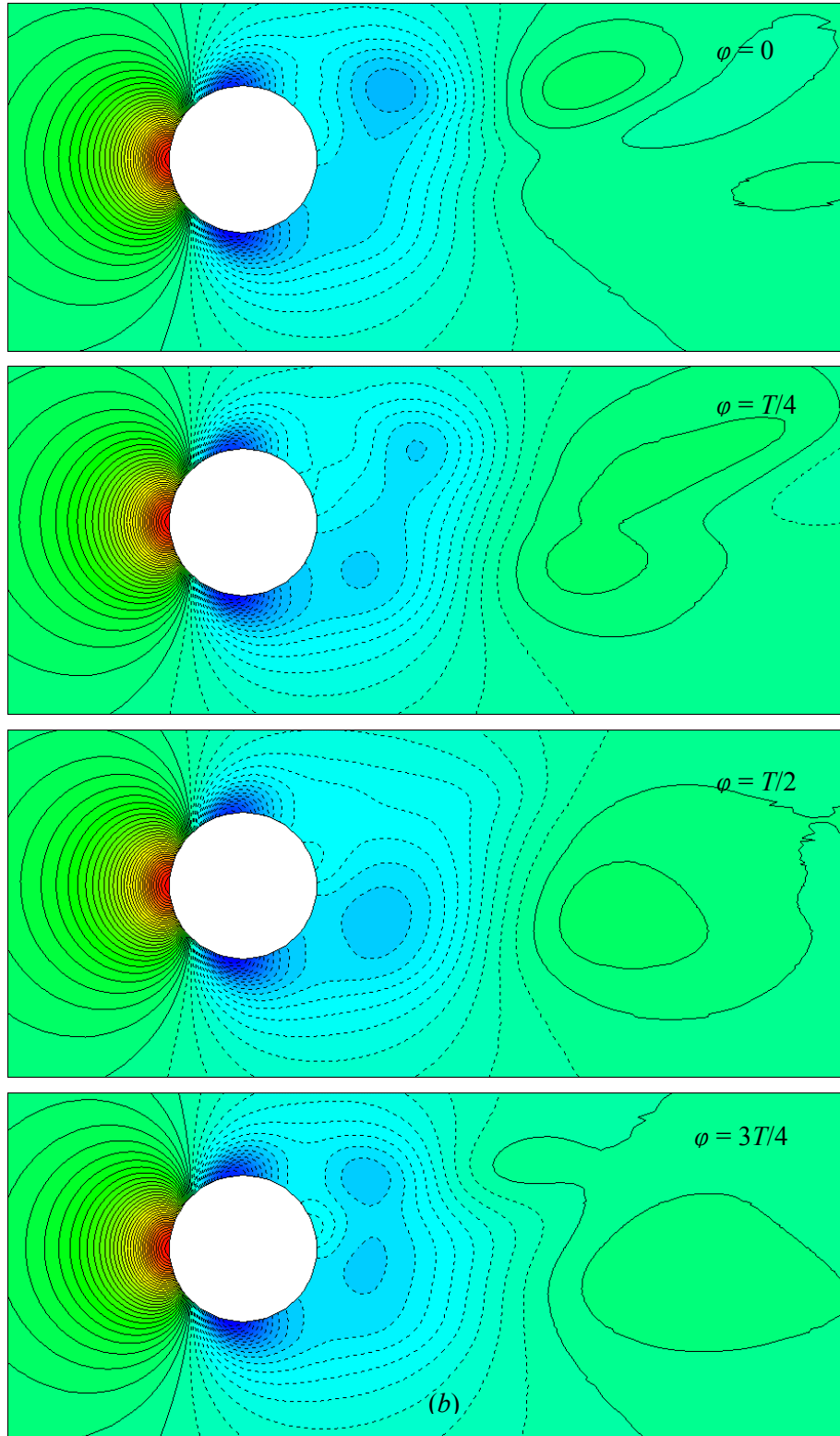


Figure 3.3.4. Continued.

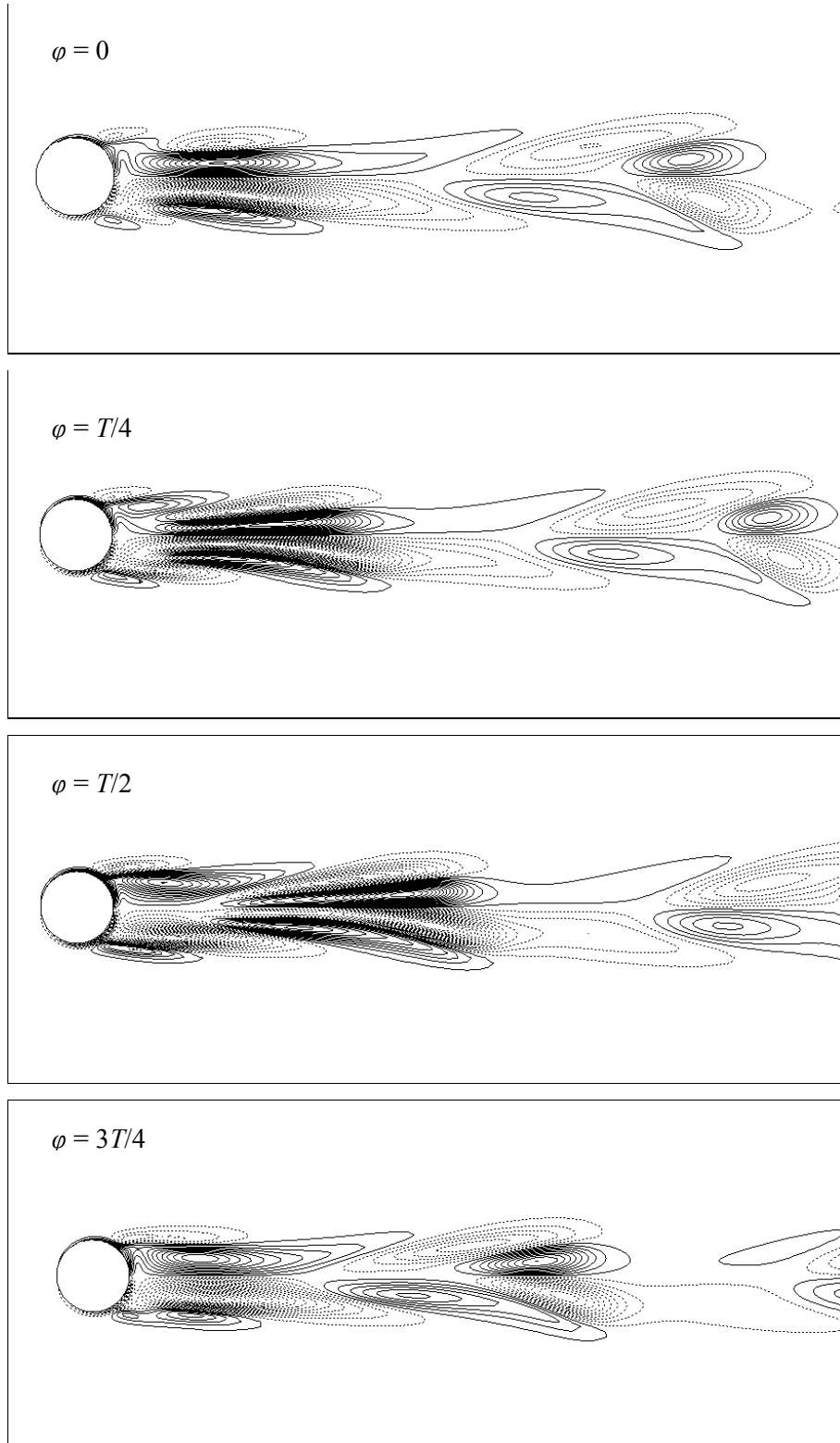


Figure 3.3.5. Instantaneous streamwise vorticity contours in the x - z plane over one period of vortex shedding for $Re = 300$.

Figure 3.3.5 shows contours of the streamwise vorticity in the x - z plane for each quarter period of motion as in Figures 3.3.3-4. The vorticity alternates sign in the streamwise direction and is antisymmetric about the x - y plane. Throughout the cycle, it is evident that the sign of the vorticity immediately adjacent to the rear surface of the sphere remains the same. Also, the alternating sign of the streamwise-propagating vorticity is due to the envelopment of the oppositely signed counter-rotating vorticity (Johnson & Patel (1999)).

3.3.5 Vortex shedding mechanism

Having characterized the nature of the near-wake flow in terms of instantaneous pressure, vorticity and streamlines, it is possible now to construct a physical mechanism describing the shedding process. Following the observations of Johnson & Patel (1999), we note that there is an initial azimuthal pressure gradient set up on the axis of the toroidal vortex (at $\varphi = T/2$) that generates azimuthal flow from the centre of the upper focus to the lower. This stable focus generates radially inward flow and entrains fluid into the wake. Unlike the steady case (see §2), the increased inertia at this higher Reynolds number causes the upper focus to grow, rather than obtain an equilibrium state. As its size increases, it entrains fluid from its own side of the sphere, and its centrifugal acceleration sets up a greater radial pressure gradient (see $\varphi = 3T/4$). As a result of the increasing strength of the upper focus, at $\varphi = 0$, it has begun changing from a stable focus to an unstable focus, and its radial motion is against its own pressure gradient. The resultant reverse flow that impinges on the upper separating shear layer generates a pressure maximum that appears to push the upper side of the vortex away from the rear surface of the sphere, thereby shedding (although not completely) the vortex into the wake ($\varphi = T/4$). Following the convection of the upper part of the vortex, a strong shear layer remains at the interface of the impinging flow and the separated flow. This shear layer quickly rolls up to produce the new upper focus, and the process is repeated.

3.3.6 Visualization of vortex structures

As with the steady flow results, we note that the streamlines and vorticity contours do not clearly elucidate the vortical structures in the wake. Therefore, as in §§2 and 3, the method of Jeong & Hussain (1995) is used to provide a clear picture of the vortex structures often observed in experiments. Figure 3.3.6 shows isometric views of the unsteady planar-symmetric wake over a single cycle of vortex shedding at a Reynolds number of $Re = 300$. At $\varphi = T/2$ which, as previously mentioned, represents the start of the vortex shedding cycle, it is clear that a vortex structure is emerging from the upper surface of the vortical region that surrounds the sphere. The legs and head

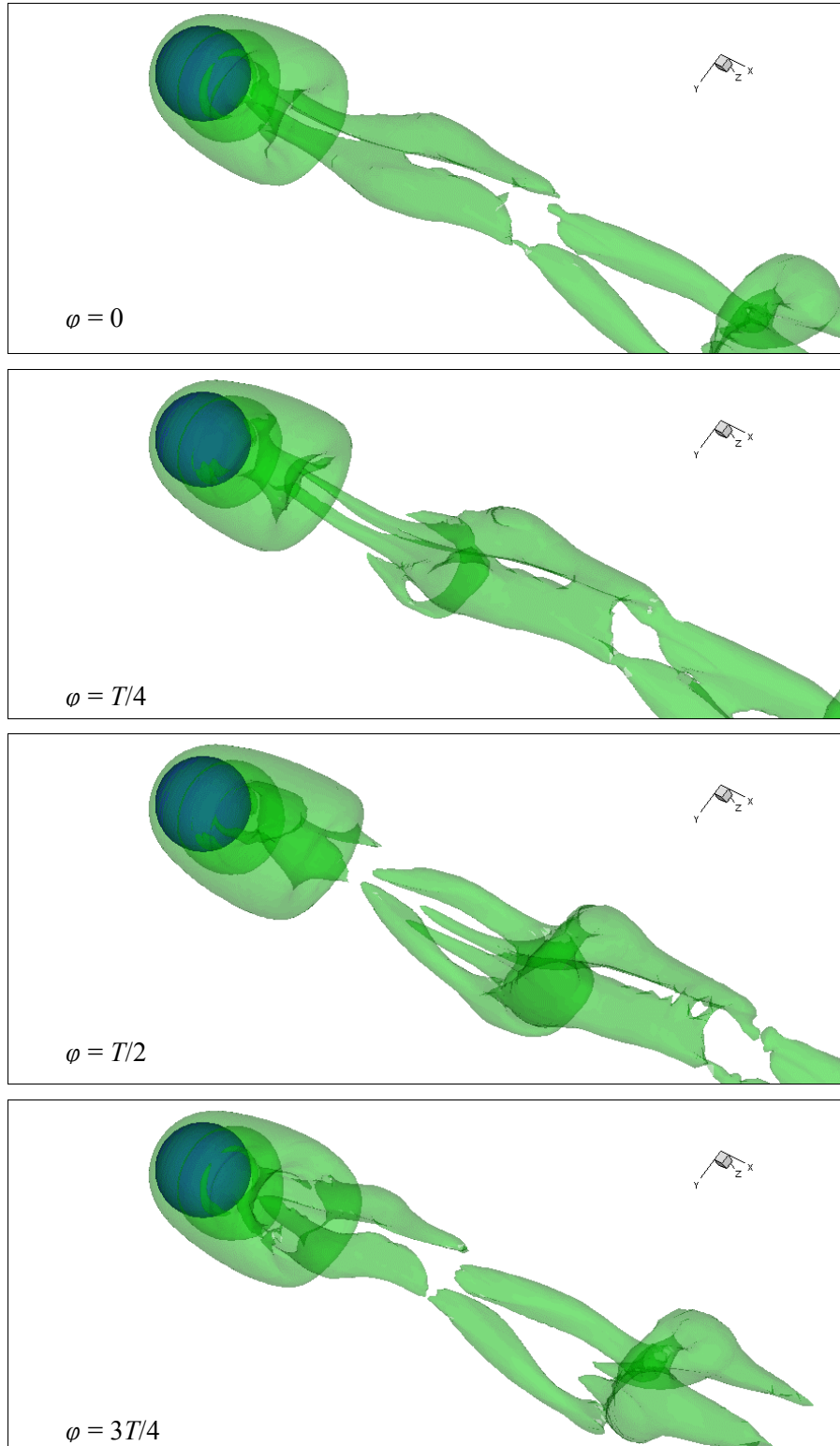


Figure 3.3.6. Visualization of vortex structures over one period of vortex shedding for unsteady planar-symmetric flow at $Re = 300$.

of the lower (induced) vortex can be clearly seen in the immediate near wake. In the next panel, the legs of this upper vortex structure begin to separate from the surrounding region, and it is apparent

that the emerging upper vortex structure at $\varphi = T/2$ is the actual head of the hairpin vortex whose legs are still attached to the vortical region surrounding the sphere, although the head does not register well enough as an isosurface of $-\lambda_2$. At $\varphi = 0$, this hairpin vortex convects downstream and at $\varphi = T/4$, a new isolated structure appears underneath the upper hairpin vortex. It is evident that this new structure is the beginning of the lower induced hairpin vortex, which was apparently insufficiently strong enough previously to be registered as a vortex structure using the method of Jeong & Hussain (1995). Furthermore, the legs of this induced hairpin vortex cannot yet be seen, even in the surrounding vortical region of the sphere. It is immediately apparent then that the upper hairpin vortex is formed from the vortical region that surrounds the sphere, whereas the lower induced vortex is the result of the vorticity induced by the near-wake flow/outer flow interaction. These numerical flow visualizations compare very well to experimental observations. Furthermore, the numerical simulations and the vortex identification method of Jeong & Hussain (1995) reveal the existence of induced hairpin vortices, which are surprisingly not observed experimentally. However, numerical simulations by Johnson & Patel (1999) show that numerical streaklines, which correspond most directly to dye visualizations in experiments, do not reveal the induced hairpin vortices, which is an unusually interesting result.

3.4 Unsteady asymmetric flow: $Re \leq 500$

3.4.1 Transition to asymmetry

At a Reynolds number of $Re = 500$, the flow past a stationary sphere is unsteady and asymmetric. Because of the asymmetry, and the corresponding lack of periodicity, little research has been performed in this regime. As the title of this section suggests, the plane of symmetry that was initially encountered at the onset of three-dimensionality (see §2) has disappeared; the Reynolds number at which this occurs is subject to debate. Sakamoto & Haniu (1990) report a loss of planar symmetry at a Reynolds number of $Re = 420$. The numerical simulations of Mittal (1999b) found a value in the range $350 < Re < 375$. In addition, the present numerical simulations at a Reynolds number of $Re = 400$ do not find a plane of symmetry. It appears, therefore, that the discrepancies between the experimental and numerical results may lie in the small-scale variations in the azimuthal location of vortex formation that indicate the loss of planar symmetry, which may be too small to register in experimental dye or smoke visualization (Mittal (1999b)).

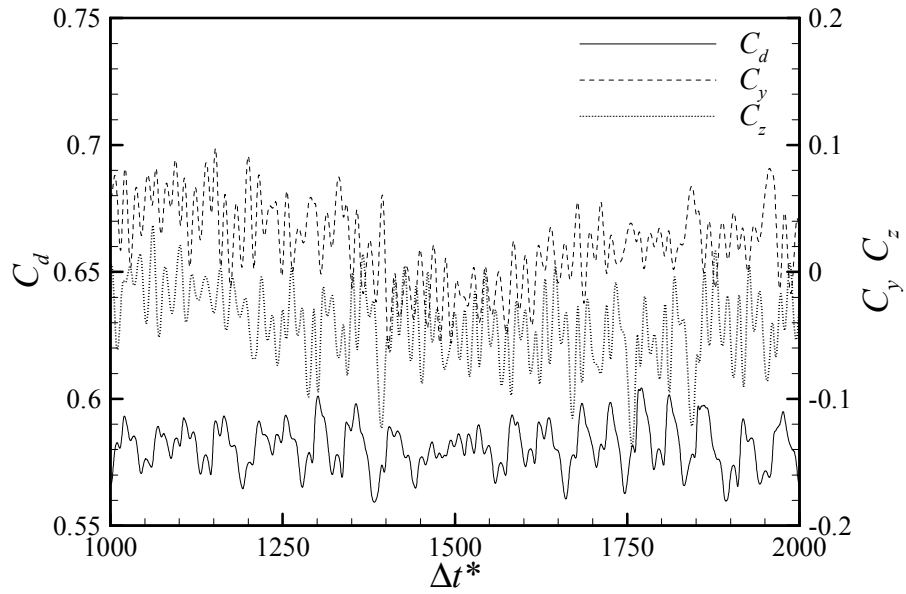


Figure 3.4.1. Sample time history of the drag, lateral and side force coefficients for $Re = 400$.

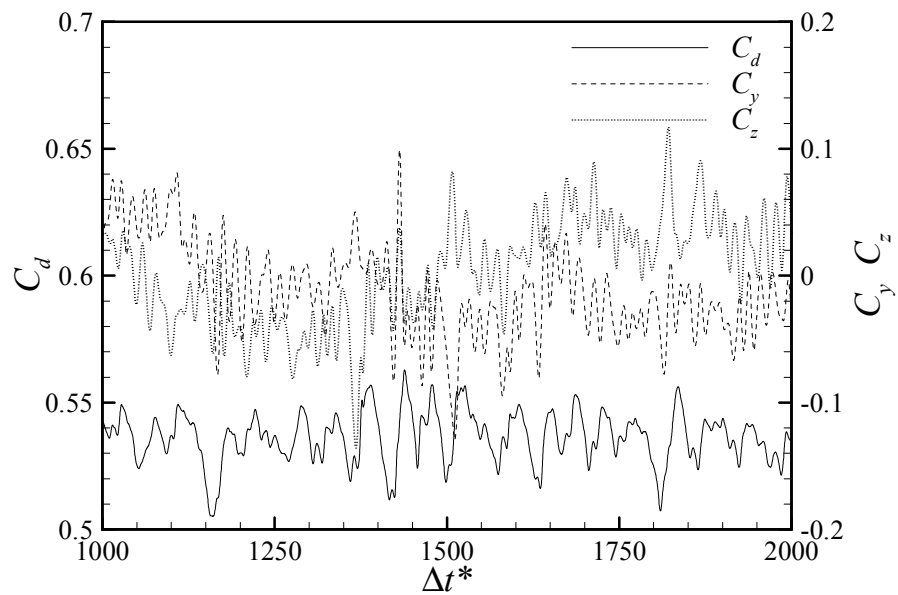


Figure 3.4.2. Sample time history of the drag, lateral and side force coefficients for $Re = 500$.

3.4.2 Drag and lift forces, Strouhal number

As mentioned, the present simulations do not reveal a plane of symmetry at Reynolds numbers of $Re = 400$ and 500 . Figures 3.4.1 and 3.4.2 show the time history of the drag, lateral and side force coefficients. The waveforms in Figures 3.4.1 - 2 illustrate a rather random behaviour, even at a

Reynolds number of $Re = 400$. This is in contrast to the periodic waveforms describing the drag and net lift coefficients for a Reynolds number of $Re = 300$ in §3. Although these force coefficients appear to be chaotic, the flow is still very laminar and appears not to have any small-scale flow structures that highlight the transition to turbulence. Vortex shedding, which is most evident through the oscillatory nature of the lateral and side forces, is less organized at these higher Reynolds numbers, as opposed to the periodic vortex shedding (and lateral and side force coefficients) observed at a Reynolds number of $Re = 300$. Also, the lateral and side force coefficients are approximately five times smaller than the drag coefficient at these Reynolds numbers. This implies that the sideways motion of spheres immersed in a uniform flow and involved in fluid-structure interactions could perhaps be neglected (Mittal (1999a)). However, this is not the case when studying the flow-induced vibrations of a tethered sphere, as shown by Williamson & Govardhan (1997). Note that the time traces obtained for both $Re = 400$ and $Re = 500$ represent approximately 2000 non-dimensional time units, although only the last 1000 time units are shown for clarity.

The Strouhal numbers corresponding to the waveforms in Figures 3.4.1 - 2 are shown in Figure 3.4.3. These plots were obtained by performing a spectral analysis of the fluctuating w -velocity component of the $m = 1$ mode in the near wake for both the $Re = 400$ and $Re = 500$ simulation results. A numerical probe was positioned at a location that was $1D$ downstream from the rear of the sphere and $0.55D$ above the flow centreline, corresponding to a point that was close to the separating shear layer, and a sample space of $\Delta t^* = 300$ time units was used to calculate the dominant frequencies. At a Reynolds number of $Re = 400$, there is a dominant frequency of $St = 0.12$, corresponding to the frequency of vortex shedding from the sphere. When the Reynolds number is increased to $Re = 500$, this dominant vortex shedding frequency becomes $St = 0.16$, as seen in Figure 3.4.3 (b). This compares well to the values obtained by Achenbach (1974) and Tomboulides & Orszag (2000) of 0.163 and 0.167 respectively. Note that the present results (and those of Tomboulides & Orszag (2000) that correspond to only 120 time units) require longer time traces for more accurate evaluations of these low frequencies.

However, what is not directly evident from these plots is the existence of a plane of symmetry. This is further investigated in the next section.

3.4.3 Analysis of fluid forces

In this section, we report on results concerning the vortex dynamics of a stationary sphere when the flow is unsteady and asymmetric. Reynolds numbers of $Re = 400$ and 500 are chosen because of the availability of previous results for the purpose of direct comparison. Unfortunately, it is not possible to analyse in any detail the shedding process, mainly because of the loss of periodicity within this

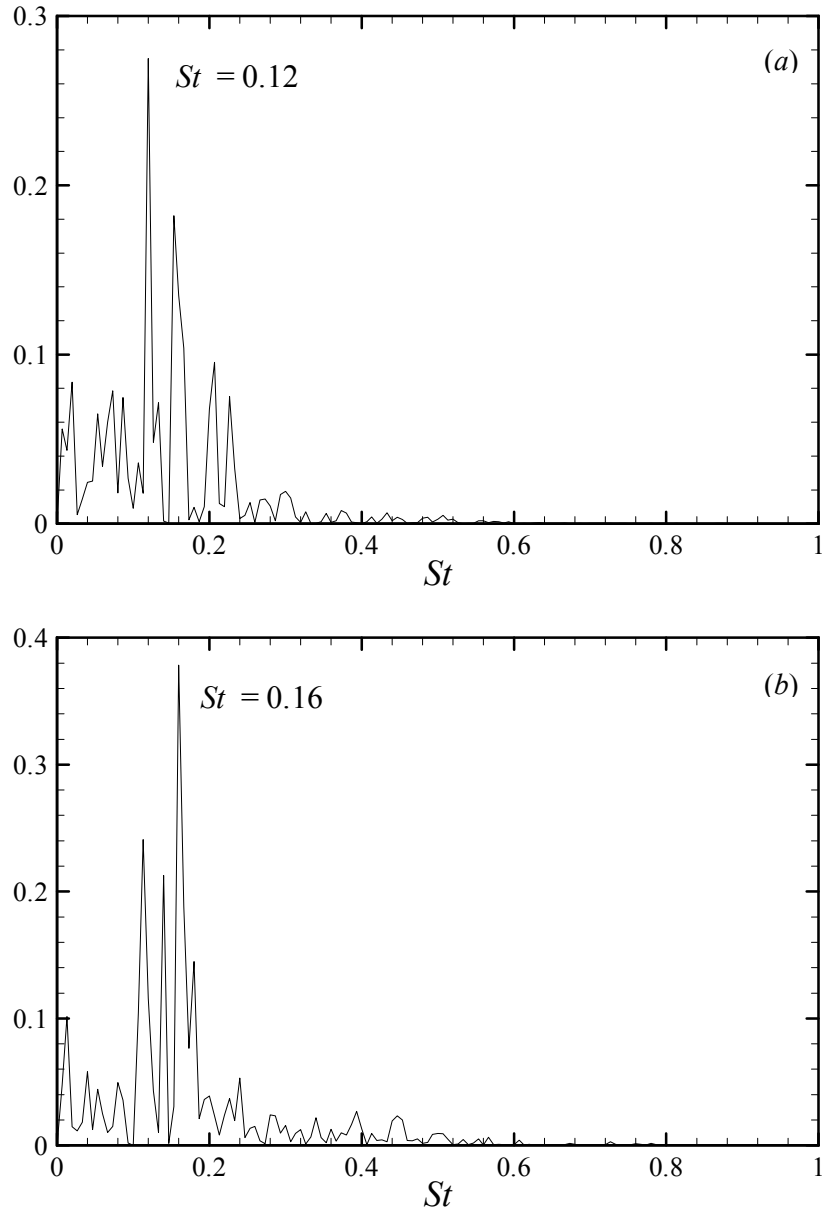


Figure 3.4.3. Dominant frequencies of the w -velocity component at $z = 1D$, $r = 0.55D$: (a) $Re = 400$; (b) $Re = 500$.

regime, unlike in §3. On the other hand, however, we focus our attention now on the instantaneous forces acting on the sphere, since these forces are the most important features from an engineering viewpoint. Furthermore, knowledge of the nature of these forces are crucial in analyzing the flow-induced vibrations of a tethered sphere, as will be shown in Chapter 5.

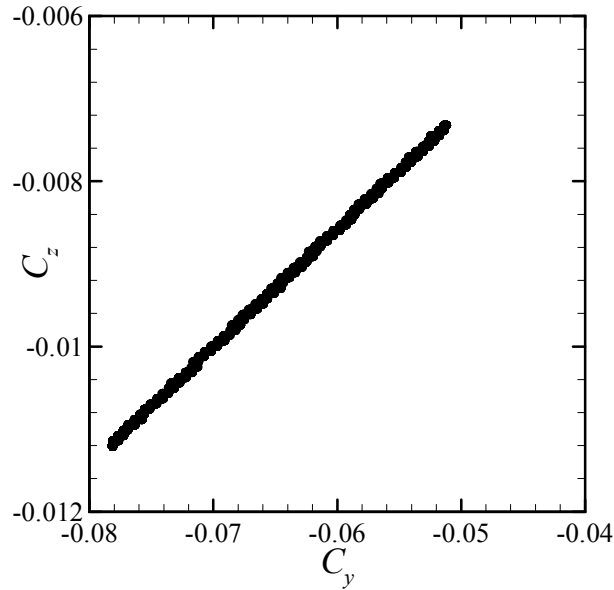


Figure 3.4.4. Phase plot for unsteady planar-symmetric flow, $Re = 300$.

The total fluid force acting on the sphere may be decomposed into its corresponding components: F_d denotes the drag force, which acts parallel to the uniform inflow (ie. parallel to the x -axis); F_y is the component of the force which acts parallel to the y -axis; and F_z indicates the component of the force acting parallel to the z -axis. At first glance, the discrepancies in using different coordinate systems (especially for the non-streamwise axes) may be obvious, and hence comparisons with various authors may be difficult to make; however, since the flow is asymmetric, this is not a major problem, and it is common practice to define a net lift force, F_l , as the total force acting perpendicular to the drag force. The angle of this force vector in the y - z plane is denoted as β . See Chapter 2 for the coordinate system used and for the definitions of the relevant parameters.

Rather than use the dimensional quantities of F_d and F_l , it is more convenient to use the force *coefficients* instead. For the purposes of comparison, Figure 3.4.4 depicts the time history of the y and z force coefficients, denoted as C_y and C_z respectively, for a Reynolds number of $Re = 300$. This type of plot is known as a *phase plot*, since it relates information of the phase of C_y with respect to C_z and vice versa. For this and all subsequent phase plots, at least 20 periods of oscillation are illustrated, based on the vortex shedding Strouhal number. The distance from the origin ($C_y = C_z = 0$) in the phase diagram is equal to the net lift C_l and the angle β is the direction of the net lift, ie. $\tan \beta = C_y/C_z$. Since the side force coefficients in Figure 3.4.4 maintain a constant phase angle for $Re = 300$, the lift force angle does not change with time, indicating the presence of a plane of symmetry. In this particular case, the angle of this symmetry plane is approximately $\beta = 81.86^\circ$.

Figures 3.4.5 (a) and (b) show the phase plots for $Re = 400$ and $Re = 500$ respectively. In both cases, the net lift coefficient C_l varies with both direction and magnitude, unlike the previous case for $Re =$

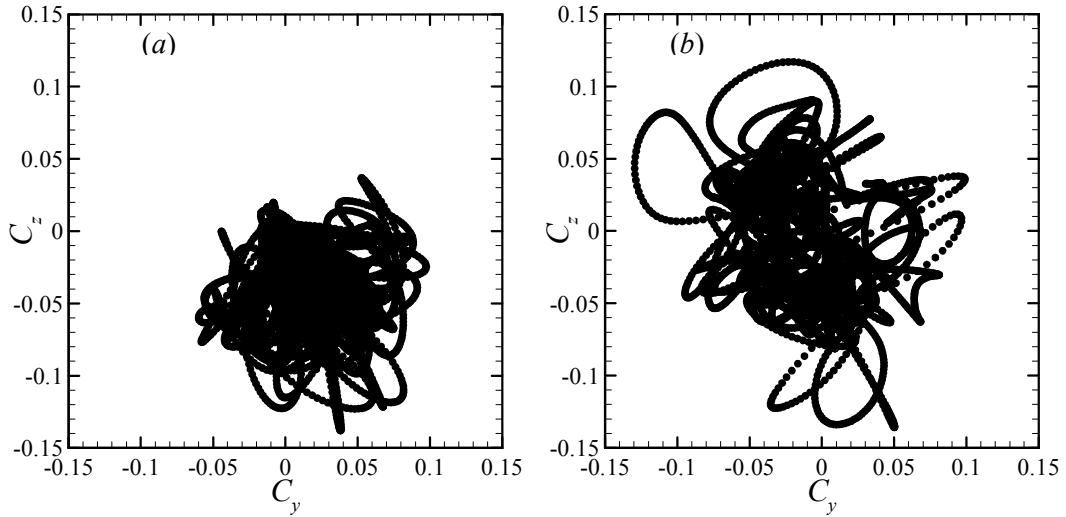


Figure 3.4.5. Phase plots for unsteady asymmetric flow: (a) $Re = 400$; (b) $Re = 500$.

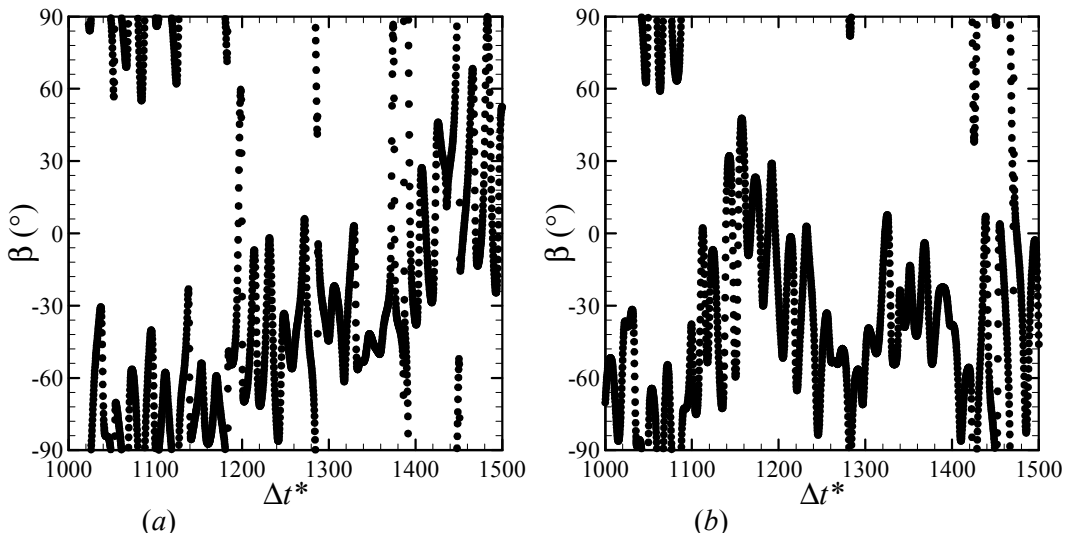


Figure 3.4.6. Sample time histories of the net lift angle β : (a) $Re = 400$; (b) $Re = 500$.

300. As a result, it is evident that a plane of symmetry no longer exists, and is lost within the range $300 < Re < 400$. As previously mentioned, Mittal (1999b) found a loss of planar symmetry in the range $350 < Re < 375$, whereas the experimental study of Sakamoto & Haniu (1990) found a value of $Re = 420$. For a Reynolds number of $Re = 400$, the net lift coefficient appears to have a preferred orientation that lies in the lower right quadrant of the phase plot. When the Reynolds number is increased to $Re = 500$, a preferred orientation of the wake is less discernible. This is in agreement with the results of Mittal *et al.* (2002) who found that with increasing Reynolds number, the preference for any particular orientation of the wake diminished.

More information on the vortex shedding process may be obtained from the angle of the lift force β . This is depicted in Figures 3.4.6 (a) and (b) for $Re = 400$ and $Re = 500$ respectively. Unlike the

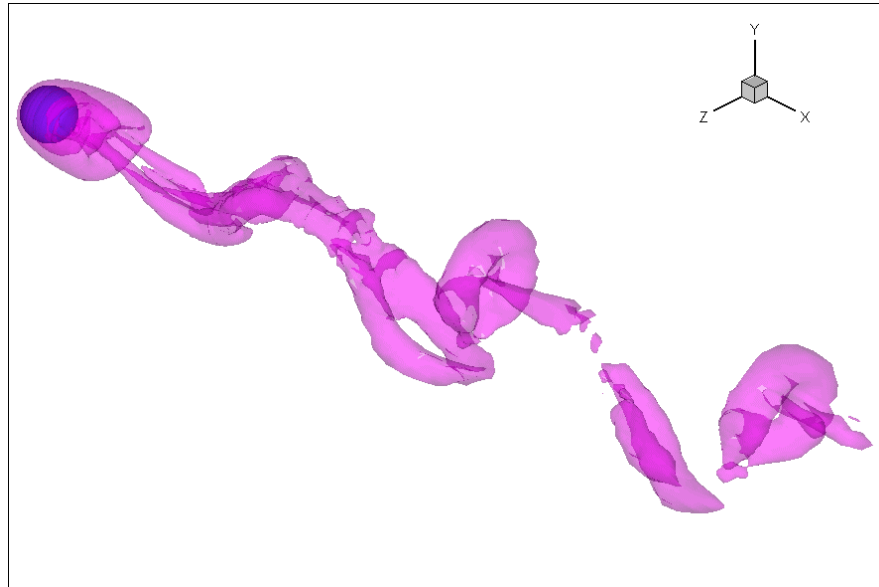


Figure 3.4.7. Visualization of vortex structures for unsteady asymmetric flow at $Re = 400$.

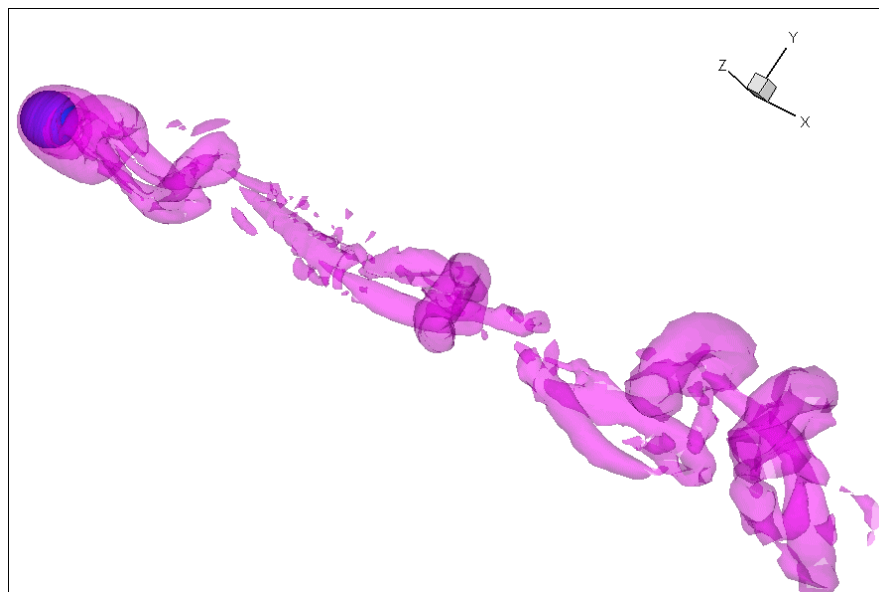


Figure 3.4.8. Visualization of vortex structures for unsteady asymmetric flow at $Re = 500$.

previous case ($Re = 300$) in which β is constant, for the unsteady asymmetric case β appears to be chaotic. It is obvious in Figure 3.4.6 that the direction of the net lift coefficient varies considerably over time, so that the azimuthal angle of vortex formation varies from shedding cycle to cycle.

3.4.4 Visualization of vortex structures

As previously mentioned, comparisons are made difficult in this regime because of the non-periodic unsteadiness of the flow. As a consequence, with regard to §3.3.6, visualization of the vortex structures over a period of vortex shedding is not possible because the period is irregular, although not in a time-averaged sense. Hence, the instantaneous vortex structures depicted in this unsteady asymmetric regime are obtained at arbitrary time instants.

Figure 3.4.7 illustrates the typical vortex structures observed for a stationary sphere at a Reynolds number of $Re = 400$, whereas Figure 3.4.8 shows the vortex structures at a Reynolds number of $Re = 500$. In both cases, isometric views are depicted in order to fully elucidate the three-dimensional configuration. At $Re = 400$, the wake appears similar to that at a Reynolds number of $Re = 300$, although in this case a plane of symmetry is not evident. The legs and head of a hairpin vortex can be seen emanating from the strong vortical region at the rear of the sphere, whereas the previously shed hairpin vortex and its corresponding induced hairpin vortex have clearly rotated as the structures convect downstream. When the Reynolds number is increased to $Re = 500$ (Figure 3.4.8), the wake is obviously less organized. The vortex formation length has also decreased substantially, as a vortex head appears to be emerging from the rear of the sphere and below this emerging head are the legs of an induced hairpin vortex. In the far wake, the vortex structures have rotated and deformed as they convect downstream. The difference in the orientation and clarity of the vortical structures between a Reynolds number of $Re = 400$ and $Re = 500$ as seen in Figures 3.4.7 – 3.4.8 is quite remarkable.

Chapter 4

Rotating Sphere

Rotating spheres are found in many applications, yet very little research has been undertaken concerning the changes in flow topology as the Reynolds number and angular rotation rate are varied. For example, the trajectories of golf balls and baseballs (Watts & Ferrer (1985)) are highly dependent on the amount of spin on the ball, which affects the ball's lift and drag characteristics. Furthermore, particle-laden and suspension flows (Höfler & Schwarzer (2000)) are widely encountered in production, and therefore it is of great practical interest to investigate particle motion in designing manufacturing equipment. The present study aims to explore the influence of rotation on the transition (or critical) Reynolds numbers for a sphere rotating about either the streamwise axis or the non-streamwise axis.

4.1 Introduction and parameter range

The majority of research on rotating spheres in the past has focused on relatively high Reynolds numbers, typically up to $Re = O(10^6)$, as this regime has many practical applications (see, for example, Watts & Ferrer (1985), Schmitt (1997) and Davies (1949)). Conversely, a few authors have considered flow past a spinning sphere theoretically at low Reynolds numbers ($Re < 10$) because of the availability of the Stokes and Oseen approximations (Rubinow & Keller (1961), Dennis *et al.* (1980)). Only recently, however, has information become available regarding intermediate Reynolds numbers, namely $10 < Re < 10^4$. Early work by Barkla and Auchterlonie (1971) provided a benchmark against which subsequent research has been measured. The experimental results obtained

by Tsuji *et al.* (1985) indicate that in the Reynolds number range $550 < Re < 1600$ and for nondimensional angular velocity $\Omega < 0.7$, the lift coefficient may be approximated by

$$C_l = (0.4 \pm 0.1)\Omega \quad (4.1.1)$$

obtained empirically by comparing measurements of the range of flight of the sphere with the solution of its equation of motion. Similarly, for $10 < Re < 100$, the drag coefficient may be calculated from

$$C_d = 0.6167 + \frac{46.5}{Re} - \frac{116.67}{Re^2}. \quad (4.1.2)$$

However, Equation (4.1.2) neglects the effects of sphere rotation (which was considered negligible), which may produce drag coefficients differing by up to 5% for rotations between $0.05 < \Omega < 0.25$, according to the present simulations.

More recent experimental data have been acquired by Oesterlé & Bui Dinh (1998) over the Reynolds number range $10 < Re < 150$ and for (dimensionless) sphere rotation rates between $1 < \Omega < 6$. This particular parameter space was chosen principally to obtain measurements that would be compared to the theoretical results of Rubinow and Keller (1961) who used matched asymptotic expansions. They found that the lift coefficient increases with increasing rotation rate and decreases with increasing Reynolds number. Moreover, the results suggest that the influence of Ω vanishes for Re greater than 100. Despite the significant scatter in the experimental results, an expression was proposed to approximate the lift coefficient in terms of Ω and Re in the form

$$C_l \cong 0.45 + (2\Omega - 0.45)\exp(-0.075\Omega^{0.4}Re^{0.7}). \quad (4.1.3)$$

Although providing a useful correlation, Equation (4.1.3) does not support rotation rates less than unity, and may be used primarily to supplement the existing results of Rubinow & Keller (1961), Barkla & Auchterlonie (1971) and Tsuji *et al.* (1985).

More applicable to the present study are the computations performed on a rotating sphere in a linear shear flow (Kurose & Komori (1999)), for the parameter ranges $1 < Re < 500$ and $0 < \Omega < 0.25$. A finite difference scheme based on the marker-and-cell method was used to calculate the drag and lift forces on the sphere. Based on simulations performed at particular Reynolds numbers and rotation rates, an approximate expression for the lift coefficient was obtained as

$$C_l = K\Omega, \quad (4.1.4)$$

where K is a function of the Reynolds number and is listed as K_2 in Table 3 of Kurose & Komori (1999). The drag coefficient was found to increase with increasing rotation rate, and the lift coefficient approached a constant value for $Re > 200$ for a given rotational speed. This asymptotic

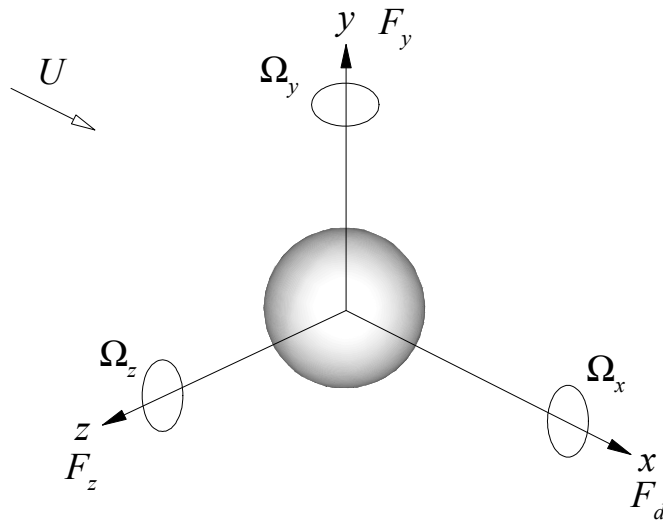


Figure 4.1.1. Coordinate system and geometry for a rotating sphere. Note that rotations are positive counterclockwise.

value of C_L increased with increasing Ω , as did the Strouhal number, St . However, no attempt was made to explain these trends as details regarding the structure of the wake were not examined in any detail.

Recently, laminar flow past a rotating sphere was investigated numerically by Kim & Choi (2002) at Reynolds numbers of 100, 250 and 300 and rotation rates of $0 < \Omega < 1$. In contrast to previous research, the rotations investigated were parallel to the streamwise axis. At $Re = 100$, the vortical structures in the wake were axisymmetric for all Ω and became stronger in the streamwise direction with increasing Ω . For $Re = 250$, at low rotation rates ($\Omega < 0.3$) one tail of the double thread vortex became stronger and the other weaker. This effect was more pronounced at $\Omega = 0.3$, at which one tail disappeared completely. However, for $\Omega \geq 0.5$ the tail reappeared and the two tails were twisted together in a complex pattern for higher rotations. For $\Omega \leq 0.3$, the vortical structure was “frozen” (ie. rotated without temporal variation in its shape and strength) and the lift and side forces were sinusoidal in time, but the magnitudes of the drag and lift forces were constant in time, a result first reported by Wang *et al.* (2001). For $Re = 300$ and low rotational speeds, the flows became unsteady asymmetric. At this Reynolds number, frozen flows were obtained at $\Omega = 0.5$ and 0.6 . However, no attempt was made to investigate the effect of different rotation rates on the wake transitions.

The coordinate system and geometry are shown in Figure 4.1.1. As defined in the nomenclature, the drag, lateral and side forces are the components of the fluid forces acting on the sphere in the x , y and z directions, and are respectively denoted as F_d , F_y and F_z . Although the nature of the transitions to asymmetry and unsteadiness have been reported for non-rotating spheres, there has been very

little exploration regarding the transitions and vortical structures for flow past a rotating sphere, especially concerning the dependence on sphere rotation for $Re > 300$. The present study finds that the transition Reynolds numbers as well as the orientation of the wake are very much dependent upon the angular rotation direction and magnitude. We focus on Reynolds numbers in the range $10 < Re < 500$ and (dimensionless) rotation rates in the range $0.05 < \Omega < 0.25$. Rotations about the x and y (or equivalently z) axes are performed. This particular parameter regime is chosen because the flow phenomena of interest, namely the transitions to asymmetry and three-dimensionality, are well observed in this regime. Furthermore, many results (such as lift, drag and Strouhal numbers) are available for a stationary sphere ($\Omega = 0$) that provide a basis from which to validate the present results. Some of the results presented here were first reported in Pregalato *et al.* (2001) and Pregalato *et al.* (2002a,c).

4.2 Non-streamwise sphere rotations

The Magnus (or Robins) effect on rotating spheres has been well documented since the early 17th century (Barkla & Auchterlonie (1971)). In these early years, when many were interested in how the flight of tennis balls was affected by spin, it was thought that the “true explanation” was that the pressure is greatest on the side where velocity was least, but this is true only for frictionless fluids. With the advent of boundary layer theory in 1904, it was soon realized that the observed motion was due to the delayed separation of the boundary layer on the high velocity side of the sphere, thereby deflecting the wake and resulting in a net lift force. The calculation of this lift force is important in many applications, and is the focus of the next section.

For the case of the non-streamwise rotating sphere, recent results have shed light on the drag and lift forces experienced by the sphere but transition Reynolds numbers have not been explored (Kurose & Komori (1999)). Moreover, the vortex shedding characteristics and nature of the flow at low Reynolds numbers have not been explored in any detail, in contrast to higher Reynolds numbers. To demonstrate the existence of (and clarify the effects of) the Magnus force, simulations were performed with the sphere rotating about the y - and z -axes independently. Moreover, y -force coefficients for z -axis rotations were numerically identical to z -force coefficients for y -axis rotations as expected, and subsequently all the results presented represent z -axis rotations.

4.2.1 Drag and lift coefficients

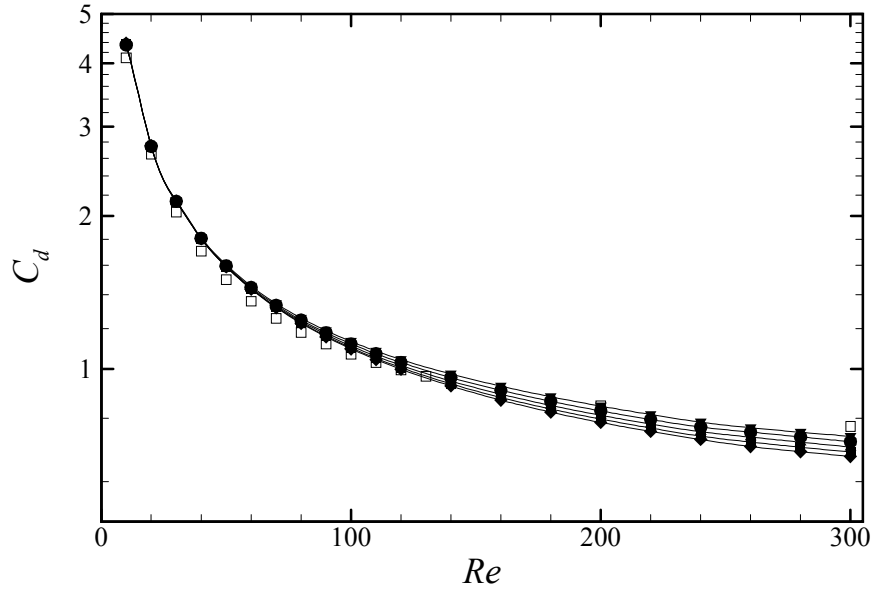


Figure 4.2.1. Effect of non-streamwise sphere rotation on the drag coefficient. Present results: \blacklozenge , $\Omega = 0.05$; \blacksquare , $\Omega = 0.10$; \blacktriangle , $\Omega = 0.15$; \bullet , $\Omega = 0.20$; \blacktriangledown , $\Omega = 0.25$. Tsuji *et al.* (1985) results: \square .

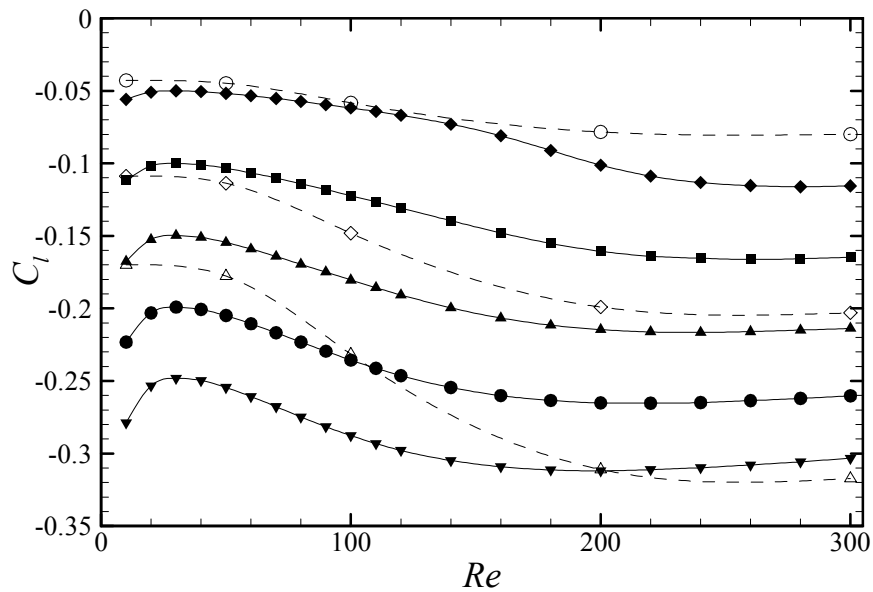


Figure 4.2.2. Effect of non-streamwise sphere rotation on the lift coefficient. Present results: symbols as in Figure 4.2.1. Kurose & Komori (1999) results: \circ , $\Omega = 0.063$; \diamond , $\Omega = 0.16$; \triangle , $\Omega = 0.25$.

Figure 4.2.1 shows the effect of non-streamwise sphere rotation rates on the drag coefficient for Reynolds numbers up to $Re = 300$. For comparison, the experimental results of Tsuji *et al.* (1985) are also displayed using Equation (4.1.2), which is obtained by assuming that the drag coefficient is not influenced by the rotation. Equation (4.1.2), which is strictly valid for Reynolds numbers less than $Re = 100$, provides a good fit in this range. Kurose & Komori (1999) numerically investigated

rotation rates of 0.063, 0.16 and 0.25 for Re up to 500. The power-law scaling of the drag coefficient compares well to that of Kurose & Komori (1999) in their Figure 17. Furthermore, similar behaviour is observed with the change in rotation rate: C_d increases with increasing Ω . This is especially noticeable at the higher Reynolds numbers, where the difference in drag between $\Omega = 0.05$ and $\Omega = 0.25$ is approximately 9% at a Reynolds number of 300.

Figure 4.2.2 shows the predicted variation of the lift coefficient with sphere rotation. Note that C_l is negative because the sphere is rotating counterclockwise. The results of Kurose & Komori (1999) are also shown using Equation (4.1.4). At low rotation rates and low Reynolds numbers, the approximation using Equation (4.1.4) is reasonable. For $Re > 200$ and higher rotation rates, the approximation is improved. However, the estimate at intermediate Reynolds numbers is inaccurate, and is probably the result of using too few points for the calculation of the interpolating functions. Initially, the predicted lift coefficient decreases at lower Re and reaches a minimum at a Reynolds number of 30, independent of the angular velocity magnitude. The magnitude of C_l then roughly increases linearly and approaches a constant value for $Re > 200$. This asymptotic value increases with increasing Ω , and compares well with the calculations of Kurose & Komori (1999) and the experimental measurements of Tsuji *et al.* (1985). However, the present results show that the magnitude of this asymptotic value is approximately equal to $C_l(\text{asymptote}) = 0.065 + \Omega$. Nonetheless, although useful for engineering applications, these drag and lift coefficients do not describe very well the features of the wake, and cannot be used to accurately predict the transition process to unsteadiness.

4.2.2 Streamlines, pressure and vorticity fields

As with Figure 3.2.2, the presence of a plane of symmetry is most obvious in the streamline plots in Figure 4.2.3 for $\Omega_z = 0.10$ and a Reynolds number of 200. Once again, the streamlines represent true three-dimensional streamlines although the out-of-plane components are not clearly discernible. The main difference between this rotating case and the stationary sphere situation is the absence of an upper focus when the sphere is rotating, which is evident in the streamline plot in the x - y plane. Note that the sphere is rotating counter-clockwise in Figure 4.2.3 (b). In contrast to Figure 3.2.2, the lower focus is fed by fluid that originates from the lower upstream flow. Because of continuity, there must be fluid flowing out of the vortex and this fluid is clearly ejected into the near wake.

Pressure coefficient contours for the x - z and x - y planes are shown in Figure 4.2.4 for $\Omega_z = 0.10$ and a Reynolds number of 200. Note that for a stationary sphere at this Reynolds number, the flow is axisymmetric. These contours are similar to the contours for non-axisymmetric flow illustrated in Figure 3.2.3 at a Reynolds number of $Re = 250$. As expected, the plane of symmetry coincides

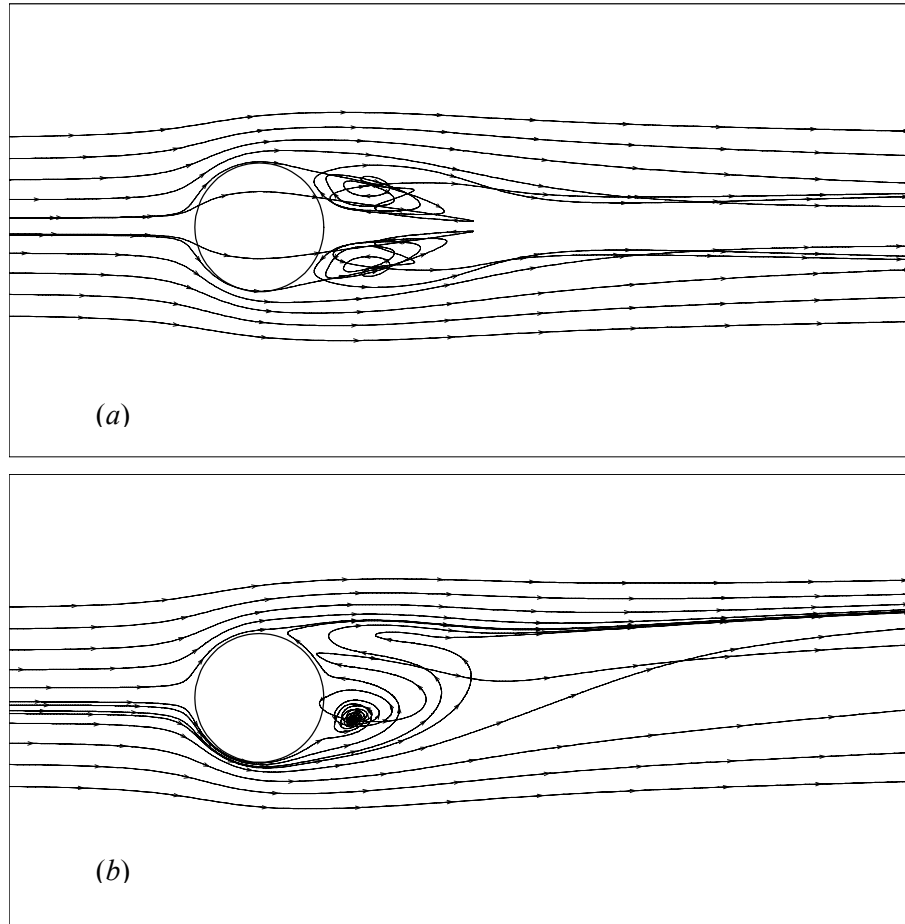


Figure 4.2.3. Streamlines for a non-streamwise rotating sphere at $Re = 200$ and $\Omega_z = 0.10$: (a) x - z plane; (b) x - y plane.

exactly with the x - y plane without the need to rotate the entire flow field, unlike the steady planar-symmetric flow past a stationary sphere in which the symmetry plane is random if the original axisymmetry is perfect and in the absence of any external perturbations (Ghidersa & Dusek (2000)). It appears then that the out-of-plane velocity component is responsible for the breakdown of axial symmetry, as pointed out by Thompson *et al.* (2001). For a stationary sphere at a Reynolds number of $Re = 200$ (Figure 3.1.3) and a Reynolds number of $Re = 250$ (Figure 3.2.3), a detached ring of low pressure exists in the near wake. However, this ring of low pressure is not present in Figure 4.2.4. Three-dimensional visualizations of the pressure coefficient in Figure 4.2.4 (c) reveal that this U-shaped ring of low pressure is attached to the rear of the sphere and is tilted, inducing flow along the vortex axis. Note that the surface of the sphere is shaded blue, whereas the front stagnation region is green, as in Figure 3.2.3.

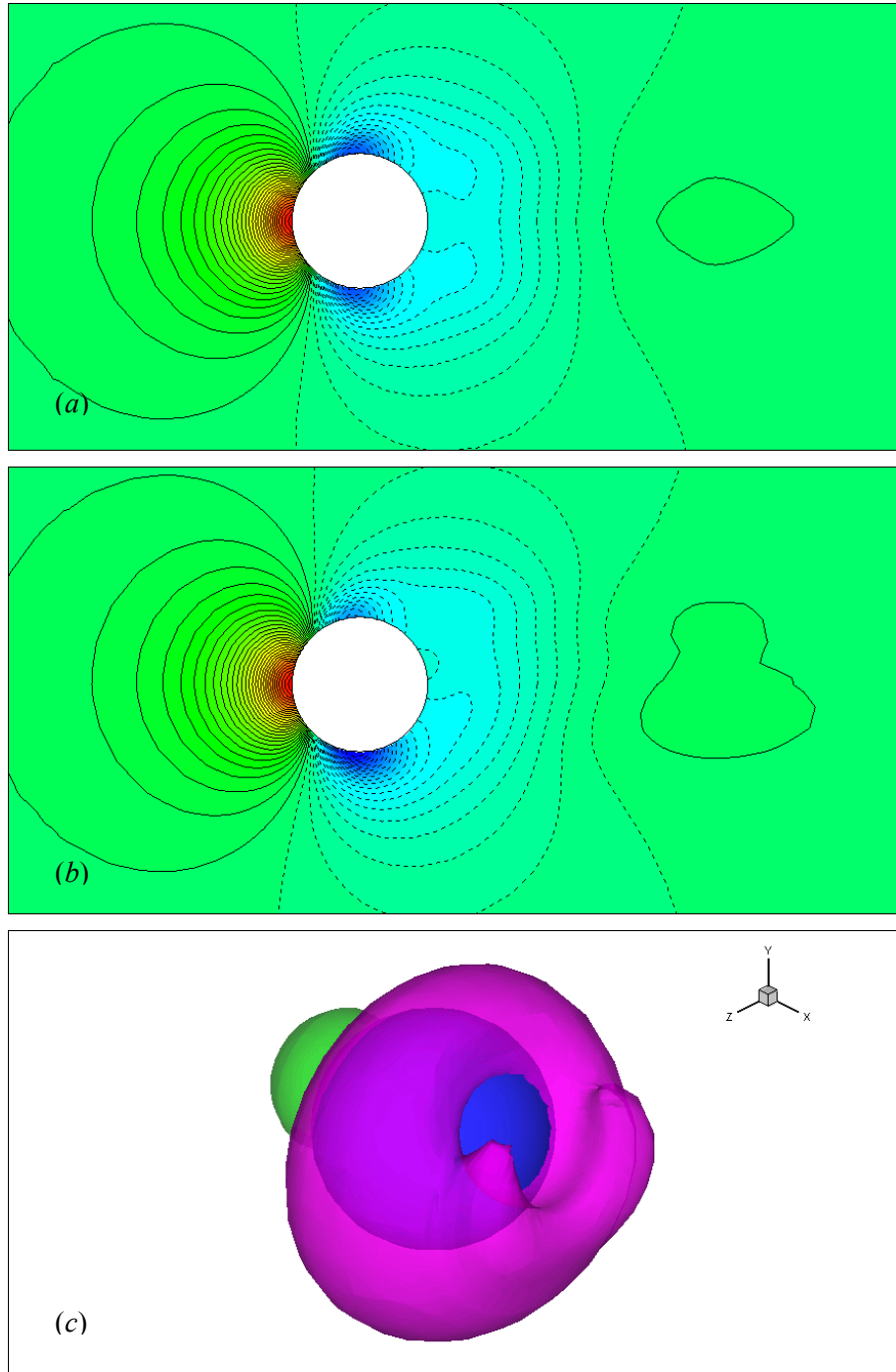


Figure 4.2.4. Pressure coefficient contours for $Re = 200$, $\Omega_z = 0.10$: (a) x - z plane; (b) x - y plane; (c) isometric view of pressure isosurfaces.

Streamwise vorticity contours are shown in Figures 4.2.5 for the same angular rotation of $\Omega_z = 0.10$ at a Reynolds number of 200. The contours in Figure 4.2.5 are not unlike those for non-axisymmetric flow past a stationary sphere, as seen in Figure 3.2.4, although there are some distinctions. One of the major differences is the direct generation of streamwise vorticity on the surface of the sphere. Also, in Figure 3.2.4, vorticity is being convected downstream and is

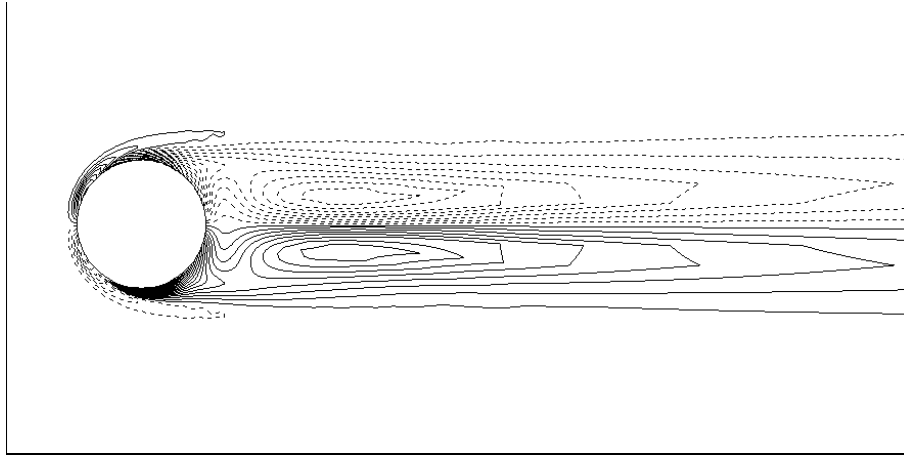


Figure 4.2.5. Streamwise vorticity contours in the x - z plane for $Re = 200$, $\Omega_z = 0.10$.

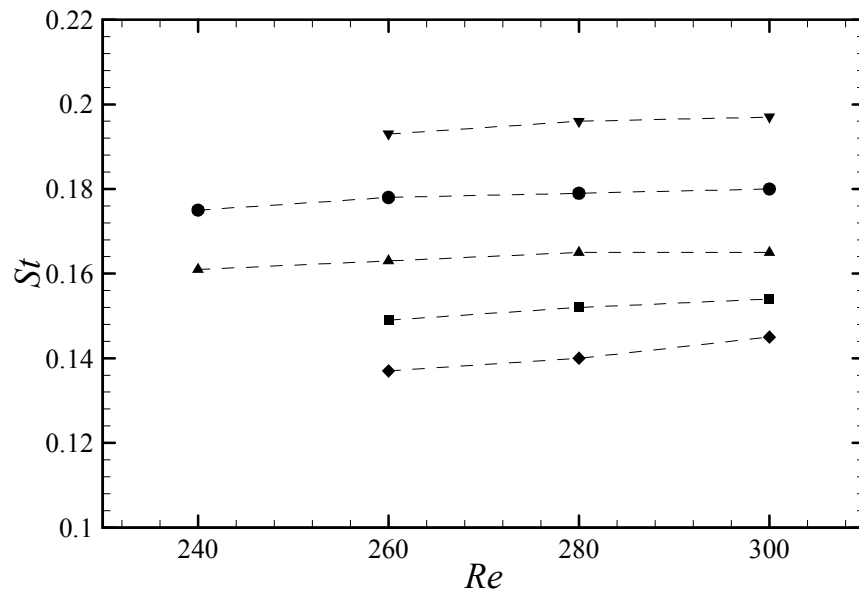


Figure 4.2.6. Vortex shedding frequencies versus Reynolds number for varying rotation rates.

Symbols as in Figure 4.2.1.

accompanied by a small oval-shaped region of opposite-signed vorticity that is detached from the rear of the sphere (see Figure 4 of Thompson *et al.* (2001)) However, for a rotating sphere, this small region of vorticity is attached to the front of the sphere (and is produced by the high velocity gradients induced by the rotation of the sphere and the no-slip condition at the surface), and does not separate as the Reynolds number is increased.

4.2.3 Vortex shedding frequencies and vortex structures

Vortex shedding frequencies f , in the form of Strouhal numbers ($St = fd/U$), were measured and are shown in Figure 4.2.6. Increasing the Reynolds number, as one might expect, increases the vortex shedding frequency. Furthermore, for any given Reynolds number, increasing the sphere rotation rate results in an increase in Strouhal number. This is probably due to the fact that the intensity of the reversed flow generated by the vortex increases with increasing rotation rate, and interferes with the separating shear layer (Johnson & Patel (1999)). This reverse flow effectively cuts off the vortex from the wake prematurely and increases the shedding frequency of the wake.

Vortical structures in the unsteady wake are depicted in Figures 4.2.7 (a-c) for a typical case of $\Omega_z = 0.10$ and $Re = 300$ in the x - y and x - z planes, as well as an oblique view to highlight its fully three-dimensional structure. As mentioned in Chapter 2, the vortex structures are visualized as an isosurface of $-\lambda_2 = 0.1$. At this Reynolds number, the flow has become unsteady, and the plane of symmetry that was observed for steady flow in the previous section is also apparent in Figure 4.2.7. The periodic shedding of hairpin vortices is instantly recognizable and resembles closely the flow past a stationary sphere at the same Reynolds number (see Chapter 3). In this case, however, the plane of symmetry that arises naturally for a stationary sphere is instead dictated by the direction of rotation of the spinning sphere.

4.2.4 Critical Reynolds numbers

For all of the Reynolds numbers investigated, the lift force was non-zero and indicates the presence of asymmetry. Recall that for a stationary sphere, axisymmetry is lost at a Reynolds number of approximately 212, and the resulting wake exhibits a two-tailed vortex structure. However, in the present simulations for a non-streamwise rotating sphere, the two-tailed wake is observed only when the Reynolds number is high enough to convect the streamwise vorticity far downstream into the wake. Furthermore, the plane of symmetry is dependent on the direction of rotation, ie. the x - y plane is the symmetry plane for rotations about the z -axis and the x - z plane for rotations about the y -axis (Pregalato *et al.* (2001)).

Because the out-of-plane velocity component (due to the sphere rotation) breaks the axisymmetry of the flow even at the low Re investigated, the transition to asymmetry was unable to be monitored. However, the transition to unsteadiness was more straightforward. As mentioned previously, the drag and lift coefficients presented in Figures 4.2.1 and 4.2.2 were steady until a Reynolds number of approximately 240. Side force coefficients, based on the force orthogonal to the mean flow

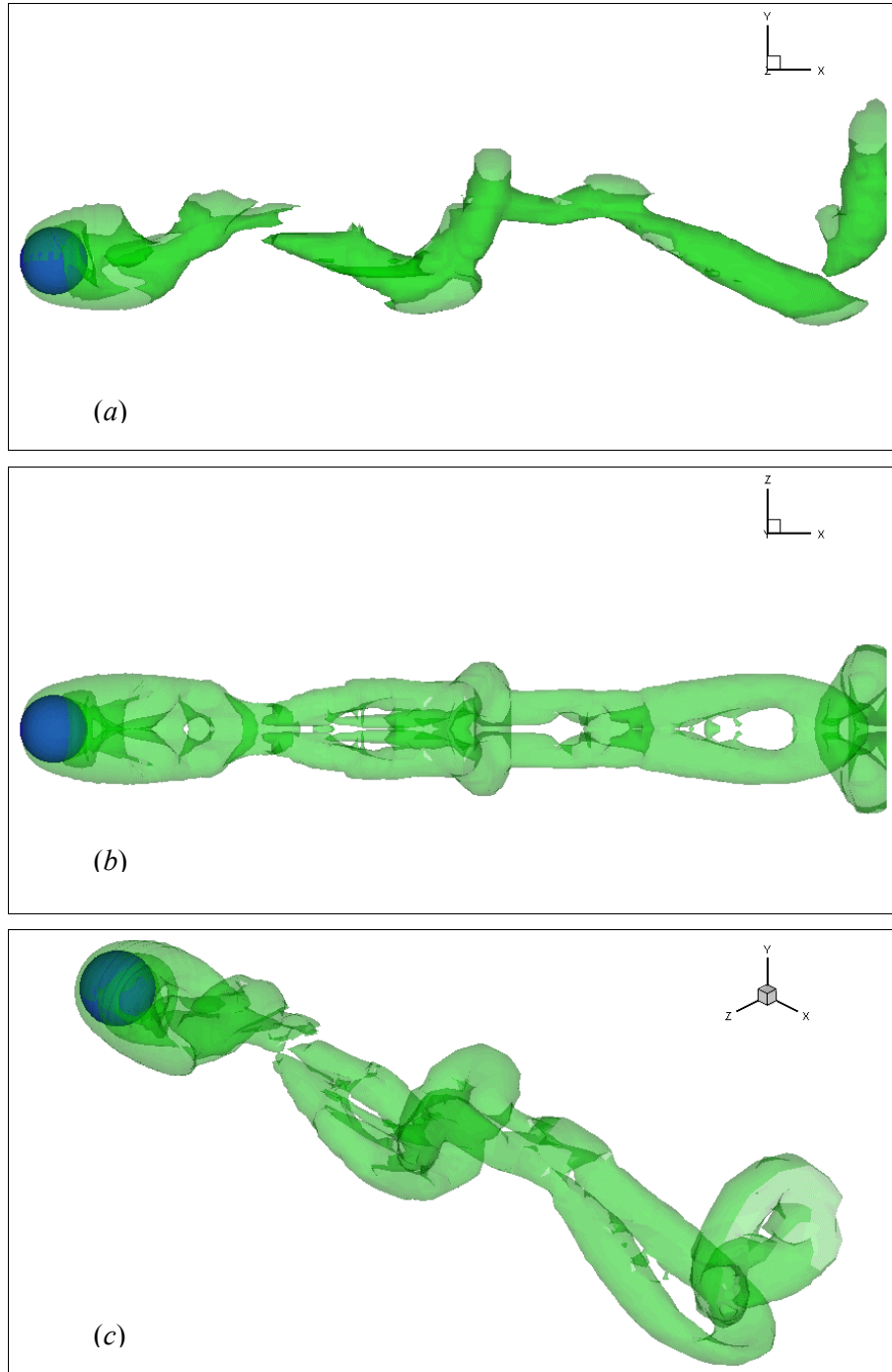


Figure 4.2.7. Vortex structures in the wake of a non-streamwise rotating sphere at $Re = 300$, $\Omega_z = 0.10$: (a) x - y plane; (b) x - z plane; (c) isometric view.

symmetry plane, were found to be zero for all of the Reynolds numbers investigated, meaning that the same x - y symmetry that was observed for steady flow was also present for unsteady flow. For $Re = 240$ onwards, the values of C_d and C_l depict time-averaged quantities and were sampled over approximately twenty periods. The critical Reynolds numbers for the transition to unsteadiness are shown in Figure 4.2.8 as a function of the rotation rate.

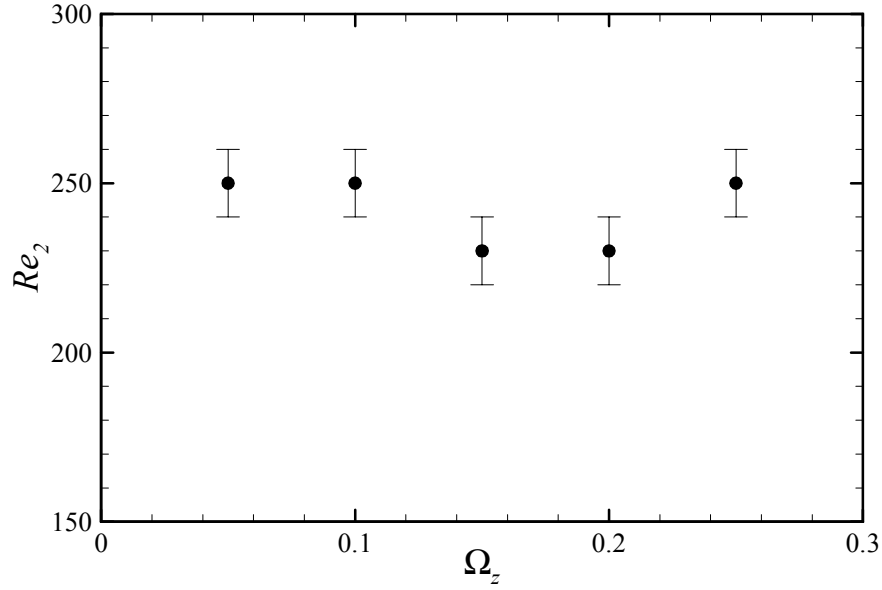


Figure 4.2.8. Critical Reynolds numbers as a function of sphere rotation rate for a non-streamwise rotating sphere.

For $\Omega_z = 0.05$ and $\Omega_z = 0.10$, the flow was found to become unsteady at a Reynolds number of $Re = 250 \pm 10$. On the other hand, unsteadiness was observed initially in the range $220 < Re < 240$ for $\Omega_z = 0.15$ and $\Omega_z = 0.20$. When the rotation rate was increased to $\Omega_z = 0.25$, the flow was initially unsteady but then decayed to a steady state. The critical Reynolds number for this case was the same as for the lower rotation rates of $\Omega_z = 0.05$ and 0.10 . Since unsteadiness is observed for a stationary sphere at $Re > 270$, it is evident that the effect of non-streamwise rotation is to reduce the critical Reynolds number at which transition is observed.

4.3 Streamwise sphere rotations

Given the number of publications regarding rotating spheres, it is somewhat surprising to note that there is a significant lack of research concerning a *streamwise* rotating sphere. Indeed, the effect of streamwise rotation has not been examined in any detail and little is known concerning the flow transitions and vortical structures in the wake. For the purpose of presenting the following results in a systematic manner, some clarification needs to be addressed regarding identification of the fluid forces. In this respect, C_d is the coefficient of the drag directed parallel to the streamwise or x -axis. Similarly, C_y (lateral) and C_z (side) are the coefficients of force parallel to the y - and z -axes respectively. The lift coefficient C_l , therefore, is defined as the magnitude of the lateral and side force coefficients, and is directed in the plane normal to the x -axis.

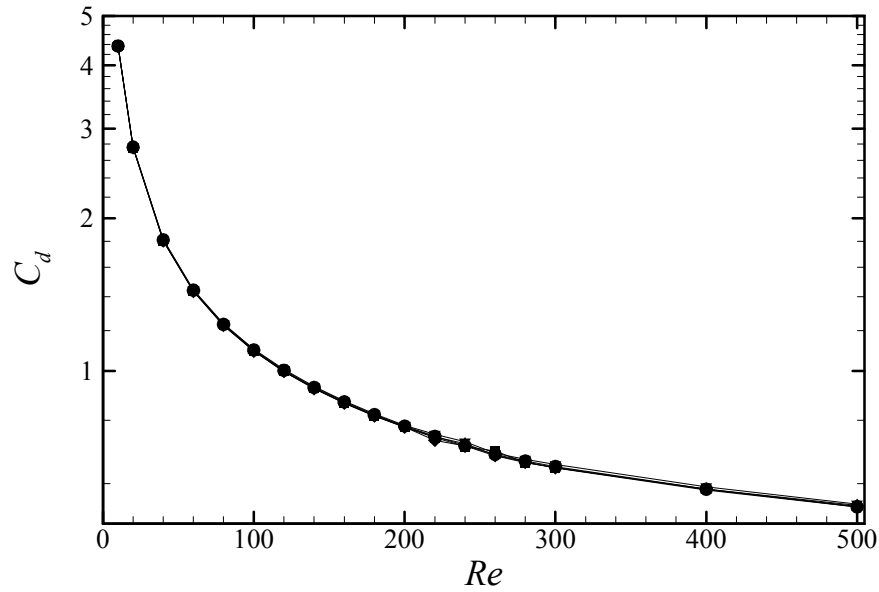


Figure 4.3.1. Effect of streamwise sphere rotation on the drag coefficient. Symbols as in Figure 4.2.1.

4.3.1 Drag coefficients

Figure 4.3.1 shows the drag coefficient for a sphere rotating about the x -axis for Reynolds numbers up to 500. Similar behaviour of C_d is observed for a non-streamwise rotating sphere, shown in Figure 4.2.1, in particular the increase in C_d as the rotation rate increases, although not as much as that which is observed for the non-streamwise rotating sphere. However, the most notable distinction between the two plots is the difference in C_d at any given Reynolds number for the different angular velocities. For the non-streamwise rotating case, the difference in C_d is approximately 7% at $Re = 200$, when the flow is still steady and asymmetric. On the other hand, for the streamwise rotating sphere the difference in C_D between $\Omega_x = 0.05$ and $\Omega_x = 0.25$ is about 0.7% at the same Reynolds number. This difference is explained by the observation that for all rotations, up to $Re = 200$, the flow was found to be axisymmetric. Furthermore, it was found that if the rate of rotation is small enough, then the tendency of the flow to remain axisymmetric is increased. This is explored further in §4.3.6.

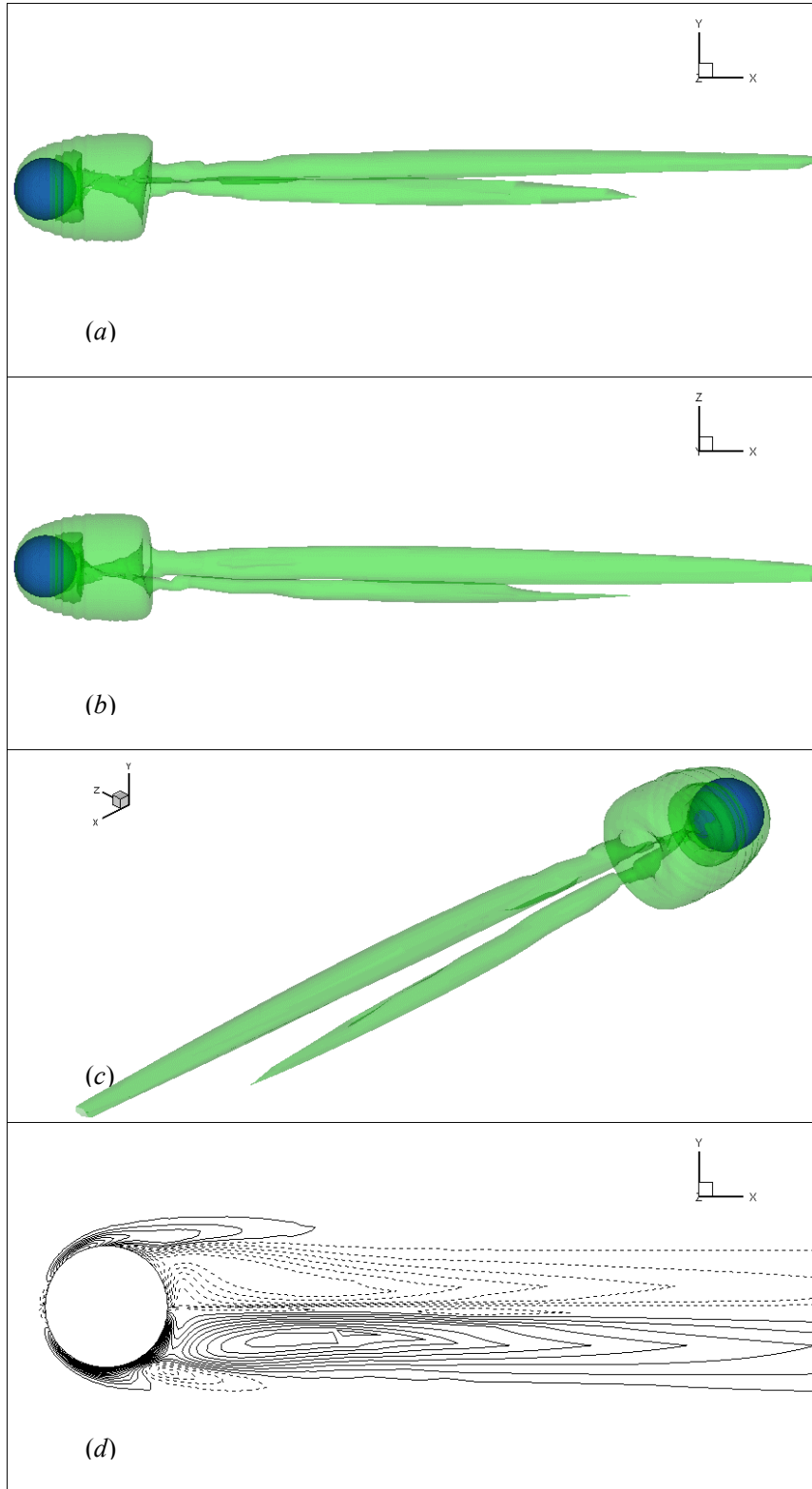


Figure 4.3.2. Vortex structures for a non-streamwise rotating sphere at $Re = 260$, $\Omega_x = 0.05$: (a) x - y plane; (b) x - z plane; (c) isometric view; (d) streamwise vorticity contours in the x - y plane.

4.3.2 Vortex structures

Different views of the vortex structures in the wake of the sphere are shown in Figure 4.3.2 for a streamwise rotation rate of 0.05 and for $Re = 260$. At this Reynolds number, the flow has become unstable enough to make a transition to an asymmetric state, and exhibits the two-tailed wake observed in Figure 3.2.5. However, in contrast to Figure 3.2.5, the wake is no longer planar symmetric and the previously balanced two tails have become skewed with respect to the streamwise axis. Furthermore, the “strength” of one tail has become greater than the other. This is apparent in Figure 4.3.2 (d), which shows the streamwise vorticity in the x - y plane. Due to the no-slip condition on the surface of the sphere, it is evident that fluid passing over the surface of the sphere attains the strong non-streamwise velocity of the sphere. This serves to increase the streamwise vorticity that is in the same direction of rotation, and annihilates the streamwise vorticity that is in the opposite direction of rotation. This leads to two counter-rotating vortices of dissimilar strength, and causes them to migrate away from the flow centreline due to their mutual vortical interaction. The vorticity contours in Figure 4.3.2 (d) are also markedly different from those for a stationary sphere and a non-streamwise rotating sphere, mainly because of the generation of the same-sign vorticity on both the upper and lower surfaces of the sphere. Furthermore, a small region of opposite-sign vorticity is generated at the front stagnation point, and the contours clearly do not show a plane of symmetry.

4.3.3 The “frozen” vortex structure

As previously mentioned, if the rotation rate is low enough ($\Omega_x < 0.15$) then a two-tailed wake structure is observed. However, for higher rotation rates, the stronger vortex overwhelms the weaker vortex and a single thread is observed immediately adjacent to the wake centreline. This is similar to the observations of Kim & Choi (2002) for their rotation rate of 0.3 at $Re = 250$. Figure 4.3.3 depicts the time variation of the drag, lateral and side force coefficients for $Re = 240$ and $\Omega_x = 0.15$. The simulation was initialized with the corresponding solution for a stationary sphere at the same Reynolds number. The drag coefficient remains constant in time, whereas the lateral and side force coefficients are sinusoidal with a frequency of $St_f = 0.017$. Note that St_f is a frequency based on the “frozen” state of the flow and is not the Strouhal frequency, St , associated with vortex shedding. Since the time-averaged lateral and side forces are zero, the vortical structures in the wake (see Figure 4.3.4) simply rotate in a frozen state. This “frozen” flow was discovered by Wang *et al.* (2001) and investigated in detail by Kim & Choi (2002) and the present results provide independent verification of such a flow feature for the spinning sphere. Note that the rotational speed of the vortical structure is in general different to that of the sphere.

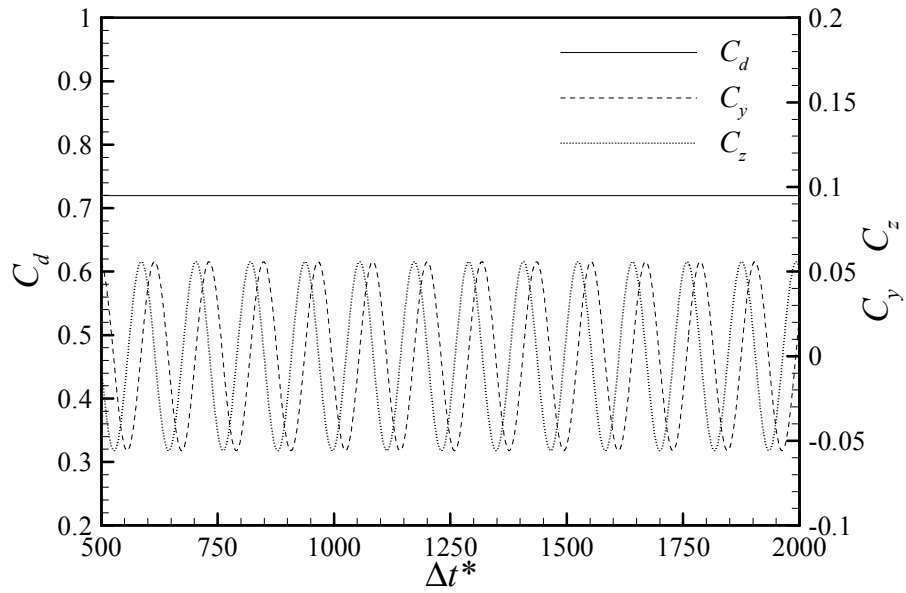


Figure 4.3.3. Sample time histories of the force coefficients for $Re = 240$, $\Omega_x = 0.15$.

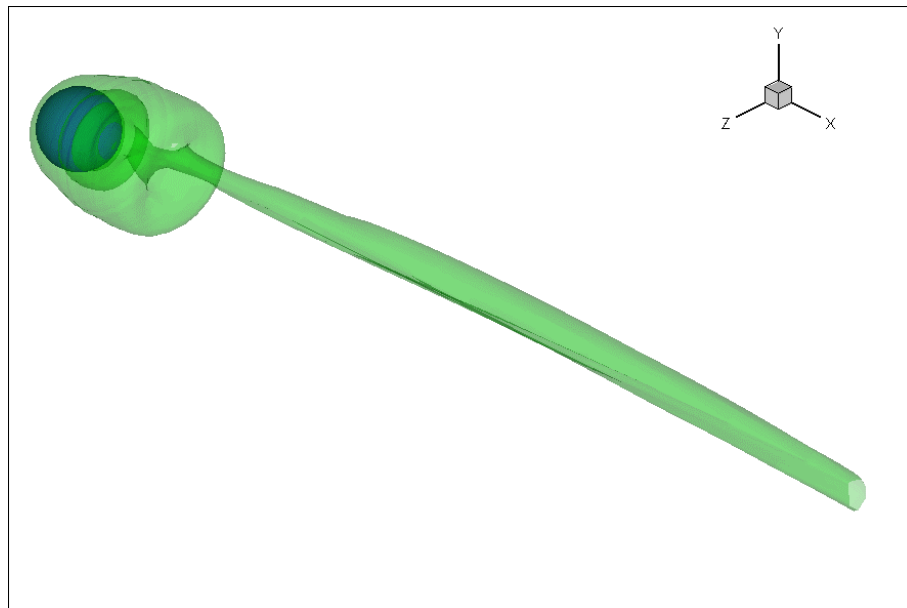


Figure 4.3.4. Isometric view of the “frozen” vortex structure in the wake of a streamwise rotating sphere at $Re = 240$, $\Omega_x = 0.15$.

Care was needed in performing the simulations to ensure that the resultant flow state was saturated. For example, for $Re = 220$ and $\Omega_x = 0.25$, a nondimensional time of $\Delta t^* \geq 500$ was required in order for the force measurements to reach a statistically steady quasi-periodic state. A further 1500 time units were required in this case to obtain a sufficiently large sample space of 20 periods of oscillation, given the low frequency of vortical rotation of $St = 0.030$. On the other hand, for many

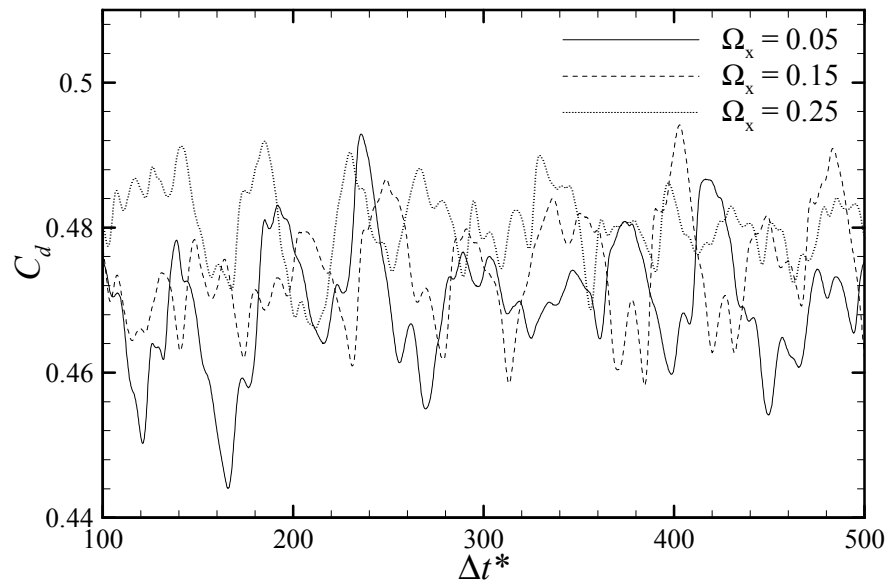


Figure 4.3.5. Sample time histories of the drag coefficient at $Re = 500$ for select streamwise rotation rates.

other simulations, the force measurements would exhibit unsteady behaviour and then saturate to a constant state. This fact highlights the importance of having a considerable time interval for integrating the governing equations and allowing for any disturbances to grow or decay.

4.3.4 Higher Reynolds number simulations

At the next Reynolds number of interest, $Re = 500$, for all rotations investigated the flow was found to be unsteady and asymmetric. Plots of the predicted drag coefficient are shown in Figure 4.3.5 where, for clarity, only angular rotation rates of $\Omega_x = 0.05$, 0.15 and 0.20 are presented. For all of these rotation rates, the drag coefficient exhibits an aperiodic behaviour, very similar to that of a stationary sphere at the same Reynolds number. Time-averaging of these coefficients reveal that the drag increases with increasing rotation rate, in accordance with Figure 4.3.1. Furthermore, an increase in the rotation rate appears to influence the drag coefficient in such a manner as to induce a more regular pattern, as if the flow is approaching a frozen state. Figure 4.3.6 depicts the vortical structures in the wake for $\Omega_x = 0.15$ and $Re = 500$. The legs and the head of a hairpin vortex can be seen in the centre of the image. Immediately downstream of this hairpin vortex appears to be an induced hairpin vortex whose orientation has twisted so that it is no longer in line with the previous hairpin vortex. Finally, beyond this induced hairpin vortex is the head of a previously shed hairpin vortex that appears as a vortex loop. It is evident that the previously frozen state of the vortical structures at $Re = 250$ had now become unfrozen and the vortical structures show a distinct

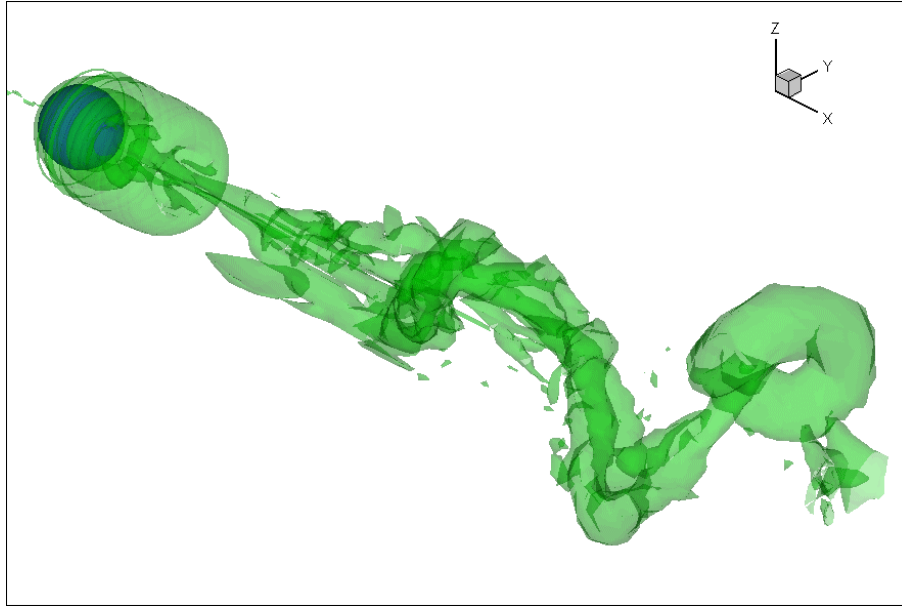


Figure 4.3.6. Isometric view of the vortex structures in the wake of a streamwise rotating sphere at $Re = 500$, $\Omega_x = 0.15$.

resemblance to that of a stationary sphere at the same Reynolds number. However, the hairpin vortices and vortex loops are clearly more distorted owing to the rotation of the sphere and the flow appears to be far more unstructured. For rotation rates in the range $0.05 < \Omega_x < 0.25$ no frozen states were observed, lending weight to the conjecture of Kim & Choi (2002) that frozen flow fields for $Re > 300$ should occur only for higher sphere rotation rates, ie. $\Omega_x \geq 0.5$.

4.3.5 Dynamics of the frozen vortex

Further insight into the behaviour of the lift coefficient may be gained by considering its phase diagram, as shown in Figure 4.3.7, which illustrate plots of C_y versus C_z for a rotation of $\Omega_x = 0.15$ at Reynolds numbers of $Re = 240, 300, 400$ and 500 . Figure 4.3.7 (a) depicts the behaviour of the force coefficients when the flow, as mentioned previously, is frozen. Here, the phase diagram is drawn for the time interval of two periods of revolution of the vortical structures. As for the case of a stationary sphere (see Chapter 3), the net lift is given by the distance from the origin to the curve, and the angle β is the direction of the lift. For $Re = 240$, the phase diagram is a circle because the net lift itself is constant but the direction in which it acts changes with time. Note that the time-averaged lateral and side force coefficients are zero. For $Re = 300$, the phase diagram is still a closed curve but is no longer a perfect circle, and the direction of the lift coefficient rotates about the origin. This is because the flow is not frozen (but still, it is periodic and asymmetric) and both the magnitude and direction of the lift change with time. For higher Reynolds numbers, the phase diagrams are no

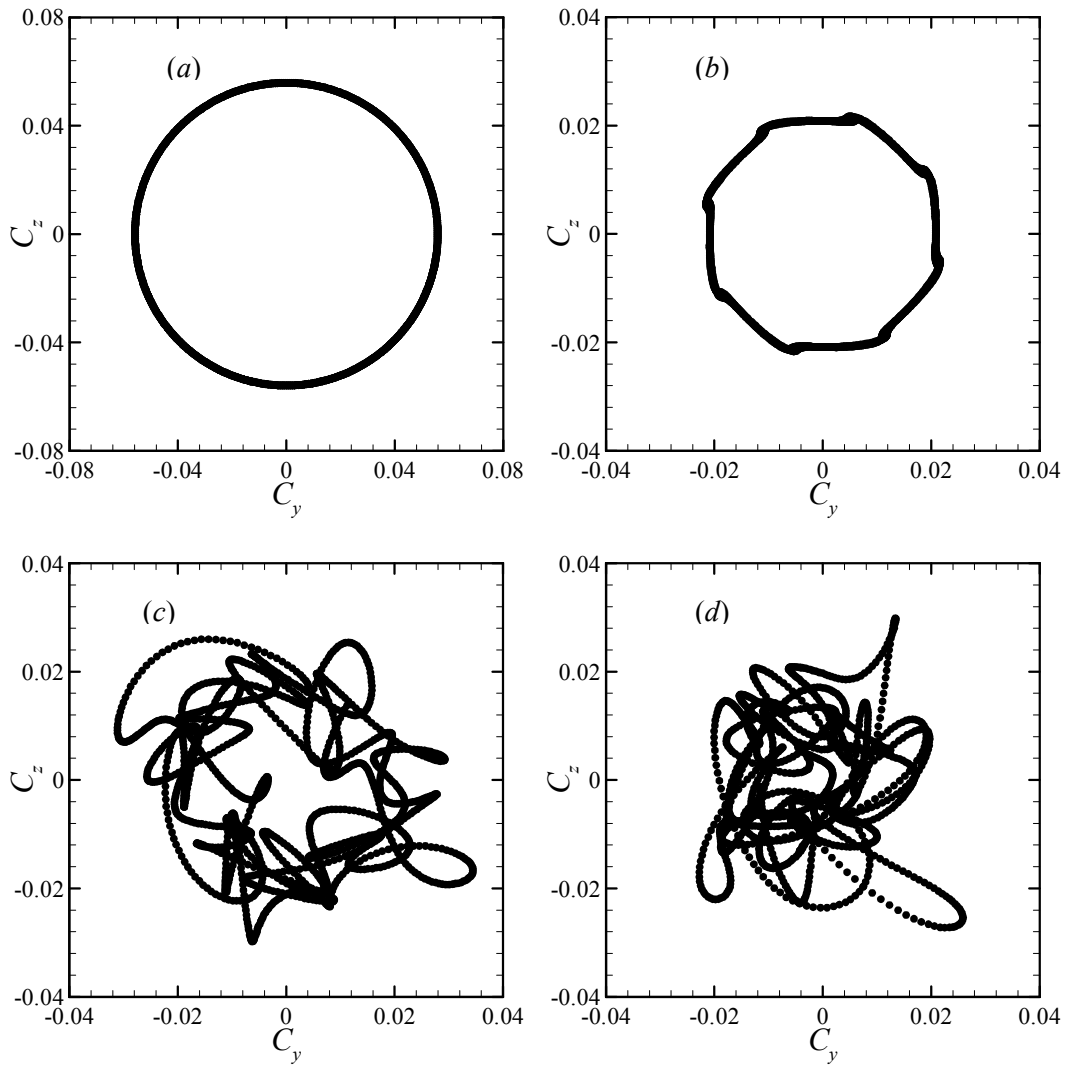


Figure 4.3.7. Phase diagrams of the net lift coefficient for $\Omega_x = 0.15$: (a) $Re = 240$; (b) $Re = 300$; (c) $Re = 400$; (d) $Re = 500$.

longer closed and show that the streamwise rotating sphere does not have a preferred azimuthal orientation of vortex loop formation, in contrast to that of a stationary sphere for $Re < 1000$ which appears to show a preferred azimuthal orientation (Mittal *et al.* (2002)). Note the different scales on the axes in the plots of Figure 4.3.7, which show that the net lift for $Re \geq 300$ may be less than half the lift for $Re = 240$ for the same streamwise rotation.

In general, the rotation rate of the vortical structures is different to that of the sphere. This may be observed by recording the time history of the lift angle β . The slope of β indicates the rotating velocity of the vortex structures, which for a stationary sphere is zero (in a time-averaged sense) at $Re = 300$ and appears to be quite erratic for $Re = 500$. For the streamwise rotating sphere, at $Re = 240$, the ratio of the period of rotation of the vortical structures to that of the sphere (T_V/T_S) was approximately 1.63 for $\Omega_x = 0.15$. At $Re = 300$, this ratio decreased to 1.56. This is because the

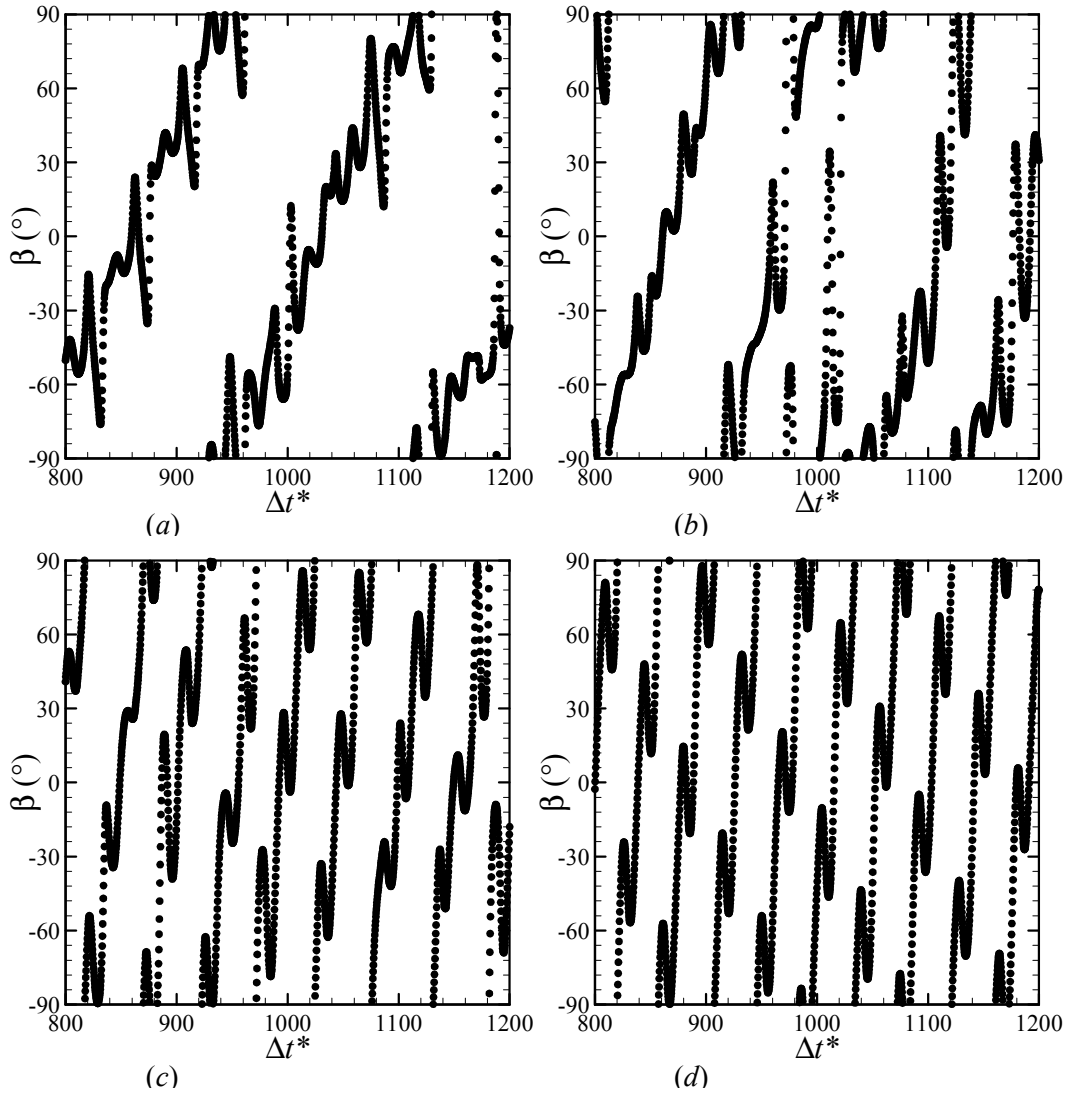


Figure 4.3.8. Sample time histories of the angle of the net lift coefficient for $Re = 400$: (a) $\Omega_x = 0.05$; (b) $\Omega_x = 0.10$; (c) $\Omega_x = 0.20$; (d) $\Omega_x = 0.25$.

vortex structures found at the two Reynolds numbers are completely different (single-thread as opposed to shedding hairpin vortices). Furthermore, for higher Reynolds numbers ($Re > 300$), the angle of lift progressively became more unpredictable as the flow became more aperiodic.

The angular velocity of the frozen vortical structures in the wake is determined by the slope of β , i.e. $\Omega_f \equiv$ angular velocity of frozen vortical structures $= d\beta/dt$ in rad/s. At a Reynolds number of $Re = 260$, for example, the frozen vortex structures are rotating at a dimensionless angular velocity of $\Omega_f = 0.034$, whereas the sphere is rotating at $\Omega_x = 0.10$. Continuing with this Reynolds number of $Re = 260$, we find that increasing the rotation rate serves to increase the rotation rate of the frozen vortical structures, in an almost one-to-one correspondence. In other words, doubling the rotation rate of the sphere will double the rotation rate of the frozen vortical structures as well, assuming that the flow is still frozen at these higher angular velocities. Figure 4.3.8 shows typical time histories of the angle

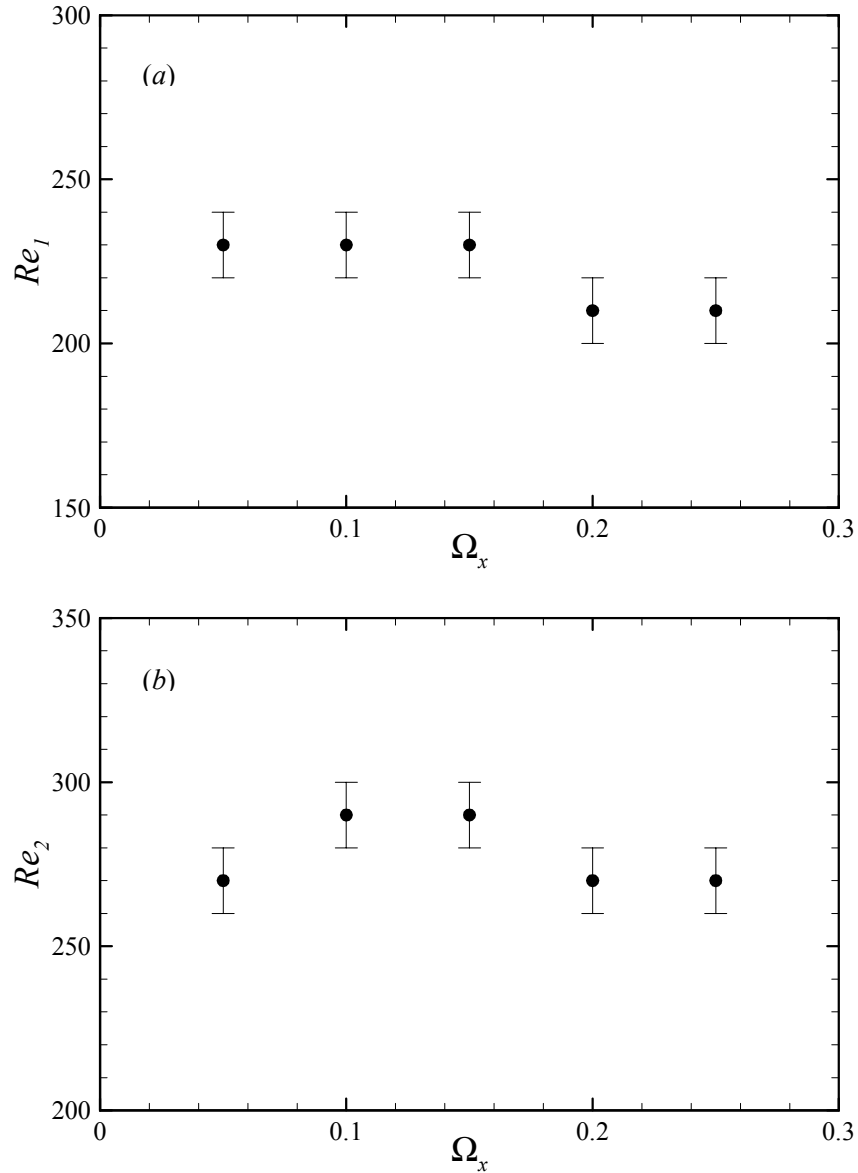


Figure 4.3.9. Critical Reynolds numbers as a function of sphere rotation rate for a streamwise rotating sphere: (a) transition to asymmetry; (b) transition to unsteadiness.

of lift β for different rotation rates at a Reynolds number of $Re = 400$. At low rotation rates, it is clear that vortices are being shed azimuthally in an aperiodic fashion, and hence Ω_f is not constant. However, as the rotation rate increases, the flow becomes more organized, and the vortex structures are shed with a relatively constant angular velocity. It appears that increasing the rotation rate further will lead to the appearance of frozen vortical structures at these higher Reynolds numbers, as pointed out by Kim & Choi (2002), which is a topic of further study. Also, for all rotation rates investigated, there is no preferred angle of vortex orientation.

4.3.6 Critical Reynolds numbers

The transition to asymmetry, which occurs at a critical Reynolds number Re_1 , is shown in Figure 4.3.9 (a). Also illustrated is the second transition to unsteadiness (Figure 4.3.9 (b)), which occurs at a critical Reynolds number Re_2 . Note that Re_2 in this sense denotes the Reynolds number at which vortex shedding first occurs and not necessarily the onset of time-dependence (since the frozen fields observed in Figure 4.3.4 are time-dependent although vortex shedding is not observed). This makes it somewhat easier to compare the present results concerning the wake transitions to that of a stationary sphere. It is apparent that for rotation rates less than $\Omega_x = 0.2$, the flow becomes asymmetric at a critical Reynolds number in the range $220 < Re_1 < 240$. For $\Omega_x \geq 0.2$, the transition occurs in the Reynolds number range $200 < Re_1 < 220$. For a stationary sphere, this transition occurs at a Reynolds number of $Re_1 \approx 212$. It follows that small streamwise rotation rates cause a delay in the transition to asymmetry, whereas higher rotation rates appear to not affect the critical Reynolds number. Furthermore, vortex shedding first occurs in the range $260 < Re_2 < 280$ for rotation rates of $\Omega_x = 0.05, 0.20$ and 0.25 , which is close to the value of $Re_2 \approx 272$ for a stationary sphere. However, for rotation rates of $\Omega_x = 0.10$ and 0.15 , the transition occurs in the Reynolds number range $280 < Re_2 < 300$.

In conclusion, the effect of streamwise rotation on the transition to unsteadiness is not as significant as that for non-streamwise rotation, as shown in Figure 4.2.8. When taking into account the uncertainties in the values of Re_1 and Re_2 , we see from Figure 4.2.8 that the flow becomes unsteady at $Re_2 \approx 240$ regardless of the non-streamwise rate of rotation, whereas Figure 4.3.9 (b) shows that this transition occurs at $Re_2 \approx 280$ regardless of the streamwise rotation rate. Thus, since the wake of a stationary sphere becomes unsteady at $Re_2 \approx 272$, it is clear that the transition to unsteadiness is more affected by non-streamwise rotation than streamwise rotation.

Chapter 5

Tethered Sphere

One of the most basic examples of fluid-structure interaction is a tethered body immersed in a uniform flow. In the maritime industry, physical examples include buoys, spars, submerged sea mines, pipelines, bathyscaphes and other underwater craft. Typical examples in the aerospace industry include weather balloons and satellite deployment. In all of these cases, it is a well-known fact that the structure will vibrate when exposed to oscillatory forcing, such as the action of surface waves on a tethered buoy. However, before the work of Williamson & Govardhan (1997), it was previously unknown whether such a system will vibrate in a uniform flow, despite the simple nature of the problem. Indeed, for a tethered sphere at least, the structure shows a remarkable tendency to vibrate over a wide range of Reynolds number and reduced velocity. It is the purpose of the present investigation to examine, in detail, under what circumstances the tethered sphere will oscillate, and in particular the physical mechanisms that cause these vibrations.

As mentioned in Chapter 2, the geometry of the tethered sphere is defined by two non-dimensional parameters: the mass ratio M^* , and the tether length L^* . Between these two parameters, the mass ratio is the more important and significant. A “heavy” sphere corresponds to $M^* > 1$, and may be thought of physically as a pendulum or a plumb line oscillating freely in an airflow. On the other hand, a “light” sphere corresponds to $M^* < 1$, and could represent an ocean buoy tethered to the sea bed. In the present study, we focus on *low* mass ratios, ie. $M^* < 1$, although the numerical procedure outlined in Chapter 2 is not limited to any particular realistic mass ratio. Furthermore, we examine a particularly significant case, $M^* = 1$, representing a neutrally buoyant sphere. Similarly, the tether

lengths that are investigated range from $L^* = 5$ to $L^* = 10$, although there is no limit to how large (or small) L^* can be (apart from the obvious limiting conditions at zero and infinity).

This chapter is organized as follows. First of all, the natural frequency f_n is defined in terms of the governing parameters, as outlined in the nomenclature. This is followed by preliminary experimental results of a tethered sphere at Reynolds numbers much lower than those previously investigated. The computational results begin by analysing the dynamics of low mass ratio tethered spheres, in particular for $M^* = 0.082$. This mass ratio is chosen so that comparisons may be made with the pioneering work of Williamson & Govardhan (1997). The next section is devoted to an analysis of high mass ratios, specifically $M^* = 0.8$, which enables some comparisons to be made with the work of Jauvtis *et al.* (2001). These results are compiled in §5.5 to investigate the suitability of using the reduced velocity as a scaling parameter. The next section analyzes the dynamics of a neutrally buoyant sphere, with particular emphasis on the oscillation trajectories. The vibrational responses observed for the tethered sphere are examined in detail in the following sections, in which the fluid forces, pressure and vorticity fields are inspected in order to determine the mechanisms of vibration. Finally, the existence of a critical mass is discussed and conclusions are presented in the final section with further work in the field.

5.1 Calculation of the natural frequency

Like any dynamical system, the tendency of the tethered sphere to vibrate is a function of the natural frequency of vibration of the system. As a result, the natural frequencies of vibration in the x , y and z directions need to be calculated. This is performed by recalling the equations of motion of the tethered sphere (Equations (2.2.1) – (2.2.4)), which we recast in the form

$$m\ddot{x} + \frac{T}{L}x = F_d \quad (5.1.1)$$

$$m\ddot{y} + \frac{T}{L}y = F_y + B \quad (5.1.2)$$

$$m\ddot{z} + \frac{T}{L}z = F_z. \quad (5.1.3)$$

From these equations, we see that the natural frequency is the same in all three directions, and is given by the expression

$$f_n = \frac{1}{2\pi} \sqrt{\frac{T}{mL}}. \quad (5.1.4)$$

This dimensional natural frequency may be put in non-dimensional form, which is given by

$$S_n \equiv \frac{f_n D}{U} = \frac{1}{2\pi} \sqrt{\frac{D^2}{U^2} \frac{T}{mL}}. \quad (5.1.5)$$

Substituting the expression for the tension in the tether, collecting terms and using the non-dimensional form of the fluid forces results in the following equation for the natural frequency of oscillation:

$$S_n = \frac{1}{2\pi} \sqrt{\frac{3}{4} \frac{1}{(C_a + M^*)L^*} \sqrt{C_d^2 + \{C_y + (1 - M^*)\alpha\}^2} + C_z^2}, \quad (5.1.6)$$

where the added mass coefficient C_a is introduced and has the value $C_a = 0.5$ for a sphere. For a stationary sphere, the time-averaged lateral and side forces are small compared to the drag force. Similarly, for the tethered sphere, the mass ratios of interest in this study are of $O(0.1)$, so that the buoyancy term in parentheses is much greater than the lateral force over the entire range of reduced velocities investigated, and hence Equation (5.1.6) may be simplified to

$$S_n \approx \frac{1}{2\pi} \sqrt{\frac{3}{4} \frac{\sqrt{C_d^2 + \{(1 - M^*)\alpha\}^2}}{(C_a + M^*)L^*}}. \quad (5.1.7)$$

The reduced velocity U^* is defined as the inverse of the natural frequency S_n , so that

$$U^* = 2\pi \sqrt{\frac{4}{3} \frac{(C_a + M^*)L^*}{\sqrt{C_d^2 + \{(1 - M^*)\alpha\}^2}}}. \quad (5.1.8)$$

For all of the numerical results to be presented, Equation (5.1.8) has been used to calculate the reduced velocity. Experimentally, however, the C_d^2 term is approximately 0.02% of the buoyancy term for many practical cases of interest. This means that the drag may be neglected in many instances, and the form of the natural frequency is then given by

$$S_n = \frac{1}{2\pi} \frac{1}{Fr\sqrt{L^*}} \sqrt{\frac{1 - M^*}{C_a + M^*}}, \quad (5.1.9)$$

where α has been replaced with the corresponding Froude term as defined in the nomenclature. It is evident that for $M^* = O(1)$ (but not equal to one) and for high Froude numbers, the drag term is significantly greater than the buoyancy term, so that Equation (5.1.9) is not valid. However, for smaller (or much larger) mass ratios, the approximation to the natural frequency given by Equation (5.1.9) is adequate. For the experimental results of Williamson & Govardhan (1997), Govardhan & Williamson (1997) and Jauvtis *et al.* (2001), the inverse of Equation (5.1.9) was used to calculate the reduced velocity U^* .

5.2 Experimental results at low Reynolds numbers

The experimental procedure and setup was described in detail in Chapter 2. In this section, we investigate experimentally the dynamics of a tethered sphere at Reynolds numbers much lower than those previously investigated by Williamson & Govardhan (1997), Govardhan & Williamson (1997) and Jauvtis *et al.* (2001). In particular, we consider a tethered sphere governed by the parameters $M^* = 0.91$ and $L^* = 10.24$. This particular mass ratio was chosen because of the availability of buoyant polypropylene spheres of diameters suitable for low Reynolds number applications. A range of reduced velocity is obtained by increasing the Reynolds number, which correspondingly increases the Froude number. The reduced velocity used here is defined as the inverse of Equation (5.1.9), as is the case with the experiments of Williamson & Govardhan (1997), mainly because at these low layover angles the $(C_d)^2$ term is much less than the $((1-M^*)\alpha)^2$ term.

As mentioned in Chapter 2, the range of flow velocities for the present experiments ranged from $0.04 < U < 0.062$ m/s. The corresponding Reynolds numbers ranged from $Re = 503$ to $Re = 780$. This represents flow states that are similar to the present numerical simulations. In other words, within this range of Reynolds numbers, the flow past a stationary sphere is dominated by a vortex shedding pattern that is irregular, and the shedding direction oscillates intermittently (Sakamoto & Haniu (1990)).

5.2.1 Time traces of the sphere response

To the author's knowledge, the flow-induced vibrations of a tethered sphere have not previously been investigated, either numerically or experimentally, when the flow (both upstream and in the wake) is laminar. It is not even known whether significant oscillations might be observed in this non-turbulent regime. In Figure 5.2.1, we present a sample time history of the experimentally obtained streamwise and transverse displacements of the sphere at a Reynolds number of $Re = 503$. Clearly, significant oscillations *are* observed experimentally, even at this relatively low Reynolds number. The magnitudes of the streamwise oscillations are evidently much smaller than the transverse oscillations, typically 16 times smaller. The higher Reynolds number experimental results of Williamson & Govardhan (1997) showed similar time responses of the sphere, although the streamwise oscillations were only 2 times smaller than the transverse oscillations. Nevertheless, we note from Figure 5.2.1 (b) that the peak-to-peak amplitude of the oscillations in the transverse

direction is approximately $0.75D$, which is quite large considering that it was previously unknown whether the sphere would oscillate at all when the flow is laminar.

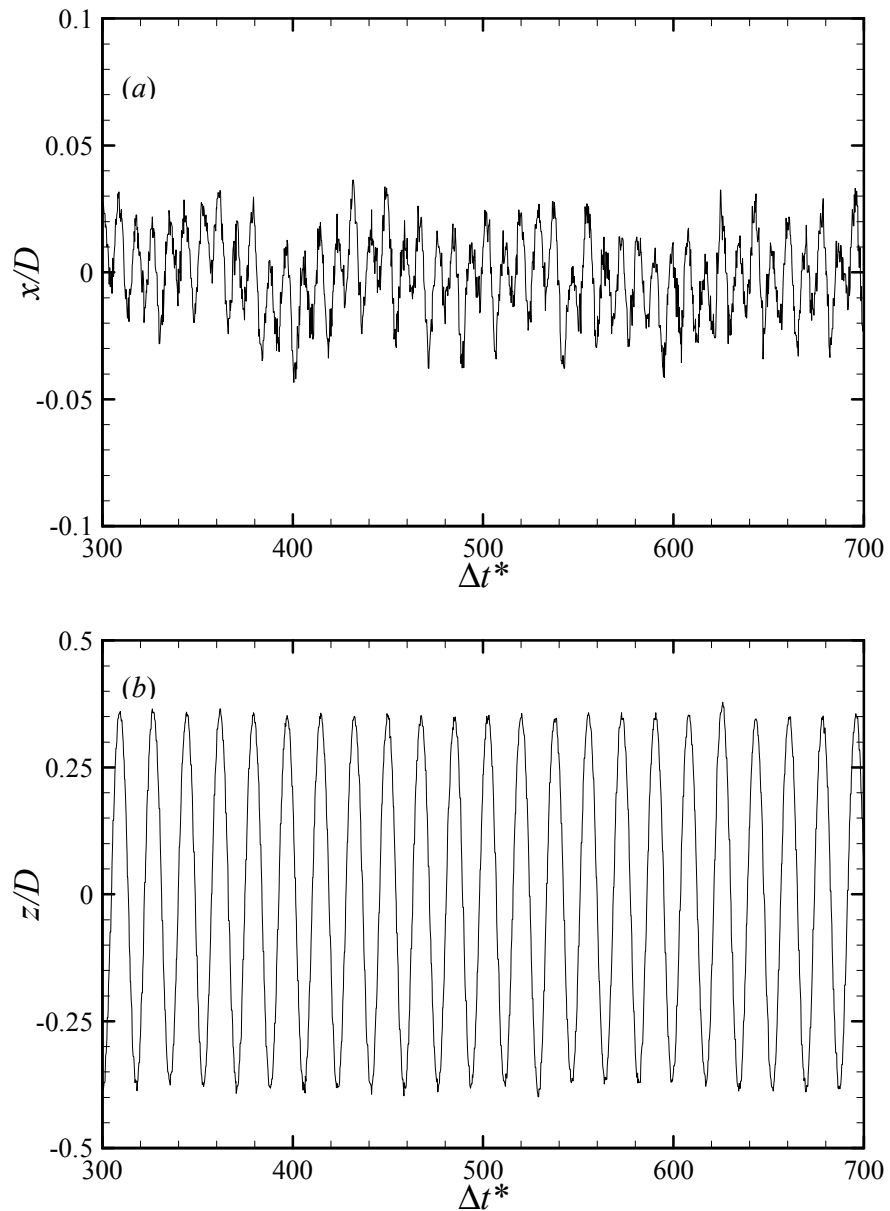


Figure 5.2.1. Sample time traces of (a) streamwise oscillations, and (b) transverse oscillations for $M^* = 0.91$, $L^* = 10.24$ at a Reynolds number of $Re = 503$.

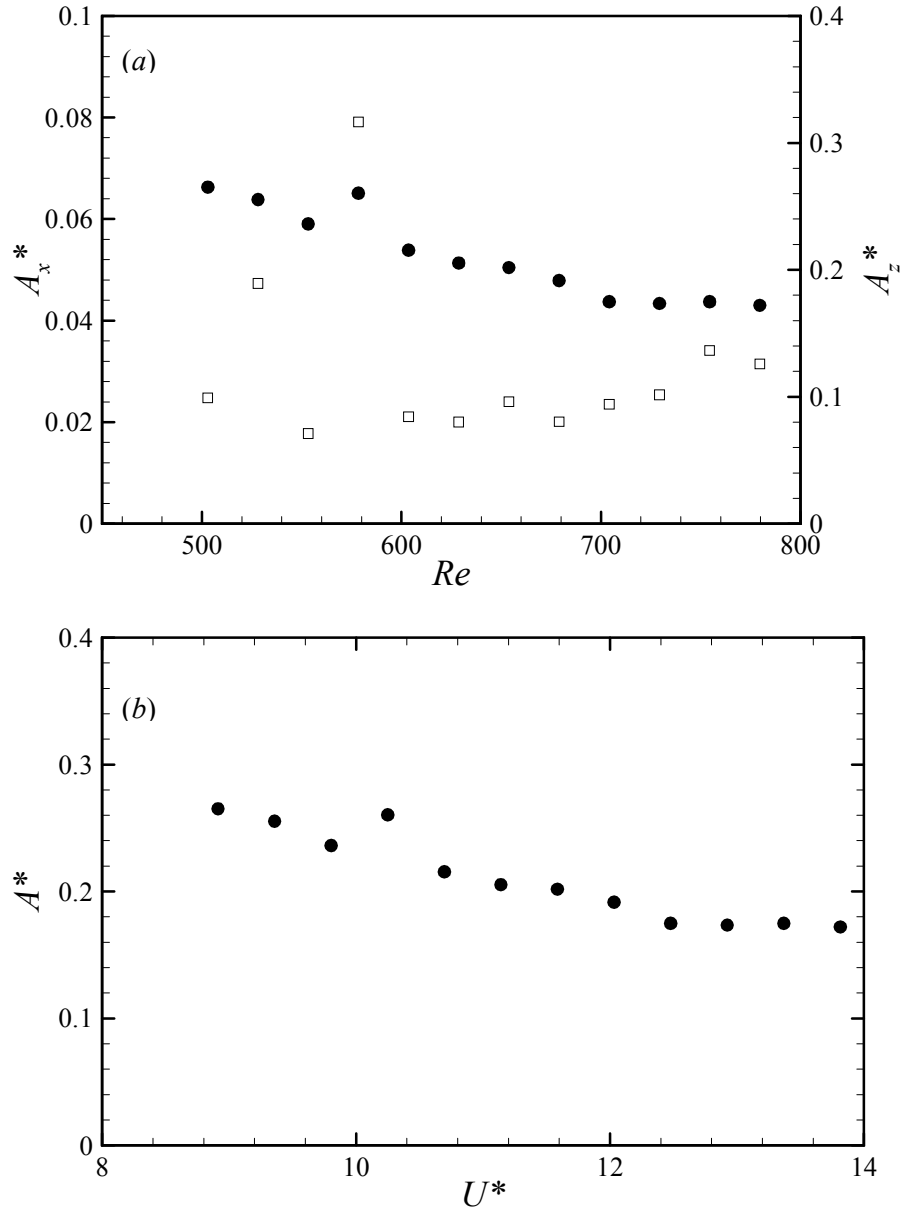


Figure 5.2.2. Normalized oscillation amplitudes A^* for $M^* = 0.91$, $L^* = 10.24$: as a function of Reynolds number, (a) x -oscillations, \square ; z -oscillations, \bullet ; as a function of reduced velocity, (b) z -oscillations, \bullet

5.2.2 Oscillation amplitudes

The normalized amplitude response of the sphere is shown in Figure 5.2.2 as a function of both Reynolds number and reduced velocity. Here, we define the normalized amplitude as $A^* = \sqrt{2}x_{rms}/D$, i.e. the normalized root-mean-square response of the sphere. Throughout the entire range of Reynolds numbers investigated, the amplitudes of oscillation in the streamwise direction are never greater than about 0.3 times the amplitudes in the transverse direction. For Reynolds numbers

greater than $Re = 600$, the amplitudes in both directions do not vary considerably, whereas the amplitudes in the streamwise direction vary considerably for Reynolds numbers in the range $500 < Re < 600$. It is also evident that the maximum amplitude in the transverse direction occurs at the lowest reduced velocity investigated, and is approximately equal to $A^* = 0.27$. As the reduced velocity is increased further, the amplitudes of oscillation in the transverse direction decrease to a value of roughly $A^* = 0.17$. As we shall see in the high mass ratio results to be presented in §5.4, the relatively large oscillation amplitudes at these reduced velocities indicate that the tethered sphere is oscillating within the Mode II regime. Note that the seemingly aberrant oscillation amplitudes at $Re = 580$ are probably due to the post-processing difficulties of the insufficient time series.

5.2.3 Frequency response

Because the large-amplitude oscillations are observed in the transverse direction, we focus now on the frequency response of those oscillations, which is depicted in Figure 5.2.3. The dash-dot line at $f^* = 1$ denotes the natural frequency of vibration of the tethered sphere system. The results of Sakamoto & Haniu (1995) on the vortex shedding frequency from a stationary sphere show that f_{vo} varies considerably within the range of Reynolds numbers used for the present experiments. For example, at a Reynolds number of $Re = 500$, the shedding frequency is approximately $St = 0.18$, which increases to $St = 0.21$ at $Re = 650$, and then decreases back to $St = 0.18$ at a Reynolds number of $Re = 800$. The frequency response of the tethered sphere, however, does not show this behaviour with increasing Reynolds number (or reduced velocity). Instead, as the reduced velocity is increased, the normalized frequency increases almost linearly, but remains more or less close to the natural frequency of the system within this range of U^* . As a result, the normalized oscillation frequency of the tethered sphere does not correspond to the vortex shedding frequency over the entire range of reduced velocities investigated, and is in fact much smaller than the vortex shedding frequency within this regime.

5.2.4 Comparisons with the numerical simulations

Even though the present experiments were performed in the laminar flow regime, comparisons with the numerical simulations are difficult to make because of the range of Reynolds numbers investigated experimentally within this laminar flow regime. However, the lowest Reynolds number investigated experimentally was $Re = 503$, close to the value of $Re = 500$ that was used for all of the numerical simulations. As a result, a single numerical simulation was performed at $Re = 500$, with exact matching of the mass ratio and tether length with the experimental values. Consequently,

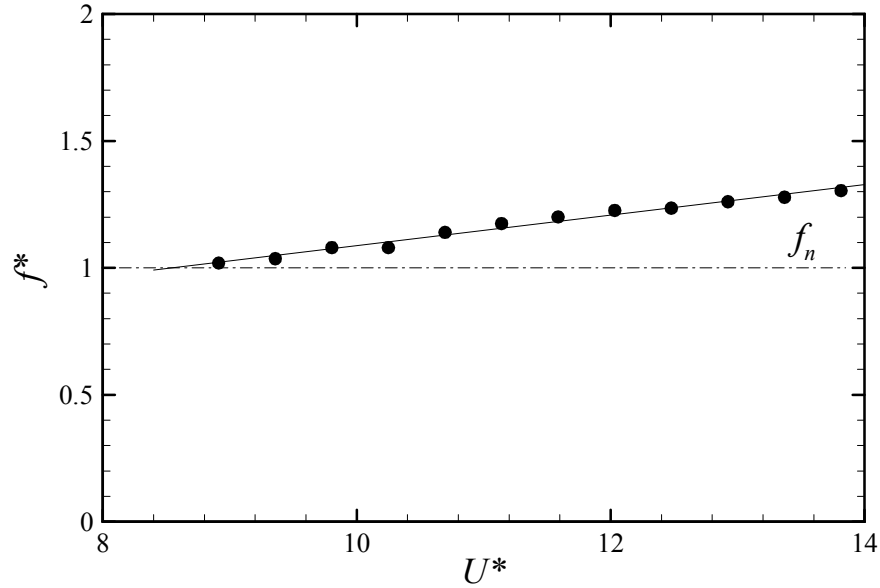


Figure 5.2.3. Normalized frequencies of oscillation in the transverse direction for $M^* = 0.91$,
 $L^* = 10.24$.

direct comparisons may be made with the experimentally observed behaviour and the numerical solution, since the mass ratio, tether length, Reynolds number and Froude number all match.

The normalized oscillations in the streamwise and transverse directions for this simulation are shown in Figure 5.2.4. These plots may be compared directly with the experimentally observed behaviour depicted in Figure 5.2.1, since the scales on both axes are the same. We see from Figure 5.2.4 (a) that the magnitudes of the oscillations are very small in the streamwise direction, characteristically less than $0.02D$, and exhibit a second frequency that is a subharmonic of the dominant frequency. The experimental results appear to show larger amplitudes of oscillation in the streamwise direction than the numerical results. However, these experimental amplitudes are roughly $0.02D$, which for the present experiments equate to amplitudes of oscillation of approximately 1 pixel. For the 1/2" diameter sphere used in these experiments, the digital video camera recorded images of the sphere whose diameter was about 50 pixels. Since the streamwise response was only about 1 pixel in amplitude, the data acquisition techniques used to compute the motion of the sphere (as outlined in Chapter 2) were evidently not very accurate for such small oscillations. As a result, the experimentally observed response in Figure 5.2.1 (a) is likely to be an overestimate of the actual response, since the amplitudes of this response are well within experimental error.

Furthermore, the amplitude response of the sphere in the transverse direction matches very closely between experiments and numerical simulations, as shown in Figures 5.2.1 (b) and 5.2.4 (b). In both plots, we see a single dominant frequency and an amplitude response that is very sinusoidal.

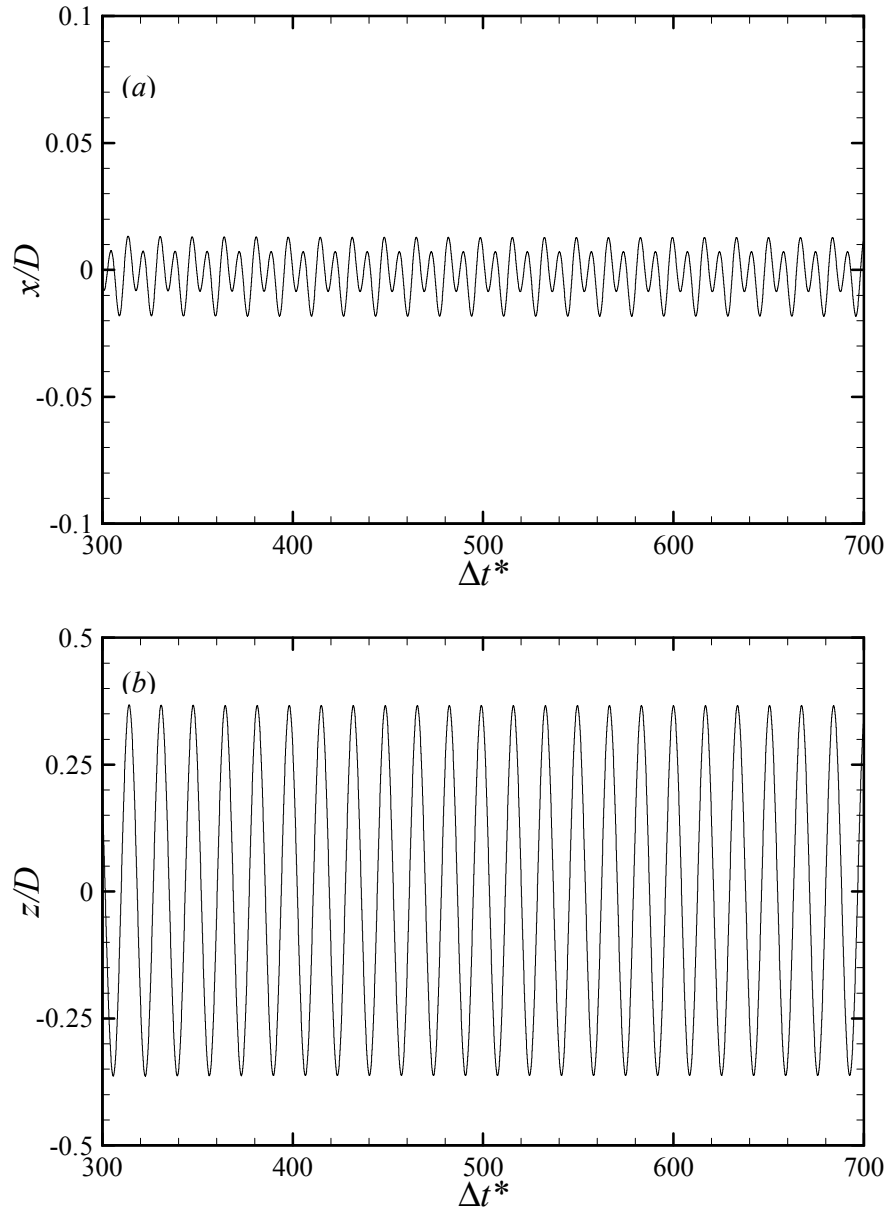


Figure 5.2.4. Sample time traces of (a) streamwise oscillations, and (b) transverse oscillations for $M^* = 0.91$, $L^* = 10.24$ from the numerical simulations.

In Table 5.2.1, we compare the (reliable) results between the experiments and the numerical simulations. For the transverse oscillation amplitudes, we find that the experimental results overestimate the amplitude response, as expected. However, this overestimate is not as significant in the transverse direction because of the large-amplitude oscillations, and we find that the difference in the amplitude response between the experiments and the numerical simulations is only about 2%. For the normalized frequencies of oscillation in both the streamwise and transverse directions, the differences between the experiments and the simulations are roughly 4%. In either case, these

discrepancies are quite small and lead to the conclusion that the direct numerical simulations do indeed accurately predict the dynamics and forcing of a tethered sphere, at least in the laminar flow conditions investigated here.

Method	A^* (transverse)	St (transverse)	St (streamwise)
Experiments	0.3717	0.114	0.228
Numerical Simulations	0.3640	0.119	0.238

Table 5.2.1. Direct comparisons between the present experiments and numerical simulations.

5.3 Low mass ratios

This section is devoted to the dynamics of a very low mass ratio tethered sphere. As mentioned in Chapter 2, a Reynolds number of $Re = 500$ was used for all simulations. The geometrical properties of the tethered sphere were chosen so as to compare these low Re results directly to higher Re results obtained from previous experiments. These experiments were performed by Williamson & Govardhan (1997), who investigated a particular case of $M^* = 0.082$ and $L^* = 9.3$. The Reynolds numbers considered ranged from $Re \approx 1500$ to approximately $Re = 13250$, which represented a reduced velocity range of $1 < U^* < 9$ using Equation (5.1.9). Unfortunately, the limits of the flow velocity attainable in the water channel did not allow a larger range of U^* to be investigated. Also, these experiments were performed by attaching the sphere to the floor of the water channel. Note that for high layover angles θ , the presence of the water channel base may affect the motion of the sphere and must be taken into account.

5.3.1 Mean layover angles

The mean layover angle θ of the tethered sphere is shown in Figure 5.3.1 as a function of reduced velocity U^* . The solid line is a line of best fit through the numerical data points. Also illustrated are the experimental results of Williamson & Govardhan (1997), which are plotted using the definition of reduced velocity given by Equation (5.1.8) as opposed to Equation (5.1.9) because of the availability of drag coefficient data. However, for this particular mass ratio and layover angles, the difference in the calculation of the natural frequency using Equation (5.1.9) as opposed to Equation (5.1.7) is less than 1%. Although these experiments were performed at Reynolds numbers typically an order of magnitude larger than those used for the simulations, it is evident that the experimental mean layover angles agree extremely well with those obtained through the numerical simulations, throughout the entire range of U^* investigated.

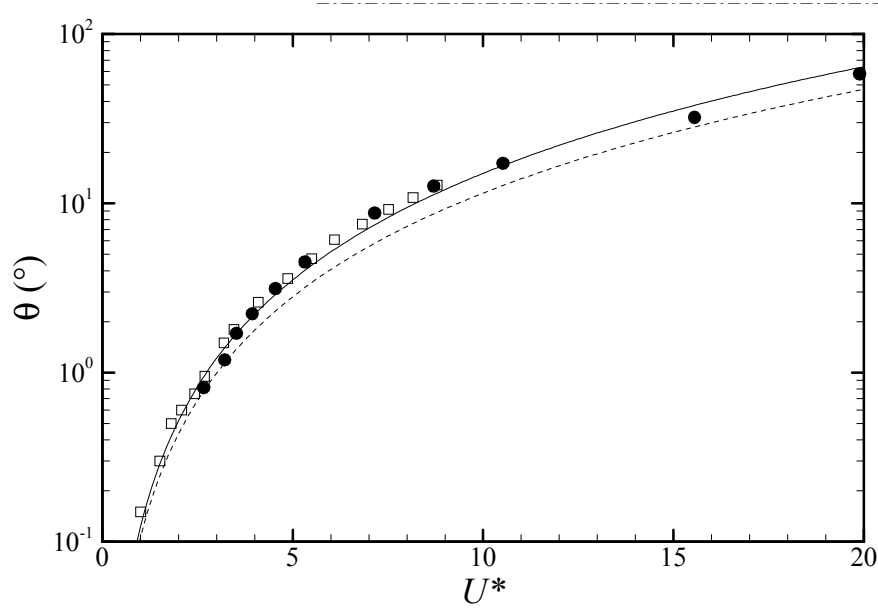


Figure 5.3.1. Mean layover angle for $M^* = 0.082$, $L^* = 9.3$: present results, \bullet ; Williamson & Govardhan (1997) results, \square . The solid line denotes a best fit through the numerical data points, whereas the dashed line is the estimate using Equation (5.3.1).

An analytical estimate of θ may be made by examining Figure 2.1.1. A simple force balance on the tethered sphere shows that the mean layover angle may be calculated from the relation

$$\tan \theta = \frac{C_d}{(1 - M^*)\alpha}. \quad (5.3.1)$$

In Figure 5.3.1, the estimates given by Equation (5.3.1) are plotted as a dashed line. Here, we have used the time-averaged drag coefficient data for a stationary sphere at a Reynolds number of $Re = 500$ which, from Chapter 3, is equivalent to $C_d \approx 0.537$. The first two numerical data points, corresponding to reduced velocities of approximately $U^* = 2.7$ and $U^* = 3.2$ respectively, lie on the line obtained using Equation (5.3.1) for a stationary sphere. It appears then, that the drag coefficient for the tethered sphere at these low reduced velocities is similar to that of a stationary sphere, since the mass ratio and α are equivalent. Furthermore, for $U^* > 3.2$, the mean layover angle obtained numerically is greater than that predicted using Equation (5.3.1), which is equivalent to the drag coefficient being greater than that for a stationary sphere. On the related study of the vortex-induced vibrations of a tethered cylinder, the two-dimensional numerical simulations of Pregalato *et al.* (2002b) found that similar behaviour occurs, although at higher reduced velocities. This departure of the drag coefficient will be explored in more detail in §5.3.3.

Note that the scale used on the dependent axis in Figure 5.3.1 is logarithmic. As a result, the differences in θ between the numerical, experimental and analytical results for $U^* < 3$ may look

quite large, but are less than 0.1° at any given reduced velocity within this range, which may certainly be within experimental errors. However, for much higher reduced velocities of $U^* = 20$, the difference in θ between the numerical and analytical results is approximately 30° . This is similar to the observations of Williamson & Govardhan (1997) who found that the sphere oscillations caused an increase in θ (and hence C_d) of up to 100% over that obtained using stationary sphere drag data. For example, at $U^* = 9$, the experimental observations show an increase in C_d of approximately 54%, whereas the numerical results show an increase in C_d of roughly 52%.

5.3.2 Oscillation amplitudes

Because the existence of the tether couples the three-dimensional motion of the sphere, oscillations are observed in all three directions. For the case of $M^* = 0.082$ and $L^* = 9.3$, the amplitudes of oscillation are shown in Figure 5.3.2. To enable comparisons with the work of Williamson & Govardhan (1997), the amplitude of oscillation is defined as $A^* = A/D$.

Figure 5.3.2 (a) depicts the normalized amplitudes of oscillation in the x (streamwise) and y (lateral) directions. For reduced velocities of $U^* \leq 3.2$, it is evident that the sphere is not oscillating much at all. At these reduced velocities, as mentioned in the previous section, the mean layover angle is less than 2° , so that the sphere is almost vertical in the framework of Figure 2.1.1, which is a result of the high buoyancy at these conditions. As U^* increases, significant oscillations are observed, especially in the streamwise direction. This is because the mean layover angle is less than 45° , and hence the sphere is more prone to vibrate in the streamwise direction. As U^* increases to $U^* = 11$, the streamwise oscillation amplitudes decrease to approximately $A^* = 0.05$, whereas the lateral oscillation amplitudes are slowly growing in magnitude. However, as θ approaches 45° , both the amplitudes of the streamwise and the lateral oscillations have the same magnitude, as one would expect, similar to the observations of a tethered cylinder (Pregalato *et al.* (2002a)). Linear interpolation reveals that the layover angle becomes 45° when the reduced velocity reaches $U^* = 17.68$, which is close to the intersection of the predicted curves in Figure 5.3.2 (a). Beyond $U^* = 11$, the amplitude of the lateral oscillations increases substantially, and at a reduced velocity of $U^* = 19.9$ it is roughly 1.7 times the amplitude of the streamwise oscillations. The maximum streamwise oscillation amplitude observed is $A^* = 0.194$; the experiments of Williamson & Govardhan (1997) found a value of $A^* = 0.16$. In either case, the maximum amplitudes were observed at the higher reduced velocities investigated.

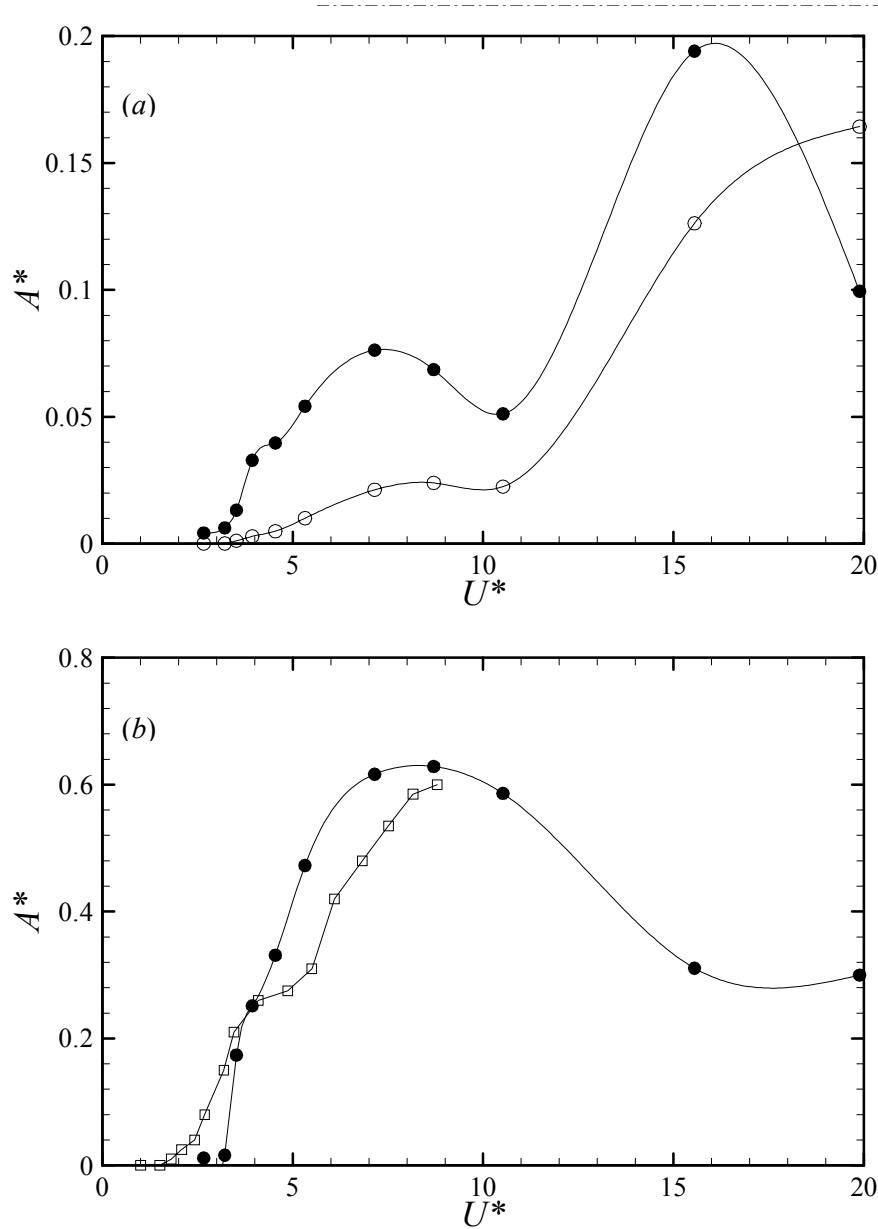


Figure 5.3.2. Normalized oscillation amplitudes A^* for $M^* = 0.082$, $L^* = 9.3$: (a) x -oscillations, \bullet ; y -oscillations, \circ ; (b) z -oscillations, \bullet ; Williamson & Govardhan (1997) results, \square .

Figure 5.3.2 (b) shows the normalized amplitudes of oscillation in the z (transverse) direction. Also illustrated are the results of Williamson & Govardhan (1997). The first feature one notices is the large vibrational response that is observed, both numerically and experimentally. For a stationary sphere at these Reynolds numbers, the magnitudes of the lateral and side (transverse) forces are similar, and typically an order of magnitude smaller than the drag force. However, for the tethered sphere, the lateral force (which is dominated by the buoyancy B) is relatively constant and typically 10 – 1000 times larger than the transverse force F_z . Because of this high buoyancy, the sphere is

more susceptible to the (fluctuating) transverse force, and hence large-amplitude vibrations are observed in the transverse direction.

Returning to Figure 5.3.2 (b), it is evident that the behaviour observed numerically and experimentally have similarities and differences. However, this is to be expected given that the simulations were performed when the flow is laminar, whereas the experiments were performed when the flow is turbulent, and hence the details of the wakes will be different. Nevertheless, similar characteristics may be noted. For example, there is a sharp increase in oscillation amplitude when a reduced velocity of approximately $U^* = 3$ is reached numerically. Experimentally, a more gradual increase in oscillation amplitude is observed when $U^* = 2.5$. Furthermore, the computational oscillation amplitude saturates at a value of roughly $A^* = 0.3$ numerically, after peaking at a value of about $A^* = 0.63$, whereas the experimental results would appear to show an asymptotic amplitude of $A^* = 0.6$ if a larger range of reduced velocity was obtainable. The major difference between the numerical and experimental responses is the observed decrease in amplitude after a reduced velocity of $U^* = 10$ is reached, a phenomenon that is not expected to occur experimentally at this low mass ratio, as is the case with the high mass ratio results to be presented shortly. In addition, another major difference between the two sets of results is the appearance, at $U^* = 5$, of a local inflection in the transverse experimental response amplitude that is not observed numerically. This “Mode I” response, as discussed by Williamson & Govardhan (1997), corresponds roughly to the natural frequency being approximately equal to the vortex formation frequency, which yields a resonance in the classical studies of vortex-induced vibrations (see, for example, Blevins (1994) and Naudascher & Rockwell (1994)). For the present numerical results, one would expect a Mode I response at a reduced velocity of $U^* = 6$, which corresponds to a natural frequency of $S_n = 0.16$, since for a stationary sphere the vortex shedding frequency at this Reynolds number of $Re = 500$ is $St = 0.16$. In addition, the larger-amplitude oscillations at intermediate reduced velocities appear to indicate the existence of another mode of vibration, the “Mode II” response. Moreover, the decrease in amplitude in the computational results indicates the existence of a Mode III response, which will be discussed shortly. From the results of Jauvtis *et al.* (2001), the Mode I response appears to become less significant at lower mass ratios ($M^* \ll 1$) and at higher mass ratios ($M^* \gg 1$). For $M^* \approx 1$, the Mode I response is clearly evident, as shown by Govardhan & Williamson (1997) for their mass ratio of $M^* = 0.76$ and Jauvtis *et al.* (2001) for their mass ratio of $M^* = 0.8$. It is somewhat surprising that the numerical simulations appear to capture what seem like Mode II and III responses but not a Mode I response.

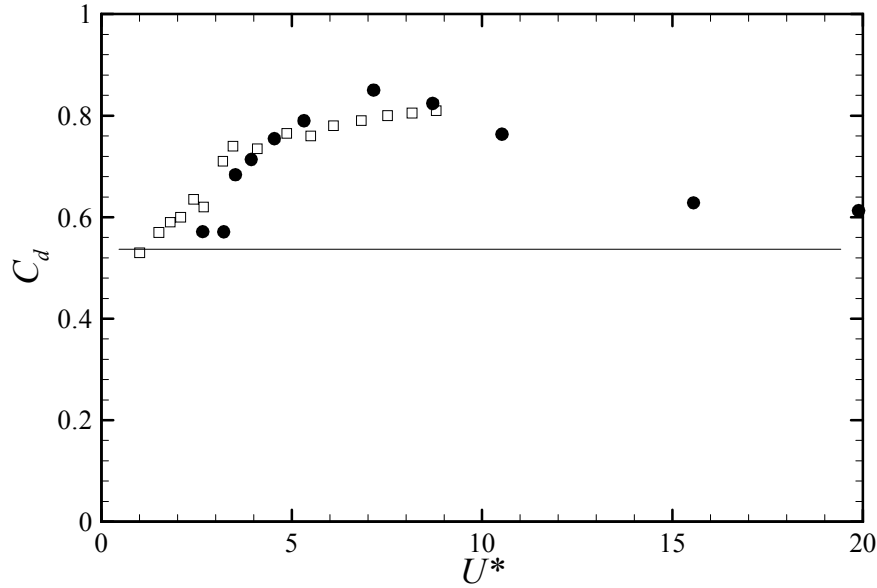


Figure 5.3.3. Change in the drag coefficient due to the tethered sphere oscillations for $M^* = 0.082$, $L^* = 9.3$. The solid line depicts C_d for a stationary sphere. Symbols as in Figure 5.3.1.

5.3.3 Force coefficient behaviour

The time-averaged drag coefficient is shown as a function of reduced velocity in Figure 5.3.3. Once again, the experimental results of Williamson & Govardhan (1997) are added for comparison, as well as the time-averaged drag coefficient for a stationary sphere at a Reynolds number of $Re = 500$ depicted by the solid line, which has a value of $C_d \approx 0.537$ (see Chapter 3). As mentioned in §5.2.1, the drag coefficient for the first two numerical data points at low reduced velocity is similar to that of a stationary sphere, which is to be expected since the motion of the tethered sphere at these low layover angles is very small. However, an increase in U^* causes the drag coefficient to gradually increase to a value of approximately $C_d = 0.85$ at $U^* = 7.15$. The experimental results also show this gradual rise in C_d . For higher U^* , the numerical results depict a monotonic decrease in C_d that appears to bottom out to a value of $C_d = 0.62$, which asymptotes as the time-averaged layover angle passes 45° . The larger-amplitude Mode II response seems to be responsible for the gradual rise in the drag, as observed in the experimental measurements of Williamson & Govardhan (1997) in Figure 5.3.3. The Mode III response observed at the highest Reynolds numbers does not seem to alter the drag a great deal. In addition, it is evident that the amplification in the drag coefficient due to the sphere oscillations is up to 58% greater than that of a stationary sphere at the same Reynolds number of $Re = 500$. For the same mass ratio (but at much higher Reynolds numbers), Williamson & Govardhan (1997) found an increase of up to 100% over the values measured by Wiselsberger (1922).

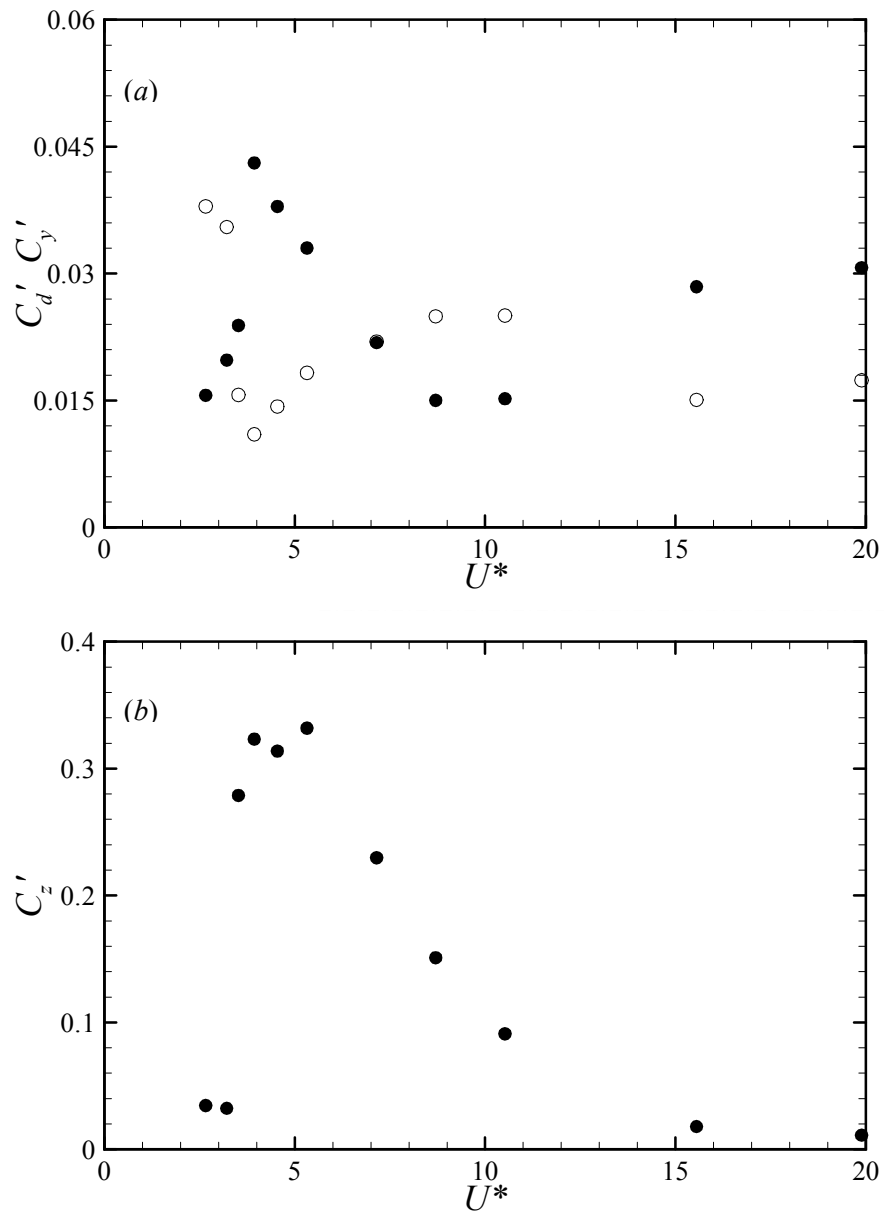


Figure 5.3.4. Amplitudes of the fluctuating force coefficients for $M^* = 0.082$, $L^* = 9.3$: (a) drag coefficient, \bullet ; lateral coefficient, \circ ; (b) transverse (z) coefficient.

More information concerning the forcing of the sphere is available in Figure 5.3.4, which shows the amplitudes of the fluctuating fluid forces in the x , y and z directions. Figure 5.3.4 (a) depicts the amplitudes corresponding to the fluctuating drag and lateral force coefficients. The amplitude of C_d' does not really follow the trend of the time-averaged drag coefficient shown in Figure 5.3.3, except at the two highest reduced velocities where the amplitudes are larger than those observed at the peak of the Mode II regime. On the other hand, the lateral (y) coefficient starts off small at the onset of the oscillations and then gradually increases to a value of approximately 0.025 at the end of the Mode II regime. As the highest reduced velocities investigated, the amplitude of C_y' remains relatively

unchanged at a value of 0.016. Overall, the magnitudes of the amplitudes for both the drag and lateral coefficients are relatively small, especially at the lower reduced velocities. In contrast, the magnitudes of the amplitudes for the transverse (z) coefficients may be 30 times as large, as shown in Figure 5.3.4 (b). A large jump in the amplitude of the transverse forcing is observed after a reduced velocity of $U^* = 3.2$ is reached. The amplitude of this transverse force coefficient peaks at about 0.4 times the mean drag coefficient, and is responsible for the large increase in the transverse oscillation amplitude observed in Figure 5.3.2 (b). However, although the oscillation amplitude in the Mode II regime stays at roughly the same value and is essentially independent of the reduced velocity as U^* is increased, the amplitude of the transverse forcing decreases almost exponentially and appears to approach zero at the highest reduced velocities investigated. This raises the question: what sustains these transverse oscillations if the transverse forcing is small? The answer to this question will be dealt with shortly.

5.3.4 Frequency response

We turn our attention now to the frequency of oscillation of the tethered sphere. The frequencies of oscillation in the x , y and z directions were computed using spectral analysis of the oscillation time traces and are shown in Figure 5.3.5. The dashed line represents the vortex shedding frequency (f_{vo}) of a stationary sphere at a Reynolds number of $Re = 500$, whereas the dashed-dotted line signifies the natural frequency of vibration of the system. In both the x and y directions, it is evident that the sphere, over the entire range of reduced velocities investigated, oscillates at neither the natural frequency of vibration nor the vortex shedding frequency. From results concerning the vortex-induced vibrations of a circular cylinder (Brika & Laneville (1993)), one would expect the oscillation frequency to be at the natural frequency, especially for high mass ratios. However, the present results for a low mass ratio tethered sphere show a similar deviation from f_n as do the low mass ratio results for a cylinder from Khalak & Williamson (1997).

For $U^* < 11$, the normalized frequency of oscillation in both the streamwise and lateral directions is much higher than both the natural frequency and the vortex shedding frequency, shown by the “upper” branch in Figure 5.3.5. However, for higher reduced velocities, the oscillation frequency switches to much lower values, as highlighted by the data points at the end of the reduced velocity extent. At the lowest reduced velocities, the frequencies of oscillation in the streamwise and lateral directions are dissimilar and do not appear to follow any trend.

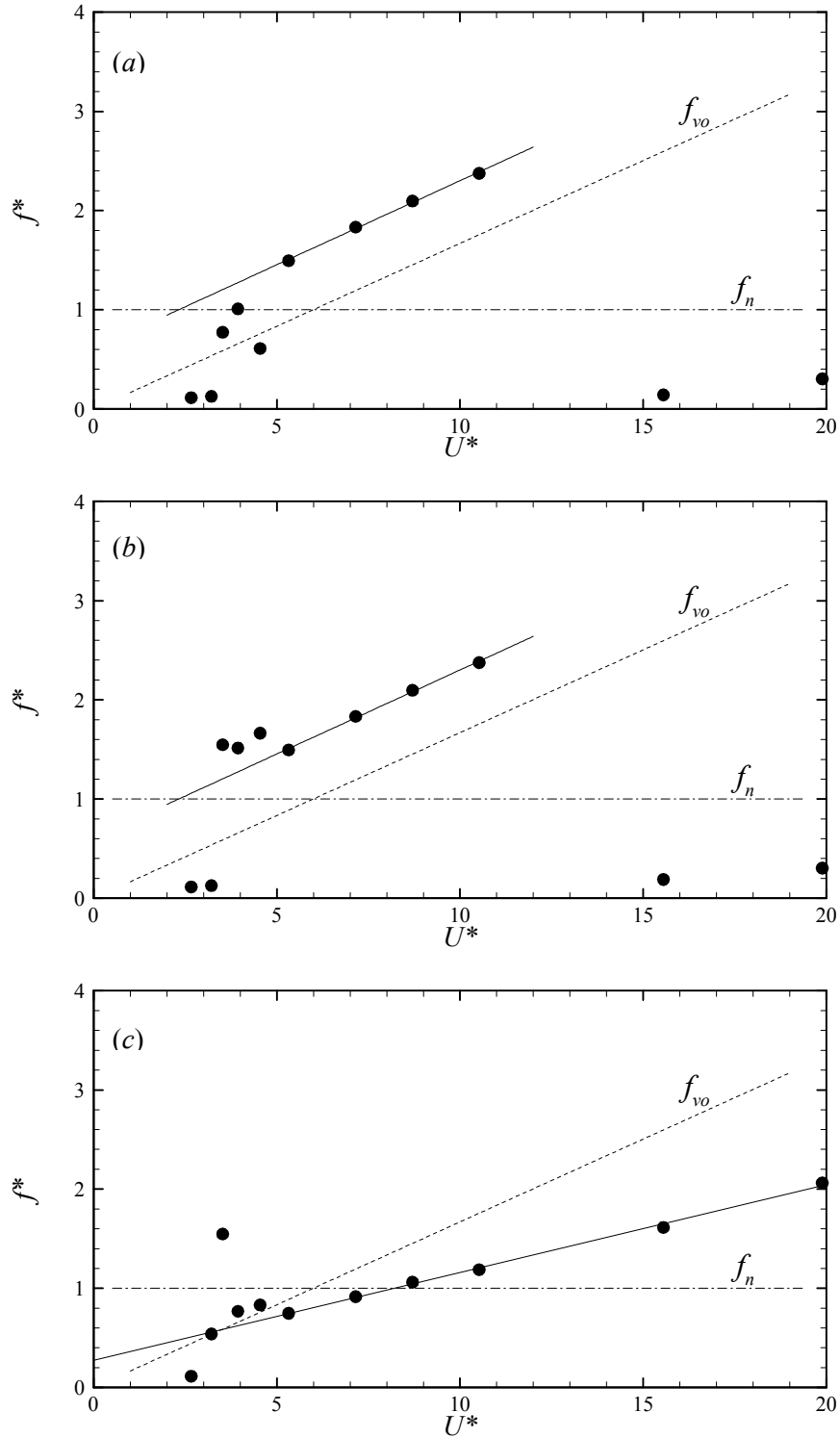


Figure 5.3.5. Normalized frequencies of oscillation for $M^* = 0.082$, $L^* = 9.3$: (a) streamwise (x) frequencies; (b) lateral (y) frequencies; (c) transverse (z) frequencies.

The normalized frequencies of oscillation in the z direction are portrayed in Figure 5.3.5 (c). It is immediately apparent that the frequencies of oscillation in the transverse direction within the Mode II regime are half the corresponding frequencies in both the streamwise and lateral directions. The

exception occurs at higher reduced velocities, at which the frequencies of oscillation are extremely small in the streamwise and lateral directions but relatively large in the transverse direction. Note that at these higher reduced velocities, the layover angle of the sphere is greater than 45° , at which a noticeable change in the sphere response is observed, for example, in the oscillation amplitude response (Figure 5.3.2). Note that in the time traces of displacement used to calculate the oscillation frequencies, there was a second, less dominant frequency in the time traces of the streamwise and lateral oscillations that was half the frequency of the more dominant oscillations. This corresponds to the frequencies observed in the transverse oscillations, since the motion in all three directions is coupled. As U^* was increased from the start of the upper branch in Figures 5.3.5 (a, b) to the end of the upper branch, this second frequency became more pronounced and appears to have dominated the vibrational response for higher reduced velocities as the frequencies switch from the upper branch to the lower values depicted in Figures 5.3.5 (a, b).

5.3.5 Oscillation time traces

Figure 5.3.6 shows sample time histories of the streamwise and transverse oscillations for a reduced velocity of $U^* = 5.32$ as well as the x - z phase plots from experiments. This reduced velocity was chosen to closely match the case studied by Williamson & Govardhan (1997), who present the oscillation time traces as a function of Reynolds number as opposed to reduced velocity. In Figure 4 of their paper, the Reynolds number was 9176, which corresponded to a reduced velocity of approximately $U^* = 6.17$. In Figure 5.3.6 (a), we plot the same streamwise and transverse oscillations, and we see that the response is very similar, although the simulations were run at a Reynolds number of $Re = 500$. In the numerical results, the amplitudes of the transverse oscillations are almost nine times that of the streamwise oscillations, and are approximately $0.5D$ in magnitude. Experimentally, Figure 4 of Williamson & Govardhan (1997) show that these transverse oscillations have a magnitude of roughly $0.4D$ at a slightly higher reduced velocity. However, at this low reduced velocity, the tethered sphere for these experiments oscillates within the Mode I regime, whereas it appears to oscillate within the Mode II regime for the numerical simulations. Furthermore, it is evident that the frequency of the in-line vibrations is at twice the frequency of the transverse vibrations, as depicted in Figure 5.3.5, despite the fact that the natural frequency of vibration is the same in all directions.

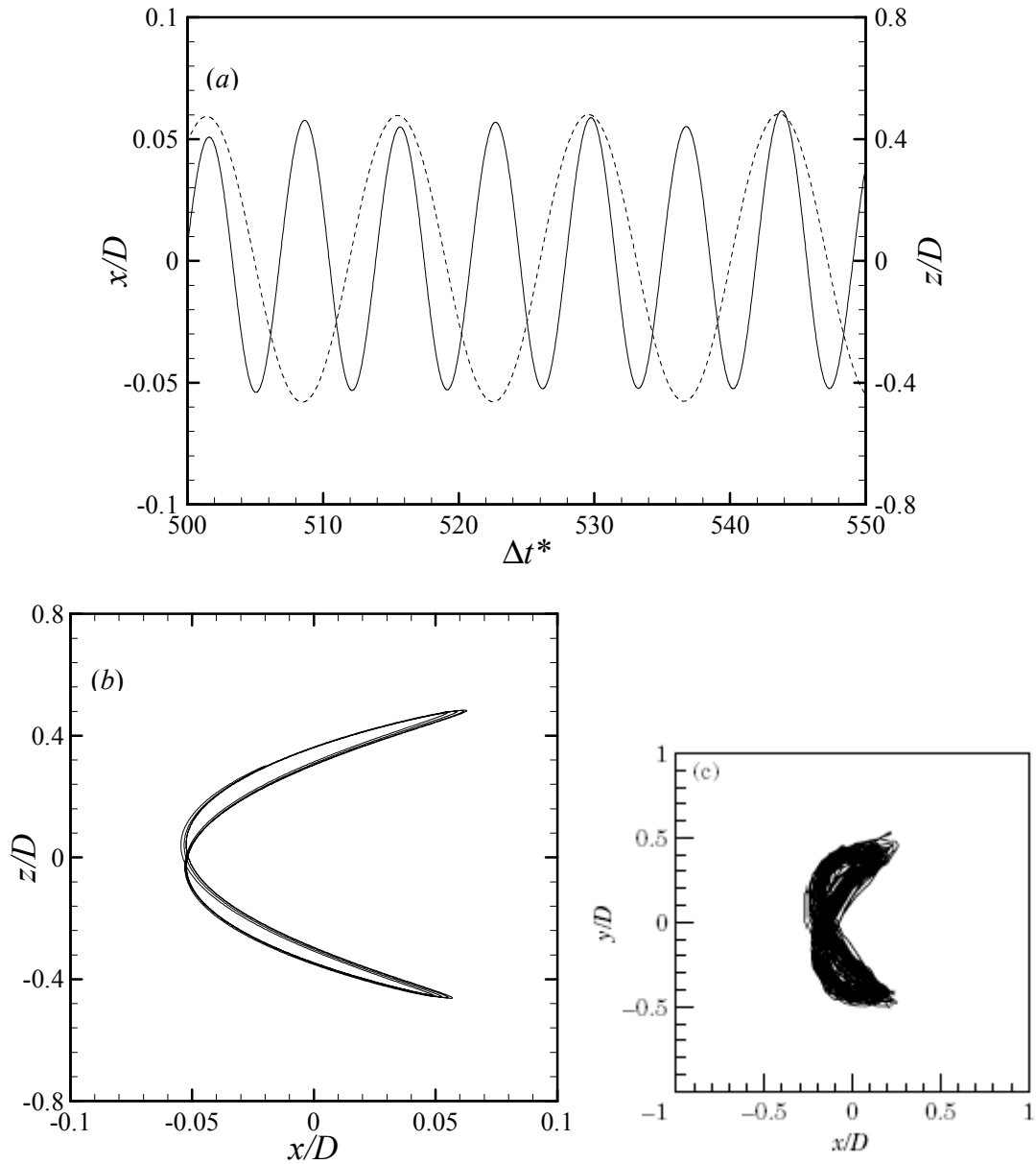


Figure 5.3.6. Time traces of sphere oscillations for $U^* = 5.32$: (a) solid line – streamwise oscillations, dashed line – transverse oscillations; (b) x - z phase plot of the oscillations; (c) Williamson & Govardhan (1997) results for $Re = 9176$, $U^* = 6.17$.

The x - z phase plot for this low reduced velocity is shown in Figure 5.3.6 (b), which demonstrates that a cycle of oscillation maps out a skewed figure-of-eight displacement pattern. This is in accordance with the experimental results of Williamson & Govardhan (1997) (see Figure 5.3.6 (c)), which shows a similar displacement pattern although with much larger streamwise vibrations. These large streamwise vibrations are probably related to the more complex wake at the large Reynolds numbers investigated. Correspondingly, the clarity of the displacement pattern is much greater in the numerical simulations than in the experiments, due to the fact that the numerical simulations were

performed in the laminar flow regime whereas the experiments were performed under turbulent flow conditions.

Figure 5.3.7 (a) shows similar time traces of the streamwise and transverse oscillations, although at a higher reduced velocity of $U^* = 7.19$. Figure 5 of Williamson & Govardhan (1997) agrees qualitatively very well with Figure 5.3.7 (a), although the Reynolds number associated with the experiments was $Re = 11310$, corresponding to a reduced velocity of approximately $U^* = 7.6$. Numerically, the transverse oscillation amplitude has grown to $0.64D$, whereas the experimental results depict an amplitude of $0.6D$. In both cases, the sphere oscillates within the Mode II response envelope, and the frequency of oscillation in the streamwise direction is still twice that of the transverse direction. The time trace of the streamwise oscillations in Figure 5.3.7 (a) clearly shows a second frequency that corresponds to the frequency of the transverse oscillations, and hence is associated with the transverse oscillations since the motion is coupled as discussed in the previous section. Furthermore, the amplitude of the transverse oscillations remains at roughly nine times the magnitude of the streamwise oscillations.

The x - z phase plot at this slightly higher reduced velocity again shows similar behaviour between the numerical and experimental results. Numerically, as before, a cycle of oscillation maps out a figure-of-eight displacement pattern, although the phase plot in this instance is not nearly as skewed as at the previous reduced velocity investigated. Once more, the phase plot in Figure 5 of Williamson & Govardhan (1997) in Figure 5.3.7 (c) shows comparable behaviour although, as stated before, the turbulence of the flow has demarcated the limit cycle response that is clearly observed numerically. Indeed, one would imagine that time-averaging of the experimental displacement patterns would result in the removal of the unwanted small-scale motions associated with the turbulence and give rise to the displacement patterns analogous to those in Figures 5.3.6 (b) and 5.3.7 (b).

5.4 High mass ratios

The high mass ratio sphere considered in this study corresponds to $M^* = 0.8$. As before, we consider a tether length of $L^* = 10$, and we investigate the effect of changing the tether length at the end of this section. This particular mass ratio was chosen to enable comparisons to be made with the work of Govardhan & Williamson (1997) and Jauvtis *et al.* (2001), who investigated mass ratios of $M^* = 0.76$ and $M^* = 0.8$ respectively. However, the tethered sphere study by Jauvtis *et al.* (2001) did not mention the tether lengths investigated. In particular, the results of Govardhan & Williamson (1997) include, among other things, the frequency response that is observed over a large range of reduced velocity, which was not obtained for the very low mass ratio tethered sphere discussed in §5.2.2. Also, the reduced velocity range they investigated varied from $U^* = 3$ to approximately $U^* = 20$.

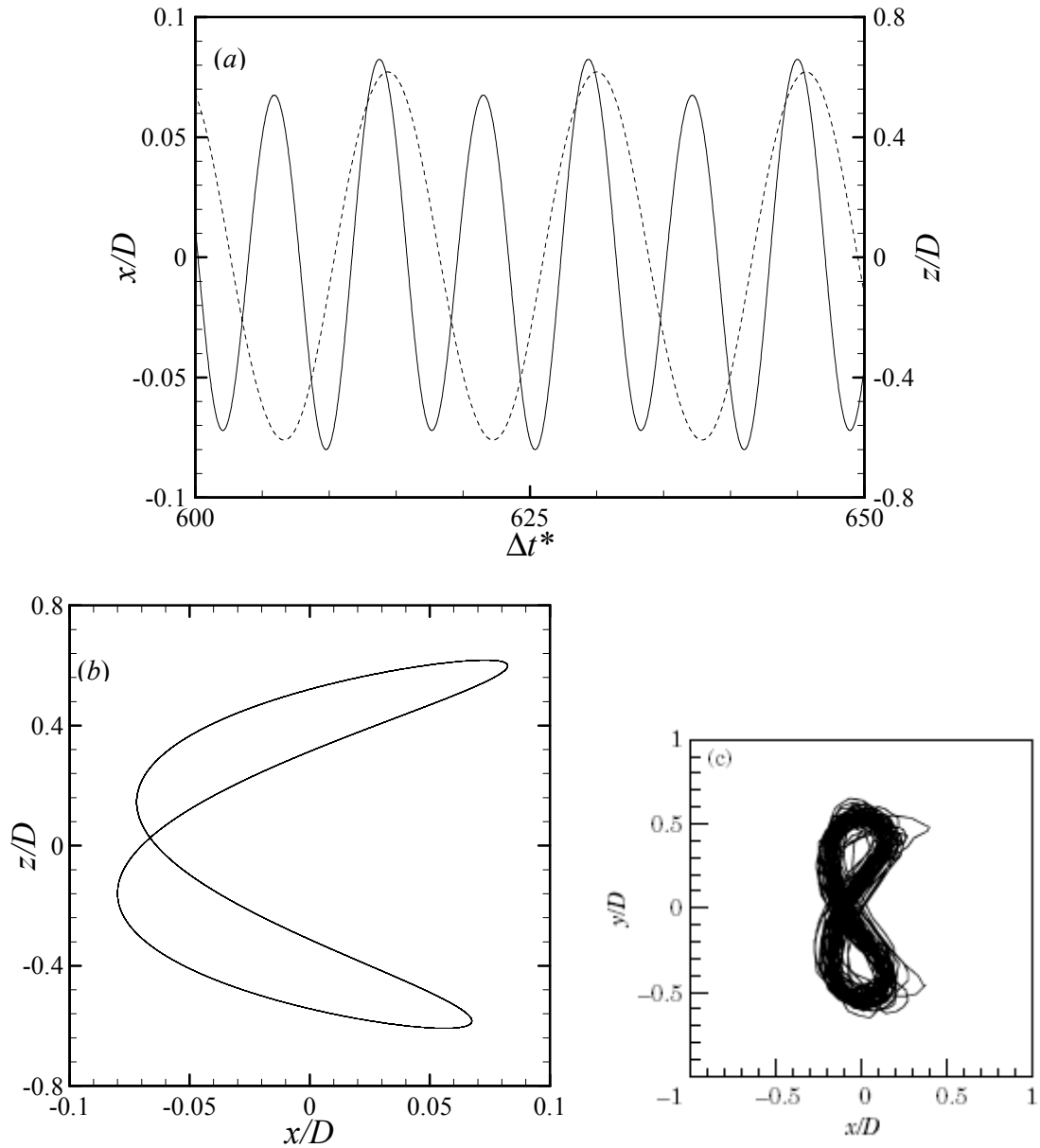


Figure 5.3.7. Time traces of sphere oscillations for $U^* = 7.19$: (a) solid line – streamwise oscillations, dashed line – transverse oscillations; (b) x - z phase plot of the oscillations; (c) Williamson & Govardhan (1997) results for $Re = 11310$, $U^* = 7.6$.

However, the slightly higher mass ratio results of Jauvtis *et al.* (2001) represented a reduced velocity range of roughly $3 < U^* < 14$. For both of these studies, the limits of the flow speeds attainable in the water channel controlled the range of reduced velocities investigated and, as a result, only the Mode I and II responses were observed. Furthermore, Govardhan & Williamson (2002b) report the existence of a critical mass for the tethered sphere having a value of $M^* = 0.30$. For a freely oscillating cylinder, the critical mass is $M^* = 0.54$ (Govardhan & Williamson (2002a)). In other words, for mass ratios less than $M^* = 0.30$, the tethered sphere will oscillate indefinitely in the Mode

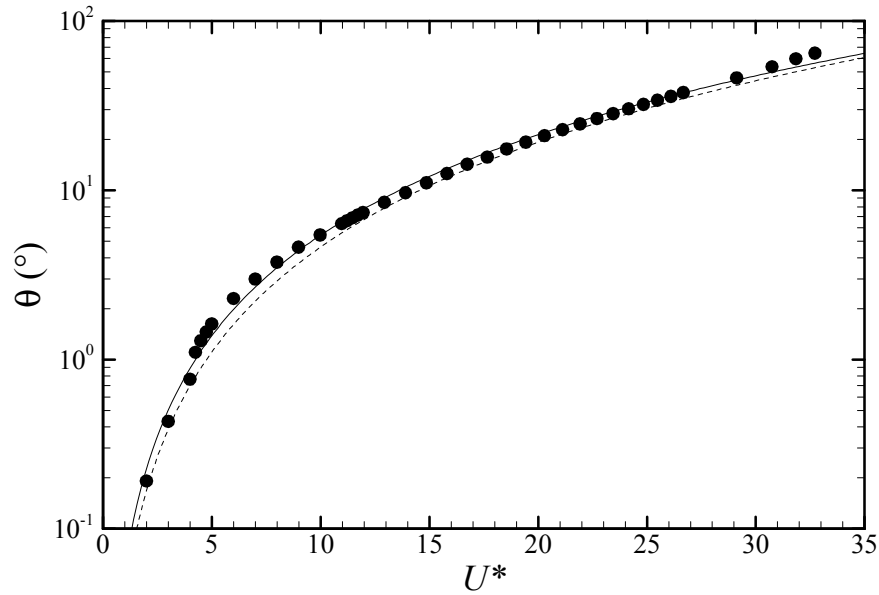


Figure 5.4.1. Mean layover angle for $M^* = 0.8$, $L^* = 10$.

II regime, regardless of how large the reduced velocity is. This appears to be the case both numerically and experimentally for the low mass ratio results presented in §5.2.2.

5.4.1 Mean layover angles

The mean layover angle θ for this high mass ratio case is depicted in Figure 5.4.1. As with the low mass ratio case investigated, the analytical estimate using Equation (5.3.1) with the drag for a stationary sphere at a Reynolds number of $Re = 500$ is also shown. Although Jauvtis *et al.* (2001) investigated a tethered sphere with an identical mass ratio, they do not present any mean layover angles and the corresponding drag coefficients. However, from Figure 5.4.1, it is evident that for reduced velocities less than or equal to 4, the mean layover angle lies on the predicted line using the analytical estimate, which is equivalent to the tethered sphere having a drag coefficient comparable to that of a stationary sphere. When the reduced velocity is slightly increased, from $U^* = 4$ to $U^* = 4.25$, the calculated mean layover angle departs significantly from that using Equation (5.3.1). As with the low mass ratio, this indicates a considerable increase in the drag coefficient to values much larger than that observed for a stationary sphere, as we shall see in §5.3.3. This trend continues until a reduced velocity of approximately $U^* = 11.2$ is reached, after which the layover angle switches back to that predicted using the analytical estimate. Any further increases in U^* have little effect on the calculated mean layover angle. These developments are similar to the response of the tethered sphere at low mass ratios which, as explained in §5.3.1, exhibits a mean layover angle that is much higher than that predicted using Equation (5.3.1) over the entire range of reduced velocity

investigated except, of course, at extremely low reduced velocities where negligible oscillations are observed and at the highest reduced velocities investigated. It appears then that there are two distinct modes of oscillation for these low Reynolds number cases, namely Mode II and Mode III responses. However, what is not clear from Figure 5.4.1 is whether a Mode I response is observed, which is considered in the next section.

5.4.2 Oscillation amplitudes

The normalized streamwise and lateral oscillation amplitudes are shown in Figure 5.4.2 (a) as a function of reduced velocity. Note that comparisons with experiments are difficult to make due to the lack of non-transverse oscillation data in the studies of Govardhan & Williamson (1997) and Jauvtis *et al.* (2001). Here, we define the amplitude of oscillation as $A_x^* = \sqrt{2}x_{rms} / D$, where x_{rms} is the root-mean-square response of the sphere in either the x , y or z directions. For purely sinusoidal oscillations, this is equivalent to $A^* = A/D$, as defined in the nomenclature. In accordance with the mean layover angle results presented in the previous section, at low reduced velocities of $U^* \leq 4$, the sphere displays minute oscillations in both the streamwise (x) and lateral (y) directions. For reduced velocities greater than $U^* = 4$, the oscillations in the streamwise direction jump up to a magnitude of approximately 0.04, whereas the lateral oscillations exhibit a magnitude of roughly 0.005. The streamwise oscillations are around 8 times the lateral oscillations, which is a consequence of the high net buoyancy (which depends on the Froude number) of the sphere at these small layover angles that resists motion in the lateral direction. The sphere continues to oscillate at more or less the same amplitude until $U^* = 11$ is reached, after which both the streamwise and lateral oscillations decrease slightly before increasing dramatically in magnitude. This is in contrast to the behaviour observed for a very low mass ratio sphere (see §5.2.2), which does not exhibit a decrease in either the streamwise or lateral oscillation amplitudes as the reduced velocity is increased. For the present high mass ratio case, further increases in reduced velocity result in a steady increase in the oscillation amplitude, which peaks at $U^* = 14$. Desynchronization appears to occur at reduced velocities in the range $22 < U^* < 24.5$, during which the sphere oscillations in both the streamwise and lateral directions are very small. Beyond these reduced velocities, the oscillations build up to values that are higher than those previously observed, especially in the lateral direction. Because of the low frequency of oscillations in this regime, as will be illustrated shortly, as well as the non-sinusoidal nature of the oscillations, much longer time traces are needed to accurately compute the observed normalized root-mean-square vibrational amplitudes of motion. However, note that for $U^* > 30$, the normalized amplitude is calculated using the *maximum* amplitude as opposed to the RMS amplitude (cf. Jauvtis *et al.* (2001)), because of the non-harmonic nature of the oscillations at these

high velocities, as will be shown shortly. For all of the data points displayed in Figure 5.4.2, time histories of at least $\Delta t^* = 1000$ units were used to calculate the RMS responses.

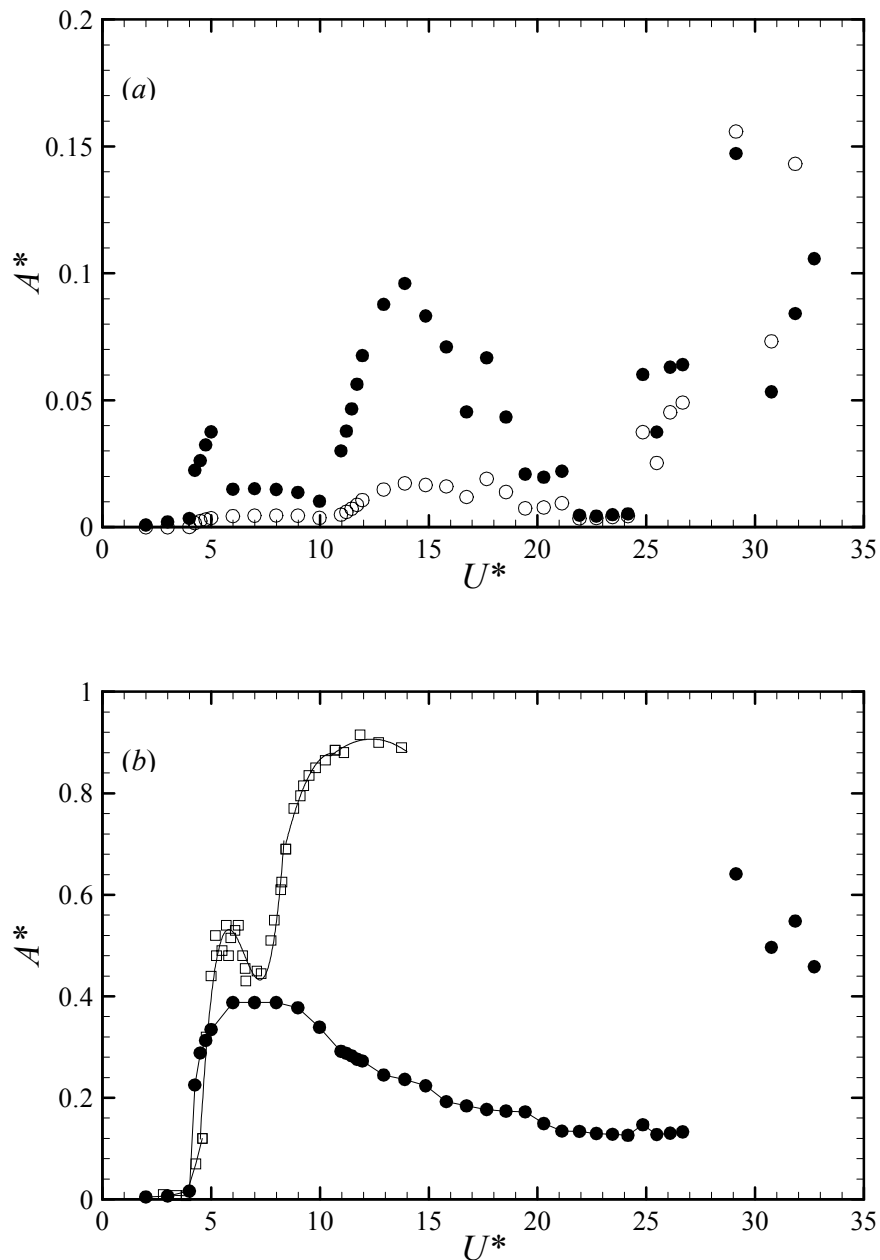


Figure 5.4.2. Normalized oscillation amplitudes A^* for $M^* = 0.8$, $L^* = 10$: (a) x-oscillations, \bullet ; y-oscillations, \circ ; (b) z-oscillations, \bullet ; Jauvtis *et al.* (2001) results for $M^* = 0.8$, $L^* = \text{unknown}$, \square .

Figure 5.4.2 (b) shows the normalized amplitude of response in the transverse (z) direction. Also illustrated for comparison are the results of Jauvtis *et al.* (2001), for the same mass ratio. It is evident that the experimental results at higher Reynolds numbers capture both the Mode I and Mode II responses. The Mode I response is depicted by the local maximum in oscillation amplitude that occurs at a reduced velocity of approximately $U^* = 5.6$, corresponding to a natural frequency of roughly $S_n = 0.18$. For these experiments, the Reynolds number was typically of the order of $Re = 10000$. For a stationary sphere, the vortex shedding frequency for Reynolds numbers in the range $5000 < Re < 14000$ (which correspond to the Reynolds numbers obtained in the experimental results of Jauvtis *et al.* (2001)) is approximately $St = 0.18$ (see Sakamoto & Haniu (1990)). It appears then that the Mode I response observed experimentally is due to a lock-in of the vortex shedding frequency with the natural frequency, as pointed out by Williamson & Govardhan (1997).

For higher reduced velocities of approximately $U^* = 10$ and above, the experiments of Jauvtis *et al.* (2001) depict a Mode II response with a saturation amplitude of $A^* = 0.89$. The maximum reduced velocity reached experimentally was $U^* = 13.7$ which, as with the experiments performed by Govardhan & Williamson (1997), represented the maximum flow velocity attainable in their experimental facility. The numerical results, on the other hand, once again do not capture a Mode I response, as with the previous mass ratio investigated. However, a Mode II response is found and occurs in the reduced velocity range of $4.25 < U^* < 10$. This Mode II response commences at a lower reduced velocity than that observed experimentally, although it is unfortunate that higher flow speeds were unobtainable experimentally to see if the observed Mode II response occurs at finite reduced velocities at this mass ratio. Furthermore, the amplitude of oscillation in this regime is $A^* = 0.4$, which is approximately 0.44 times that observed experimentally. It is also evident that a comparison with the very low mass ratio results in §5.3.2 shows that increasing the mass ratio results in a decrease in the synchronization regime (of the Mode II response), a result confirmed by the tethered sphere experiments of Jauvtis *et al.* (2001) and well known in the field of vortex-induced vibrations of a cylinder (see Khalak & Williamson (1999)).

As previously mentioned, the regime of synchronization ends at a reduced velocity of $U^* = 10$. Beyond this, the (transverse) oscillation amplitude decreases gradually to an amplitude of roughly $A^* = 0.12$. It is somewhat surprising that these low Reynolds number simulations do not exhibit a sudden decrease in transverse amplitude at the end of the Mode II synchronization regime. Nevertheless, the large-amplitude sinusoidal oscillations exhibited at higher reduced velocities are defined here as a Mode III response, which will be explored in more detail in §5.8. Furthermore, at the highest reduced velocities investigated (which occurs when the mean layover angle passes 45°), the very large-amplitude non-sinusoidal oscillations are defined as a Mode IV response. For this particular mass ratio of $M^* = 0.8$, a Mode III response was not observed experimentally because of the inability to reach higher reduced velocities. However, this problem was overcome by

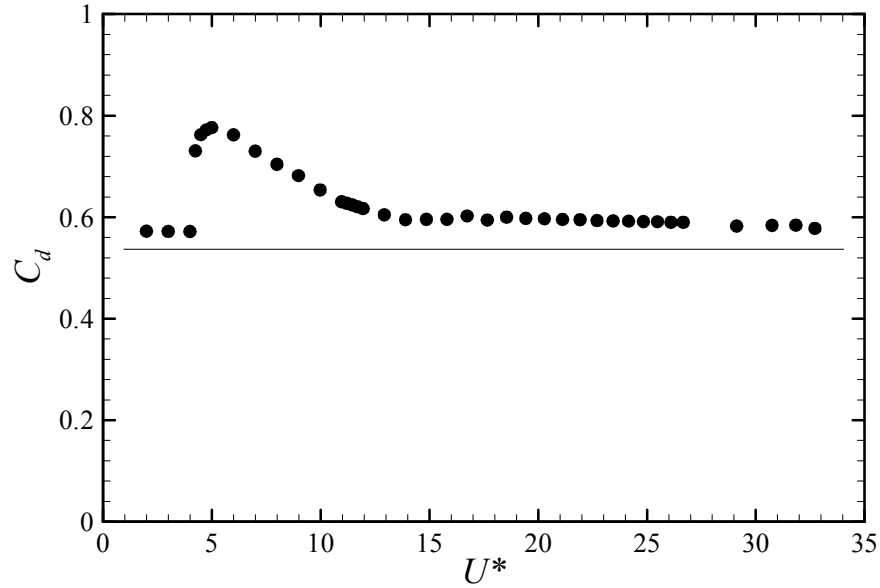


Figure 5.4.3. Change in the drag coefficient due to the tethered sphere oscillations for $M^* = 0.8$, $L^* = 10$.

investigating higher mass ratios, since the definition of reduced velocity in Equation (5.1.8) is highly dependent on M^* . Using tethered spheres of mass ratios of $O(10)$, Jauvtis *et al.* (2001) were then able to reproduce similar Mode III and IV responses as observed numerically, although with much larger amplitudes, and the transition from the desynchronization region to the Mode III regime was clearly more pronounced probably owing to the high mass ratios of the spheres in this case. However, what is significant is that the present results show that the Mode III and Mode IV regimes are real phenomena that exhibit vortex dynamics that cannot be explained, unlike the Mode I response, as a classical lock-in phenomenon that is so prevalent in vortex-induced vibration studies.

5.4.3 Force coefficient behaviour

Figure 5.4.3 shows the drag coefficient as a function of reduced velocity for this high mass ratio case. Also shown as the solid line is the drag coefficient for a stationary sphere at this Reynolds number of $Re = 500$, equal to $C_d = 0.537$. As with the results for $M^* = 0.082$, the drag coefficient at low reduced velocities is similar to that of a stationary sphere, since the vibrations of the sphere are quite modest at these small layover angles. However, as soon as the large-amplitude vibrations of the Mode II response kick in at a reduced velocity of $U^* = 4.25$, the drag coefficient responds accordingly with a large increase in C_d from 0.572 before the transition to 0.731 at the start of the Mode II synchronization regime. The maximum increase in C_d is approximately 36%; the results of Govardhan & Williamson (1997) for a mass ratio of $M^* = 0.76$ and tether length of $L^* = 8.93$

indicated an increase in C_d of roughly 79%. As the reduced velocity is increased in this Mode II regime the drag coefficient steadily decreases until the end of the synchronization region, after which it attains a relatively constant value of roughly $C_d = 0.592$. This is in contrast to the very low mass ratio results (Figure 5.3.3), which show an initial slight decrease in the drag that then appears to saturate to a constant value that is much greater than that of a stationary sphere. Because the drag for the very low mass ratio sphere never approaches that of a stationary sphere, it seems that the Mode II regime extends indefinitely for that case. However, for the present case of $M^* = 0.8$, the drag does indeed decrease back to that of a stationary sphere, signaling the end of the Mode II regime. Any further increases in U^* seem to have little effect on the drag coefficient.

The root-mean-square drag, lateral and transverse force coefficients are depicted in Figure 5.4.4. Because of the large variation in the observed forces, a logarithmic scale is used to compare the differences. At low reduced velocities ($U^* \leq 4$), the variations in the lateral and transverse force coefficients are comparable and typically twice as large as the corresponding variations in the drag coefficient. When the Mode II oscillations begin at $U^* = 4.25$, the variations in the lateral force coefficient decrease by approximately 87%, whereas those of C_z increase to a value of $C_z' = 0.34$, which represents a relative increase of almost 10 times the previous value. The same trend in the transverse force coefficient is observed for the lower mass ratio cases. It is apparent that this large transverse forcing is initially responsible for the large-amplitude vibrations observed in the transverse direction, leading to a Mode II response. However, further increases in the reduced velocity result in a reduction in C_z , until desynchronization occurs after $U^* = 10$.

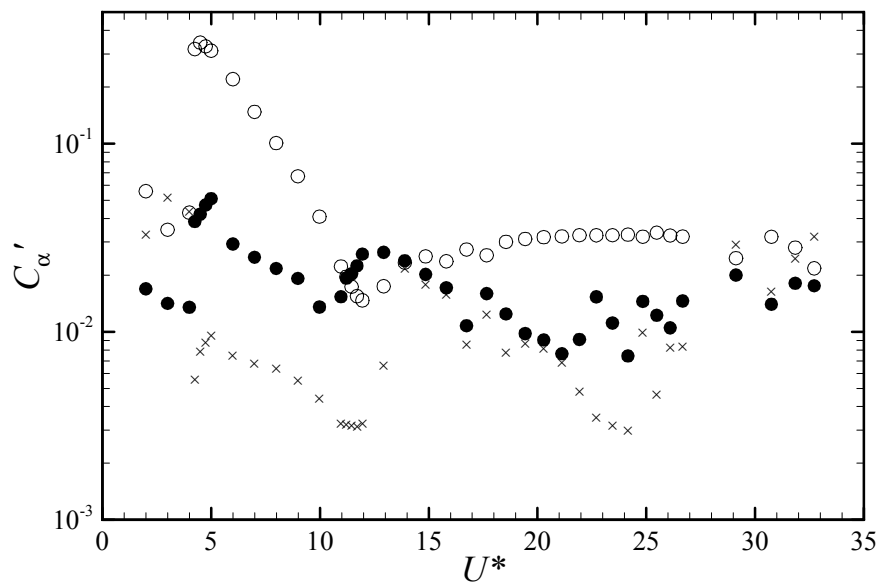


Figure 5.4.4. RMS force coefficients for $M^* = 0.8$, $L^* = 10$: drag coefficient, \bullet ; lateral (y) coefficient, \times ; transverse (z) coefficient, \circ .

It is interesting to note that towards the end of the Mode II regime, the variations in the transverse forcing that initially gave rise to the large-amplitude vibrations approach values comparable to that of the lateral forcing. In other words, although the transverse forcing changes from $C_z = 0.34$ at the start of the regime to $C_z = 0.019$ at the end of the regime (a decrease of approximately 18 times), the large-amplitude vibrations persist until the end of the synchronization regime. A better understanding of this Mode II response will be presented in §5.8.

For $U^* > 15$ and less than $U^* = 27$, the variations in the transverse force coefficient are relatively constant, although the variations in the drag and lateral force coefficients are not uniform and relatively small. However, within this range of reduced velocity, the tethered sphere experiences further oscillations in the transverse direction, as shown in Figure 5.4.2 (b). The fact that significant vibrations are observed although the forcing is quite small (together with the observation that the forcing is at a much higher frequency) makes this region quite unlike that of the Mode II regime. Jauvtis *et al.* (2001) were the first to discover this Mode III vibrational response, albeit by investigating higher mass ratios ($M^* > 1$). That the present numerical results show that this mode is observed at much lower mass ratios and amplitudes is a significant finding in itself, and is evidence that at least one of the higher modes of vibration of a tethered sphere is not due to the high mass ratios that are typically used experimentally. In addition, for $U^* > 30$, the variations in all three of the force coefficients are relatively the same, although very large-amplitude non-harmonic oscillations are observed which, as mentioned before, are indicative of a Mode IV response. The dynamics of both of these responses will be explored in detail in §§5.9 and 5.10.

5.4.4 Frequency response

From the previous results concerning the low mass ratios, we know that the frequency of oscillation in both the streamwise and transverse directions are the same, but not necessarily the same as that in the transverse direction. Figure 5.4.5 (a) shows these frequencies in the x (or y) direction. It is evident that throughout the range of reduced velocities investigated, the sphere does not oscillate at either the vortex shedding frequency or the natural frequency. Furthermore, the frequency of oscillation in the lateral direction is the same as that in the streamwise direction for all reduced velocities investigated, except for $U^* \leq 5$. The normalized frequency of oscillation for reduced velocities in the range $6 < U^* < 12$ is much higher than the natural frequency and vortex shedding frequency, which is in agreement with the Mode II response that was observed for the lower mass ratios and the corresponding observed frequencies. At the end of the Mode II regime, the oscillation frequencies in both the x and y directions drop to much lower values, typically lower than the natural frequency, during which the sphere displays very slow oscillations in the x and y directions.

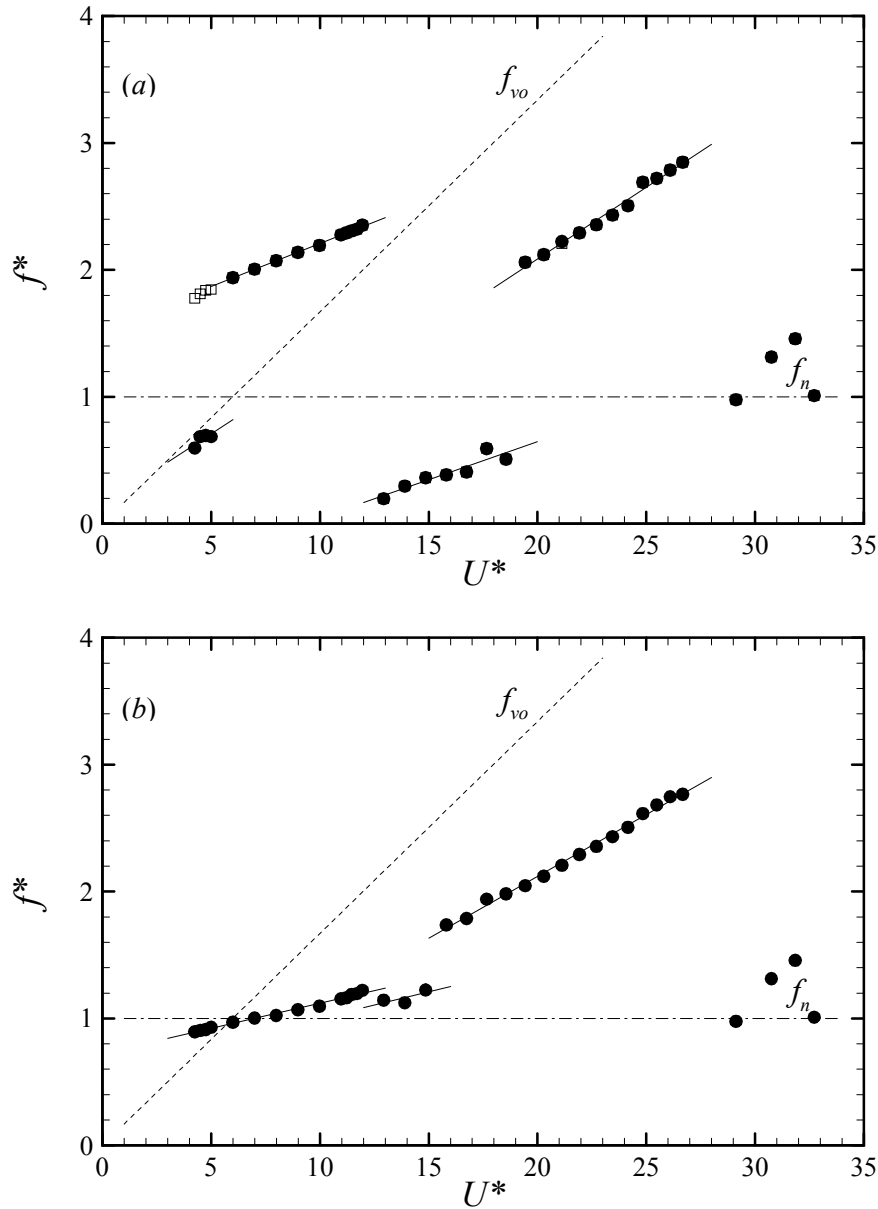


Figure 5.4.5. Normalized frequencies of oscillation for $M^* = 0.8$, $L^* = 10$: (a) streamwise (●) and lateral (□) frequencies; (b) transverse (z) frequencies.

For reduced velocities higher than $U^* = 19$, the normalized frequencies of oscillation increase substantially to more than twice the natural frequency. Finally, at the highest reduced velocities investigated, both the streamwise and transverse oscillation frequencies decrease to values in the range $1 < f^* < 2$ as the sphere exhibits slow, non-sinusoidal vibrations.

The normalized frequencies of oscillation in the transverse direction are shown in Figure 5.4.5 (b). For reduced velocities in the range of the Mode II response, it is clear that the transverse oscillation frequency is at half the streamwise (and lateral) oscillation frequency, in agreement with the results of the lower mass ratio presented in §5.3.4. Also, within this regime, the sphere appears to be

vibrating at close to the natural frequency of the system, in contrast to the oscillations in the streamwise and lateral directions. However, at the end of the Mode II regime, the transverse frequency of oscillation remains at values slightly above the natural frequency, whereas both the streamwise and lateral oscillations display extremely low-frequency oscillations. For reduced velocities greater than $U^* = 19$, the frequency of oscillation in all three directions is the same. For the low mass ratio sphere results, the frequency of oscillation was the same in all three directions when the layover angle passed through 45° . However, for the present results with a mass ratio of $M^* = 0.8$, the frequencies are the same when the mean layover angle exceeds 18° . Govardhan & Williamson (1997) investigated a sphere of mass ratio $M^* = 0.76$ and tether length $L^* = 8.93$, and found that the Mode II response existed up until a mean layover angle of at least 23° . Jauvtis *et al.* (2001) investigated a mass ratio of $M^* = 0.8$ and found a similar result. In both cases, the maximum flow velocities were attained before the end of the synchronization regime was reached, and hence the determination of the onset of the Mode III oscillations was unattainable.

The transverse normalized frequencies of oscillations in the Mode III regime are evidently linearly increasing with increasing reduced velocity, similar to the observations for the Mode II response. However, the onset of the Mode IV response at reduced velocities greater than $U^* = 28$ results in oscillation frequencies that are independent of the direction of oscillation, as previously mentioned. For the Mode III and IV responses observed by Jauvtis *et al.* (2001), the oscillation frequency remained very close to the natural frequency, which was to be expected since the high mass ratio spheres they investigated were typically of the order of $M^* = 80$. They also point out that it is apparent that the Mode III dynamics of the sphere cannot be explained as a lock-in of the vortex shedding frequency with the oscillation frequency since f_{vo} is much greater than f_n , although it is possible that the vortex shedding is altered by the low-frequency body motion such that self-excited motion will follow. However, because of the high mass ratios they investigated, the frequency of oscillation always coincided with the natural frequency, thus not providing much insight into the wake vortex dynamics. The present results, on the other hand, are not affected by such problems and show a large variation in the oscillation frequency as the reduced velocity increases. They also present a more realistic situation that is of practical use to the ocean engineering industry.

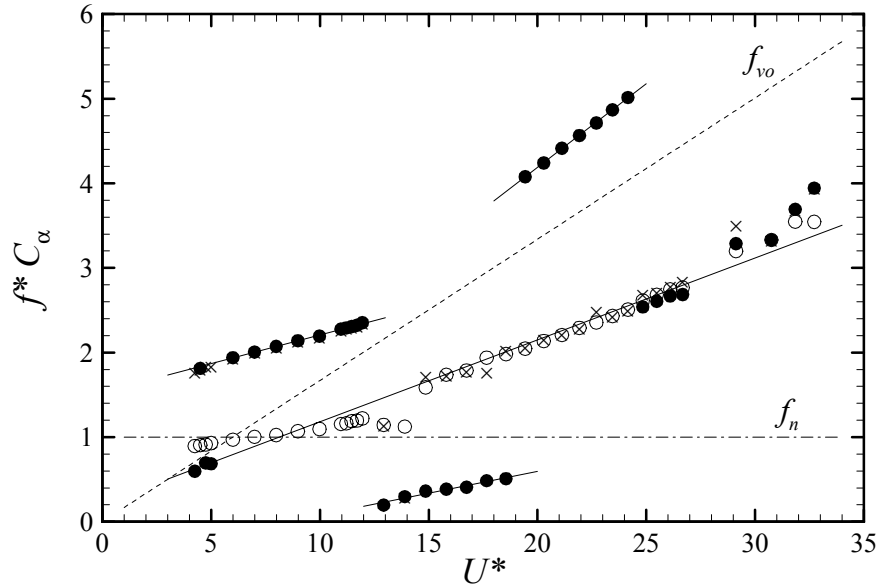


Figure 5.4.6. Normalized frequencies of the fluid force components for $M^* = 0.8$, $L^* = 10$: drag coefficient, \bullet ; lateral (y) coefficient, \times ; transverse (z) coefficient, \circ .

To investigate whether the fluid forcing frequency coincides with the body oscillation frequency, we plot in Figure 5.4.6 the dominant frequencies of the drag, lateral and transverse force coefficients as a function of reduced velocity. As with the body oscillation frequencies, the frequencies of the fluid force coefficients in the streamwise and lateral directions do not correspond to either the natural frequency or the vortex shedding frequency of a stationary sphere over the entire range of reduced velocities investigated. For $U^* < 19$, the frequencies of the drag force are the same as the streamwise oscillation frequency, except at $U^* = 4.5$ at which the body oscillation frequency is roughly 0.4 times that of the drag frequency. Similarly, over this same range of reduced velocity, the lateral frequency of oscillation corresponds directly with the lateral force frequency, except at reduced velocities in the range $14.9 < U^* < 18.6$ and $U^* = 12.9$, during which the lateral forcing frequency is roughly 4 times the oscillation frequency. For higher reduced velocities in the range $19 < U^* < 24$, the drag frequency is approximately twice that of the streamwise oscillations, whereas the lateral forcing frequency is the same as that of the oscillations. The transverse forcing frequency, on the other hand, is essentially the same as that of the transverse oscillations throughout the entire range of U^* . However, the most notable exception occurs at the highest reduced velocities investigated (ie. $U^* > 29$), which corresponds to the Mode IV response and at which the mean layover angle of the sphere is greater than 45° . In this regime, the frequencies of all three fluid force components are relatively the same and greater than the corresponding oscillation frequencies by up to a factor of four. It is apparent that these large-scale vibrations in this Mode IV regime cannot be explained as a lock-in of the fluid forcing frequency with the body oscillation frequency. Nevertheless, the dynamics of this response will be explored in more detail shortly.

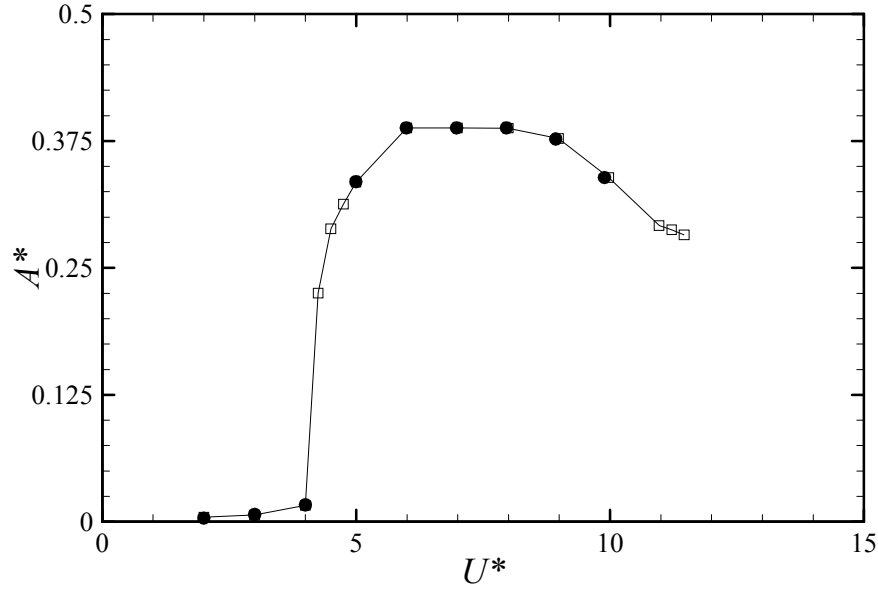


Figure 5.4.7. Effect on the normalized transverse oscillation amplitude of changing the tether length from $L^* = 10$ to $L^* = 5$ for $M^* = 0.8$: $L^* = 5$, ●; $L^* = 10$, □.

5.4.5 Effect of changing L^*

Having gone through the process of investigating the dynamics of the tethered sphere as a function of mass ratio, we now turn our attention briefly to the outcome of altering the tether length L^* . Because a longer tether length will invariably require a longer time to reach equilibrium, it was decided to decrease the tether length, so that numerical simulations were performed with the parameters $L^* = 5$ and $M^* = 0.8$. Due to the limited computational resources available, only a few simulations were performed representing reduced velocities in the range $2 < U^* < 10$. Figure 5.4.7 shows the normalized transverse oscillation amplitude as a function of reduced velocity for the two cases of $L^* = 5$ and $L^* = 10$. It is apparent that there is very little change in the transverse amplitude response when a shorter tether is used. This phenomenon is also observed in the drag coefficient, which is plotted in Figure 5.4.8 along with the previous results for $L^* = 10$. Again, very little change is apparent in the drag coefficient when the tether length is altered. Govardhan & Williamson (1997) investigated a mass ratio of $M^* = 0.76$ and varied the tether length from $L^* = 3.83$ to $L^* = 8.93$. When plotting the normalized transverse RMS amplitude against the Reynolds number, they found that the saturation value of the amplitude (of the Mode II response) was unaffected by variations in the tether length. Furthermore, the RMS response for $L^* = 3.83$ was shifted to higher Reynolds numbers than the RMS response for $L^* = 8.93$, which suggested that the Reynolds number might not be the most suitable parameter to normalize the fluid velocity with.

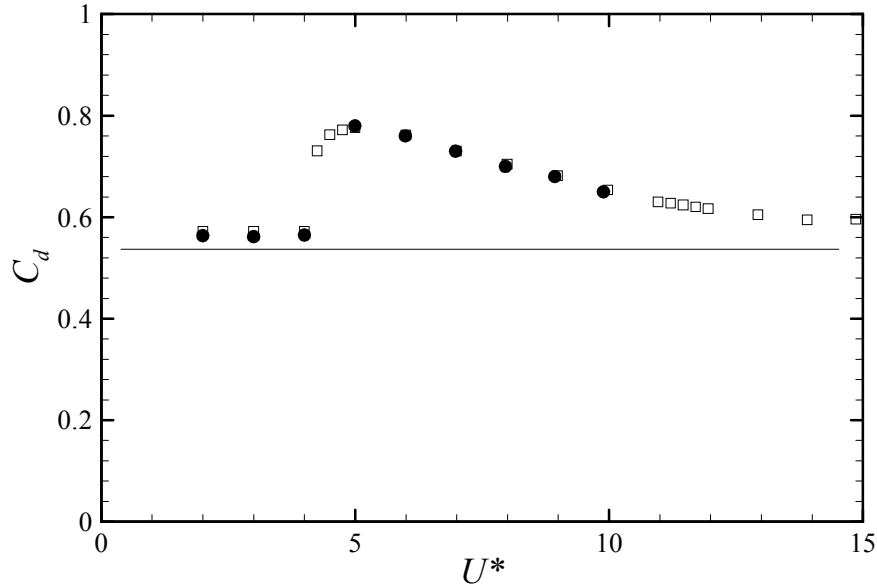


Figure 5.4.8. Effect on the drag coefficient of changing the tether length from $L^* = 10$ to $L^* = 5$ for $M^* = 0.8$: $L^* = 5$, \bullet ; $L^* = 10$, \square .

However, when plotting the amplitude response against the reduced velocity, they found an excellent collapse of the response data. For example, the onset and peak amplitude of the Mode I response was virtually identical, as was the onset and saturation amplitude of the observed Mode II response. Numerically and experimentally, it is apparent then that the effect of changing the tether length is insignificant and by far the most important parameter governing the tethered sphere system is the mass ratio.

5.5 Putting the results together: suitability of the reduced velocity

So far, we have computationally investigated the response of a tethered sphere for mass ratios ranging from $M^* = 0.082$ to $M^* = 0.8$. We have also investigated tether lengths ranging from $L^* = 5$ to $L^* = 10$. In addition, we have performed experiments at low Reynolds numbers for a mass ratio of $M^* = 0.91$ and tether length of $L^* = 10.24$. We put all of these results together in this section to observe the changes in amplitude response, drag coefficient and frequency response as a function of reduced velocity when the mass ratio and tether length are varied.

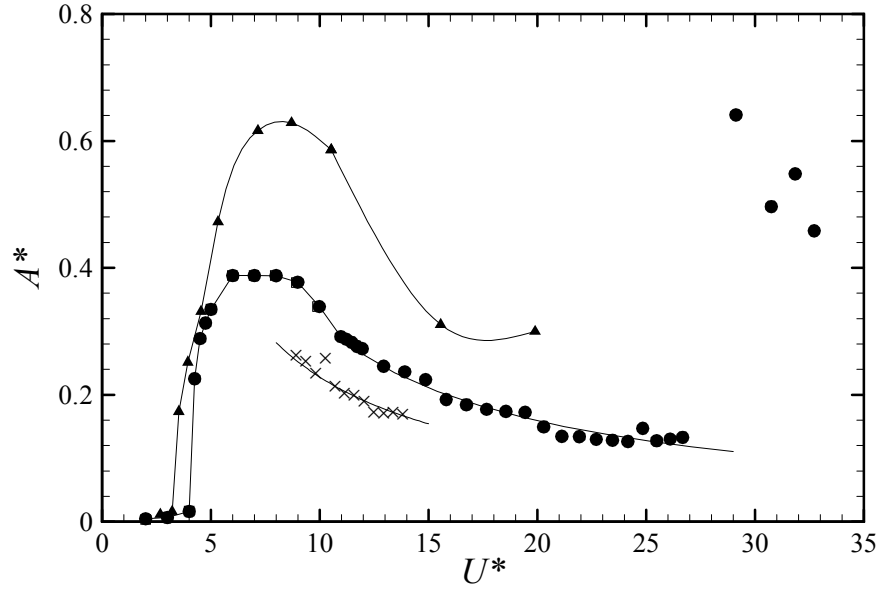


Figure 5.5.1. Amplitude response as a function of reduced velocity: $M^* = 0.082, L^* = 9.3, \blacktriangle$; $M^* = 0.8, L^* = 5, \square$; $M^* = 0.8, L^* = 10, \bullet$; $M^* = 0.91, L^* = 10.24, \times$ (experiments).

Figure 5.5.1 shows the effect of increasing the mass ratio and tether length on the normalized amplitude response. First of all, we note that for the sphere with mass ratio $M^* = 0.8$, increasing the tether length from $L^* = 5$ to $L^* = 10$ results in practically no change in the amplitude response, as mentioned in §5.4.5. Furthermore, increasing the mass ratio from $M^* = 0.082$ to $M^* = 0.91$ appears to decrease the normalized oscillation amplitude. The Mode II response is observed for all of the mass ratios investigated. In addition, a Mode III response is observed for the numerical simulations, regardless of the mass ratio. However, the limited range of the present experiments did not allow higher reduced velocities to be evaluated, and hence a Mode III response was unobtainable. Nevertheless, the numerical simulations and the experimental results all show a gradual decrease in amplitude at the end of the Mode II regime. The slope of this decrease is more severe for the lower mass ratios, and appears to be less severe as the mass ratio increases.

Also note the appearance of a Mode IV response that only exists for the higher mass ratios. As pointed out in §5.4, this Mode IV response occurs when the mean layover angle exceeds 45° . However, for the low mass ratio case ($M^* = 0.082$), the layover angle exceeds 45° well before a reduced velocity of $U^* = 20$ is reached, although the sphere still exhibits Mode III-type oscillations. This apparent lack of a Mode IV response highlights the existence of a *critical mass*, which will be discussed more detail in §5.11.

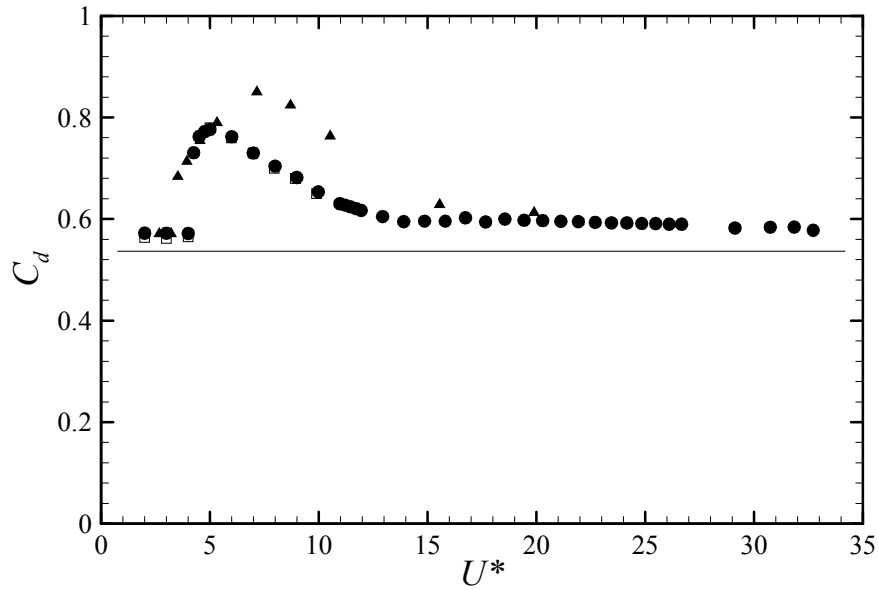


Figure 5.5.2. Change in the drag coefficient as a function of reduced velocity. Symbols as in Figure 5.5.1.

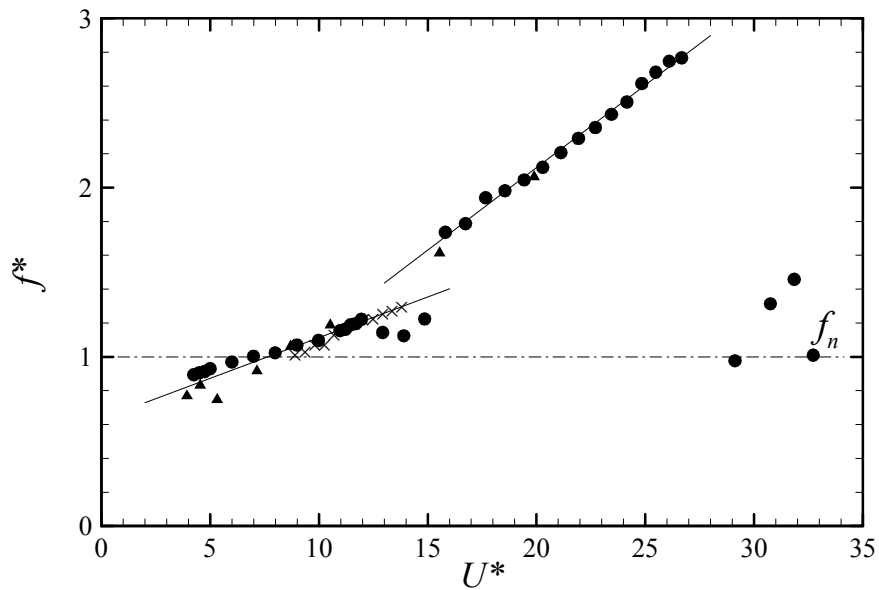


Figure 5.5.3. Frequency response as a function of reduced velocity. Symbols as in Figure 5.5.1.

The relationship between the drag coefficient and the mass ratio is depicted in Figure 5.5.2. For the high mass ratio cases, it is clear once again that a change in the tether length yields very little change in the drag coefficient. Furthermore, decreasing the mass ratio results in an increase in the drag coefficient, which is a direct consequence of the larger-amplitude oscillations that occur for the lower mass ratio as shown in Figure 5.5.1. As the reduced velocity is increased, the drag coefficient gradually decreases to values slightly above that of a stationary sphere, regardless of the mass ratio.

In addition, we have seen from the previous sections that the harmonic oscillations cause an upsurge in the drag coefficient, for example, in the Mode II regime as seen in Figure 5.5.2. However, for $M^* = 0.8$, even larger-amplitude oscillations are observed within the Mode IV regime, but the drag coefficient hardly changes at all. This is because the oscillations in the Mode IV regime are *not* harmonic, as we shall see in §5.10.

Finally, the normalized frequency response of the sphere is shown in Figure 5.5.3. At low reduced velocities (ie. $U^* < 4$), the sphere is desynchronized and significant oscillations are not observed, in spite of the mass ratio. On the other hand, throughout the entire Mode II regime, the sphere oscillations become synchronized and oscillate harmonically. The agreement in the frequency response for all of the mass ratios investigated, both numerically and experimentally, within this Mode II regime is remarkable. Furthermore, with increasing reduced velocity, a large jump occurs in the frequency response between the “lower” Mode II branch and the “upper” branch, which signifies a change in dynamics from the Mode II response to the Mode III response. The agreement in f^* within this Mode III regime is also remarkable, for both the high and low mass ratio cases investigated. It is also clear from this plot that the sphere with mass ratio $M^* = 0.082$ does indeed oscillate within the Mode III regime. As a final point, at the highest reduced velocities investigated, the response of the high mass ratio sphere switches to a Mode IV response, which is highlighted by the presence of extremely low-frequency vibrations, even though the vortex shedding frequency is much higher.

In conclusion then, we see from Figures 5.5.1 – 5.5.3 that the reduced velocity (as defined in Equation (5.1.8)) as a scaling parameter does indeed collapse the data suitably. This is especially true for the normalized frequency response, which shows the different modes of vibration and the corresponding range of U^* at which they occur to be essentially independent of the mass ratio and tether length. Nevertheless, for the oscillation amplitude (and the corresponding drag coefficient), the vibration modes exist at more or less the same reduced velocities, but the magnitudes differ depending on the mass ratio. However, similar trends were observed by Williamson & Govardhan (1997).

5.6 The neutrally buoyant tethered sphere: $M^* = 1$

So far, we have investigated in detail the dynamics of a tethered sphere for mass ratios of $M^* < 1$. Higher mass ratios of $M^* \gg 1$ have been investigated by Jauvtis *et al.* (2001) and to some extent by Govardhan & Williamson (1997). However, a particularly significant case is the neutrally buoyant sphere, $M^* = 1$ of which, to the author’s knowledge, despite the significance of studying the dynamics of a neutrally buoyant tethered sphere in a steady flow, there are virtually no experimental

or numerical investigations concerning such a problem, apart from the preliminary work of Provansal (2003, private communications).

However, before we begin the analysis of the dynamics of a neutrally buoyant tethered sphere, some clarification needs to be addressed concerning the definition of reduced velocity in Equation (5.1.8). In particular, note that the buoyancy term in braces becomes zero for the present case. As a result, increasing the Froude number (or decreasing α) has no effect on the natural frequency, and hence the reduced velocity. Accordingly, the procedure of obtaining a wide range of reduced velocity as outlined in Chapter 2 and applied in the previous sections has no meaning when the buoyancy is zero. Instead, at least for the present simulations, we adopt the practice of increasing the Reynolds number, as is the case with experiments.

In this light, the present simulations were performed at Reynolds numbers of $Re = 300, 350, 400, 450$ and 500 . This represents a range of flow states from unsteady, planar-symmetric flow at the lowest Reynolds numbers to unsteady asymmetric flow at the highest Reynolds numbers. Note that mesh independence, as examined in Chapter 2, has not been verified for Reynolds numbers greater than $Re = 500$ and as a result, simulations were not performed for $Re > 500$. In addition, each simulation was initialized with a small perturbation that was random in space, and hence any preferred orientation of the wake was only dependent on the initial perturbation.

5.6.1 Amplitudes of oscillation

We begin by investigating the vibrational response of the sphere as the Reynolds number is increased. This is depicted in Figure 5.6.1 (a), where the axis on the left of the figure represents the normalized amplitude response in the streamwise and transverse directions, and the axis on the right corresponds to the lateral oscillations. Note that at a Reynolds number of $Re = 300$, the response of the sphere is not particularly harmonic, and so the relative amplitude response depicted in Figure 5.6.1 should not be taken as meaningful. On the other hand, as will be shown shortly, the response of the sphere at the higher Reynolds numbers is quite harmonic, resulting in accurate determinations of the corresponding normalized amplitudes of motion. It is somewhat surprising that at a Reynolds number of $Re = 300$ such a disordered response is observed, even though the flow is laminar and characterized by periodically shed vortices as described in Chapter 3.

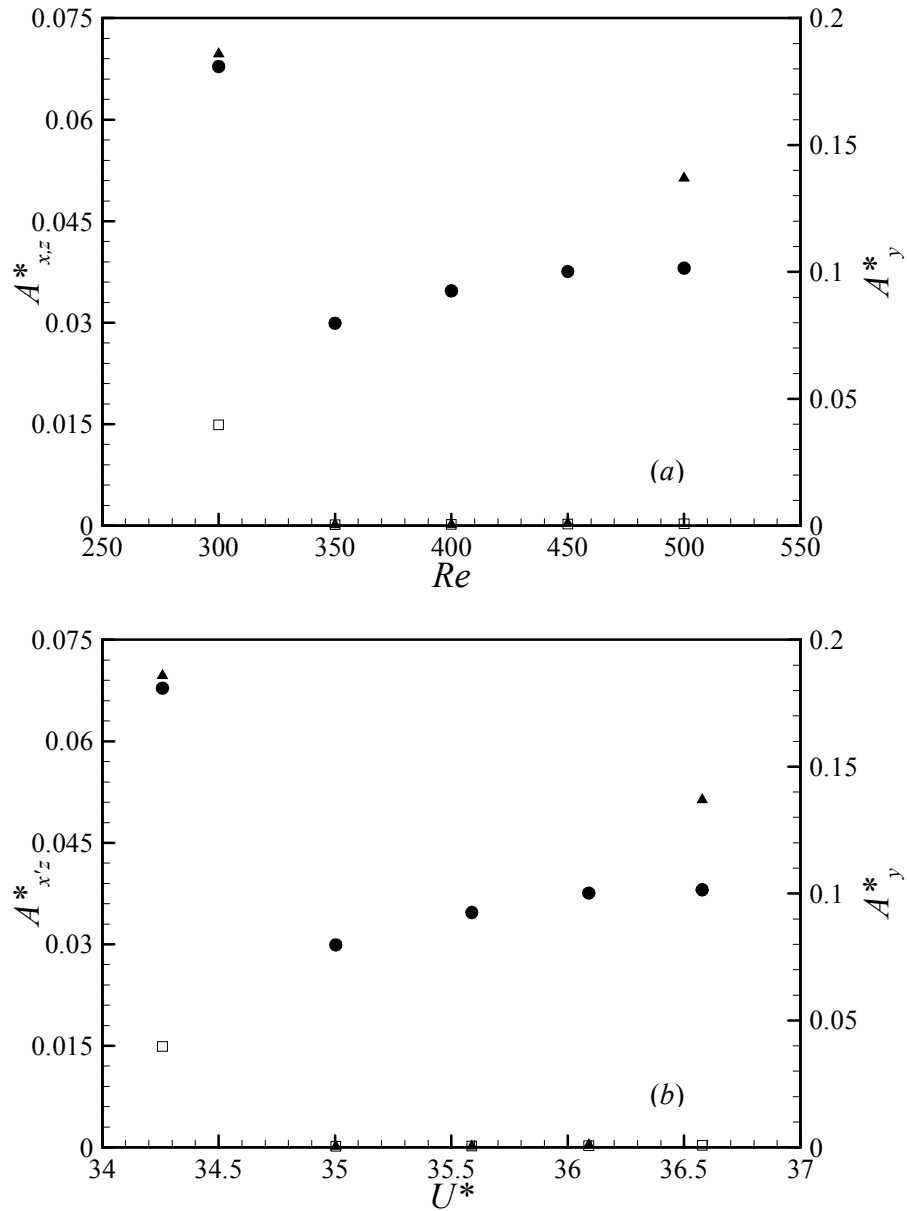


Figure 5.6.1. Normalized oscillation amplitudes A^* for $M^* = 1$, $L^* = 10$: x -oscillations, \square ; y -oscillations, \bullet ; z -oscillations, \blacktriangle ; (a) dependence on Reynolds number; (b) dependence on reduced velocity.

As the Reynolds number is increased from $Re = 300$, the amplitudes of oscillation in the streamwise and transverse directions are relatively small. Alternatively, the oscillations in the lateral direction build up to an amplitude of approximately $A^* = 0.1$. It is somewhat surprising to note that for the neutrally buoyant sphere, the large-amplitude oscillations are observed in the *lateral* direction, whereas for the case $M^* \neq 1$, the large-amplitude oscillations are observed in the *transverse* direction. At a Reynolds number of $Re = 350$, the wake for a stationary sphere is planar-symmetric, as is the case for a Reynolds number of $Re = 300$. For Reynolds numbers of $Re = 400$ and above, the

flow past a stationary sphere is unsteady and asymmetric. Figure 5.6.1 shows that for $Re > 300$, the transverse oscillations are insignificant, except at a Reynolds number of $Re = 500$, at which the transverse oscillation amplitude is roughly $A^* = 0.052$. This represents an increase in A^* of almost 130 times greater than that observed at the previous Reynolds number. This is probably due to the increasing complexity of the wake as the shedding direction oscillates intermittently and the vortex shedding pattern becomes irregular, as discussed in Chapter 1. In any case, the oscillations observed when the tethered sphere is neutrally buoyant are much smaller than the oscillations observed for non-zero mass ratio spheres, at least for the Reynolds numbers (and reduced velocities) investigated in this study.

5.6.2 Force coefficient behaviour

The changes in the drag coefficient when the sphere is oscillating are depicted in Figure 5.6.2 as a function of Reynolds number. For comparison, also shown are the stationary sphere drag data obtained at Reynolds numbers of $Re = 300, 400$ and 500 from Chapter 3. For both the stationary and tethered sphere cases, the flow was unsteady and hence the data represent time-averaged values. At all of the Reynolds numbers investigated, the drag for both the tethered sphere and the stationary sphere decrease monotonically in accordance with the power law model put forth in Chapter 3. However, at the lowest Reynolds numbers investigated, the drag coefficient for the tethered sphere is greater than that of the stationary sphere by approximately 4.3%. When the Reynolds number is increased to $Re = 400$, this difference becomes roughly 7.3%.

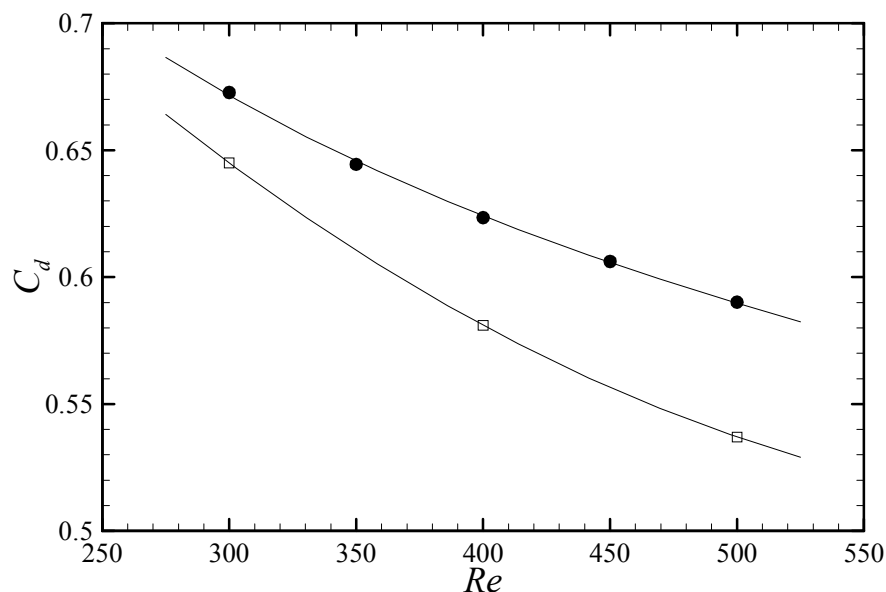


Figure 5.6.2. Change in the drag coefficient due to the tethered sphere oscillations for $M^* = 1, L^* = 10$: tethered sphere results, ●; stationary sphere results from Chapter 3, □.

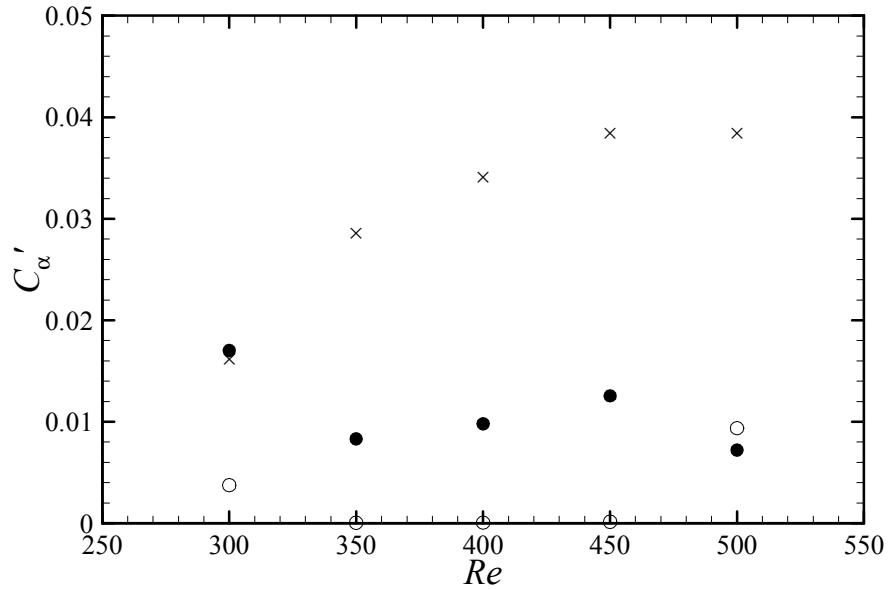


Figure 5.6.3. RMS force coefficients for the neutrally buoyant sphere, $M^* = 1$: drag coefficient, ●; lateral (y) coefficient, ×; transverse (z) coefficient, ○.

Finally, at a Reynolds number of $Re = 500$, the difference in drag between the tethered sphere and the stationary sphere is about 9.9%. It is clear that as the Reynolds number increases and the flow develops on its way to turbulence, the oscillations of the neutrally buoyant sphere increase in magnitude and the drag coefficient adjusts accordingly. As the oscillations become more harmonic for $Re > 300$, the drag coefficient departs more significantly from that of a stationary sphere. At a Reynolds number of $Re = 300$, the oscillations are far from harmonic (even though the amplitudes are quite large), and so the drag coefficient departs considerably less from that of a stationary sphere. This increase in C_d for harmonic excitations is a well-observed phenomenon in flow-induced vibration problems.

Figure 5.6.3 shows the amplitudes of the fluid force coefficients. It is evident that the fluctuations of the lateral force coefficient are greater than those of the streamwise and transverse force coefficients for all of the Reynolds numbers except $Re = 300$. However, at this Reynolds number, the oscillations are not very ordered, as discussed in the previous section. It is also clear that the amplitude of the transverse force coefficient over the entire range of Reynolds numbers investigated is less than $C_z' = 0.01$. Nevertheless, the amplitude of this force coefficient does not depart significantly from zero except at Reynolds numbers of $Re = 300$ and $Re = 500$. A comparison with Figure 5.6.1 shows that this increase in C_z' at these Reynolds number extremes is responsible for the observed increase in amplitude. A similar scenario occurs for the fluctuating drag coefficient and the corresponding streamwise oscillation response. At a Reynolds number of $Re = 300$, C_d' is larger than that observed

at the higher Reynolds numbers. Accordingly, the amplitude response in the streamwise direction is larger at $Re = 300$ than at the higher Reynolds numbers. For the fluctuating lateral force component, C_y' increases logarithmically to a value of approximately $C_y' = 0.039$. The corresponding amplitude response of the lateral oscillations also increases logarithmically, except at a Reynolds number of $Re = 300$, as shown in Figure 5.6.1. It follows then that for the neutrally buoyant tethered sphere, the oscillations in all three directions are caused directly by the fluctuations of the equivalent fluid forces.

5.6.3 Frequency response

The dominant frequencies of oscillation for the neutrally buoyant sphere are depicted in Figure 5.6.4 as a function of reduced velocity. Also shown as the dashed line are the (normalized) vortex shedding frequencies for a stationary sphere, which range from $St = 0.134$ at $Re = 300$ to $St = 0.16$ at a Reynolds number of $Re = 500$. Note that the relationship between the shedding frequency and the Reynolds number is presumed to be linear within this range of Re , solely for the purposes of comparison. For Reynolds numbers greater than $Re = 300$, the oscillation frequency of the tethered sphere in all three directions does not correspond to either the natural frequency of the system or the vortex shedding frequency at the equivalent Reynolds number. At a Reynolds number of $Re = 300$, the oscillation frequencies in the streamwise and lateral directions are the same and twice that of the transverse oscillations.

For $U^* > 35$ (corresponding to $Re \geq 400$), the frequency of oscillation in the streamwise direction is much greater than both the natural frequency and vortex shedding frequency. On the other hand, the oscillation frequencies in the lateral and transverse directions are greater than the natural frequency but less than the vortex shedding frequency of a stationary sphere. In addition, for $U^* = 36.6$ (ie. $Re = 500$), the transverse frequency of oscillation decreases as the relatively large-amplitude vibrations commence. In either case, the normalized frequencies of oscillation for the neutrally buoyant sphere at these reduced velocities are greater than those observed over the same range of U^* for non-zero mass ratio conditions. For example, Figure 5.4.5 for a mass ratio of $M^* = 0.8$ shows that the normalized oscillation frequencies in all three directions lie in the range $1 < f^* < 2$ for reduced velocities in the range $29 < U^* < 34$, which is representative of a Mode IV response. For the neutrally buoyant sphere, f^* varies in the range $7 < f^* < 8$ for the streamwise oscillations and $3.5 < f^* < 4$ for the non-streamwise oscillations. Obviously, the dynamics of the sphere when the buoyancy is not zero are very different from the dynamics observed when the buoyancy is zero.

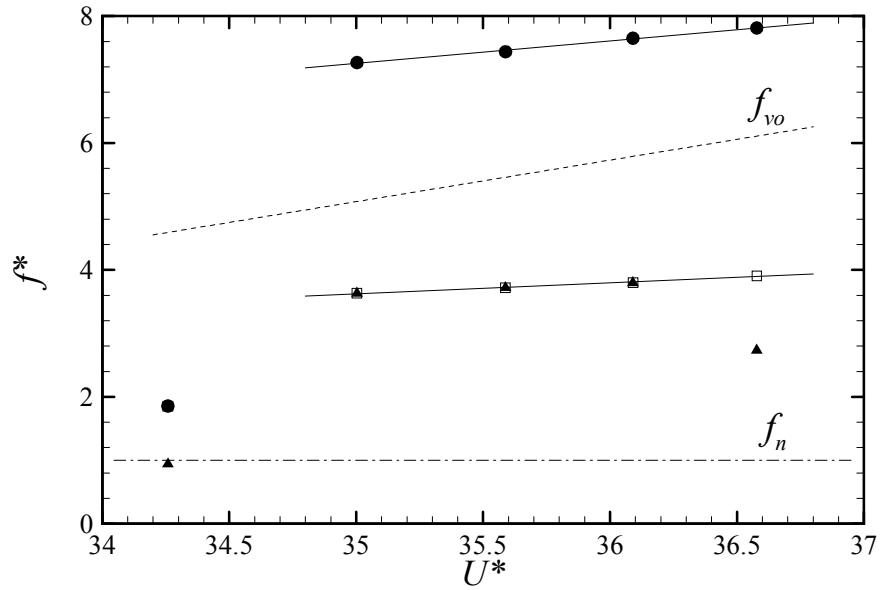


Figure 5.6.4. Normalized frequencies of oscillation for $M^* = 1, L^* = 10$: streamwise frequencies, ●; lateral frequencies, □; transverse frequencies, ▲.

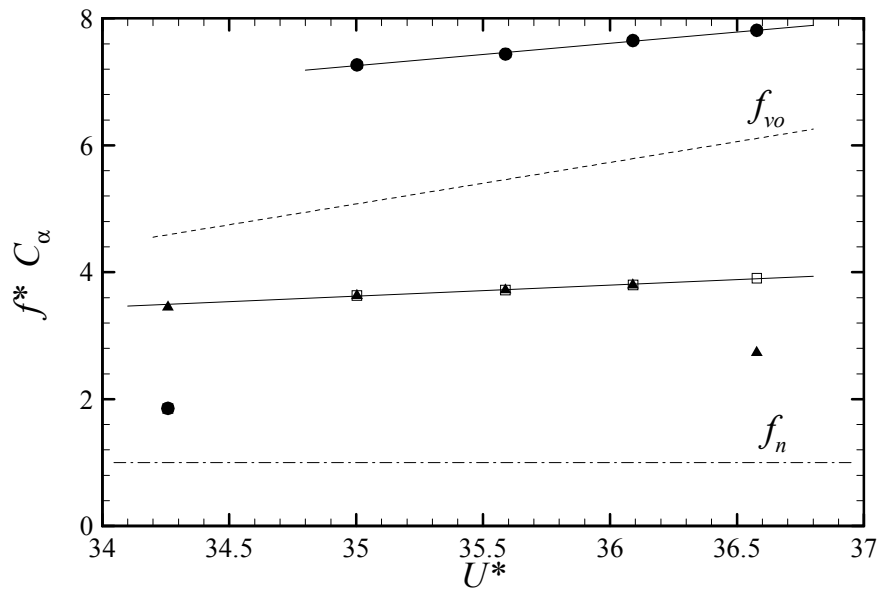


Figure 5.6.5. Normalized frequencies of the fluid force components for $M^* = 1, L^* = 10$: drag coefficient, ●; lateral coefficient, □; transverse coefficient, ▲.

The dominant normalized frequencies of the fluid forces are shown in Figure 5.6.5. It is clear that for the entire range of reduced velocities investigated, the frequencies of the fluid forces give rise to the frequencies of the sphere oscillations, since the fluid forces themselves are directly responsible for the sphere oscillations, as discussed in the previous subsection. The only exception occurs at a reduced velocity of $U^* = 34.3$, which corresponds to a Reynolds number of $Re = 300$. As already

mentioned, at this Reynolds number, the motions are not harmonic and as a result the frequencies of the forces and the oscillations are not expected to be identical.

5.6.4 Trajectories of sphere motion

We have seen that the motion of a neutrally buoyant sphere is highly dependent on the Reynolds number. Also, it is known that the sphere trajectories vary experimentally from a zigzag-type motion to a circular displacement pattern, depending on the Reynolds number and the timescale used to observe the dynamics (Provansal (2003), private communication). . This section investigates the trajectories of the sphere displacements as a function of the Reynolds number, in order to observe whether the aforementioned zigzag or circular displacement patterns can be obtained numerically.

The timeframe used for each simulation corresponded to $\Delta t^* = 2000$ units. However, only the last approximately 1000 time units were statistically steady and used for computing the displacement trajectories shown in Figure 5.6.6. Here, we increase the Reynolds number in increments of 50 and record the y - z displacement as a function of time. Because harmonic oscillations were not observed at a Reynolds number of $Re = 300$, the y - z displacement pattern is not plotted. However, at higher Reynolds numbers, the oscillations were harmonic and the resultant motion of the sphere is depicted in Figure 5.6.6. At a Reynolds number of $Re = 350$, the oscillations in the lateral direction are more than 500 times greater than those in the transverse direction, and exhibit a limit cycle behaviour. Accordingly, the sphere oscillates more or less vertically on a straight line. In an experimental towing tank facility, these displacements may be viewed as a zigzag-type motion as the sphere is towed through the channel.

When the Reynolds number is increased to $Re = 400$, the magnitudes of the lateral and transverse oscillations remain relatively unaltered. Furthermore, the limit cycle observed at the previous Reynolds number still exists and the sphere oscillates on almost the same vertical plane as it did at the previous Reynolds number. In addition, the vibration cycles appear to be slightly more “rounded” than the oscillations at $Re = 350$.

At a Reynolds number of $Re = 450$, the magnitude of the oscillations in the lateral direction remain virtually unchanged, but the transverse oscillations experience an increase in magnitude of approximately twice that observed at $Re = 400$. Like the previous case, the oscillations are slightly more elliptical, and it appears that further increases in the Reynolds number might lead to circular displacement patterns. However, at a Reynolds number of $Re = 500$, the displacement pattern is an irregular figure-of-eight shape. Furthermore, the oscillations in the lateral direction have increased slightly in magnitude, whereas those in the transverse direction have increased by almost 20 times.

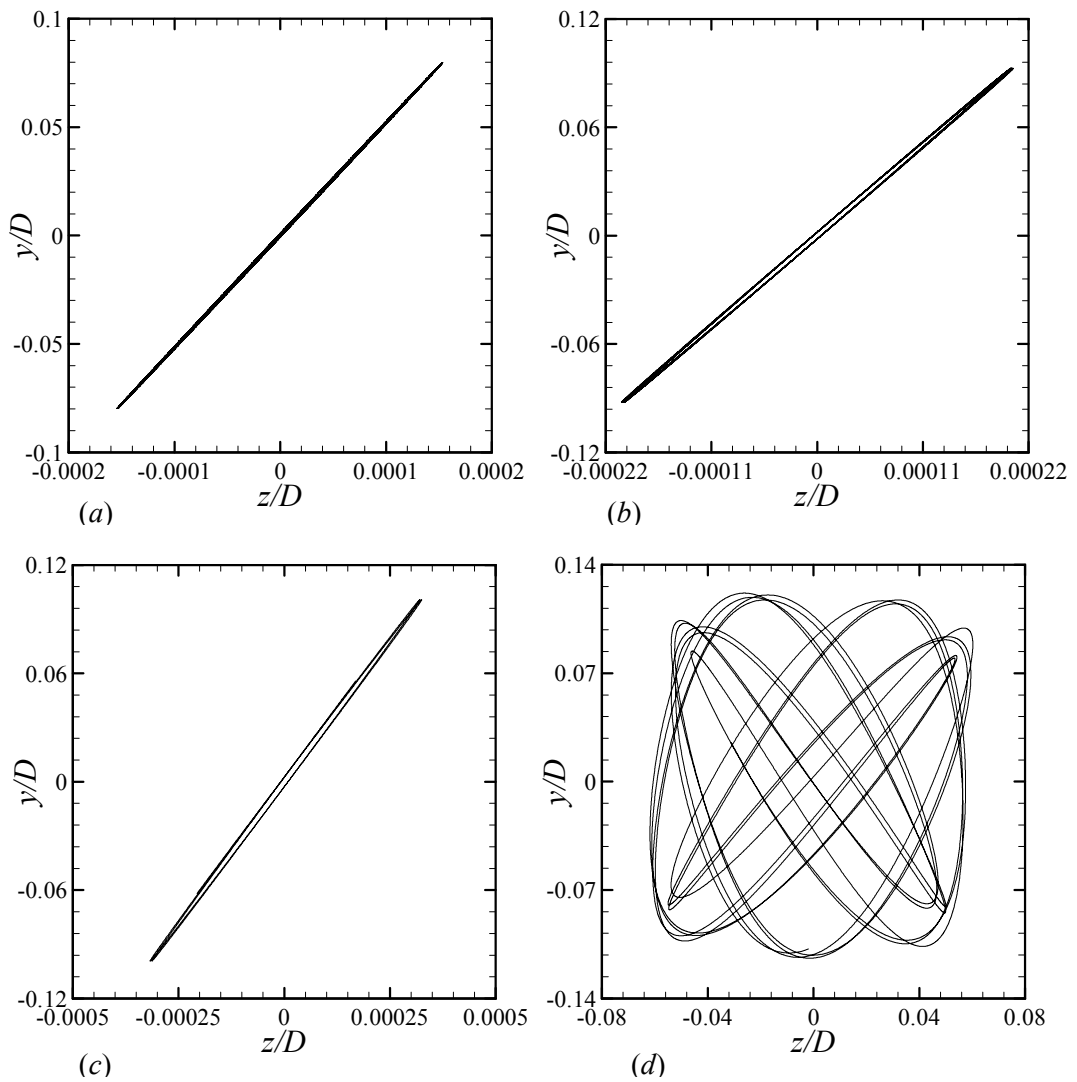


Figure 5.6.6. Time traces of sphere oscillations for $M^* = 1$: (a) $Re = 350$; (b) $Re = 400$; (c) $Re = 450$; (d) $Re = 500$.

At this Reynolds number, the vortex shedding oscillates intermittently about the flow centreline, and as a result larger-amplitude vibrations occur.

For the Reynolds numbers investigated, zigzag-type motions were obtained but circular displacement patterns were not. However, as mentioned at the start of this section, typical sample spaces of $\Delta t^* = 1000$ time units were used to calculate the displacement patterns, mainly due to the time restraints imposed on the computational resources. Experimentally, however, the oscillations of rising spheroids (Mougin & Magnaudet (2002)) have been known to start off as a zigzag pattern and then develop into spiral motions as time grows. It is therefore possible that more time is needed numerically for the oscillations to transition from the observed zigzag behaviour to possible circular trajectories. This interesting aspect will be addressed in the near future.

5.7 Mode I response

Because the numerical simulations do not reveal the existence of the Mode I response for all of the mass ratios, tether lengths and reduced velocities investigated, it is impossible to investigate in any detail the dynamics of the sphere in this regime. However, the experimental results of Williamson & Govardhan (1997), Govardhan & Williamson (1997) and Jauvtis *et al.* (2001) all show clearly a Mode I response for the range of mass ratios of $0.082 < M^* < 80$. Furthermore, altering the tether length merely changed the Reynolds number at which the Mode I response was observed, although the change in reduced velocity and oscillation amplitude (as well as the overall shape of the response curve) was found to be relatively independent of the tether length. It is apparent then that the appearance of the Mode I response, as well as the higher modes of vibration discussed in §§5.8 and 5.9, are primarily dependent on the mass ratio.

With this in mind, it is useful to look at the shape of the response curve when the mass ratio is very low ($M^* = 0.082$), low ($M^* = 0.8$) and high ($M^* = 2.8$ to $M^* = 80$). In Figure 5.7.1, the maximum oscillation amplitude results of Williamson & Govardhan (1997) are reproduced for their mass ratio of $M^* = 0.082$. Figure 5.7.2 shows the RMS-amplitude results of Govardhan & Williamson (1997) for their mass ratio of $M^* = 0.76$, whereas Figure 5.7.3 duplicates the RMS-amplitude results of Jauvtis *et al.* (2001) for their mass ratio of $M^* = 2.8$. Note that with the work of Jauvtis *et al.* (2001), the normalized amplitude A^* is plotted (defined in §5.4.2) which, for the Mode I response, corresponds to the RMS-amplitude since the oscillations are sinusoidal. First of all, it is immediately clear that when the maximum amplitude is plotted (as opposed to the RMS-amplitude), the local peak corresponding to the Mode I response is not very clear. This is because the RMS provides more information about the oscillations (namely the energy of the motions) than the maximum amplitude. This is especially the case when the oscillations are non-harmonic and display strong amplitude modulation, which is the case for many of the numerical (and also experimental) results presented in this study.

Since the response plotted using the maximum amplitude does not provide much information from a physical point of view, we compare now the shape of the response curve for $M^* = 0.76$ and $M^* = 2.8$, ie. Figure 5.7.2 and Figure 5.7.3. For the Mode II response, as discussed in §5.4, it is clear that increasing the mass ratio decreases the synchronization regime. For the Mode I response, the range of synchronization is approximately $5 < U^* < 6$ for a mass ratio of $M^* = 0.76$. Although not reproduced here, for a mass ratio of $M^* = 0.8$ the synchronization regime increases to $5 < U^* < 7$ (Jauvtis *et al.* (2001)). For the high mass ratio of $M^* = 2.8$, the Mode I response is hardly noticeable and does not even register as a local peak in the normalized oscillation amplitude A^* . In either case,

the amplitudes of the oscillations for the Mode I response are smaller than those of the other three modes of vibration (see Jauvtis *et al.* (2001)).

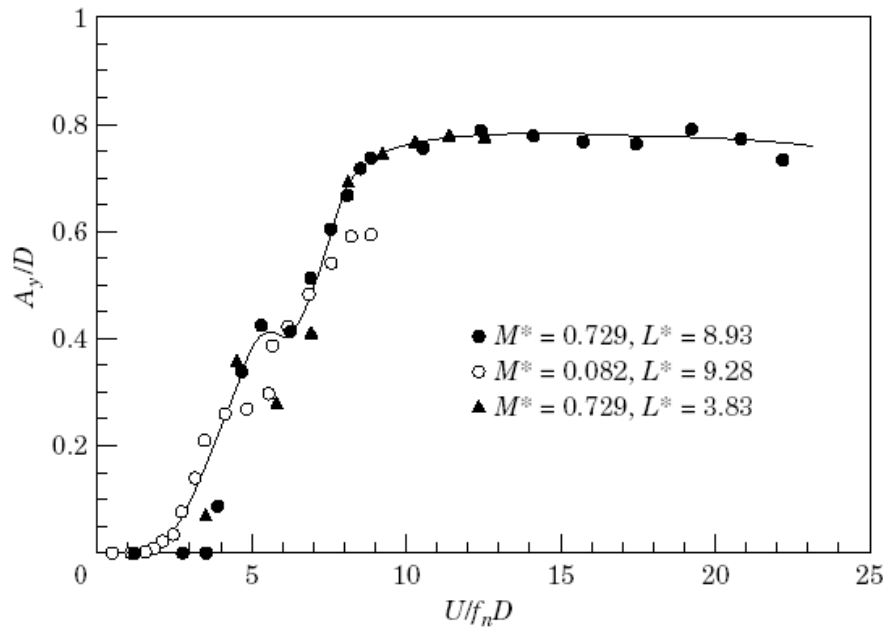


Figure 5.7.1. Transverse amplitude response for mass ratios of $M^* = 0.082, 0.729$ from Williamson & Govardhan (1997).

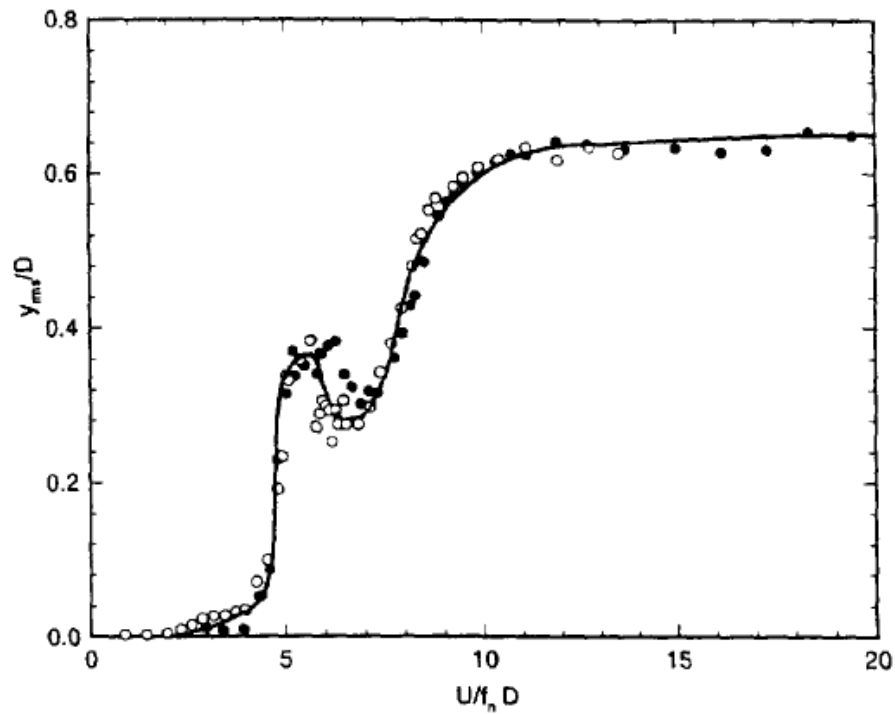


Figure 5.7.2. Transverse amplitude response for $M^* = 0.76$ of Govardhan & Williamson (1997): \bullet , $L^* = 8.93$; \circ , $L^* = 3.83$.

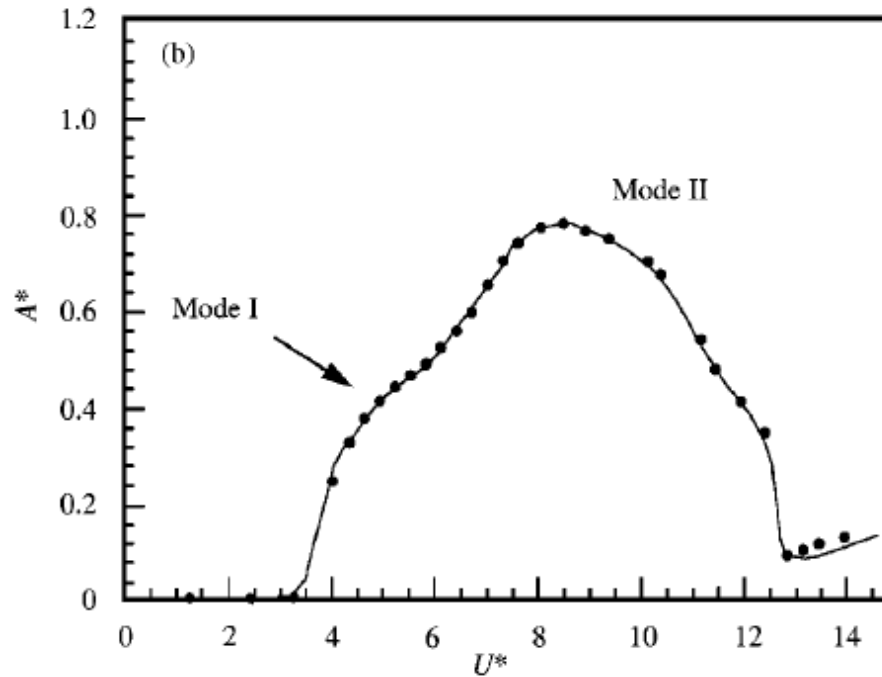


Figure 5.7.3. Transverse amplitude response for $M^* = 2.8$ of Jauvtis *et al.* (1997).

An analysis of Figures 5.7.1 - 5.7.2 reveals that the Mode I response occurs at a reduced velocity of approximately $U^* = 5 - 6$. This corresponds to a natural frequency of $S_n = 0.2 - 0.167$. For the range of Reynolds numbers investigated experimentally, the Strouhal number of the vortex shedding for a stationary sphere is roughly $St = 0.18$ (Sakamoto & Haniu (1990)). Because the natural frequency is approximately equal to the vortex shedding frequency, it is this condition that yields a resonance in the classical studies of the vortex-induced vibrations of cylinders, as pointed out by Williamson & Govardhan (1997). It appears then that the Mode I response is a result of the vortex shedding frequency locking-on to the natural frequency of the system.

The question remains as to why the Mode I response is clearly observed experimentally but not numerically, regardless of the mass ratios investigated. From §§5.3 and 5.4, it is possible that the incremental steps in reduced velocity investigated may have been too large to reveal a local peak corresponding to a Mode I response whose range of synchronization is of order unity. However, the vortex shedding frequency for a stationary sphere for the Reynolds numbers investigated numerically (ie. $Re = 500$) is approximately $St = 0.16$. If the tethered sphere was oscillating in the Mode I regime, the natural frequency would thus also be $S_n = 0.16$, corresponding to a reduced velocity of $U^* = 6.25$. At this reduced velocity, from Figure 5.3.2 and Figure 5.4.2, the sphere is clearly oscillating in the Mode II regime, so that the scenario of the scale of computed reduced velocities being too small is unlikely. This discrepancy, however, may lie in the range of Reynolds numbers under investigation. From Chapter 2, the lowest experimental Reynolds number in the

results of Govardhan & Williamson (1997) was approximately $Re = 1000$; the highest Reynolds number was roughly $Re = 14000$. Under these conditions, the flow was fully turbulent with a relatively constant vortex shedding frequency. On the other hand, the numerical simulations were performed exclusively at a Reynolds number of $Re = 500$, representing a flow that was laminar and asymmetric. The observed differences between laminar and turbulent flow may well result in the existence (or lack thereof) of a Mode I response.

5.8 Mode II response

Having discussed the vibrational response of the tethered sphere in the Mode I regime, we now turn our attention to the Mode II response. Although a Mode I-type response was not revealed from the numerical simulations, the DNS results presented in §§5.3 – 5.4 clearly revealed a Mode II-type response in the nomenclature of Jauvtis *et al.* (2001). The dynamics of this Mode II response are unlike those of the Mode I response, which is a result of the vortex shedding frequency locking on to the natural frequency of the system, a phenomenon that leads to the large-amplitude vibrations of a cylinder undergoing vortex-induced vibrations (see Khalak & Williamson (1999) and Govardhan & Williamson (2000)). For a tethered sphere, on the other hand, at least for the mass ratios investigated in this study, the oscillation frequency does not correspond to the vortex shedding frequency, although large-amplitude oscillations are observed. This section aims to analyze in detail the dynamics of the Mode II response, focusing on the mechanisms causing the vibrations via detailed examinations of the flow fields throughout a typical oscillation cycle. In this respect, as with the case of a stationary sphere in Chapter 3, we concentrate mainly on the pressure fields, as well as the vortex structures that would be observed if dye visualization was possible.

To investigate how the sphere responds when the reduced velocity is increased within the Mode II regime, reduced velocities of $U^* = 5$ and $U^* = 10$ are chosen for the mass ratio of $M^* = 0.8$ and tether length of $L^* = 10$. From §5.4.2, the range of synchronization of the Mode II response corresponds to reduced velocities in the range $4.25 < U^* < 10$, so that the chosen values of $U^* = 5$ and $U^* = 10$ lie close enough to highlight the dynamics at the onset of synchronization, as well as far enough to observe how the flow develops within this regime as the large-amplitude oscillations sustain. Furthermore, because the large-amplitude vibrations are observed in the transverse direction, we focus on the dynamics of the tethered sphere in the transverse (z) direction.

In both cases, we consider a typical oscillation cycle and examine the displacement, forces, pressure and vortex structures at four equally spaced increments of $\varphi = T/4$, where T is the period of oscillation. In this way, as with the vortex shedding process for a stationary sphere described in Chapter 3, we hope to obtain a straightforward and coherent explanation of the dynamics of this

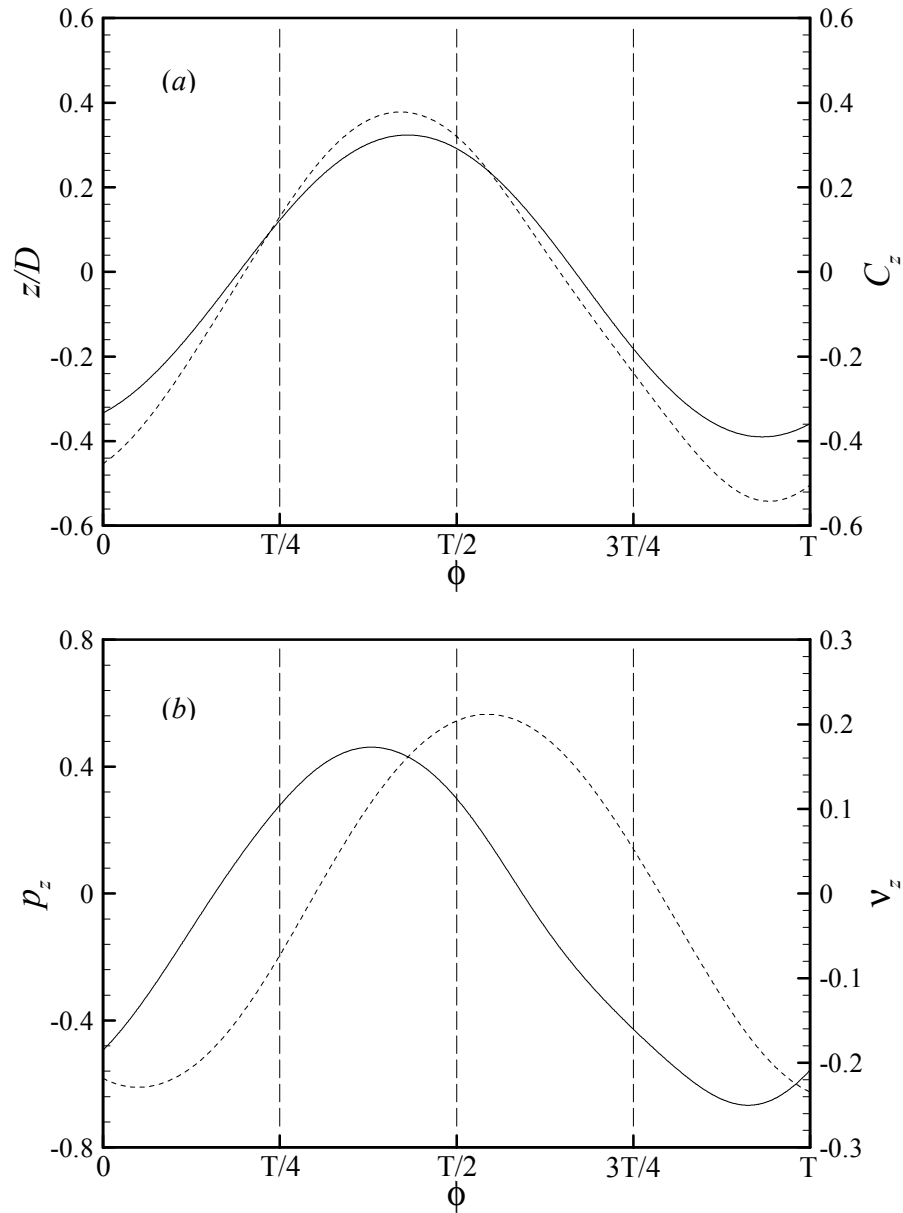


Figure 5.8.1. A typical oscillation cycle for $M^* = 0.8$, $L^* = 10$ at $U^* = 5$: (a) transverse displacement (solid line) and force (dashed line); (b) pressure (solid line) and viscous (dashed line) components of the transverse force.

Mode II response. We begin by examining the dynamics at the start of the synchronization regime, ie. $U^* = 5$.

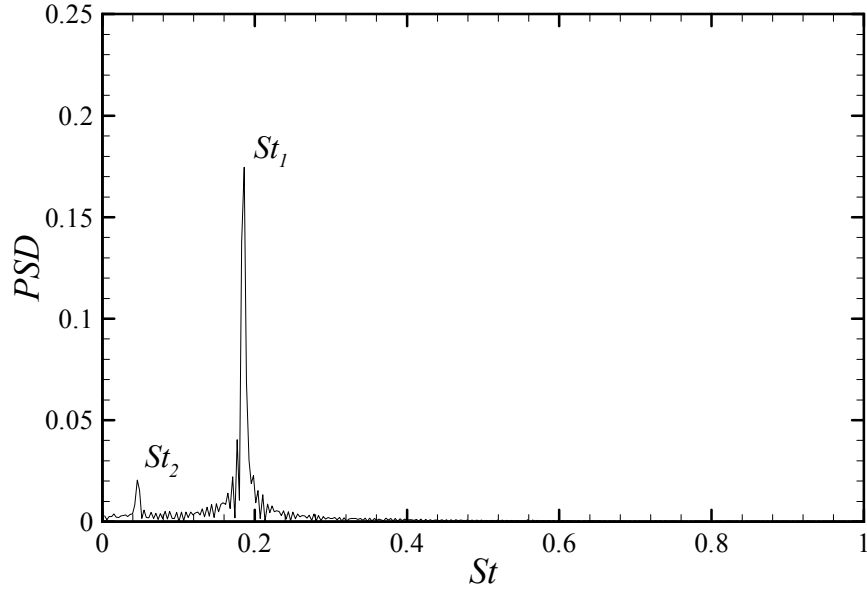


Figure 5.8.2. Dominant oscillation frequencies at $U^* = 5$ for $M^* = 0.8$, $L^* = 10$.

5.8.1 Sphere displacement and forces, $U^* = 5$

Figure 5.8.1 shows the transverse displacement and forcing over a typical cycle of oscillation for $U^* = 5$. Note that for this reduced velocity, there is a second, less dominant frequency that is 0.25 times the dominant frequency, as shown in Figure 5.8.2. As a result, the motion of the sphere is not purely sinusoidal, and so the oscillation cycle in Figure 5.8.1 is merely a best approximation. In part (a) of Figure 5.8.1, it is clear that the fluid forcing is *in phase* with the body oscillations. In other words, the maximum positive (negative) displacement occurs when the fluid forcing is maximum and positive (negative). As the fluid force increases, the sphere responds by displacing in the direction of the force. Similarly, as the fluid force decreases, the sphere responds by displacing in the opposite direction. At this particular value of reduced velocity, the amplitude of the oscillations is approximately $A/D = 0.35$, and the amplitude of the total transverse force is roughly $C_z' = 0.5$.

The pressure and viscous components of the total fluid transverse force are shown in Figure 5.8.1 (b). At this reduced velocity, it is evident that the pressure component of the fluid force leads the viscous component by approximately $\phi = T/8$. Furthermore, the maximum (in magnitude) pressure observed in the cycle is approximately $p_z = -0.64$, and this occurs when the sphere is displaced at its minimum position. On the other hand, the maximum viscous force observed is roughly $v_z = 0.24$. That is, the maximum pressure force is greater than the maximum viscous force by almost three times.

5.8.2 Pressure fields

The pressure contours over a cycle of oscillation for $U^* = 5$ are shown in Figure 5.8.3. At $\varphi = T/4$, the tethered sphere is being displaced towards the positive z -axis. On the upper surface of the sphere, there is an extremely strong region of negative pressure (shown by the dashed lines and the dark blue shaded areas) on the upper surface of the sphere. In contrast, on the lower surface of the sphere, there is a weak region of negative pressure. This large (and negative) pressure gradient between the upper and lower surfaces produces a suction effect that moves the sphere upwards. In addition, there is a local pressure minimum in the immediate near wake, which extends downstream in between two ovals of high pressure, as well as a local pressure minimum in the intermediate wake at approximately $x/D = 5$.

By $\varphi = T/2$, the sphere has reached its maximum position and is on its way back down. The previously strong negative pressure on the upper surface has diminished in size, and is now accompanied on the opposite surface by an equally strong pressure minimum. However, this new pressure minimum is slightly larger in size, resulting in a small negative pressure gradient that slowly pulls the sphere downwards, as is evident in the displacement plot shown in Figure 5.8.1. The region of low pressure in the near wake extends into a thin protrusion that terminates at a streamwise distance of $x/D = 2.5$, and is separated from the surrounding wake by a local pressure maximum at $x/D = 1.6$. Furthermore, the local pressure minimum that existed at $x/D = 5$ has now convected downstream to roughly $x/D = 6$.

At $\varphi = 3T/4$, it is clear that the pressure field is not 180° out of phase with the pressure field at $\varphi = T/4$. This is indicative of an oscillation cycle that may have more than one frequency, which is indeed the case as shown in Figure 5.8.2. Nevertheless, at this point in the cycle, the pressure minimum on the upper surface of the sphere has diminished greatly in size and magnitude. On the other hand, the pressure minimum on the lower surface has increased in magnitude, resulting in a strong negative pressure gradient that drives the sphere downwards. The magnitude of the gradient of this force is evident in Figure 5.8.1, which shows both the pressure force and the viscous force to have steep negative slopes. Furthermore, the protrusion of low pressure that extended to $x/D = 2.5$ at the previous time instant has now convected downstream to $x/D = 3.5$, and is seen to have separated from the surrounding low-pressure region. This finger of low pressure is encircled by three regions of high pressure, and the local pressure minimum previously located at $x/D = 6$ has convected to approximately $x/D = 7$.

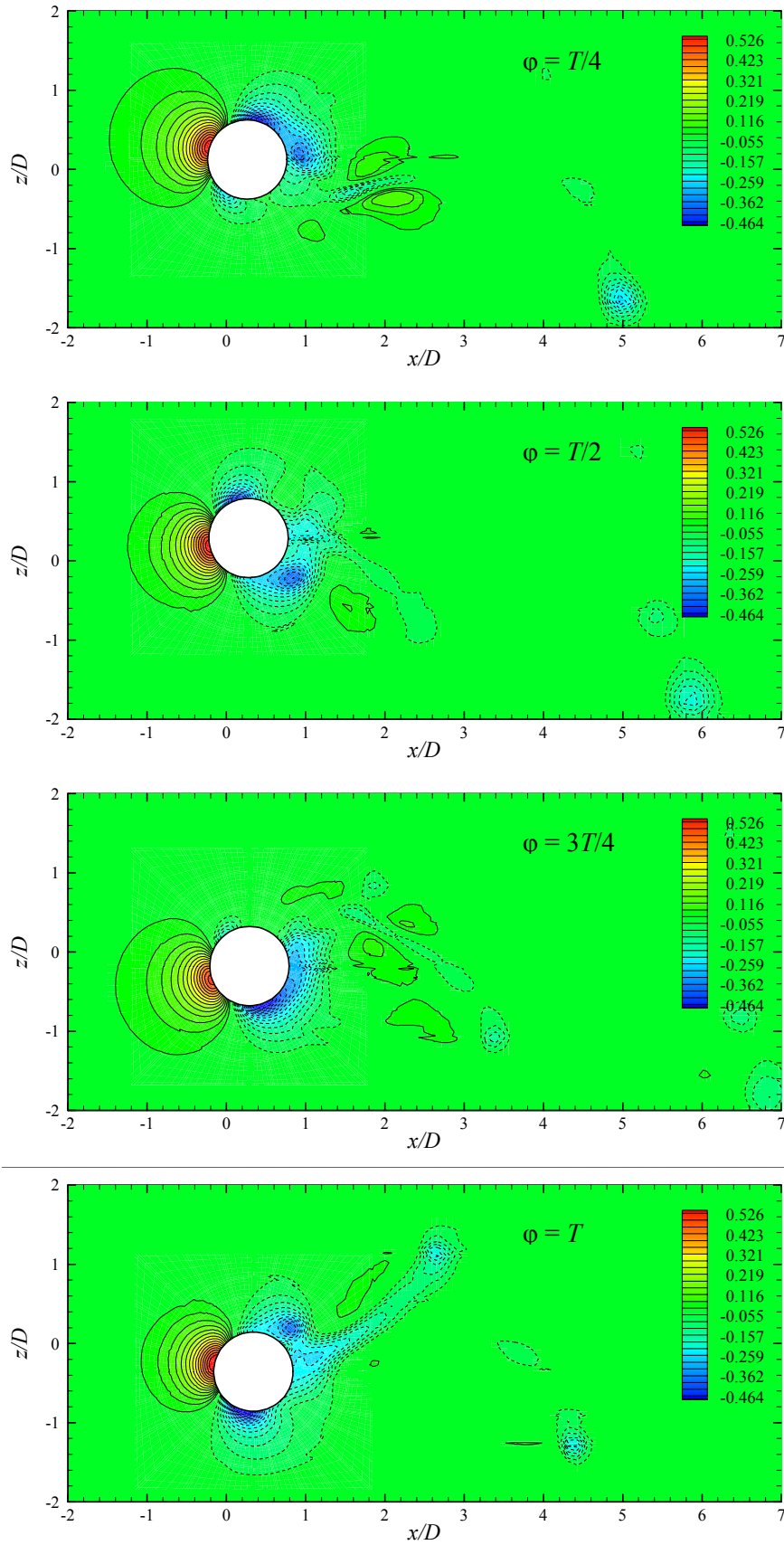


Figure 5.8.3. Pressure coefficient contours at $U^* = 5$ for $M^* = 0.8$, $L^* = 10$.

At the end of the cycle at $\varphi = T$, the sphere has reached its minimum position and is on its way upwards. This is evident in the pressure plots, which shows that there is a strong pressure minimum on the lower surface of the sphere. On the opposite side of the sphere, there is also a strong pressure minimum that extends along the surface from about $x/D = 0.2$ to the rear of the sphere. This extended region of low pressure above the x -axis is slightly greater than that below the axis, resulting in a slightly positive pressure gradient that slowly pulls the sphere upwards, analogous to the pressure field at $\varphi = T/4$. A relatively strong projection of low pressure extends from the rear of the sphere diagonally upwards to roughly $x/D = 3$. In addition, the oppositely oriented extension of low pressure that extended to $x/D = 3.5$ at the previous time instant has convected to $x/D = 4.5$, and the local pressure minimum that existed at $x/D = 7$ has now traveled out of the frame.

5.8.3 Visualization of vortex structures

As described in Chapter 3, visualizations of vorticity in the wake of a sphere do not adequately correspond to the vortex structures that are observed experimentally using dye visualization, for example. On the other hand, the Mode A and B vortex structures that are observed experimentally in the wake of a circular cylinder are satisfactorily visualized by plotting isosurfaces of streamwise vorticity. Thus, we choose not to examine the vorticity fields over a cycle of sphere oscillation, but instead examine the flow structures that should be observed experimentally by plotting isosurfaces of $-\lambda_2$, which was defined in Chapter 2.

These vortex structures are shown in Figure 5.8.4 in the x - z plane (a) and the x - y plane (b) respectively. A glance at the structures in the x - y plane shows that there exists a plane of symmetry that happens to be the x - z plane. Furthermore, although these plots represent the vortex structures at a Reynolds number of $Re = 500$, they look much more ordered than the stationary sphere vortex structures (see Chapter 3) observed at the same Reynolds number. Indeed, the vortices and the vortex shedding process (not to mention the presence of a plane of symmetry) look much more like the stationary sphere data at a Reynolds number of $Re = 300$.

At $\varphi = T/4$, the sphere is moving upwards and there is a vortical region in the immediate near wake that is angled diagonally downwards. Out of this vortical region extend the legs of a hairpin vortex, which showed up on the corresponding pressure plots as a thin, elongated region of low pressure. It is interesting to note that the head of this hairpin vortex does not appear to register very strongly as a pressure minimum. Also, there is an induced vortex that emanates from underneath the previous hairpin vortex. However, the head (and to some extent the legs) of this induced hairpin vortex does register as a local pressure minimum, which is located at $x/D = 5$ in the pressure plots. Further

downstream in the wake, the vortex loops that were shed in the previous cycle can be seen propagating downstream above and below the flow centreline.

A quarter of a cycle later, the vortical region emanating from the rear of the sphere has convected downstream. It is evident that this vortical region has developed into a hairpin vortex. The head and the legs of this vortex may be seen as a low-pressure region on the corresponding pressure contour plots. At this point in the cycle, the sphere has reached its uppermost position and is in the process of moving downwards. This is apparent in the isosurface of $-\lambda_2$ that envelops the front and lower surface of the sphere and not the upper surface, as was the case at the previous time instant. The previous hairpin vortex does not register anymore as a region of low pressure, but the induced hairpin does and is now located at $x/D = 6$ as it convects downstream.

By $\varphi = 3T/4$, the sphere is on its way to its minimum displacement. The legs and head of the hairpin vortex that was located within the vortical region surrounding the sphere have traveled downstream and still register as a pressure minimum. However, the base of the legs is not connected to the surrounding vortical region anymore and is seen to be cut off from this region by the local spots of high pressure that essentially push the vortex away from the sphere. At this same location there appears a new hairpin vortex, with the legs emanating from the rear of the sphere and the head clearly visible in Figure 5.8.4 (b). The previously shed hairpin vortex whose head was located at $x/D = 6$ can still be seen in the lower half of the figure, and is strong enough to register as a pressure minimum at a location of approximately $x/D = 7$.

In the final frame of the oscillation cycle, the sphere has reached its minimum displacement and is traveling slowly upwards. The separated vortical region at the rear of the sphere is obviously the head of a developing hairpin vortex. Above the head of this emergent vortex are the legs and head of the previously developing hairpin vortex. Both the legs and head of this vortex can be clearly seen in Figure 5.8.4 (b), and exposes very strongly as a pressure minimum in Figure 5.8.3. To the left of this vortex is a local region of high pressure that appears to push the vortex away from the sphere, effectively “shedding” it into the wake. In addition, the head of the shed vortex from the previous frame may be seen as a pressure minimum located at $x/D = 4.5$. The vortex loops and hairpin vortices are unmistakably distinguished in Figure 5.8.4 (b).

It is apparent from visualizations of the vortex structures in the wake at this reduced velocity that two vortices are shed for the oscillation cycle shown in Figure 5.8.1. It is also clear that the lower vortex is shed at the top of the oscillation cycle (ie. between $\varphi = T/4$ and $\varphi = T/2$) and the upper vortex is shed at the bottom of the oscillation cycle (ie. between $\varphi = 3T/4$ and $\varphi = T$). This is equivalent to the observation that the frequency of the drag coefficient is *twice* the frequency of the transverse force coefficient, which is indeed the case as shown in Figure 5.4.6.

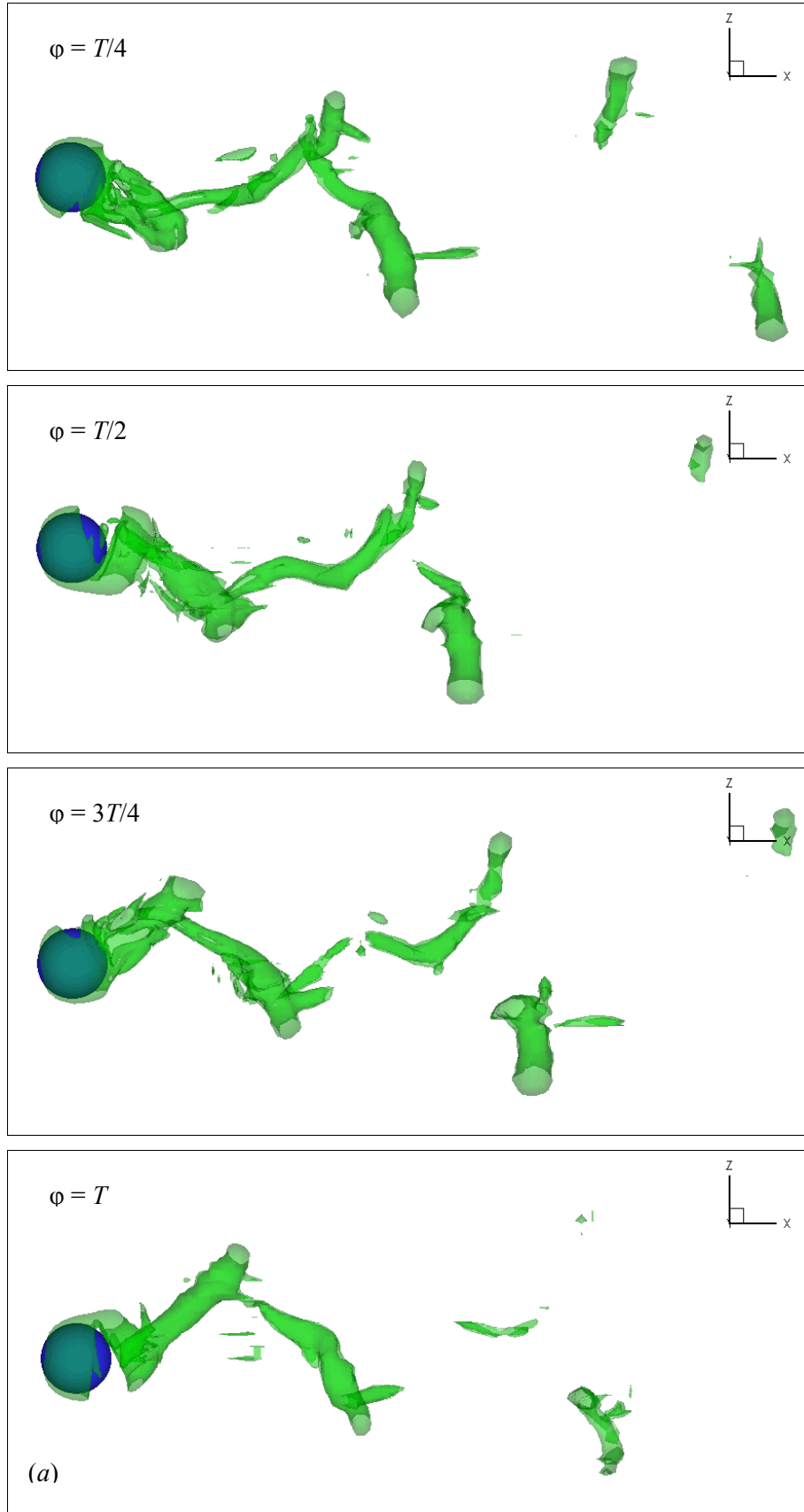


Figure 5.8.4. Visualization of vortex structures (plotted using an isosurface of $-\lambda_2$) at $U^* = 5$ for $M^* = 0.8$, $L^* = 10$: (a) x - z plane; (b) x - y plane.

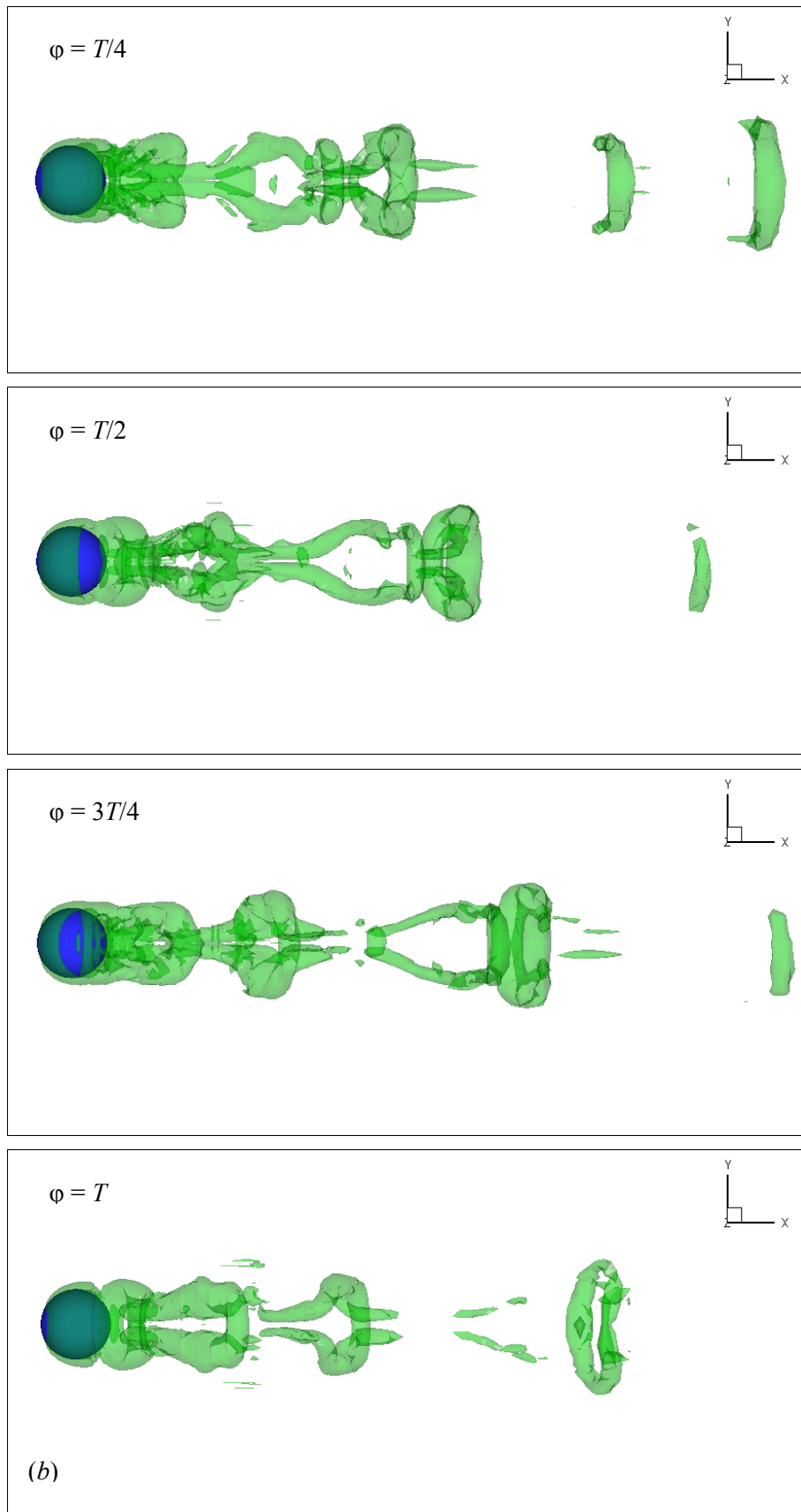


Figure 5.8.4. Continued.

5.8.4 Sphere displacement and forces, $U^* = 10$

When the reduced velocity is increased to $U^* = 10$, the resultant motion of the body with respect to the forces acting on it are shown in Figure 5.8.5. Once again, as with the previous reduced velocity investigated, it is clear that the body motion and the fluid forcing are in phase. However, this time the oscillations are sinusoidal with a single dominant frequency, as shown in the power spectral density plot in Figure 5.8.6. Furthermore, the sphere oscillations remain at roughly the same amplitude as those observed for the $U^* = 5$ case.

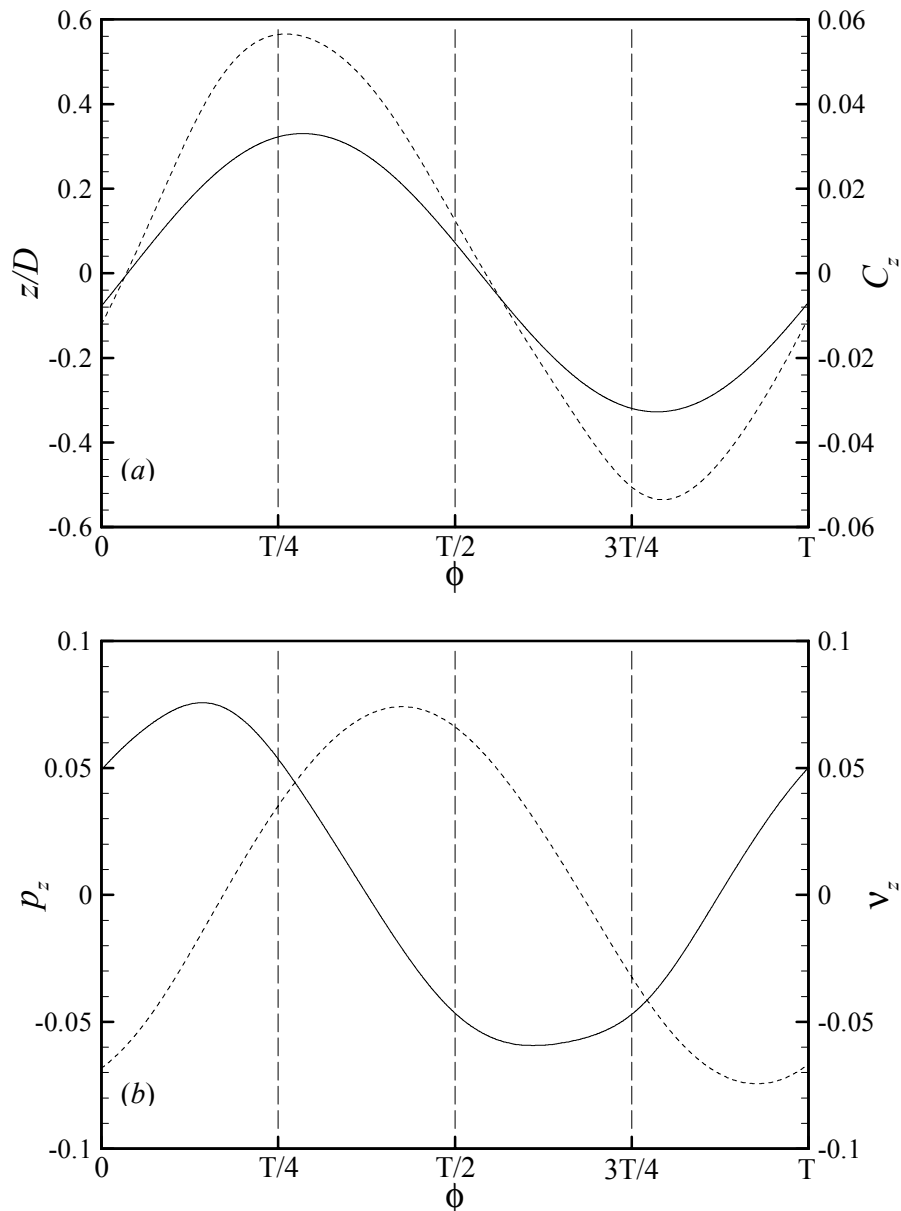


Figure 5.8.5. A typical oscillation cycle for $M^* = 0.8$, $L^* = 10$ at $U^* = 10$: (a) transverse displacement (solid line) and force (dashed line); (b) pressure (solid line) and viscous (dashed line) components of the transverse force.

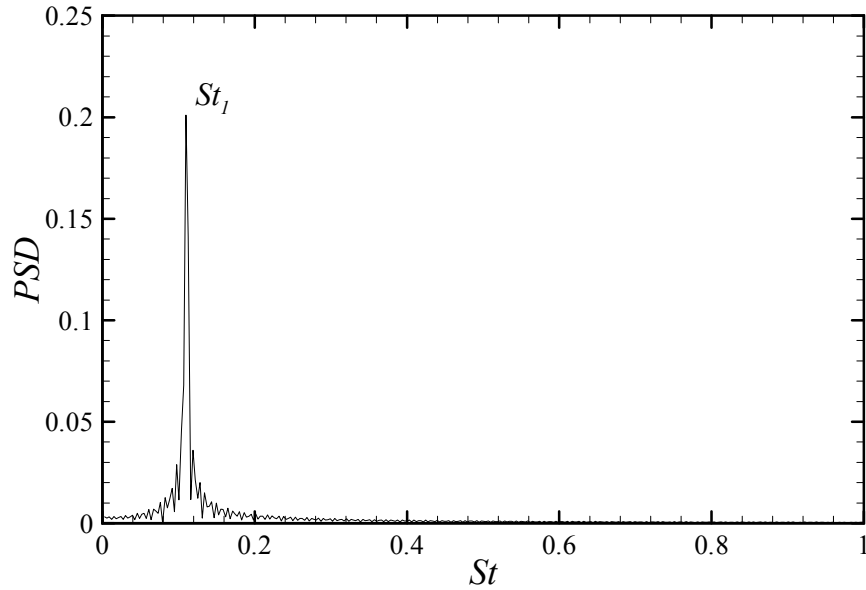


Figure 5.8.6. Dominant oscillation frequencies at $U^* = 10$ for $M^* = 0.8$, $L^* = 10$.

On the other hand, quite surprisingly, the total fluid force in the transverse direction has decreased almost an order of magnitude.

Figure 5.8.5 (b) shows the components of the fluid forces over the same cycle of sphere oscillation. At this reduced velocity, which is at the end of the Mode II synchronization regime, the lag of the viscous component with respect to the pressure component of the total fluid transverse force has increased to approximately $\phi = T/4$. In addition, because the total fluid force has decreased by almost an order of magnitude, the corresponding pressure and viscous components have decreased by roughly 8 times and 3 times respectively, and both the pressure and viscous contributions to the total fluid force are of the same order. It is somewhat surprising to note that although the fluid forcing has decreased by almost an order of magnitude, large-amplitude vibrations still occur.

5.8.5 Pressure fields

The pressure contours over a cycle of sphere oscillation for $U^* = 10$ are shown in Figure 5.8.7. A quick comparison with Figure 5.8.3 shows that the downstream extent of the region of low pressure in the near wake has increased at this higher reduced velocity, which lies near the end of the Mode II synchronization regime. At $\phi = T/4$, the sphere has almost reached the top of its oscillation cycle. Accordingly, at this point, the fluid forcing is a maximum because the pressure component is positive (although decreasing) and the viscous component is positive and increasing. The pressure

minimum on the upper surface of the sphere is stronger than that on the lower surface, providing a suction effect that results in a strong positive pressure. At the rear of this low-pressure region that envelops the base of the sphere, there exists a protruding arm of low pressure that terminates at $x/D = 4$. In addition, this arm is flanked on both sides by small elliptical regions of high pressure.

At $\varphi = T/2$, the sphere has almost reached its equilibrium position. The low-pressure regions on the upper surface has diminished in size and magnitude, and is overpowered by the much stronger negative-pressure on the lower surface of the sphere. This strong negative pressure gradient pulls the sphere downwards. However, at this instant the pressure and viscous components of the transverse force are almost the exact opposite, producing a net force that is not quite zero. Nevertheless, the pressure component is strong and negative and the viscous component is positive but decreasing, resulting in a total force that is steadily decreasing. There also exists a small oval of low pressure in the lower half of the near wake at roughly $x/D = 1.8$. The previous arm of low pressure in the wake appears to have been pushed downstream by the two ovals of high pressure that bordered it. This low-pressure arm is seen to have convected now to $x/D = 5.5$.

By $\varphi = 3T/4$, the sphere is approaching its minimum displacement. The most noticeable feature of the pressure plots at this point in the oscillation cycle is that the pressure contours are completely symmetric about the x - y plane with respect to the contours a half a cycle earlier, ie. at $\varphi = T/4$. This is not surprising considering that the oscillations are sinusoidal with a single dominant frequency, as seen in Figure 5.8.6. Because the sphere is near its minimum location, the pressure component is strongly negative (but increasing) and the viscous component is also strongly negative (and decreasing), resulting in a total fluid force that is strongly negative and almost a minimum. The small oval of low pressure that was previously in the lower half of the wake at $x/D = 1.8$ has shifted across to the upper half of the wake to $x/D = 1.6$, and is helping the pressure minimum on the upper surface of the sphere to pull the sphere up. Furthermore, there is a new arm of low pressure that extends diagonally upwards to $x/D = 4$, again bordered by two elliptical regions of high pressure.

At the end of the oscillation cycle, the small oval of low pressure that was previously at $x/D = 1.6$ has drifted down slightly because of the accelerated flow over the upper surface of the sphere and the fact that the sphere is moving upwards. At this instant, the total fluid force is almost zero, and the relative contributions of the pressure and viscous components are positive and negative respectively, both of which are increasing. The previous arm of low pressure that extended to $x/D = 4$ has now been pushed away from the sphere and into the wake to $x/D = 5.5$ by the two elliptical regions of high pressure that are now located behind the sphere. Once more, the pressure contours at this phase in the cycle are symmetric about the x - y plane with respect to the contours at $\varphi = T/2$. In addition, as with the previous locations in the cycle, the strong negative pressure gradient that exists between the upper and lower surfaces of the sphere acts to pull the sphere upwards.

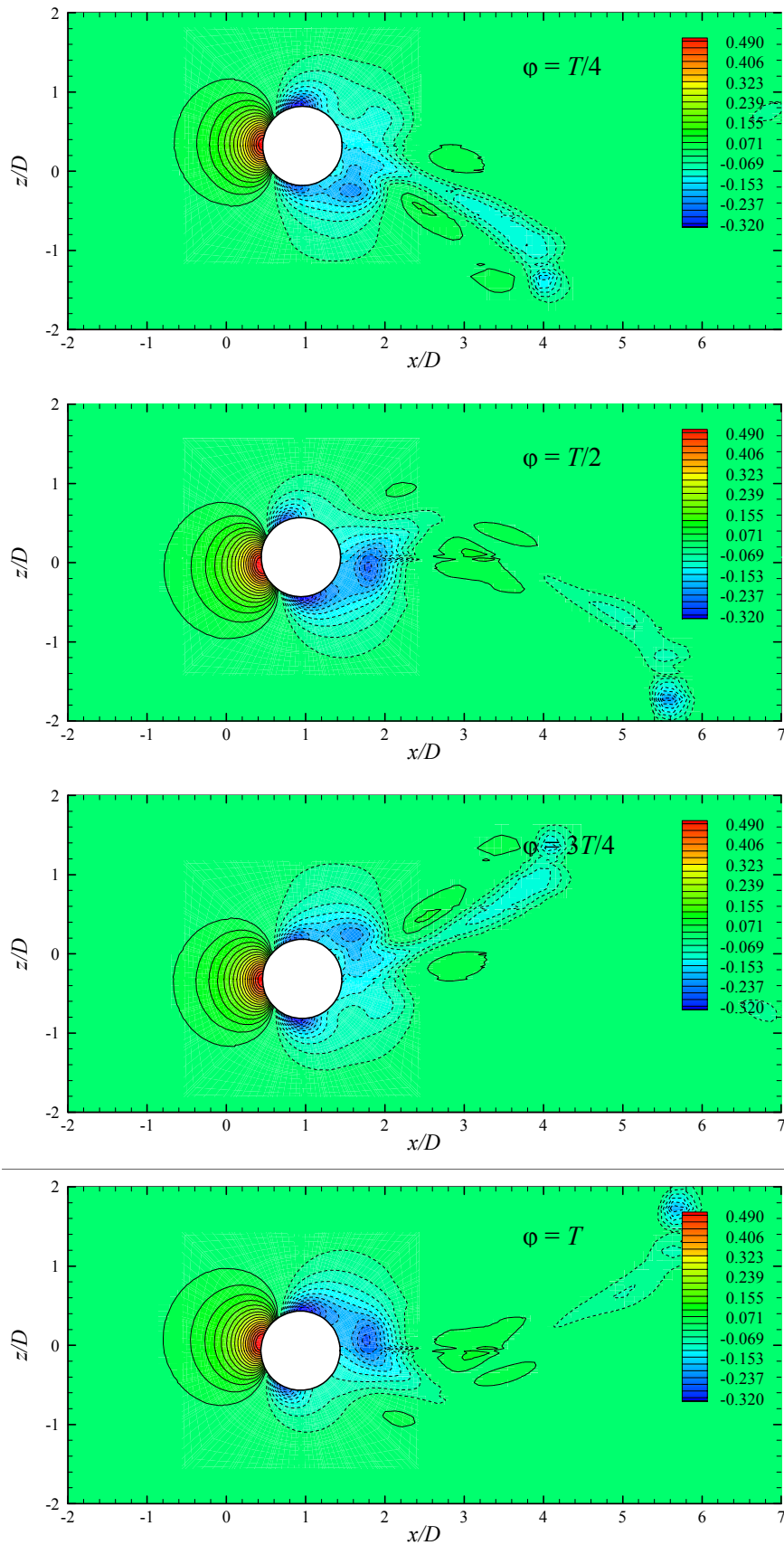


Figure 5.8.7. Pressure coefficient contours at $U^* = 10$ for $M^* = 0.8$, $L^* = 10$.

5.8.6 Visualization of vortex structures

As with the previous reduced velocity, we now show visualizations of the vortex structures in the wake of the tethered sphere at $U^* = 10$, again by plotting isosurfaces of $-\lambda_2$. These plots are shown in Figure 5.8.8 (a) in the x - z plane and Figure 5.8.8 (b) in the x - y plane respectively. Again, as with the results at $U^* = 5$, the vortex structures are symmetrical about the x - z plane, even though the Reynolds number is $Re = 500$ which, for a stationary sphere, does not exhibit a plane of symmetry. In addition, comparisons between Figures 5.8.8 (b) and 5.8.4 (b) show that at the higher reduced velocity investigated, the vortex structures appear more unambiguous and ordered. This is not very surprising considering the fact that the observed motions near the end of the Mode II synchronization regime are more harmonic than the oscillations at the start of the regime. Furthermore, the spacing between the vortices indicate that the vortex formation length has increased as the reduced velocity increases from $U^* = 5$ to $U^* = 10$, although the Reynolds number is fixed at $Re = 500$.

At $\varphi = T/4$, the sphere is nearing its maximum displacement. There exists a vortical region that envelops the entire surface of the sphere except the upper rear exterior. The large vortical region immediately behind the sphere appears to be the developing head of a hairpin vortex. In the vicinity of this vortex are the legs of another hairpin vortex. The legs and head of this vortex extend diagonally downwards all the way to $x/D = 4$, and register on the pressure contours in Figure 5.8.7 as an elongated arm of low pressure. Beyond this fully developed vortex is another hairpin vortex that was shed in the previous cycle, and whose head and legs are clearly visible in Figure 5.8.8 (b). The small oval region of low pressure at $x/D = 1.6$ marks the beginning of the legs of the hairpin vortex, and the soon-to-be-developed head of the next hairpin vortex.

A quarter of a cycle later, the hairpin vortex that emerged out of the vortical region surrounding the sphere has been shed into the wake. This is clearly seen in the pressure plots, which shows that the elliptical regions of high pressure have pushed the vortex away from the sphere and into the wake, thereby disconnecting it from the surrounding vortical region. The head of this vortex has traveled to $x/D = 5.5$ and still registers strongly as a concentrated region of low pressure. The head of the previously developing hairpin vortex has convected downstream to approximately $x/D = 2.5$, and the base of the legs of this vortex register as a strong local pressure minimum in Figure 5.8.7. In addition, the vortical region on the lower surface of the sphere appears to highlight the emergence of a new hairpin vortex.

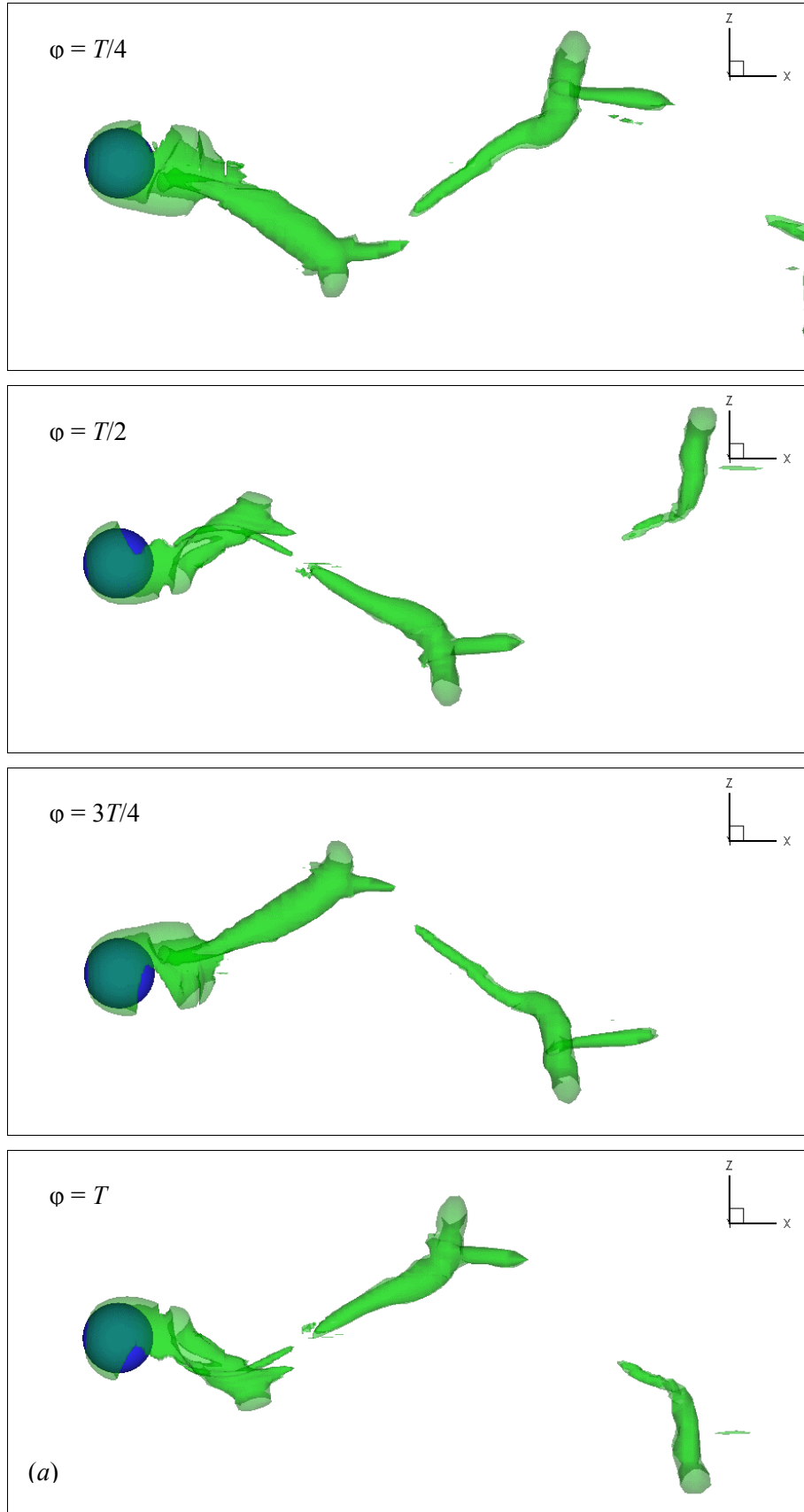


Figure 5.8.8. Visualization of vortex structures (plotted using an isosurface of $-\lambda_2$) at $U^* = 10$ for $M^* = 0.8$, $L^* = 10$: (a) x - z plane; (b) x - y plane.

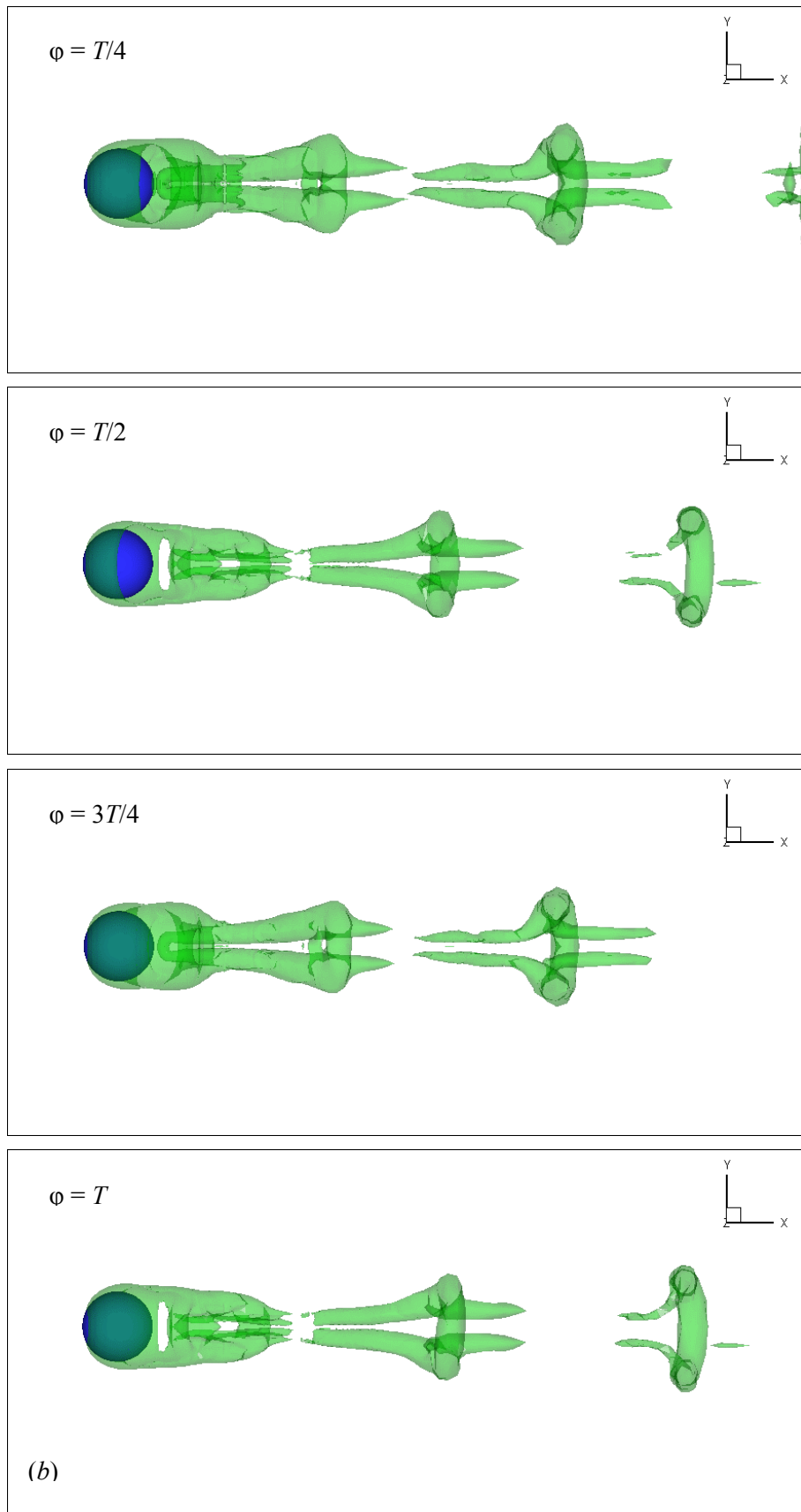


Figure 5.8.8. Continued.

At $\varphi = 3T/4$, the head of a new vortex appears and is separated from the rear of the sphere by about $0.5D$. At this time instant, the pressure minimum previously located at the base of the legs of the hairpin vortex that was developing has now shifted to the upper half of the wake, as the sphere moves down to its minimum displacement and the vortex convects downstream. The head and legs of this vortex can clearly be seen in the pressure plots, denoted as an arm of low pressure that protrudes from the low-pressure region at the rear of the sphere and extends diagonally upwards to roughly $x/D = 4$. The previously shed vortex that was cut off from the surrounding vortical region can be seen traveling downstream, and the legs and head are noticeably discernible in the x - y plane as shown in Figure 5.8.8 (b). Along with the pressure contours, the vortex structures are clearly symmetrical between $\varphi = T/4$ and the present frame at $\varphi = 3T/4$.

At the end of the oscillation cycle, at $\varphi = T$ the sphere is approaching its equilibrium position of $z/D = 0$. The vortex in the near wake that registered as a strong pressure minimum has been shed into the wake. This is clear from both the isosurfaces of $-\lambda_2$ and from the pressure contours, which show the vortex being pushed out to $x/D = 5.5$ by the localized regions of high pressure that essentially pinch the base of the legs off from the surrounding vortical region. The head of the developing vortex has convected from $x/D = 2$ to about $x/D = 3$. Even in the far wake, the vortex structures can clearly be seen, even though they are convecting away from the flow centreline (where the computational resolution is not as good as it could be) as the sphere completes its oscillation cycle.

As with the vortex structures observed at the start of the Mode II regime, at the present reduced velocity of $U^* = 10$ it is evident from Figure 5.8.8 that two vortices are shed per oscillation cycle, one at the top of the cycle and one at the bottom of the cycle. The major differences between the two reduced velocities are the single-frequency nature of the oscillations at the higher reduced velocity, as well as the increased formation length. This increase in formation length is equivalent to an increase in the period of oscillation, or more importantly a decrease in the vortex shedding frequency.

5.8.7 Dynamics of the Mode II response

From the previous subsections, it is clear that the Mode II response is kicked off by the large transverse fluid forcing that causes the sphere to oscillate vigorously with large amplitudes. For the stationary sphere at a Reynolds number of $Re = 500$, this fluid forcing (in both the transverse and streamwise directions) is of the order of 0.1. On the other hand, for the tethered sphere we see from Figures 5.3.4 and 5.4.4 that the transverse fluid forcing at the start of the Mode II regime jumps up to roughly $C_z' = 0.35$. However, as the reduced velocity is increased within this regime, the fluid

forcing dies down substantially to values smaller than those observed for the stationary sphere. Evidently, this decrease in the fluid forcing does not sustain the large-amplitude vibrations.

We have also seen from visualizations of the vortex structures in the wake near the start and close to the end of the Mode II regime that two vortices are shed for each cycle of oscillation, resulting in a drag force that has twice the frequency of the transverse force. In addition, the normalized oscillation frequency increases from $f^* = 0.93$ to $f^* = 1.10$ as the reduced velocity increases from $U^* = 5$ to $U^* = 10$. Although the oscillation frequency increases, the number of vortices shed per cycle stays the same, so that the normalized frequency of vortex shedding also increases from $f^* = 0.93$ to $f^* = 1.10$. It appears then that the large-amplitude vibrations that occur at the onset of the Mode II regime are due to the vortex shedding frequency being close to the natural frequency of vibration, a classical “lock-in” effect that was described in Chapter 1 for both the tethered sphere at high Reynolds numbers and for the vortex-induced vibrations of circular cylinders.

However, as the reduced velocity is increased within this regime, the large-amplitude oscillations modulate the vortex shedding from the sphere such that the vortex shedding frequency remains the same as the oscillation frequency. This modulation between the vortex shedding frequency and the oscillation frequency guarantees that self-excited motion ensues and remains until the end of the synchronization regime, after which the oscillation amplitude decreases and the frequency of the drag force is no longer twice the frequency of the transverse force.

5.9 Mode III response

The Mode III response discovered by Jauvtis *et al.* (2001) was observed for mass ratios of $M^* = 28$ and above. Because of this high mass ratio, the oscillations were always at the natural frequency, which was quite high, and it was assumed that the vortex formation frequency was the same as that of a stationary sphere. As a result, the oscillation frequency was assumed to be much greater than the vortex shedding frequency, so what was the cause of these vibrations?

In the present case, the oscillation frequency in this Mode III regime is not the same as the natural frequency, as shown in Figure 5.5.3, because of the much lower mass ratios investigated. In light of this, we expect the oscillation frequency of the sphere to be close to the vortex shedding frequency, since the Mode II results presented in the previous section showed that the oscillations modulate the vortex shedding frequency such that both frequencies remain “locked” within the regime.

To investigate the dynamics of the tethered sphere in this Mode III regime, we choose the same geometric parameters of $M^* = 0.8$ and $L^* = 10$, and a reduced velocity of $U^* = 24$, which lies close to the middle of the synchronization regime as depicted in Figure 5.5.3. As with the Mode II

response, we analyze the pressure fields and the vortex structures observed in the wake in order to develop a consistent mechanism of vibration.

Note that at this reduced velocity, the oscillations (especially in the streamwise and lateral directions) are not entirely sinusoidal, and the transverse oscillations are not symmetric about the flow centreline. In other words, the transverse oscillations migrate away from the axis and then approach the axis again after a few hundred time units, and this process appears to continue indefinitely. Accordingly, for the purpose of presenting the results in a coherent manner, the entire flow field (including the pressure contours to be presented shortly) has been shifted so that the oscillations appear to be balanced about the flow centreline.

5.9.1 Sphere displacement and forces

The transverse displacement of the sphere and the forces acting on it are shown in Figure 5.9.1 over one cycle of sphere oscillation. It is immediately obvious from Figure 5.9.1 (a) that the transverse displacement and corresponding force are *out of phase*, in contrast to the Mode II response in which the displacement and forcing were *in phase*. In the Mode III regime, it is clear that the maximum (minimum) displacement of the sphere occurs when the fluid forcing is a minimum (maximum). Furthermore, the amplitudes of oscillation within this regime are smaller than those observed in the Mode II regime, and the amplitude of the total fluctuating fluid forcing in the transverse direction has decreased slightly from the end of the Mode II synchronization regime.

The pressure and viscous components of the total transverse fluid force are depicted in Figure 5.9.1 (b) for this reduced velocity of $U^* = 24$. Comparisons with Figures 5.8.1 and 5.8.5 illustrate that the magnitude of the pressure has not changed much since the end of the Mode II regime, but the magnitudes of the viscous stresses have decreased almost 5 times. The pressure component of the total transverse fluid force thus dominates the viscous component and would be expected to contribute considerably more to the dynamics of the sphere. Evidence of this is seen in the almost zero phase difference between the total fluid force and the pressure component. In addition, the phase between the pressure and viscous forces has increased marginally to roughly $\phi = T/3$.

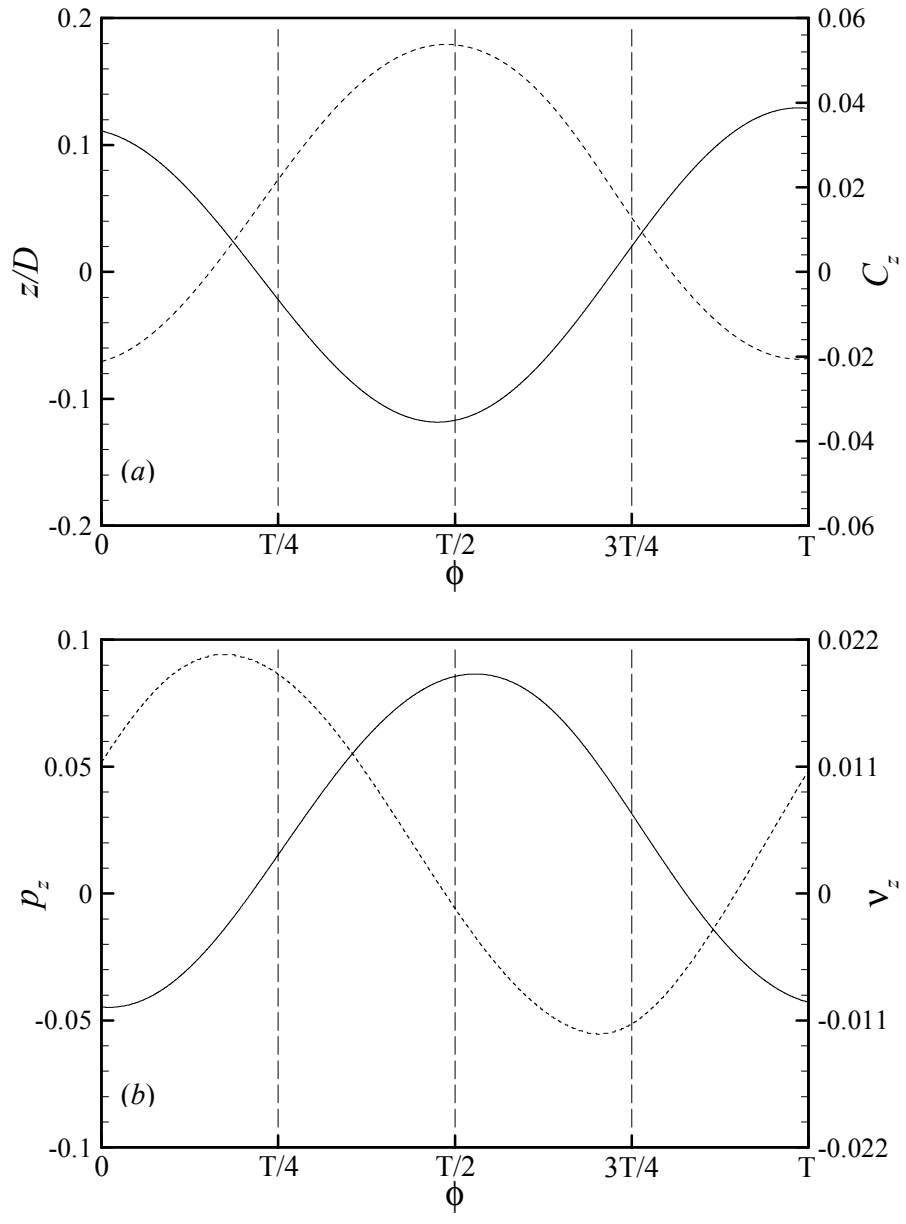


Figure 5.9.1. A typical oscillation cycle for $M^* = 0.8$, $L^* = 10$ at $U^* = 24$: (a) transverse displacement (solid line) and force (dashed line); (b) pressure (solid line) and viscous (dashed line) components of the transverse force.

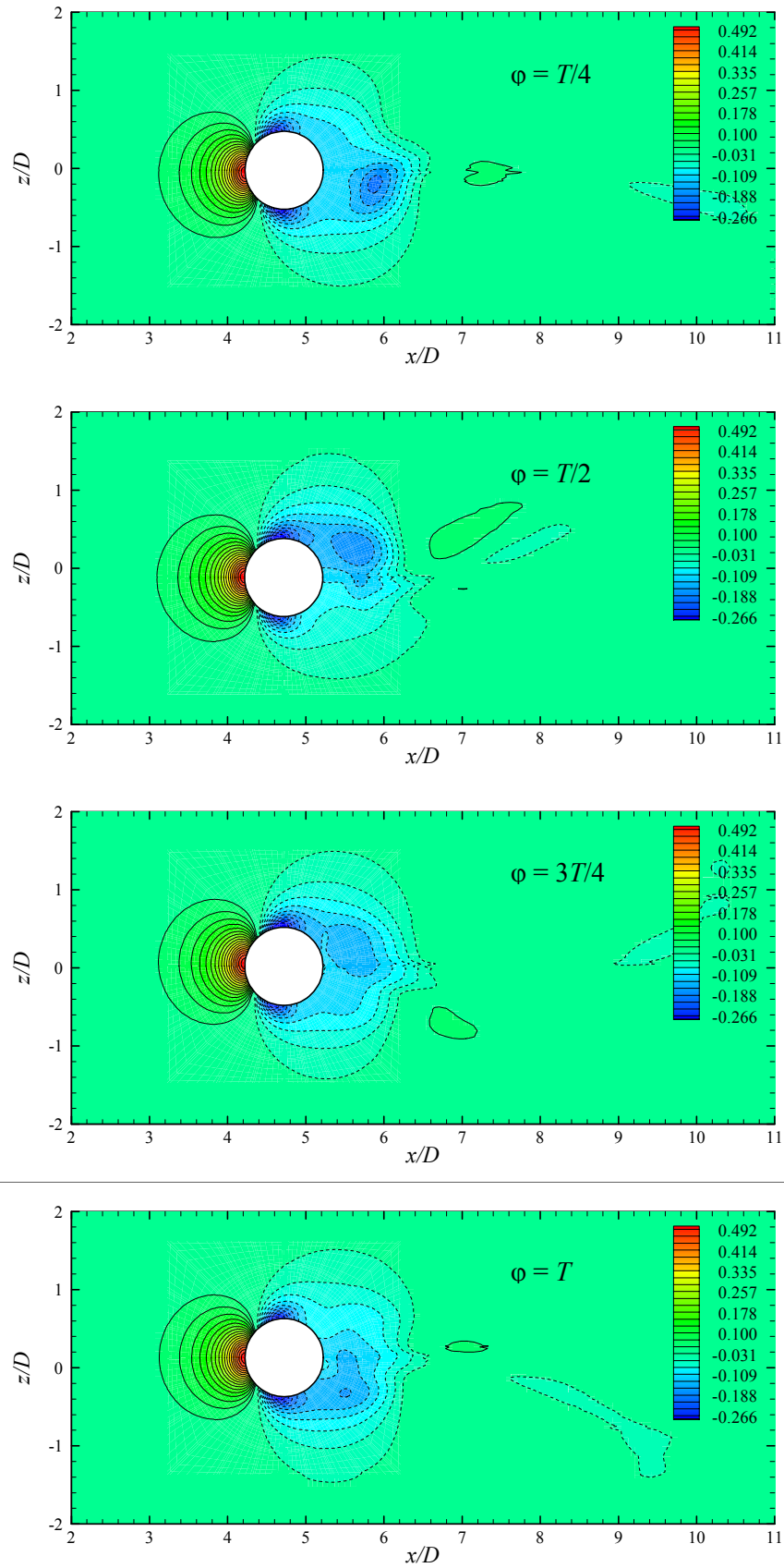


Figure 5.9.2. Pressure coefficient contours at $U^* = 24$ for $M^* = 0.8$, $L^* = 10$.

5.9.2 Pressure fields

The pressure contours for this cycle of sphere oscillation in the Mode III regime are shown in Figure 5.9.2. At $\phi = T/4$, the sphere has passed through its equilibrium position and is being displaced towards its minimum position, although the forcing is positive and increasing. The pressure field on the surface of the sphere is almost symmetric, owing to the close proximity of the sphere to its mean position at this time instant. Furthermore, in the lower half of the plane at approximately $x/D = 5.5$, there exists a strong local pressure minimum in the near wake.

A quarter of a cycle later, at $\phi = T/2$, the sphere has reached its minimum position and is slowly on its way upwards. Accordingly, the fluid forcing in the transverse direction has reached a maximum. At this point in the cycle, the pressure field on the surface of the sphere is no longer balanced, and the pressure on the entire upper surface is much lower than that on the lower surface. The result is a large pressure gradient that acts towards the positive z -axis, effectively providing a suction effect that pulls the sphere upwards. In contrast to the previous frame, the pressure minimum that existed in the lower half of the plane is no more and is replaced by an almost equally strong pressure minimum in the upper half of the plane, located at a streamwise distance of $x/D = 5.6$. There is also a local region of high pressure at the same transverse location as the local pressure minimum but outside the immediate near wake at a location of roughly $x/D = 7$. This high pressure region trails a localized oval region of low pressure fluid that is convecting downstream.

More than halfway through the cycle, it is apparent that the sphere has passed its equilibrium position en route to its maximum displacement. The pressure field at this instant of $\phi = 3T/4$ is clearly not symmetric with respect to the pressure contours half a cycle earlier, as shown in Figure 5.9.2. This is indicative of an oscillation cycle that is not sinusoidal, similar to the Mode II response at $U^* = 5$ discussed in the previous section. Here, there still exists a strong pressure minimum on the upper surface of the sphere that is larger in magnitude and surface area than the pressure minimum on the lower surface, although the difference is not as large as in the previous frame. Evidently, although the fluid forcing is decreasing in the transverse direction, it is still positive and pulls the sphere upwards. Furthermore, the local pressure minimum that existed at $x/D = 5.6$ has decreased in magnitude, and the disconnected oval region of low pressure that subsisted at $x/D = 8$ has now convected to $x/D = 9.5$. The high-pressure region that appeared to push the aforementioned pressure minimum downstream has now relocated to $x/D = 7$ in the lower half of the wake.

In the final frame of the oscillation cycle, the sphere has reached its maximum displacement, despite the fact that the transverse forcing was decreasing on its way upward. Between $\phi = 3T/4$ and $\phi = T$, we see that the fluid forcing becomes negative and as it does the upward momentum of the sphere diminishes, eventually reaching zero at the top of the cycle when the fluid forcing is a minimum.

Beyond this time instant, the fluid forcing is a minimum and begins to increase again, thereby pulling the sphere downwards. This is clearly seen in the pressure plots in Figure 5.9.2, which shows a large region of low pressure enveloping the entire lower surface of the sphere. This pressure minimum is now much greater than that on the upper surface, causing a large pressure gradient that acts towards the negative z -axis and is responsible for driving the sphere downwards. A local pressure minimum exists in the near wake at $x/D = 5.5$, analogous to the pressure minimum that existed a half cycle earlier in the opposite half of the x - z plane. Furthermore, there exists a localized extension of low pressure in the wake that terminates at approximately $x/D = 9.5$. As we shall see shortly, this pressure minimum represents the head and legs of a shed hairpin vortex that is convecting downstream.

5.9.3 Visualization of vortex structures

Visualizations of the vortex structures in this Mode III regime in the x - z and x - y planes are shown in Figure 5.9.3 (a) and (b) respectively. As in the previous sections, the vortex structures are visualized by plotting an isosurface of $-\lambda_2$, which indicates a region of low pressure where the rate-of-rotation is more dominant than the rate-of-strain, as described in Chapter 2. Furthermore, we choose to plot isosurfaces of $-\lambda_2$ as opposed to contours of streamwise vorticity because in the wake of a sphere, the vortex structures observed experimentally using dye visualization techniques are not highlighted very well by contours of streamwise vorticity, as shown in Chapter 3.

Near the end of the Mode II regime, at $U^* = 10$, it was shown that the vortex formation length increases compared to the start of the regime at $U^* = 5$. Similar behaviour is observed at the present reduced velocity of $U^* = 24$. Comparing Figures 5.9.3 and 5.8.8 reveals that the vortex formation length has increased substantially, despite the fact that the Reynolds number is the same for all of the simulations. Evidently, as expected the response of the sphere depends strongly on the Froude number (rather than the Reynolds number), although whether the flow is laminar or turbulent also affects the nature of the observed response modes.

Returning to Figure 5.9.3, we see that at $\varphi = T/4$ there is a developing hairpin vortex emerging from the vortical region at the rear of the sphere as the sphere moves downwards. The legs of this vortex are clearly visible, although the head has not formed yet. Beyond this budding vortex is a fully developed hairpin vortex that extends roughly 6 diameters downstream from the rear of the sphere. The head and legs of this vortex are plainly discernible in the x - y view of these vortex structures, and the legs can even be seen extending well into the vortical region surrounding the sphere.

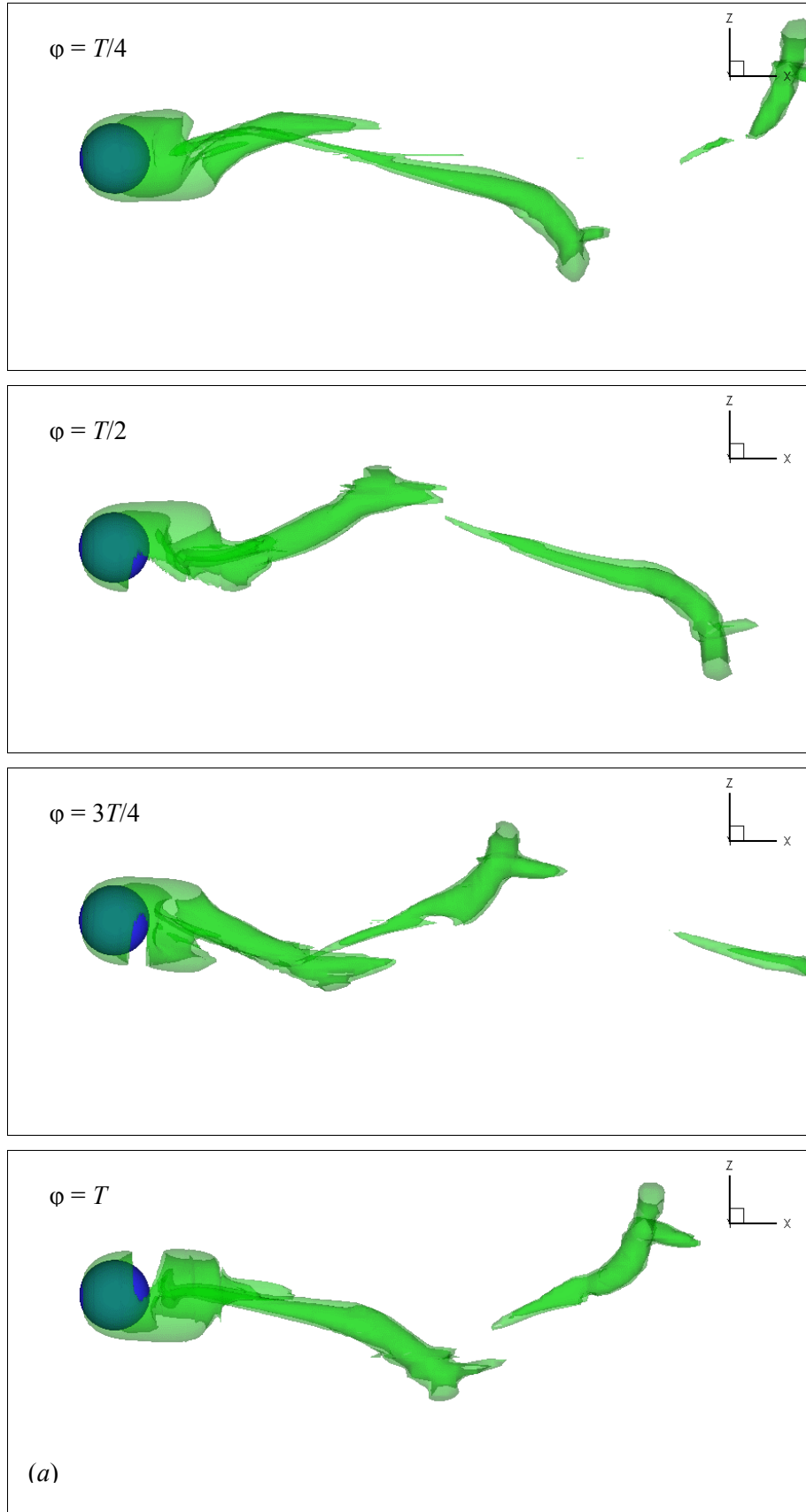


Figure 5.9.3. Visualization of vortex structures (plotted using an isosurface of $-\lambda_2$) at $U^* = 24$ for $M^* = 0.8, L^* = 10$: (a) x - z plane; (b) x - y plane.

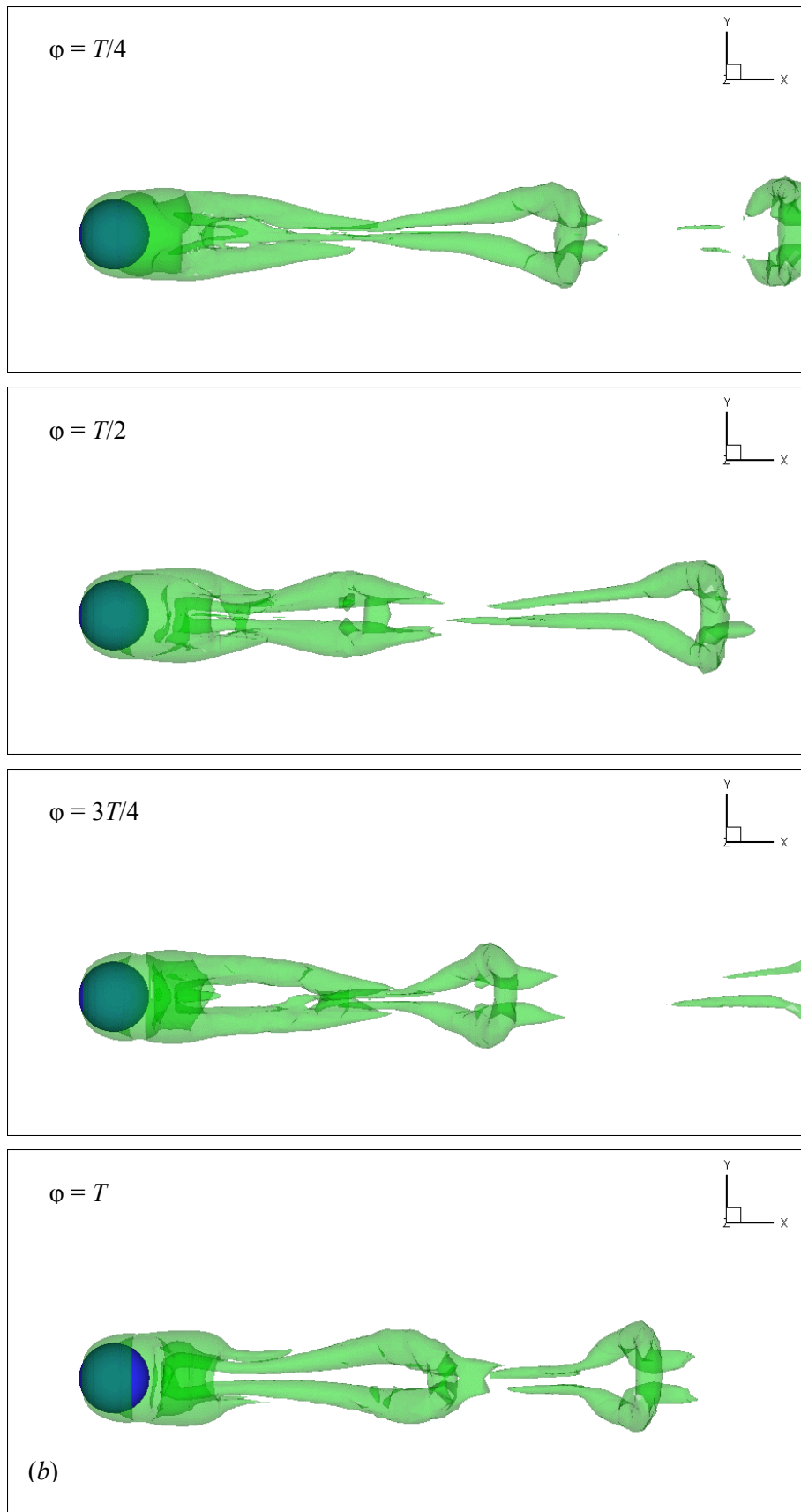


Figure 5.9.3. Continued.

By $\varphi = T/2$, the sphere has reached its minimum position and is slowly on its way upwards. The vortex that previously extended approximately 6 diameters downstream has now shed into the wake, since its legs are no longer connected to the vortical region surrounding the sphere. Furthermore, the vortex that was developing in the near wake has now formed a head, and the legs that were previously separated are now connected via this head. Note that the legs of this hairpin vortex register as a pressure minimum in Figure 5.9.2. The high-pressure region situated between this hairpin vortex and the sphere pushes the vortex away from the sphere and into the wake. The strong local region of low pressure at $x/D = 5.6$ highlights the core of the vortical region out of which the hairpin vortices develop. In addition, the magnitude of the region of low pressure above the surface of the sphere and 1 diameter downstream, as well as the small low-pressure region on the lower-front surface of the sphere, register strongly as a vortical region in Figure 5.9.3 (a).

A quarter of a cycle later, at $\varphi = 3T/4$ the sphere has passed through its equilibrium position and is on its way to the top of its motion. The previously developing hairpin vortex has now fully formed, and its head and legs can clearly be seen in the x - y plane. Both the head and the legs of this vortex, which is located at about $x/D = 10$, still register as a pressure minimum in Figure 5.9.2, and the high-pressure region that shed the vortex into the wake has moved to the opposite side of the flow centreline as the sphere moves upwards. The extended region of low pressure above and downstream of the sphere surface (and to some extent on the lower-front surface of the sphere) has decreased in magnitude, but still registers strongly as a vortical region. Furthermore, the legs of a hairpin vortex have emerged from the vortical region surrounding the sphere, but no head is yet apparent. The downstream extent of these legs terminate near the legs of the previously shed hairpin vortex.

In the final frame of the oscillation cycle, at $\varphi = T$ the sphere has reached its uppermost displacement. The vast region of low pressure that existed on the upper surface of the sphere has switched to the lower surface, and the corresponding smaller low-pressure region on the lower surface has switched to the upper surface. This is indicative of the sphere being displaced to its maximum position, and is on the journey downwards. This low-pressure region registers strongly as a vortical region that envelops the entire lower surface of the sphere and two-thirds of the upper surface, in accordance with the pressure contours shown in Figure 5.9.2. A well-developed hairpin vortex can be seen in Figure 5.9.3 (b) that extends roughly 5 diameters downstream of the rear of the sphere. This vortex has now formed a head from near the base of the legs of the previously shed vortex. Once again, both the legs and the head of this vortex reveal themselves as a pressure minimum.

As with the response of the sphere in the Mode II regime, it is clear from visualization of the vortex structures in the Mode III regime that two vortices are shed for each cycle of oscillation. As

previously mentioned, it is also apparent that the vortex formation length has increased substantially. Since the Reynolds number is the same for all simulations, this amounts to a decrease in the vortex shedding frequency.

5.9.4 Dynamics of the Mode III response

We have seen that one of the major differences between the dynamics of the sphere in the Mode II regime and the Mode III regime is the switching of the phase between the fluid forcing and the body motion from being in-phase (in the Mode II regime) to out-of-phase (in the Mode III regime). Furthermore, Figure 5.4.5 shows that the frequency of oscillation in all three directions is the same for the Mode III response. For the Mode II response, the streamwise frequency of oscillation was *twice* the transverse frequency of oscillation. This is because in the Mode II regime, the oscillations mapped out a figure-of-eight shape in the x - z plane.

In contrast, the oscillations in the Mode III regime do not map out a figure-of-eight shape. The layover angle has increased to the point that the streamwise frequency of oscillation is no longer twice that of the transverse oscillation frequency. As a result, the dynamics of the sphere adjust so that the oscillations are out of phase with the forcing, which is often the case in flow-induced vibration problems.

Furthermore, we see from Figure 5.4.5 that the normalized oscillation frequency at a reduced velocity of $U^* = 24$ is roughly $f^* = 2.7$. This equates to an oscillation frequency of $St = 0.11$, although the vortex shedding frequency for a stationary sphere at the same Reynolds number of $Re = 500$ is about $St = 0.16$. The magnitudes of the fluid forces acting on the sphere in this Mode III regime are also much smaller than those observed near the onset of the Mode II oscillations, and are closer to those observed near the end of the Mode II regime. This fact, together with the observation that the sphere does not oscillate close to the natural frequency within this regime, leads to the conclusion that the oscillation frequency (and the vortex shedding frequency) are not locked-in to the natural frequency of vibration, unlike the onset of the Mode II oscillations.

However, like the response observed in the Mode II regime, the sphere oscillations modulate the vortex shedding frequency such that self-excited motion ensues. As previously discussed, the Mode III response discovered by Jauvtis *et al.* (2001) was observed for mass ratios of $M^* = 28$ and above. The consequence of using these high mass ratios was that the oscillation frequency always coincided with the natural frequency, regardless of the response mode. The present results have shown that a Mode III response is observed, at least for laminar flow conditions, for low mass ratios (and hence

reduced velocities). Furthermore, these low-frequency Mode III oscillations are a result of the sphere oscillations modulating the vortex shedding from the sphere, as postulated by Jauvtis *et al.* (2001).

5.10 Mode IV response

Unlike the Mode II and Mode III responses, the dynamics of the tethered sphere in the Mode IV regime are a lot more difficult to analyse. The primary reason for this is the non-harmonic nature of the oscillations, and the existence of multiple frequencies in the wake. Jauvtis *et al.* (2001) discovered this mode, which is characterized (at least at high Reynolds numbers) by intermittent bursts of large-amplitude vibration. This mode was found when investigating a tethered sphere of mass ratio $M^* = 940$. Because of this high mass ratio, the oscillation frequency coincided with the natural frequency throughout the entire regime. The reduced velocities investigated varied up to $U^* = 300$, which corresponded to a natural frequency (and hence oscillation frequency) of about $S_n = 0.003$. Within this range of Reynolds numbers, the frequency of vortex shedding from a stationary sphere is roughly $St = 0.18$. This is equivalent to the fact that the vortex shedding frequency is up to 54 times greater than the oscillation frequency, assuming that the vortex shedding frequency is not modulated by the oscillations which happens to be the case for the previous response modes. Clearly, this vortex shedding frequency cannot be responsible for the large-amplitude vibrations.

For the present simulations, a Mode IV response is observed for a mass ratio of $M^* = 0.8$. Figure 5.10.1 shows sample time histories of the transverse oscillations and the corresponding transverse forces at $U^* = 33$ for this mass ratio. The oscillations are clearly not sinusoidal, but nevertheless large-amplitude vibrations are observed that have a very low frequency. At this reduced velocity, these amplitudes may reach a maximum value of $A^* = 0.46$. On the other hand, the transverse force coefficient exhibits similar non-sinusoidal behaviour, again unlike the responses observed in the Mode II and Mode III regimes. However, in contrast to the oscillations, the transverse forcing displays a much higher dominant frequency.

The dominant frequencies of the transverse oscillations and the transverse force are shown in Figure 5.10.2. It is clear that there exist many frequencies, for both the oscillations and the force. The extremely low frequencies at $St < 0.01$ are due to the small sample space used to calculate the power spectral density plots. By disregarding these frequencies, we see that the dominant oscillation frequencies of the sphere lie in the range $0.02 < St < 0.04$. A little further down the scale, there is a local peak at about $St = 0.11$. Beyond this frequency, there are no further significant higher frequencies of oscillation observed.

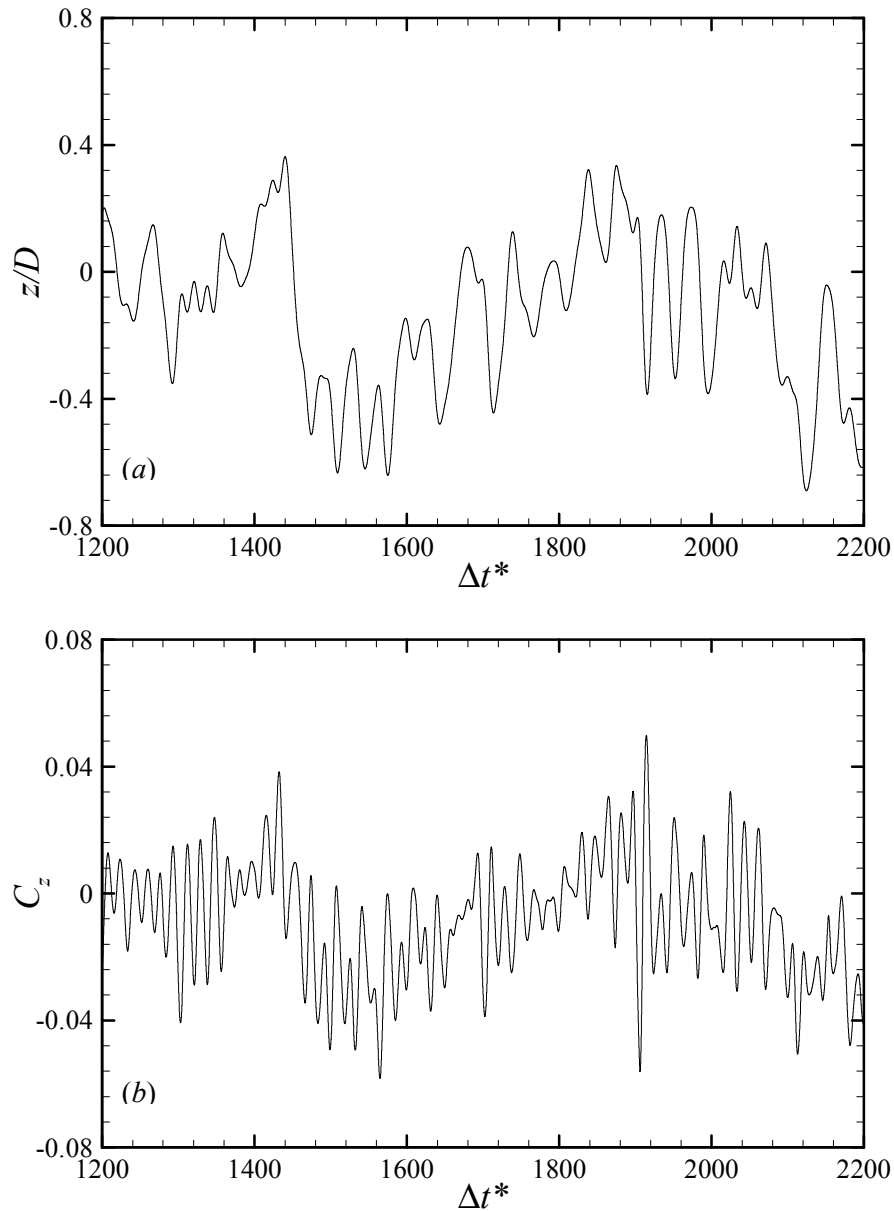


Figure 5.10.1. Sample time histories of (a) transverse oscillations, and (b) transverse fluid forces in the Mode IV regime, $U^* = 50$.

On the other hand, the transverse fluid force shows a dominant frequency of approximately $St = 0.11$. This corresponds to the local peak in the spectra of the transverse oscillations that was observed at the same frequency. Another local peak is observed at frequencies in the range $0.02 < St < 0.04$, which corresponds to the dominant frequency of oscillation. It is clear then that the dominant frequency of the transverse force is approximately 3 – 4 times the oscillation frequency. This is equivalent to the fact that the vortex shedding frequency is 3 – 4 times greater than the oscillation frequency.

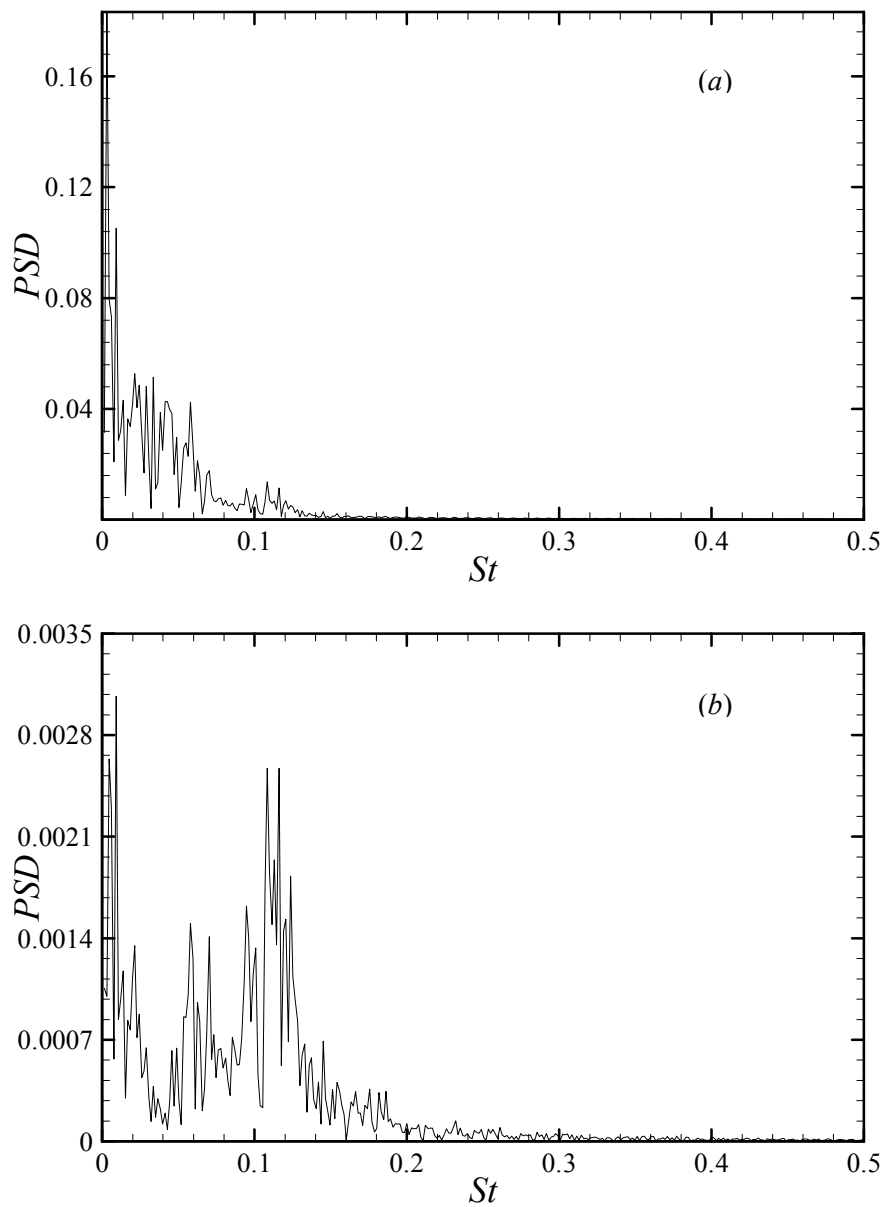


Figure 5.10.2. Dominant frequencies of (a) transverse oscillations, and (b) transverse fluid forces in the Mode IV regime, $U^* = 50$.

For both the experimental results of Jauvtis *et al.* (2001) at high Reynolds numbers and the present numerical results at low Reynolds numbers, the transverse oscillation frequency of the sphere appears to coincide with the natural frequency of vibration. However, for the present simulations, the range of U^* investigated is finite (because the drag becomes a factor at large layover angles), and as a result the reduced velocity does not extend to values in the hundreds, corresponding to very low natural frequencies. Unlike the Mode III response, in which the computations showed the same dominant frequency for both the oscillations and the forcing, the fact that both the computations and

the experiments show that multiple vortices are shed for each cycle of sphere oscillation within this Mode IV regime is remarkable.

The cause of these vibrations still remains a mystery. However, since the frequency ratio of the oscillations to the vortex shedding is less than unity, it is entirely possible that subharmonic excitation may occur that results in the large-amplitude vibrations shown in Figure 5.10.1. This is a well-known case of instability-induced excitation (IIE), as discussed by Naudascher & Rockwell (1994). For example, for a cylinder that experiences cross-flow vibrations, subharmonic resonance may occur when the frequency ratio of the oscillations to the vortex shedding is $1/3$. As explained by Durgin *et al.* (1980), this is because compatibility between the vortex-induced and movement-induced forces on the cylinder demands three vortex shedding events for each cycle of body vibration. Another explanation of the sphere response in this Mode IV regime was put forth by Jauvtis *et al.* (2001), who suggested that the vibrations might be a result of movement-induced excitation (MIE) (see Naudascher & Rockwell (1994)). In this case, the body dynamics may be explained in terms of quasi-steady analysis (such as flutter and galloping), although a direct link was not evident. Nevertheless, the present numerical simulations have shown the tendency of the sphere to vibrate at more or less its natural frequency in this regime, and is not a product of high mass ratios as were the spheres investigated by Jauvtis *et al.* (2001).

5.11 Existence of a critical mass ratio

From §5.5, recall that a Mode IV response exists for the highest mass ratio investigated numerically, i.e. for $M^* = 0.8$. As discussed in §5.4, this occurs when the mean layover angles exceed 45° . However, for the sphere with mass ratio $M^* = 0.082$, these large-amplitude, almost chaotic vibrations do not occur, even though the mean layover angle is much greater than 45° at a reduced velocity of $U^* \approx 20$. The lack of a Mode IV response for the low mass ratio means that there exists a *critical mass* somewhere in the vicinity $0.082 < M^* < 0.8$. Govardhan & Williamson (2002b) report a critical mass of $M^* = 0.30$ for a sphere free to vibrate in the transverse direction. This is also similar to the dynamics of a hydroelastically-mounted cylinder with no restoring force, which has a critical mass of $M^* = 0.54$ (Govardhan & Williamson (2002a)). However, no value has yet been reported for a tethered sphere, and for the present laminar flow conditions, it appears that this critical mass marks the location below which a Mode III response dominates and above which a Mode IV response is observed.

The limits of the flow speeds obtainable in the experimental facility of Govardhan & Williamson (1997) did not allow high reduced velocities to be investigated. In contrast, the experiments of Jauvtis *et al.* (2001) were performed at reduced velocities up to $U^* = 300$. However, this was

achieved by investigating mass ratios ranging from $M^* = 80$ to $M^* = 940$. As a result of these exceptionally high mass ratios, the tethered sphere was found to oscillate at its natural frequency of vibration throughout the entire range of reduced velocities. In addition, the mean layover angles were not even close to 45° (Williamson, private communication (2003)), so that the dynamics of the sphere at high layover angles remains an experimental mystery. It is not too surprising, therefore, that the present numerical simulations, together with the fact that the flow is laminar and the layover angles are quite large, uncover sphere dynamics that are quite remarkable and straightforward to analyze in detail because of the relatively low reduced velocities. These low reduced velocities are equivalent to relatively high natural frequencies, in contrast to the results of Jauvtis *et al.* (2001) which were lacking in the sense that the dynamics of the sphere were purely a result of the sphere oscillating at its natural frequency of vibration. The ability to investigate high layover angles has thus resulted in the discovery of both the Mode III and IV responses at relatively low reduced velocities and mass ratios.

5.12 Further work

The dynamics of a tethered sphere when subjected to a uniform flow has been analyzed in detail. Further work may include looking at a shear (or even oscillatory) flow, as opposed to a uniform flow. This may be useful to ocean engineers when the submergence depth of the spheres is quite small.

The numerical procedure outlined in Chapter 2 is very general and as a result may be extended to a wide variety of problems. For example, higher mass ratios may be easily investigated, even for the very high mass ratios of order $M^* = 1000$ examined by Jauvtis *et al.* (2001). Couple this with an accurate turbulence model (or maybe a large-eddy simulation approach) and one has the ability to essentially investigate the full, as yet four-mode dynamics of a tethered sphere at high Reynolds numbers (ie. turbulent flow). This means that the behaviour observed experimentally by Jauvtis *et al.* (2001) may be duplicated computationally, and the flow physics giving rise to the dynamics may be analyzed without difficulty. Another alternative to adopting the full DNS procedure for this flow-induced vibration scenario is to use reduced-order models, as described by Dowell & Hall (2001). For example, a simple modal approach such as proper orthogonal decomposition (POD) has been used quite successfully to model the flow-induced vibrations of cylinders (see, for example, Newman & Karniadakis (1997)).

Also, the existence of a critical mass needs to be addressed at these lower Reynolds numbers. In addition, it would be useful to perform more experiments at these low Reynolds numbers in order to

obtain a wide range of reduced velocities and layover angles which will hopefully unearth the Mode III and IV responses experimentally. In either case, the possibilities of further work are limitless.

Chapter 6

Summary/Conclusion

From the outset, the major aim of the present study was to investigate the dynamics of a tethered sphere, and in particular under what conditions large-amplitude vibrations are observed. The use of direct numerical simulations restricted the Reynolds number range to laminar flows, in which it was previously unknown whether the tethered sphere would oscillate at all. The present results have shown that the tethered sphere does indeed experience large-amplitude vibrations, over a range of reduced velocities, even at these laminar flow conditions. Furthermore, different modes of vibration have been identified and analyzed in detail where possible. These modes are similar to the oscillation modes observed by Jauvtis *et al.* (2001), which were studied under turbulent flow conditions.

6.1 Computational procedure and methodology

The computational procedure outlined in Chapter 2 is well suited to the problem of the flow-induced vibrations of tethered bodies. Furthermore, since tethered *spheres* are the main focus of this study, existing numerical codes that have been used extensively for axisymmetric geometries can be adapted to solve the combined fluid-structure system of equations that govern the response of the tethered sphere subject to a uniform flow. For the fluid, these equations are the viscous, incompressible Navier-Stokes and continuity equations. The (nonlinear) equations of motion for the tethered sphere were obtained from Newton's 2nd Law and by assuming that the tether is inextensible. The dimensionless parameters governing the sphere response were the mass ratio M^* ,

the tether length L^* and the Froude number Fr . In addition, the need for a deforming mesh was eliminated by using a coordinate transformation that served as a bridge connecting the inertial (accelerating) reference frame to the non-inertial reference frame attached to the sphere.

6.1.1 Discretization and solution procedure

As previously mentioned, the governing equations of the sphere were nonlinear and coupled and therefore most efficiently solved using predictor-corrector techniques. The fluid equations were discretized in time using a three-step time-splitting procedure developed by Karniadakis *et al.* (1991) that has become the preferred method for higher-order schemes over the last decade. This scheme reduces the coupled system of fluid equations into a set of separately solvable equations for the pressure and velocity, a crucial requirement for accurate high-resolution simulations of complex flows. The equations of motion for the sphere were advanced in time by using the initial displacement of the sphere and predicting the displacement and velocity at the end of timestep. This was achieved via Adams-Bashforth predictors and Adams-Moulton correctors, and the fluid equations were then solved to compute the fluid forces giving rise to the motion of the sphere. Finally, the velocity and displacement of the sphere was corrected, utilizing underrelaxation techniques to improve the convergence characteristics of the solver. Convergence was monitored by three criteria: the normalized change in the velocity of the sphere, the normalized maximum change in the velocity field, and the normalized change in the force of the body.

Spatial discretization was performed using spectral elements in the z - r plane and Fourier expansions in the azimuth. Similar techniques have been used recently by Tomboulides (1992), Ghidersa & Dusek (2000) and Blackburn & Lopez (2002). A change of variables was used to decouple the equations and, following time-discretization as discussed in the previous paragraph, resulted in a set of Helmholtz-like equations for the velocity and pressure modes. The spatial discretization of these Helmholtz equations was obtained using two-dimensional spectral elements, as described in detail in Maday & Patera (1989).

6.1.2 DNS and experimental differences

The experiments of Williamson & Govardhan (1997), Govardhan & Williamson (1997) and Jauvtis *et al.* (2001) were all performed in water channel facilities and wind tunnels. As a result, increases in reduced velocity were obtained by increasing the experimental flow velocity, which increases the Froude number but also has the side effect of increasing the Reynolds number. However, the present

simulations were executed by keeping the Reynolds number fixed at $Re = 500$ and altering the Froude number by effectively changing the gravitational term in Fr , as described in §2.4. Furthermore, the experiments were performed at Reynolds numbers in the range $750 < Re < 14000$. The flow was thus highly turbulent in the range that most of the experiments were performed in, whereas the numerical simulations were carried out at laminar (albeit unsteady and asymmetric) flow conditions. Nevertheless, despite the differences in the way the numerical results and the experimental results were obtained, many features of the sphere response were observed and were similar in both cases. These features are summarized in §6.4.

6.1.3 Numerical flow visualization techniques

There have been a number of flow visualization techniques that have been used by numericists to visualize vortex structures in complex flows. In the present study, the vortex structures are visualized by plotting an isosurface of $-\lambda_2$, which is the second eigenvalue of the $\mathbf{S}^2 + \mathbf{Q}^2$ tensor. Here, \mathbf{S} is the rate-of-strain tensor and \mathbf{Q} is the rate-of-rotation tensor. This definition is equivalent to the fact that the $\mathbf{S}^2 + \mathbf{Q}^2$ tensor determines the existence of a local pressure minimum due to vortical motion, and disregards the effects of unsteady irrotational straining and viscous diffusion that would otherwise inhibit an effective indication for the existence of a vortex. Jeong & Hussain (1995) provide many examples of the use of this method when the vortex geometry is intuitively clear. This technique has also been used successfully for visualizing vortex structures in the wake of a stationary sphere by Johnson & Patel (1999).

6.1.4 Mesh independence

A detailed grid independence study was performed for a stationary sphere in §2.6. Flow quantities such as drag and lift coefficients, vortex shedding Strouhal numbers and measurements of the streamwise fluctuating velocity component were obtained and compared to previously published and accepted results. For all of these flow parameters, the most cost-effective value of p was found to be $p = 8$. For the tethered sphere simulations, accurate resolution of the boundary layer was demonstrated for $p \geq 5$, up to a Reynolds number of $Re = 1000$. Furthermore, increasing the azimuthal resolution from $k = 24$ to $k = 32$ planes resulted in negligible differences in the measured flow quantities. However, in order to accurately capture the evolution of the vortical structures in the wake, all tethered sphere simulations were thus performed with the parameters $p = 8$ and $k = 32$, unless otherwise noted.

6.1.5 Relaxation parameter and convergence criteria

A final study was performed to verify that the results for the tethered sphere simulations were independent of the relaxation parameter and convergence criteria. This was achieved by increasing the relaxation parameter from $\varepsilon = 0.2$ up to $\varepsilon = 0.8$ for two separate reduced velocities that represented harmonic and non-harmonic oscillation behaviour respectively. For both of these oscillation states, the differences resulting from the changes in ε were found to be negligible. This was to be expected since theoretically, the results should be independent of ε if the solution is converged. A more appropriate check was to ensure that the results were independent of the convergence criteria, which was performed by decreasing the tolerances an order of magnitude from $u_{tol} = 0.0001$ and $F_{tol} = 0.01$ to $u_{tol} = 0.00001$ and $F_{tol} = 0.001$. With these modifications, the corresponding changes in the observed response were also found to be negligible.

6.2 Stationary sphere

The flow past a stationary sphere was investigated for Reynolds numbers of $Re = 100, 250, 300, 400$ and 500 . This range incorporated various flow and wake characteristics such as the presence of axisymmetry, the transitions to asymmetry and unsteadiness, and the loss of planar symmetry. Detailed analyses of the pressure and vorticity fields were undertaken with the aim of understanding the different wake states and the processes involved with the vortex shedding and the near wake vortex dynamics.

6.2.1 Steady, axisymmetric flow

For Reynolds numbers less than $Re = 24$, the flow past a sphere is known to be axisymmetric and attached (Taneda (1956)). However, for $Re > 24$ but less than $Re = 212$, the numerical simulations found that the flow was laminar, steady and axisymmetric, with a toroidal vortex in the immediate near wake of the sphere. The separation angle, length, and drag coefficient, as well as the location of the centre of the vortex, was found to agree extremely well with the results of Taneda (1956), Shirayama (1992) and Magnaudet *et al.* (1995), to name but a few. Computed streamlines showed that the flow was indeed axisymmetric, and contours of the pressure coefficient revealed a ring of low pressure located very close to the centre of rotation of the toroidal vortex. Within this regime, the centrifugal force of the vortex's rotation was balanced by viscous forces as opposed to a radial pressure gradient, as mentioned by Johnson & Patel (1999).

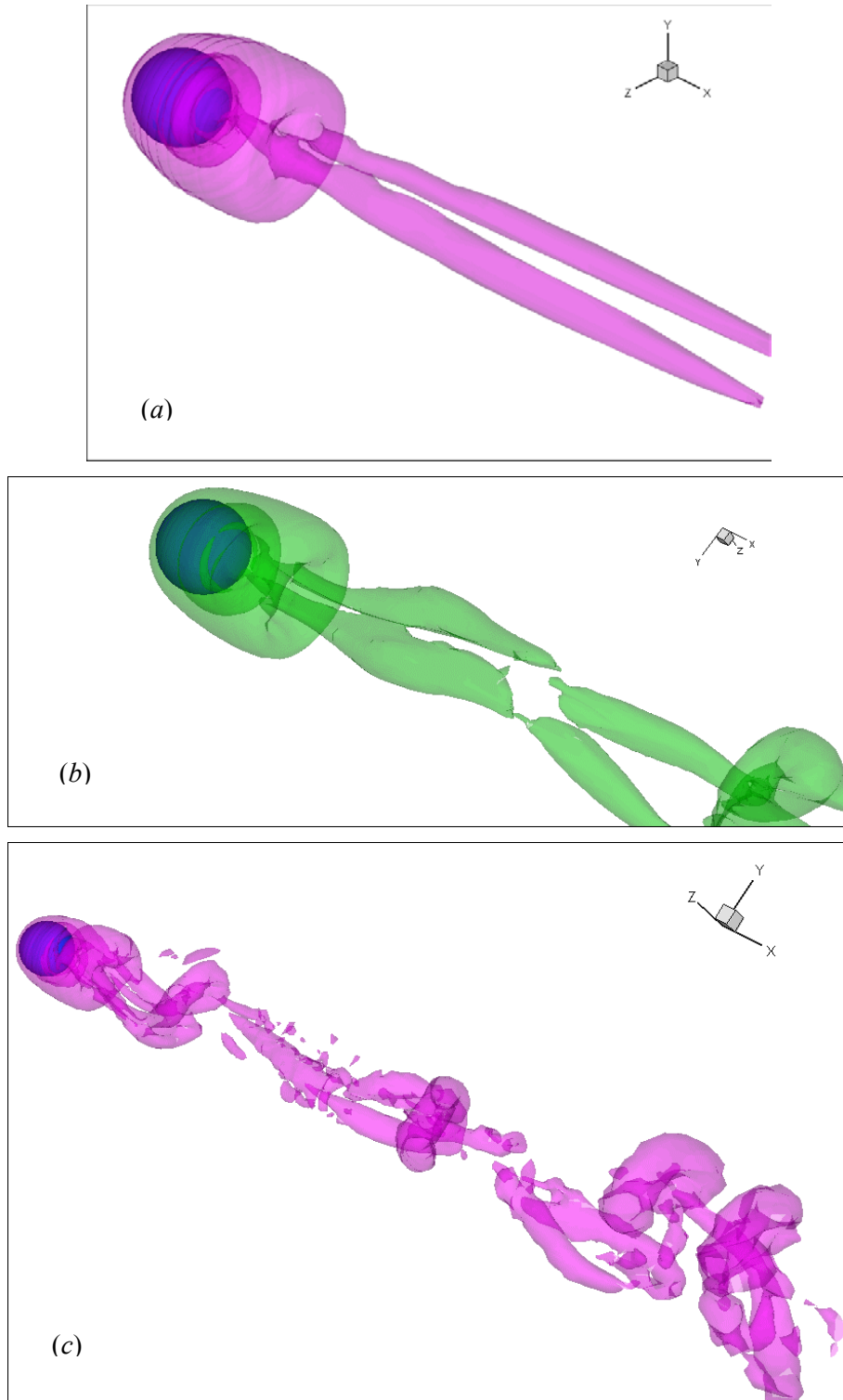


Figure 6.2.1. Visualizations of the vortex structures in the wake of a sphere (plotted using an isosurface of $-\lambda_2$) at (a) $Re = 250$; (b) $Re = 300$; (c) $Re = 500$.

6.2.2 Steady, planar-symmetric flow

Direct numerical simulations in §3.2 were performed at incremental Reynolds numbers of unity in the range $209 < Re < 213$. These simulations found a breakdown of axial symmetry when a Reynolds number of $Re_l = 212$ was reached. This value compares very well to the value of $Re_l = 210$ obtained by Natarajan & Acrivos (1993), which was computed using a linear stability analysis. Furthermore, this bifurcation was found to be a regular (supercritical) one in the sense that there are no observed hysteresis effects (Tobak & Peake (1982)).

The drag and lift coefficients in this regime were found to compare very well with those of previous research. Furthermore, the plane of symmetry was most obvious when plotting the streamlines, which happen to correspond to actual particle paths since the flow was steady. The pressure field revealed that the previously axisymmetric ring of low pressure in the near wake was now tilted, resulting in the conversion of azimuthal vorticity to streamwise vorticity. This streamwise vorticity was then convected downstream via two tails, known as the “double-thread” or “two-tailed” wake, which is clearly observed experimentally (see, for example, Ormieres & Provansal (1999)), and is shown in Figure 6.2.1 (a).

6.2.3 Unsteady, planar-symmetric flow

When the Reynolds number exceeds $Re_2 \approx 375$, the flow past a sphere becomes unsteady with the appearance of periodic vortex shedding. Like the transition to asymmetry, this transition occurs with $m = 1$ being the most unstable mode. However, unlike the previous transition, this transition occurs via a Hopf bifurcation. The drag and lift coefficients, as well as the vortex shedding Strouhal number at a Reynolds number of $Re = 300$, were found to agree very well with previous numerical and experimental results. The vortices were composed of shed hairpin vortices and induced hairpin vortices. Note that experimental dye visualization only elucidates the shed hairpin vortices, since the induced vortices result from the near wake vortex dynamics and not from the boundary layer separation off the surface of the sphere.

The pressure and vorticity fields were analyzed in detail in §3.3 and helped in understanding the vortex shedding process, which is summarized as follows. Initially, there was an azimuthal pressure gradient that generated azimuthal flow from the centre of the upper focus to the lower. The upper focus then increased in strength, and changed from a stable focus to an unstable focus, resulting in a reverse flow that impinged on the upper separating shear layer and disconnected (ie. shed) the vortex into the wake. The remaining shear layer then rolled up to produce the new upper focus, thereby

restarting the process. As with the steady flow results, visualizations of the hairpin vortices were obtained by plotting an isosurface of $-\lambda_2$. This yielded clear and unmistakable vortex structures that compared well with the experimental visualizations of Sakamoto & Haniu (1995) and Ormieres & Provansal (1999), as shown in Figure 6.2.1 (b).

6.2.4 Unsteady, asymmetric flow

Planar symmetry is known to be lost in the range $350 < Re < 375$ (Mittal (1999b)). The experiments of Sakamoto & Haniu (1990) reported a loss of planar symmetry when a Reynolds number of $Re = 420$ was exceeded. Numerical simulations were performed in this unsteady asymmetric regime at Reynolds numbers of $Re = 400$ and $Re = 500$. For both cases, the flow was found to be highly unsteady and did not exhibit a plane of symmetry. Spectral analysis of the fluctuating azimuthal velocity component of the $m = 1$ mode revealed dominant peaks corresponding to the frequency of vortex shedding. These values compared favourably to those of previous research.

Analysis of the fluid forces revealed that the net lift coefficient appeared to have a preferred orientation for a Reynolds number of $Re = 400$. When the Reynolds number was increased to $Re = 500$, a preferred orientation of the wake was not discernible. This result was in agreement with that of Mittal *et al.* (2002) who found that the preference for any particular wake orientation diminished with increasing Reynolds number. Visualizations of the vortex structures revealed that the hairpin vortices and vortex loops rotate and deform as they convect downstream, which is a consequence of the irregular angle of vortex formation off the surface of the sphere, as depicted in Figure 6.2.1 (c).

6.3 Rotating sphere

Direct numerical simulations of the flow past a rotating sphere were performed for Reynolds numbers in the range $10 < Re < 500$. The dimensionless rotation rates investigated ranged from $\Omega = 0.05$ to $\Omega = 0.25$ in increments of 0.05. This particular range of Reynolds numbers was chosen because the major transitions that the sphere experiences are well documented for stationary spheres within this regime. Furthermore, the relatively low rotation rates were chosen to enable comparisons with previous research and to take full advantage of the available computational resources.

6.3.1 Non-streamwise sphere rotations

Non-streamwise rotations were performed about both the y and z axes (see Figure 4.1.1). Numerical results of the y -axis rotations were identical to the z -axis rotations, and as a result only the results concerning the z -axis rotations were presented. The most notable difference between the non-streamwise rotating sphere and the stationary sphere was the lack of axisymmetry over the entire range of Reynolds numbers investigated. Nonetheless, the drag coefficient for these non-streamwise rotation rates was found to increase with increasing Ω . Furthermore, the lift coefficient initially increased at the lowest Reynolds numbers investigated and subsequently decreased, eventually reaching an asymptotic value of approximately $C_l = 0.065 + \Omega$.

When the sphere was rotating about the z -axis, streamline plots showed that a plane of symmetry was observed that coincided *exactly* with the x - y plane. For a stationary sphere, the plane of symmetry arose naturally and in general did not coincide with the x - y plane. This loss of axial symmetry at the lowest Reynolds numbers investigated was due to the out-of-plane velocity component. Furthermore, pressure and vorticity contours were similar to those of a stationary sphere in the appropriate flow regime, with some distinctions as discussed in §4.2.2.

Vortex shedding frequencies in the form of Strouhal numbers were measured and found to increase with increasing Reynolds number. In addition, at any given Reynolds number, an increase in Ω resulted in an increase in St . This was probably due to the fact that the intensity of the reversed flow generated by the vortex increases with increasing rotation rate and interferes with the separating shear layer, thereby effectively cutting off the vortex from the wake prematurely and increasing the shedding frequency of the wake.

Visualizations of the vortex structures in the wake were similar to that of a stationary sphere. However, the major difference was that for both the steady and unsteady planar-symmetric regimes, the vortex structures were clearly symmetric about a plane that was dictated by the direction of rotation of the spinning sphere.

6.3.2 Streamwise sphere rotations

Rotation rates similar to those investigated in the previous section were also used to perform simulations for a streamwise rotating sphere. Unlike the non-streamwise rotations, the flow was found to be axisymmetric for the lower half of the Reynolds numbers examined. Drag coefficients were computed as a function of Reynolds number and rotation rate and were found to increase as Ω increases, as with the non-streamwise sphere rotations. However, the difference in C_d at any given Reynolds number was much smaller for the streamwise rotating sphere, typically an order of

magnitude smaller especially at the higher Reynolds numbers. This was due to the fact that if the rotation rate was low enough, the tendency of the wake to remain axisymmetric was increased.

The vortex structures observed were much more dependent on the sphere rotation rate than the corresponding non-streamwise rotation simulations. For example, at low enough rotation rates, the two-tailed wake was no longer planar symmetric as one tail was “weaker” and skewed with respect to the streamwise axis. For higher rotation rates, one tail disappeared completely, as discussed in the next subsection. Simulations at higher Reynolds numbers (when the flow was unsteady) revealed that the vortex structures were much more distorted, especially in the far wake region, because of the influence of the streamwise rotation.

6.3.3 The “frozen” vortex structure

As previously mentioned, for the two-tailed wake at higher rotation rates one tail disappeared completely. Under these steady flow conditions, the drag coefficient remained constant whereas the lateral and side force coefficients were sinusoidal with a very low frequency of St_f that was different to that of the vortex shedding. Although the lateral and side force coefficients were sinusoidal, the *net* lift coefficient was steady, so that the vortex rotated about the wake centreline without temporal variation in its shape or strength. This “frozen” vortex structure was first recently reported by Kim & Choi (2002), although Wang *et al.* (2001) appear to have discovered it without going into any detail about the dynamics of it.

In general, the rate of rotation of the frozen vortex was different to that of the sphere. This was observed by recording the time history of the lift angle β , the slope of which indicates the rotating velocity of the vortex structure. Furthermore, it was found that increasing the rate of rotation serves to increase the rotation rate of the frozen vortical structures, in an almost one-to-one correspondence. In other words, doubling the rotation rate of the sphere will double the rotation rate of the frozen vortical structures as well, assuming that the flow is still frozen at these higher angular velocities.

6.3.4 Critical Reynolds numbers

The present study reports for the first time the influence of sphere rotation on the wake transitions to planar-symmetry and unsteadiness. For non-streamwise sphere rotations, it was found that the transition to asymmetry occurred at $Re_l < 10$. This was because the out-of-plane component of velocity breaks the axisymmetry even at the lowest Reynolds numbers investigated. However, for the streamwise sphere rotations, the transition to asymmetry occurred at $200 < Re_l < 220$ for rotation

rates of $\Omega \geq 0.2$, and at $220 < Re_1 < 240$ for lower rotation rates. Note that for a stationary sphere, this transition occurs at a Reynolds number of approximately $Re_1 = 212$, so that lower streamwise rotation rates serve to delay the transition at which asymmetry occurs.

For the non-streamwise rotating sphere, the transition to unsteadiness was much easier to measure. This transition occurred at $Re_2 = 250 \pm 10$ for rotation rates of $\Omega = 0.05$ and 0.10 . For higher rotation rates of $\Omega = 0.15$ and 0.20 , this transition occurred at a Reynolds number of $Re_2 = 230 \pm 10$. However, for the case of $\Omega = 0.25$, the transition occurred at a critical Reynolds number in the range of that observed for the lower rotation rates. For the streamwise rotating sphere, for rotation rates of $\Omega = 0.10$ and 0.15 , unsteadiness first appeared at a Reynolds number in the range $280 < Re_2 < 300$, whereas for the other rotation rates, it occurred in the range $260 < Re_2 < 280$. For a stationary sphere, this transition is observed at a Reynolds number of approximately $Re_2 = 272$. It appears then that a non-streamwise rotation rate causes the transition to unsteadiness to occur at lower Reynolds numbers, whereas a streamwise rotation rate appears to delay the transition, especially at the intermediate rates of rotation investigated in this study.

6.4 Tethered sphere

This study has focused on tethered spheres that involve applications such as tethered sea mines, weather balloons and bathyscaphes, to name a few. All of these applications represent structures whose mass is less than that of the fluid that is displaced, ie. $M^* < 1$. The experimental results of Williamson & Govardhan (1997) and Govardhan & Williamson (1997) involved similar mass ratios, and found only two modes of vibration, mainly because small layover angles were investigated. The ability of the present computational procedure to investigate layover angles approaching 90° have resulted in the appearance of additional oscillation modes, similar to the extremely high mass ratio results of Jauvtis *et al.* (2001). In addition, the numerical procedure has the potential to efficiently investigate the dynamics of *any* tethered structure, since the formulation developed in Chapter 2 is independent of the body geometry. In light of this, the dynamics of a two-dimensional circular cylinder have been investigated by Pregalato *et al.* (2002b) and Ryan *et al.* (2003), and have produced a rich variety of oscillation dynamics.

6.4.1 Experimental results at low Reynolds numbers

For the first time, experiments for a tethered sphere were performed in the present study entirely in laminar flow conditions. A polypropylene sphere of mass ratio $M^* = 0.91$ and tether length $L^* =$

10.24 was used at Reynolds numbers ranging from $Re = 503$ to $Re = 780$. This corresponded to reduced velocities approximately in the range $8.9 < U^* < 13.8$. At the lowest Reynolds number investigated ($Re = 503$), time traces of the sphere response clearly revealed significant oscillations, even at this relatively low Reynolds number. The magnitudes of the streamwise oscillations were typically 16 times smaller than the transverse oscillations. The high Reynolds number results of Williamson & Govardhan (1997) depicted a streamwise oscillation amplitude that was about twice as small as the transverse oscillation amplitude. Evidently, the difference in flow states between the present experiments and those of Williamson & Govardhan (1997) results in a large difference in the oscillation response, especially in the streamwise direction.

For the range of reduced velocities (and Reynolds numbers) investigated, the frequency of oscillation in the streamwise direction was twice the frequency of oscillation in the transverse direction, similar to the observations of Govardhan & Williamson (1997). Furthermore, the normalized frequency of oscillation increased with increasing U^* , in an almost linear trend. For a stationary sphere within this range of Reynolds numbers, Sakamoto & Haniu (1995) showed that the vortex shedding frequency varies considerably. As a result, one would imagine that the sphere oscillations are not a result of the vortex shedding frequency locking on to the oscillation frequency. However, the sphere was oscillating within the Mode II regime at these Reynolds numbers, as will be discussed shortly, and hence the oscillations modulated the vortex shedding frequency such that self-excited motion ensued.

In order to compare these experiments directly to the numerical simulations, a single simulation was performed with matching mass ratio, tether length and Froude number. Also, the numerical Reynolds number was kept at $Re = 500$, whereas the experimental Reynolds number was slightly higher at $Re = 503$. The experimentally observed streamwise oscillation amplitude was within the experimental error, and was thus likely to overestimate the actual response. However, the difference in the transverse amplitude response between the experiments and the numerical simulation was about 2%. Similarly, the differences in the normalized frequency response in both the streamwise and transverse directions were approximately 4%. These discrepancies are quite small and provide evidence of the accuracy of the present computational procedure.

6.4.2 Mean layover angles

An analytical estimate of the mean layover angle for a tethered sphere was made by referring to Figure 2.1.1. This estimate is given by the expression

$$\tan \theta = \frac{C_d}{(1-M^*)\alpha}, \quad (6.4.1)$$

where C_d is the drag coefficient for a stationary sphere and is equivalent to $C_d = 0.537$ (see Chapter 3). In Figure 6.4.1, we plot the mean layover angles for mass ratios of $M^* = 0.082$ (a) and $M^* = 0.8$ (b). The analytical estimate given by Equation (6.4.1) is also shown as the dashed line in both plots. For the low mass ratio, Equation (6.4.1) underestimates the predicted mean layover angle for reduced velocities in the range $4 < U^* < 11$. This is equivalent to the drag coefficient being greater than that for a stationary sphere, as we shall see shortly.

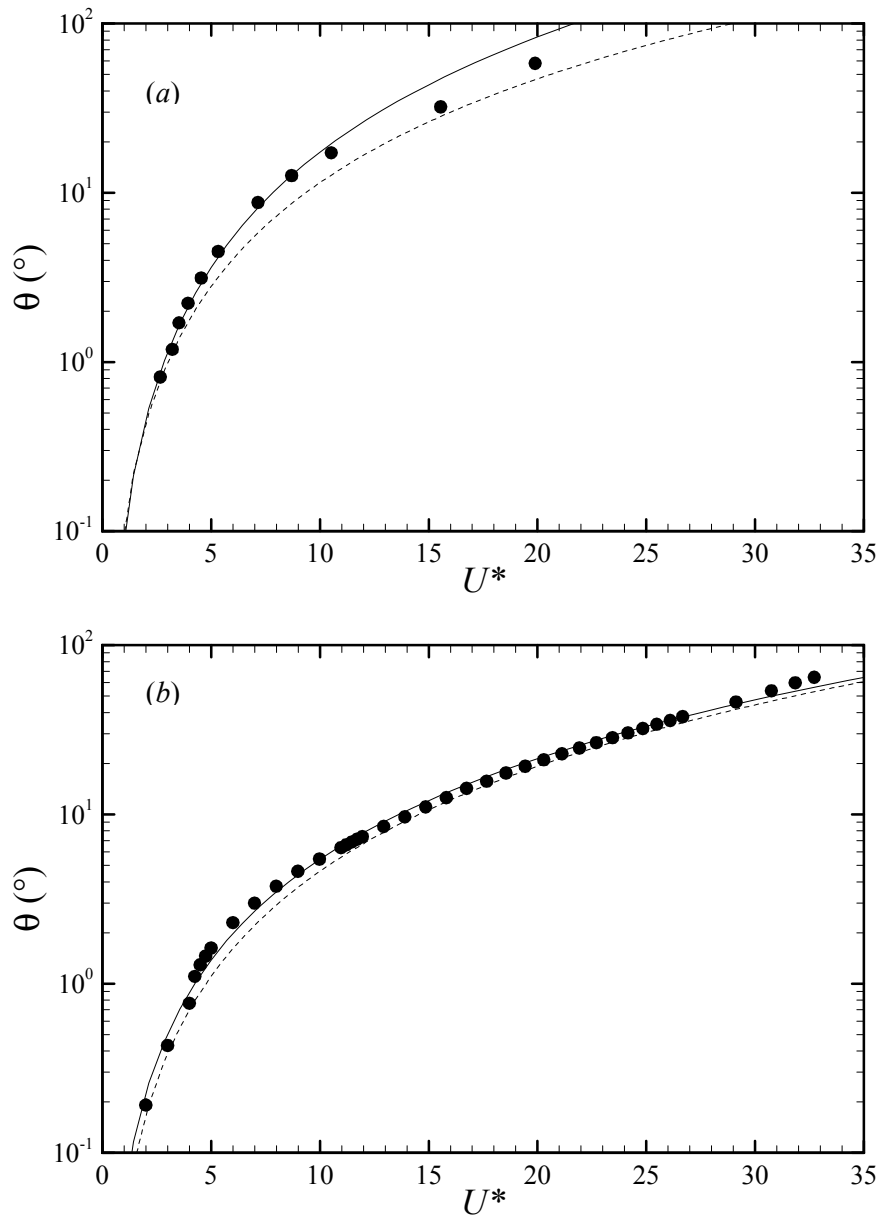


Figure 6.4.1. Mean layover angles for (a) $M^* = 0.082$, $L^* = 9.3$, and (b) $M^* = 0.8$, $L^* = 10$. Dashed lines represent the predicted response using stationary sphere drag data.

For the higher mass ratio, Equation (6.4.1) underestimates the predicted mean layover angle for reduced velocities in the range $4.25 < U^* < 11.2$. Any further increases in U^* have little effect on the calculated mean layover angle. The fact that the mean layover angles exhibit such a pronounced jump at incremental reduced velocities leads to the conclusion that at least two modes of oscillation are present for these mass ratios. These modes will be discussed in §§6.4.7 – 6.4.10.

6.4.3 Oscillation amplitudes

The amplitude response of the sphere was found to be strongly dependent on the mass ratio. This is shown in Figure 6.4.2, which puts together the results from the numerical simulations and the present experiments at low Reynolds numbers. For the sphere with mass ratio $M^* = 0.8$, increasing the tether length from $L^* = 5$ to $L^* = 10$ resulted in practically no change in the normalized amplitude response. Furthermore, increasing the mass ratio from $M^* = 0.082$ to $L^* = 0.91$ decreased the amplitudes of oscillation.

For all of the mass ratios investigated, a Mode II response was observed at reduced velocities roughly in the range $5 < U^* < 10$. This mode was discernible as a large-amplitude vibrational response whose amplitude was highest at the lower mass ratios. The experimental results, unfortunately, were limited to reduced velocities at the end of the Mode II regime, but nevertheless still exhibited a decreasing trend with increasing reduced velocity that was common to all of the mass ratios investigated. The nature of the oscillations in this Mode II regime (especially towards the end of the regime) was highly harmonic and very sinusoidal. The results of Jauvtis *et al.* (2001) display similar behaviour: the “periodicity” of their Mode II response was close to unity, meaning that the oscillations were exceptionally sinusoidal.

For the higher reduced velocities, greater than those that incorporate the Mode II regime, a Mode III response was observed. The oscillations within this regime were also highly sinusoidal, which represent a “periodicity” of close to unity, similar to the Mode II response. However, the dynamics of the sphere in this regime have some differences, which will be covered in §6.4.9.

For the low mass ratio sphere, the maximum reduced velocity investigated was equivalent to the sphere being displaced with a mean layover angle of almost 60° . However, only a Mode III response was observed for this low mass ratio case. For the high mass ratio sphere, at the highest reduced velocities investigated, the mean layover angle of the sphere was about 65° . At these high layover angles (ie. $\theta > 45^\circ$), a Mode IV response was observed. The lack of a Mode IV response for the low mass ratio case investigated leads to the existence of a *critical mass*, which will be discussed in §6.4.11.

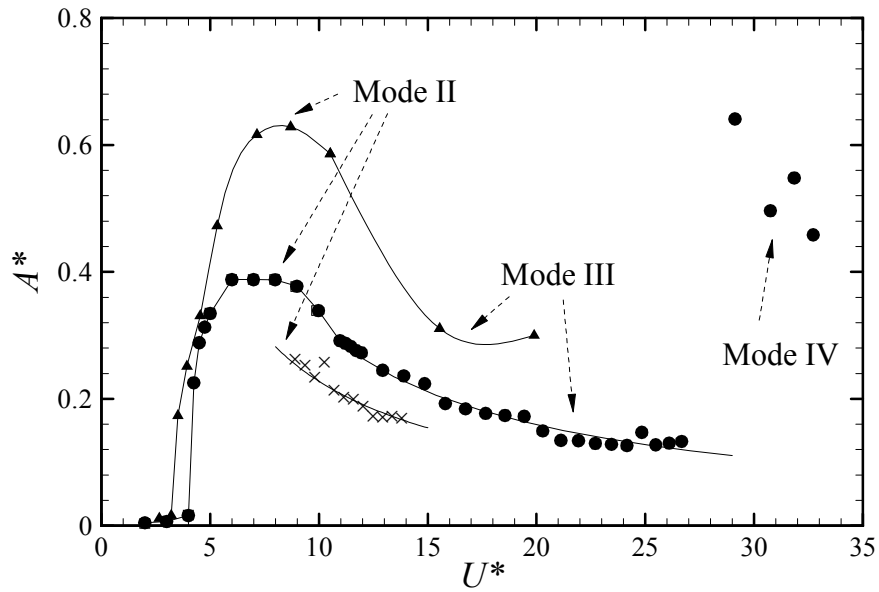


Figure 6.4.2. Amplitude response as a function of reduced velocity: $M^* = 0.082, L^* = 9.3, \blacktriangle$; $M^* = 0.8, L^* = 5, \square$; $M^* = 0.8, L^* = 10, \bullet$; $M^* = 0.91, L^* = 10.24, \times$ (experiments).

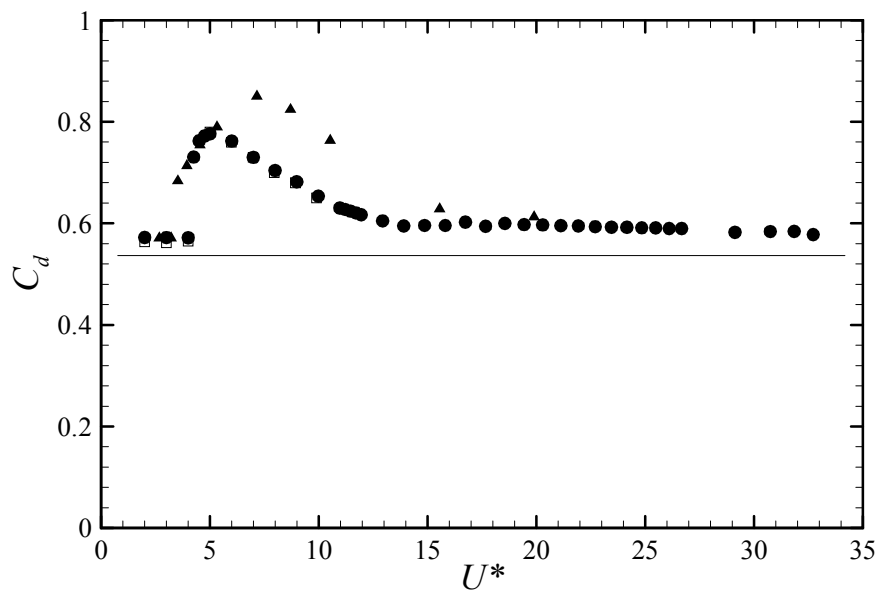


Figure 6.4.3. Change in the drag coefficient as a function of reduced velocity. Symbols as in Figure 6.4.2.

6.4.4 Drag coefficients

The drag coefficients for the different mass ratios as a function of reduced velocity are shown in Figure 6.4.3. Once again, for the $M^* = 0.8$ sphere, increasing the tether length from $L^* = 5$ to $L^* =$

10 resulted in negligible difference in the drag coefficient, as expected, since the change in the oscillation amplitude was also minimal. Furthermore, because of the larger-amplitude oscillations that were observed for the lower mass ratios, decreasing the mass ratio resulted in an increase in the drag coefficient. However, as the reduced velocity was increased, the drag coefficient gradually decreased to values slightly above that of a stationary sphere. This trend was independent of the mass ratio.

We have seen that the nature of the oscillations is reflected in the changes in the drag coefficient. This is especially true when the oscillations are harmonic. For example, the amplitudes of oscillation within the Mode II regime were quite large and the oscillations were quite harmonic. This combination resulted in a large increase in the drag coefficient, as shown in Figure 6.4.3. However, even larger-amplitude oscillations were observed in the Mode IV regime, but the drag coefficient remained close to that of a stationary sphere. As described in Chapter 5, this is because the oscillations in the Mode IV regime were not harmonic, but were instead quite erratic.

6.4.5 Frequency response

In contrast to the mean layover angle, oscillation amplitude and drag coefficient, the normalized frequency response of the sphere was found to be relatively independent of the mass ratio. This result is depicted in Figure 6.4.4, as a function of reduced velocity. At the lower end of the scale, the sphere was desynchronized and significant oscillations were not observed, regardless of the mass ratio. On the other hand, the sphere oscillations became synchronized within the Mode II regime as the oscillations became harmonic. The agreement in the normalized frequency response for all of the mass ratios investigated is remarkable. With increasing reduced velocity, the normalized frequency of oscillation was observed to jump from the “lower” branch to the “upper” branch. This change in f^* signifies a change in sphere dynamics from the Mode II response to the Mode III response. The collapse of data within this Mode III regime is also quite remarkable, for both the high and low mass ratios investigated.

It is also clear from Figure 6.4.4 that the sphere with mass ratio $M^* = 0.082$ experienced oscillations within the Mode III regime at the highest reduced velocities. In contrast, the high mass ratio sphere exhibited oscillations that were close to the natural frequency of the system at the highest reduced velocities. This behaviour is indicative of a Mode IV response, which is highlighted by the presence of extremely low-frequency vibrations, although the vortex shedding frequency (at least for a stationary sphere) is much higher. The dynamics of this Mode IV response will be summarised in §6.4.10.

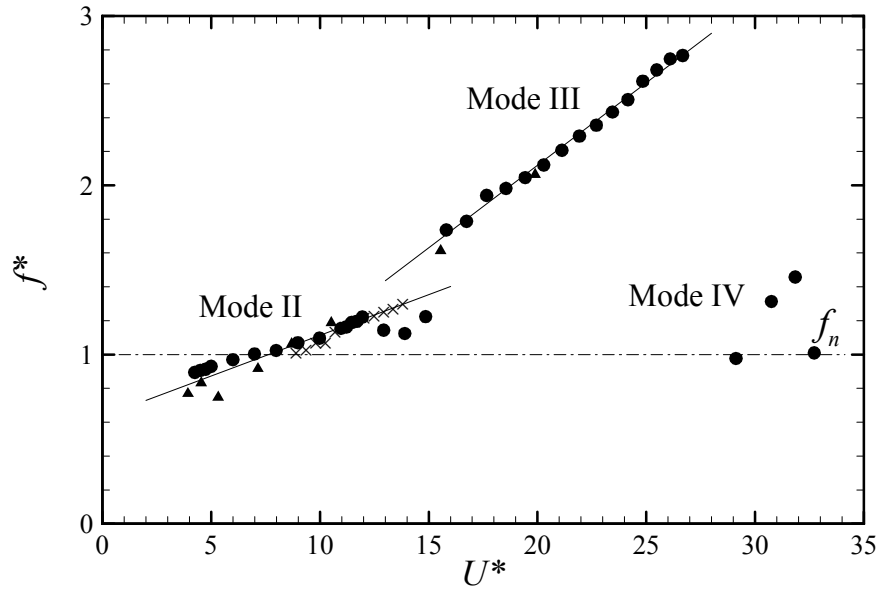


Figure 6.4.4. Frequency response as a function of reduced velocity. Symbols as in Figure 6.4.2.

6.4.6 Neutrally buoyant tethered sphere

The dynamics of a tethered sphere have been investigated in this study for mass ratios of $M^* < 1$. Furthermore, higher mass ratios of $M^* \gg 1$ have been experimentally investigated by Jauvtis *et al.* (2001). However, a particularly significant case is the neutrally buoyant sphere, with $M^* = 1$. This case has received virtually no experimental or numerical attention apart from the preliminary investigation by Provansal (2003, private communication). With this in mind, numerical simulations were performed at Reynolds numbers of $Re = 300, 350, 400, 450$ and 500 .

Because each simulation was initialized with a small random perturbation, any preferred orientation of the wake depended only on these initial conditions. At a Reynolds number of $Re = 300$, the response of the sphere was not particularly harmonic, despite the fact that the flow past a stationary sphere maintains planar symmetry at this Reynolds number. On the other hand, the sphere response at the higher Reynolds numbers was found to be very harmonic.

As the Reynolds number was increased from $Re = 300$, the oscillations in the streamwise and transverse directions remained relatively small. However, the oscillations in the lateral direction increased to about $A^* = 0.1$. Note that for the present neutrally buoyant case, the large-amplitude vibrations were observed in the *lateral* direction, whereas for the other mass ratios the *transverse* direction displayed the large-amplitude oscillations. However, this was probably due to the fact that the sphere did not have a preferred spatial orientation. For $Re < 500$, the transverse oscillations were

insignificant, but for $Re = 500$, the oscillations in the transverse direction increased in magnitude by almost 130 times over those observed at the previous Reynolds number.

For all of the Reynolds numbers investigated, the drag for the neutrally buoyant sphere decreased monotonically, similar to that of a stationary sphere. However, at the lowest Reynolds number of $Re = 300$, the difference in drag between the tethered sphere and the stationary sphere was about 4.3%. When the Reynolds number was increased to $Re = 500$, the difference in C_d increased to 9.9%. This occurred because as the Reynolds number increased and developed on its way to turbulence, the oscillations of the neutrally buoyant sphere increased in magnitude and the drag adjusted accordingly. This was especially true for the harmonic oscillations that were observed for $Re > 300$, which were shown to result in a drag coefficient that departed significantly from that of a stationary sphere. This increase in C_d for harmonic oscillations is a well-observed phenomenon in flow-induced vibration problems.

For $Re > 300$, the normalized oscillation frequency of the neutrally buoyant sphere in all three directions did not correspond to either the natural frequency of the system or the vortex shedding frequency of a stationary sphere at the equivalent Reynolds number. For $Re = 300$, the oscillation frequencies in the streamwise and lateral directions were the same and twice that of the transverse oscillations. Furthermore, for $Re \geq 400$, the frequency of oscillation in the streamwise direction was much greater than both f_n and f_{vo} , but the oscillation frequencies in the lateral and transverse directions were greater than f_n and less than f_{vo} .

The work of Mougin & Magnaudet (2002) for a rising bubble has shown that both zigzag and spiral sphere trajectories may occur depending on the controlling parameters. Moreover, Provansal (2003, private communications) has shown that the displacement pattern of a neutrally buoyant sphere may vary from a zigzag motion to a circular trajectory. For the present results, for Reynolds numbers in the range $350 \leq Re \leq 450$, the displacement pattern produced a limit cycle behaviour in which the sphere oscillated on more or less a straight line. Furthermore, as the Reynolds number was increased to $Re = 500$, the displacement pattern turned into an irregular figure-of-eight shape. However, for all of these simulations, more time was needed numerically for the oscillations to possibly transition to the circular trajectories that may be observed experimentally.

6.4.7 Mode I response

The results of Williamson & Govardhan (1997) and Govardhan & Williamson (1997) showed a local peak in the amplitude response of the tethered sphere at a reduced velocity of approximately $U^* = 5$. This value of U^* is equivalent to a natural frequency of vibration of $S_n = 0.2$. For the range

of Reynolds numbers used in their experiments, the vortex shedding frequency of a stationary sphere was about $St = 0.2$. Because the natural frequency was almost equal to the vortex shedding frequency, harmonic oscillations were observed, a condition that yields a resonance in the classical studies of the vortex-induced vibrations of cylinders. This local peak in the amplitude response of the tethered sphere was named a “Mode I” response.

For a Mode I response to exist for the present simulations and experiments at low Reynolds numbers, one would expect to observe a local peak in the amplitude response (and to some extent, the frequency response) at a reduced velocity of $U^* = 6$. This is because at the present Reynolds number of $Re = 500$, the vortex shedding frequency of a stationary sphere is about $St = 0.16$, so that the natural frequency of vibration should also be about $S_n = 0.16$. However, Figures 6.4.2 and 6.4.4 do not show any local peaks or irregular behaviour at $U^* = 6$. It is apparent then, that for laminar flow conditions, a Mode I response would not be expected to occur for a tethered sphere, and it appears that this response exists at higher Reynolds numbers because of the difference in the wake states at laminar and turbulent flow conditions.

6.4.8 Mode II response

Although a Mode I response was not observed in the present study, a Mode II response did occur as shown in Figures 6.4.2 – 6.4.4. The dynamics of the Mode II response are unlike those of the Mode I response, which is a result of the vortex shedding frequency locking on to the natural frequency of the system. For a tethered sphere, Govardhan & Williamson (1997) showed that in the Mode II regime, the oscillation frequency did not correspond to either the natural frequency or the vortex shedding frequency of a stationary sphere.

The dynamics of the tethered sphere in this Mode II regime were analyzed in detail in Chapter 5. In addition, to investigate how the sphere responded by increasing the reduced velocity, two particular values of the reduced velocity were chosen: $U^* = 5$ and $U^* = 10$. These values lied near the start of the synchronization regime and near the end respectively. The pressure fields and visualizations of the vortex structures were examined and a mechanism describing the dynamics of the sphere was described. In addition, the fluid forcing was found to be in-phase with the body motion.

It was found that the Mode II response was kicked off by the large transverse fluid forcing that caused the sphere to oscillate vigorously with large amplitudes. As U^* increased within this regime, however, the fluid forcing was found to decrease substantially, and could not evidently sustain the large-amplitude vibrations. However, visualizations of the vortex structures over a typical cycle of sphere oscillation showed that two vortices were shed for each cycle of sphere motion, throughout

the entire synchronization regime, as shown in Figure 6.4.5 for $M^* = 0.8$, $L^* = 10$ at $U^* = 10$. Note that the vortices resemble more closely those of a stationary sphere when the wake is planar-symmetric rather than unsteady asymmetric, which is the case at $Re = 500$. Although the oscillation frequency increased as U^* increased, the number of shed vortices per cycle stayed the same, so that the (normalized) vortex shedding frequency also increased. It is apparent that the large-amplitude oscillations in the Mode II regime modulated the vortex shedding from the sphere such that the vortex shedding frequency remained the same as the oscillation frequency. This modulation between f and f_{vo} guaranteed that self-excited motion ensued until the end of the synchronization regime.

6.4.9 Mode III response

At higher reduced velocities, beyond the Mode II regime, the tethered sphere displayed oscillations that were indicative of another response mode, namely the Mode III response. This vibration mode was discovered by Jauvtis *et al.* (2001) who investigated very high mass ratios, typically $M^* \geq 28$. Because of these high mass ratios, the sphere was always found to vibrate at its natural frequency, regardless of the reduced velocity. The present results, on the other hand, show that a Mode III response occurs not only for high mass ratios, but for the lowest mass ratio investigated of $M^* = 0.082$. Also, this Mode III response was found to occur roughly in the reduced velocity range $15 < U^* < 27$.

A major difference between the sphere response in the Mode II regime and the Mode III regime was that the fluid forcing in the Mode III regime was *out-of-phase* with the body motion. Also, the streamwise frequency of oscillation in the Mode II regime was twice that of the transverse frequency, whereas the frequencies of oscillation in all directions was the same for the Mode III response. Nevertheless, as with the Mode II response, the pressure fields and visualizations of the vortex structures in the Mode III regime shed light on the mechanism of vibration.

For a typical reduced velocity of $U^* = 24$ in the Mode III regime, Figure 6.4.4 shows that the normalized frequency of oscillation is $f^* = 2.7$. This amounts to an oscillation frequency of $St = 0.11$, although the vortex shedding frequency for a stationary sphere at the same Reynolds number of $Re = 500$ is about $St = 0.16$. Clearly, the oscillation frequency does not coincide with either the natural frequency or the vortex shedding frequency of a stationary sphere.

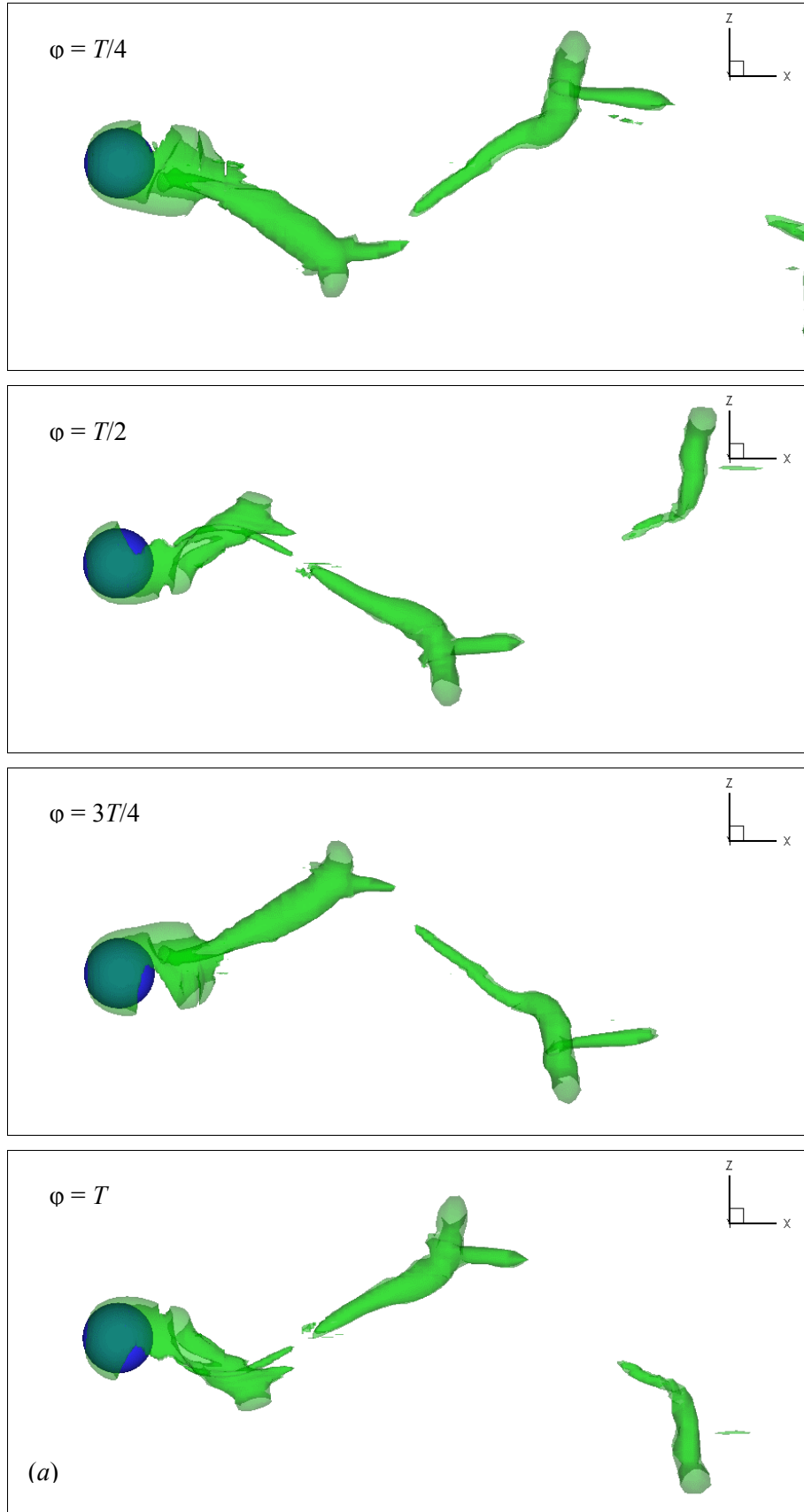


Figure 6.4.5. Visualization of vortex structures (plotted using an isosurface of $-\lambda_2$) at $U^* = 10$ for $M^* = 0.8$, $L^* = 10$: (a) x - z plane; (b) x - y plane.

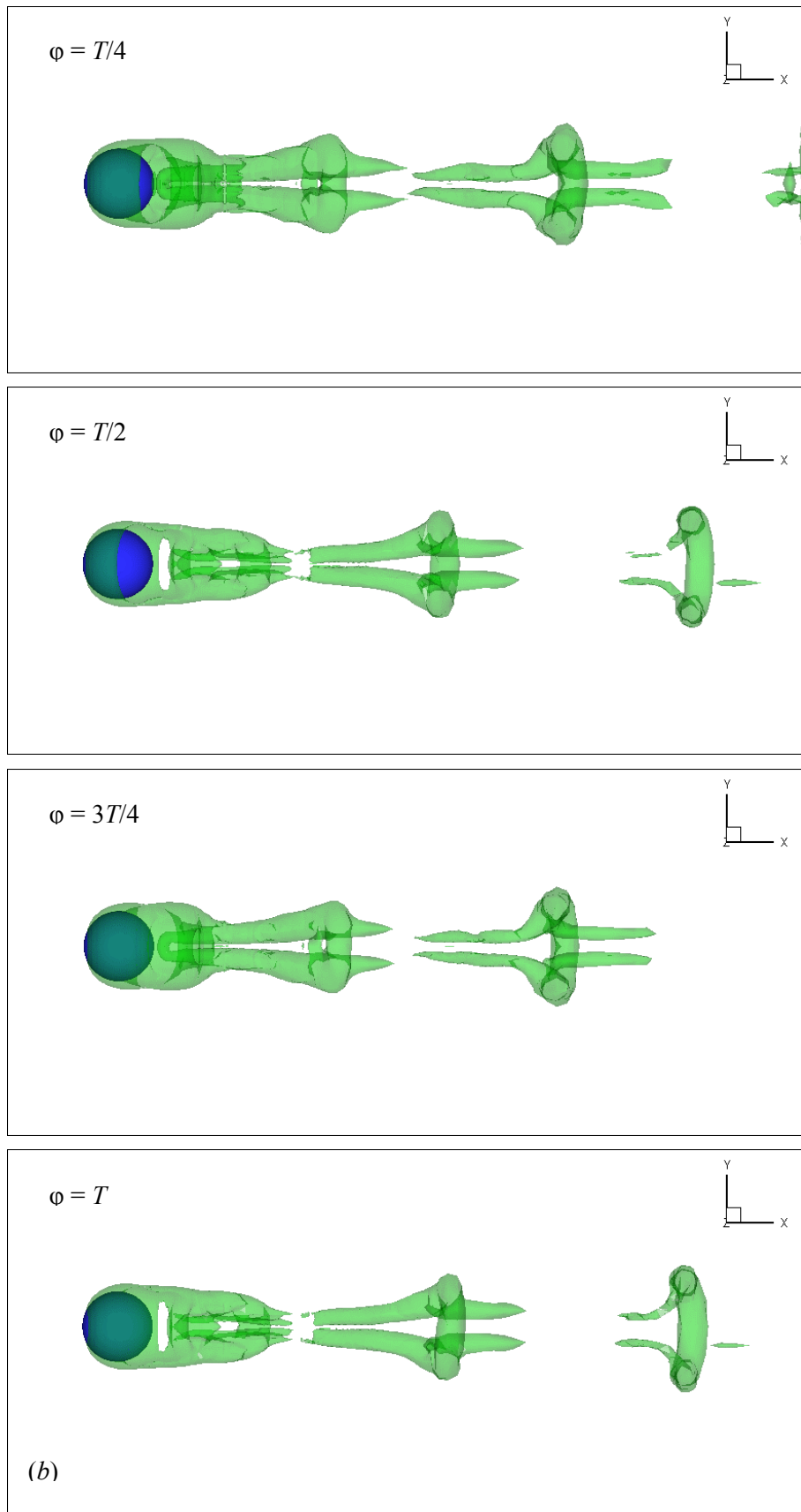


Figure 6.4.5. Continued.

However, as with the Mode II response, visualizations of the vortex structures in Chapter 5 showed that in the Mode III regime, two vortices were shed for each cycle of sphere motion, despite the fact that the oscillation frequency was much lower than the shedding frequency of a stationary sphere. It is evident then that the sphere oscillations modulate the vortex shedding frequency within this Mode III regime, leading to self-excited oscillations, as with the Mode II response.

6.4.10 Mode IV response

Finally, at still higher reduced velocities, it was found that a Mode IV response occurs when the mean layover angle exceeds 45° , although only for the sphere with mass ratio $M^* = 0.8$. The oscillations in this regime were not sinusoidal, and also not very harmonic, although large-amplitude vibrations occurred, as shown in Figure 6.4.2. Furthermore, it is evident that a Mode IV response does not occur for the low mass ratio of $M^* = 0.082$.

Jauvtis *et al.* (2001) discovered this Mode IV response by using spheres of mass ratio $M^* \geq 80$. Like the Mode III response, the spheres were found to vibrate at the natural frequency, presumably because of the extremely large mass ratios. The corresponding oscillation frequencies were thus determined to be much lower than the principal vortex shedding frequency, since large-amplitude oscillations were observed at exceptionally high reduced velocities. However, the present results show that the sphere does indeed vibrate close to its natural frequency within this Mode IV regime, depicted in Figure 6.4.4, despite the relatively low mass ratios (and reduced velocities) investigated in this study.

For example, at a reduced velocity of $U^* = 33$, the dominant oscillation frequency was about $St = 0.03$ for the sphere with mass ratio $M^* = 0.8$. On the other hand, the transverse fluid force displayed a dominant frequency of $St = 0.11$. In other words, the dominant vortex shedding frequency was approximately was roughly 3 – 4 times greater than the oscillation frequency, meaning that multiple vortices were shed for each cycle of sphere motion. Unfortunately, the erratic nature of the oscillations and the limited computational resources available meant that a detailed analysis into the dynamics of this response mode was unfeasible. However, possible mechanisms of vibration for the Mode IV response were put forth in Chapter 5, and include possible movement-induced excitation (such as flutter and galloping), or instability-induced excitation (such as subharmonic resonance). These mechanisms are described in more detail in Naudascher & Rockwell (1994).

6.4.11 Existence of a critical mass ratio

We have seen from Figure 6.4.2 and Figure 6.4.4 that a Mode IV response is observed for a mass ratio of $M^* = 0.8$, but not for a mass ratio of $M^* = 0.082$, despite the fact that the mean layover angle is greater than 45° in both cases. The lack of a Mode IV response for the low mass ratio sphere means that there exists a *critical mass* in the vicinity $0.082 < M^* < 0.8$. For a sphere free to vibrate in the transverse direction, Govardhan & Williamson (2002b) report a critical mass of $M^* = 0.30$. On the related topic of the vortex-induced vibrations of hydroelastically-mounted cylinders, the critical mass takes the value $M^* = 0.54$. Although it has been postulated that the existence of a critical mass is a generic phenomenon in vortex-induced vibration (Govardhan & Williamson (2002a)), no value for the critical mass of a tethered sphere has yet been reported.

References

- Achenbach, E. 1974 Vortex shedding from spheres. *J. Fluid Mech.* **62**, 209-221.
- Barkla, H.M. & Auchterlonie, L.J. 1971 The Magnus or Robins effect on rotating spheres. *J. Fluid Mech.* **47**, 437-447.
- Barkley, D. & Henderson, R.D. 1996 Three-dimensional Floquet stability analysis of the wake of a circular cylinder. *J. Fluid Mech.* **322**, 215-241.
- Batchelor, G.K. 1967 *An Introduction to Fluid Dynamics*. Cambridge University Press, London.
- Bearman, P.W. 1984 Vortex shedding from oscillating bluff bodies. *Ann. Rev. Fluid Mech.* **16**, 195-222.
- Blackburn, H.M. & Henderson, R.D. 1999 A study of two-dimensional flow past an oscillating cylinder. *J. Fluid Mech.* **385**, 255-286.
- Blackburn, H.M., Govardhan, R.N. & Williamson, C.H.K. 2000 A complementary numerical and physical investigation of vortex-induced vibration. *J. Fluids Struct.* **15**, 481-488.
- Blackburn, H.M. & Lopez, J.M. 2002 Modulated rotating waves in an enclosed swirling flow. *J. Fluid Mech.* **465**, 33-58.
- Blevins, R.D. 1994 *Flow-Induced Vibration*. Krieger Pub., Malabar.
- Brika, D. & Laneville, A. 1993 Vortex-induced vibrations of a long flexible circular cylinder. *J. Fluid Mech.* **250**, 481-508.
- Canuto, C., Hussaini, M.Y., Quarteroni, A. & Zang, T.A. 1988 *Spectral Methods in Fluid Dynamics*. 2nd Edition, Springer-Verlag,
- Chapra, S. & Canale, R.P. 1998 *Numerical Methods For Engineers*. McGraw-Hill, Singapore.

- Chen, S.S., Zhu, S. & Cai, Y. 1995 An unsteady flow theory for vortex-induced vibration. *J. Sound Vib.* **184**, no. 1, 73-92.
- Chester, W. & Breach, D.R. 1969 On the flow past a sphere at low Reynolds number. *J. Fluid Mech.* **37**, no. 4, 751-760.
- Chong, M.S., Perry, A.E. & Cantwell, B.J. 1990 A general classification of three-dimensional flow fields. *Phys. Fluids A* **2**, 765-777.
- Clift, R., Grace, J.R. & Weber, M.E. 1978 *Bubbles, Drops and Particles*. Academic Press, New York.
- Constantinescu, G.S. & Squires, K.D. 2000 LES and DES investigations of turbulent flow over a sphere. *AIAA Paper* 2000-0540.
- Davies, J.M. 1949 The aerodynamics of golf balls. *J. Applied Phys.* **20**, no. 9, 821-828.
- Dennis, S.C.R. & Walker, J.D.A. 1971 Calculation of the steady flow past a sphere at low and moderate Reynolds numbers. *J. Fluid Mech.* **48**, no. 4, 771-789.
- Dennis, S.C.R., Singh, S.N. & Ingham, D.B. 1980 The steady flow due to a rotating sphere at low and moderate Reynolds numbers. *J. Fluid Mech.* **101**, 257-279.
- Dowell, E.H. & Hall, K.C. 2001 Modeling of fluid-structure interaction. *Ann. Rev. Fluid Mech.* **33**, 445-490.
- Durgin, W.W., March, P.A. & Lefebvre, P.J. 1980 Low-mode response of circular cylinders in cross-flow. *ASME J. Fluids Eng.* **102**, 183.
- Feng, C.C. 1968 The measurement of vortex-induced effects in flow past stationary and oscillating circular and D-section cylinders. MASC Thesis, University of British Columbia.
- Gear, C.W. 1973 *Numerical Initial Value Problems in Ordinary Differential Equations*. Prentice-Hall, Englewood Cliffs.
- Gerritsma, M.I. & Phillips, T.N. 2000 Spectral element methods for axisymmetric Stokes problems. *J. Comp. Phys.* **164**, 81-103.
- Ghidersa, B. & Dušek, J. 2000 Breaking of axisymmetry and onset of unsteadiness in the wake of a sphere. *J. Fluid Mech.* **423**, 33-69.
- Goldberg, A. & Florsheim, B.H. 1966 Transition and Strouhal number for the incompressible wake of various bodies. *Phys. Fluids* **9**, no. 1, 45-50.
- Gottlieb, D. & Orszag, S.A. 1977 *Numerical Analysis of Spectral Methods: Theory and Applications*. SIAM, Philadelphia.

- Gottlieb, O. 1997 Bifurcations of a nonlinear small-body ocean-mooring system excited by finite-amplitude waves. *Trans. ASME J. OMAE* **119**, 234-238.
- Gottlieb, O. & Perlin, M. 1998 Period-doubling of an elastically tethered sphere: theory and experiment. *17th Int. Conf. Offshore Mech. Arctic Eng.*, Paper OMAE98-0324.
- Govardhan, R. & Williamson, C.H.K. 1997 Vortex-induced motions of a tethered sphere. *J. Wind Eng. Ind. Aerodyn.* **69-71**, 375-385.
- Govardhan, R. & Williamson, C.H.K. 2000 Modes of vortex formation and frequency response of a freely vibrating cylinder. *J. Fluid Mech.* **420**, 85-130.
- Govardhan, R. & Williamson, C.H.K. 2002a Resonance forever: existence of a critical mass and an infinite regime of resonance in vortex-induced vibration. *J. Fluid Mech.* **473**, 147-166.
- Govardhan, R. & Williamson, C.H.K. 2002b Vortex-induced vibration of a sphere. *J. Fluid Mech.* (submitted).
- Gresho, P.M. & Sani, R.L. 2000 *Incompressible Flow and the Finite Element Method*. Wiley, New York.
- Guckenheimer, J. & Holmes, P. 1986 *Nonlinear Oscillations, Dynamical Systems, and Bifurcations of Vector Fields*. Springer-Verlag, New York.
- Harleman, D.R.F. & Shapiro, W.C. 1961 The dynamics of a submerged moored sphere in oscillatory waves. *Coastal Eng.* **2**, 746-765.
- Henderson, R.D. 1995 Details of the drag curve near the onset of vortex shedding. *Phys. Fluids* **7**, 2102-2104.
- Henderson, R.D. & Karniadakis, G.E. 1995 Unstructured spectral element methods for simulation of turbulent flows. *J. Comp. Phys.* **122**, 191-217.
- Hiejima, S., Nomura, T., Kimura, K. & Fujino, Y. 1997 Numerical study on the suppression of the vortex-induced vibration of a circular cylinder by acoustic excitation. *J. Wind Eng.* **67-68**, 325-335.
- Höfler, K. & Schwarzer, S. 2000 Navier-Stokes simulation with constraint forces: Finite-difference method for particle-laden flows and complex geometries. *Phys. Rev. E* **61**, no. 6, 7146-7160.
- Hover, F.S., Techet, A.H. & Triantafyllou, M.S. 1998 Forces on oscillating uniform and tapered cylinders in crossflow. *J. Fluid Mech.* **363**, 97-114.
- Hover, F.S., Tvedt, H. & Triantafyllou, M.S. 2001 Vortex-induced vibrations of a cylinder with tripping wires. *J. Fluid Mech.* **448**, 175-195.

- Howe, M.S., Lauchle, G.C. & Wang, J. 2001 Aerodynamic lift and drag fluctuations of a sphere. *J. Fluid Mech.* **436**, 41-57.
- Huerre, P. & Monkewitz, P.A. 1990 Local and global instabilities in spatially developing flows. *Ann. Rev. Fluid Mech.* **22**, 473-537.
- Hunt, J.C.R., Wray, A.A. & Moin, P. 1988 Eddies, stream and convergence zones in turbulent flows. Center for Turbulence Research Rep. CTR-S88.
- Hussain, A.K.M.F. & Hayakawa, M. 1987 Eduction of large-scale organized structure in a turbulent plane wake. *J. Fluid Mech.* **180**, 193-229.
- Iooss, G. & Joseph, D.D. 1990 Elementary Stability and Bifurcation Theory. 2nd Edition, Springer-Verlag, New York.
- Jauvtis, N., Govardhan, R. & Williamson, C.H.K. 2001 Multiple modes of vortex-induced vibration of a sphere. *J. Fluids Struct.* **15**, 555-563.
- Jeong, J. & Hussain, F. 1995 On the identification of a vortex. *J. Fluid Mech.* **285**, 69-94.
- Johnson, T.A. & Patel, V.C. 1999 Flow past a sphere up to a Reynolds number of 300. *J. Fluid Mech.* **378**, 19-70.
- Joseph, D.D. 1976 Stability of Fluid Motions I. Springer, New York.
- Karniadakis, G.E. 1989 Spectral element simulations of laminar and turbulent flows in complex geometries. *App. Num. Math.* **6**, 85-105.
- Karniadakis, G.E. 1990 Spectral element-Fourier methods for incompressible turbulent flows. *Comp. Meth. Applied Mech. Eng.* **80**, 367-380.
- Karniadakis, G.E. & Henderson, R.D. 1998 Spectral Element Methods for Incompressible Flows, in *The Handbook of Fluid Dynamics* (ed. R. W. Johnson), CRC Press, Boca Raton.
- Karniadakis, G.E. & Triantafyllou, G.S. 1992 Three-dimensional dynamics and transition to turbulence in the wake of bluff objects. *J. Fluid Mech.* **238**, 1-30.
- Karniadakis, G.E., Israeli, M. & Orszag, S.A. 1991 High-order splitting methods for the incompressible Navier-Stokes equations. *J. Comp. Phys.* **97**, 414-443.
- Karniadakis, G.E., Orszag, S.A., Rönquist, E.M. & Patera, A.T. 1991 Spectral element and lattice gas methods for incompressible fluid dynamics, in *Incompressible Fluid Dynamics* (eds. M. D. Gunzberger & R.A. Nicolaides), Cambridge University Press, Cambridge.
- Khalak, A. & Williamson, C.H.K. 1997 Fluid forces and dynamics of a hydroelastic structure with very low mass and damping. *J. Fluids Struct.* **11**, 973-982.

- Khalak, A. & Williamson, C.H.K. 1999 Motions, forces and mode transitions in vortex-induced vibrations at low mass-damping. *J. Fluids Struct.* **13**, 813-851.
- Kim, D. & Choi, H. 2002 Laminar flow past a sphere rotating in the streamwise direction. *J. Fluid Mech.* **461**, 365-386.
- Kim, H.J. & Durbin, P.A. 1988 Observations of the frequencies in a sphere wake and of drag increase by acoustic excitation. *Phys. Fluids* **31**, 3260-3265.
- Kim, I. & Pearlstein, A.J. 1990 Stability of the flow past a sphere. *J. Fluid Mech.* **211**, 73-93.
- Kurose, R. & Komori, S. 1999 Drag and lift forces on a rotating sphere in a linear shear flow. *J. Fluid Mech.* **384**, 183-206.
- Lamb, H. 1945 Hydrodynamics. 6th Edition, Dover, New York.
- Landau, L.D. & Lifshitz, E.M. 1987 Fluid Mechanics. 2nd Edition, Butterworth-Heinemann, Oxford.
- Leweke, T., Provansal, M., Ormières, D. & Lebescond, R. 1999 Vortex dynamics in the wake of a sphere. *Phys. Fluids* **11**, no. 9, S12.
- Lugt, H.J. 1979 The dilemma of defining a vortex, in *Recent Developments in Theoretical and Experimental Fluid Mechanics* (eds. U. Muller, K.G. Roesner & B. Schmidt), Springer-Verlag, Berlin.
- Maday, Y. & Patera, A.T. 1989 Spectral element methods for the incompressible Navier-Stokes equations, in *State-of-the-Art Surveys in Computational Mechanics* (eds. A. K. Noor & J.T. Oden), ASME, New York.
- Magarvey, R.H. & Bishop, R.L. 1961a Transition ranges for three-dimensional wakes. *Can. J. Phys.* **39**, 1418-1422.
- Magarvey, R.H. & Bishop, R.L. 1961b Wakes in liquid-liquid systems. *Phys. Fluids* **4**, 800-805.
- Magarvey, R.H. & MacLatchy, C.S. 1965 Vortices in sphere wakes. *Can. J. Phys.* **43**, 1649-1656.
- Magnaudet, J., Rivero, M. & Fabre, J. 1995 Accelerated flows past a rigid sphere or a spherical bubble. Part 1. Steady straining flow. *J. Fluid Mech.* **284**, 97-135.
- Marques, F. & Lopez, J.M. 1997 Taylor-Couette flow with axial oscillations of the inner cylinder: Floquet analysis of the basic flow. *J. Fluid Mech.* **348**, 153-175.
- Melander, M.V. & Hussain, F. 1993 Polarized vorticity dynamics on a vortex column. *Phys. Fluids A* **8**, no. 8, 1992.

- Mittal, R. & Balachandar, S. 1995 Generation of streamwise vortical structures in bluff body wakes. *Phys. Rev. Lett.* **75**, no. 7, 1300-1303.
- Mittal, R. 1999a A Fourier-Chebyshev spectral collocation method for simulating flow past spheres and spheroids. *Int. J. Num. Meth. Fluids* **30**, 921-937.
- Mittal, R. 1999b Planar symmetry in the unsteady wake of a sphere. *AIAA J.* **37**, no. 3, TN 388-390.
- Mittal, R., Wilson, J.J. & Najjar, F.M. 2002 Symmetry properties of the transitional sphere wake. *AIAA J.* **40**, no. 3, TN 579-582.
- Modi, V.J. & Akutsu, T. 1984 Wall confinement effects for spheres in the Reynolds number range of 30 - 2000. *Trans. ASME J. Fluids Eng.* **106**, 66-73.
- Monkewitz, P.A. 1988a A note on vortex shedding from axisymmetric bluff bodies. *J. Fluid Mech.* **192**, 561-575.
- Monkewitz, P.A. 1988b The absolute and convective nature of instability in two-dimensional wakes at low Reynolds numbers. *Phys. Fluids* **31**, no. 5, 999-1006.
- Mougin, G. & Magnaudet, J. 2002 Path instability of a rising bubble. *Phys. Rev. Lett.* **88**, no. 1, 145021-145024.
- Nakamura, I. 1976 Steady wake behind a sphere. *Phys. Fluids* **19**, no. 1, 5-8.
- Natarajan, R. & Acrivos, A. 1993 The instability of the steady flow past spheres and disks. *J. Fluid Mech.* **254**, 323-344.
- Naudascher, E. & Rockwell, D. 1994 *Flow-Induced Vibrations: An Engineering Guide*. A.A. Balkema, Rotterdam.
- Newman, D.J. & Karniadakis, G.E. 1997 A direct numerical simulation study of flow past a freely vibrating cable. *J. Fluid Mech.* **344**, 95-136.
- Oesterlé, B. & Bui Dinh, T. 1998 Experiments on the lift of a spinning sphere in a range of intermediate Reynolds numbers. *Exp. Fluids* **25**, 16-22.
- Ormières, D. & Provansal, M. 1999 Transition to turbulence in the wake of a sphere. *Phys. Rev. Lett.* **83**, no. 1, 80-83.
- Orszag, S.A. 1974 Fourier series on spheres. *Mon. Weath. Rev.* **102**, 56.
- Owens, R.G. & Phillips, T.N. 1996 Steady viscoelastic flow past a sphere using spectral elements. *Int. J. Num. Meth. Eng.* **39**, 1517-1534.
- Patera, A.T. 1984 A spectral element method for fluid dynamics; laminar flow in a channel expansion. *J. Comp. Phys.* **54**, 468-488.

- Perry, A.E. & Chong, M.S. 1987 Description of eddying motions and flow patterns using critical-point concepts. *Ann. Rev. Fluid Mech.* **19**, 125-155.
- Pregalato, C.J., Thompson, M.C. & Hourigan, K. 2001 Flow transition in the wake of a rotating sphere. *Proc. of 14th Australasian Fluid Mech. Conf.* (ed. B. Dally), Adelaide, SA, Australia.
- Pregalato, C.J., Thompson, M.C. & Hourigan, K. 2002a Forces and wake transitions in the flow past a rotating sphere. *Phys. Fluids* (submitted).
- Pregalato, C.J., Ryan, K., Thompson, M.C. & Hourigan, K. 2002b Numerical simulations of the flow-induced vibrations of tethered bluff bodies. *Proc. of IMECE 2002: 5th Int. Symp. on FSI, AE, FIV & N*, New Orleans, LA, USA.
- Pregalato, C.J., Thompson, M.C. & Hourigan, K. 2002c Flow transitions in the wake of a streamwise-rotating sphere. *Proc. of Bluff Body Wakes & Vortex-Induced Vibrations 3 (BBVIV 3)*, Port Douglas, QLD, Australia.
- Proudman, I. & Pearson, J.R.A. 1957 Expansions at small Reynolds numbers for the flow past a sphere and a circular cylinder. *J. Fluid Mech.* **2**, 237-262.
- Pruppacher, H.R., Le Clair, B.P. & Hamiliec, A.E. 1970 Some relations between drag and flow pattern of viscous flow past a sphere and a cylinder at low and intermediate Reynolds numbers. *J. Fluid Mech.* **44**, 781-790.
- Rimon, Y. & Cheng, S.I. 1969 Numerical solution of a uniform flow over a sphere at intermediate Reynolds numbers. *Phys. Fluids* **12**, no. 5, 949-959.
- Robichaux, J., Balachandar, S. & Vanka, S.P. 1999 Three-dimensional Floquet instability of the wake of square cylinders. *Phys. Fluids* **11**, 560-578.
- Roos, F.W. & Willmarth, W.W. 1971 Some experimental results on sphere and disk drag. *AIAA J.* **9**, no. 2, 285-291.
- Roshko, A. 1956 On the development of turbulent wakes from vortex streets. NACA Rep. 1191.
- Rubinow, S.I. & Keller, J.B. 1961 The transverse force on a spinning sphere moving in a viscous fluid. *J. Fluid Mech.* **11**, 447-459.
- Ryan, K., Pregalato, C.J., Thompson, M.C. & Hourigan, K. 2003 Flow-induced vibrations of a tethered circular cylinder. *J. Fluids Struct.* (accepted).
- Sakamoto, H. & Haniu, H. 1990 A study on vortex shedding from spheres in a uniform flow. *Trans. ASME J. Fluids Eng.* **112**, 386-392.

- Sakamoto, H. & Haniu, H. 1995 The formation mechanism and shedding frequency of vortices from a sphere in uniform shear flow. *J. Fluid Mech.* **287**, 151-171.
- Schlichting, H. 1979 *Boundary Layer Theory*. 7th edition, McGraw Hill, New York.
- Schmitt, H. 1997 *Flows at Large Reynolds Numbers*. Computational Mechanics, Boston.
- Schoppa, W. & Hussain, F. 2000 Coherent structure dynamics in near-wall turbulence. *Fluid Dyn. Res.* **26**, 119-139.
- Shi-Igai, H. & Kono, T. 1969 Study on vibration of submerged spheres caused by surface waves. *Coastal Eng. Japan* **12**, 29-40.
- Shirayama, S. 1992 Flow past a sphere: Topological transitions of the vorticity field. *AIAA J.* **30**, no. 2, 349-358.
- Spalart, P.R., Jou, W.H., Strelets, M. & Allmaras, S.R. 1997 Comments on the feasibility of LES for wings, and on a hybrid RANS/LES approach. *1st AFOSR Int. Conf. on DNS/LES*, Rouston LA, USA.
- Stokes, G.G. 1851 On the effect of internal friction of fluids on the motion of pendulums. *Camb. Phil. Trans.* **9**, 8-106.
- Taneda, S. 1956 Experimental investigation of the wake behind a sphere at low Reynolds numbers. *J. Phys. Soc. Japan* **11**, 1104-1108.
- Thompson, M.C., Hourigan, K. & Sheridan, J. 1996 Three-dimensional instabilities in the wake of a circular cylinder. *Exp. Therm. Fluid Sci.* **12**, 190-196.
- Thompson, M.C., Leweke, T. & Provansal, M. 2001 Kinematics and dynamics of sphere wake transition. *J. Fluids Struct.* **15**, no. 3/4, 575-585.
- Tobak, M. & Peake, D.J. 1982 Topology of three-dimensional separated flows. *Ann. Rev. Fluid Mech.* **14**, 61-85.
- Tomboulides, A.G. 1992 Direct and large-eddy simulation of wake flows: flow past a sphere. PhD Thesis, Princeton University.
- Tomboulides, A.G., Orszag, S.A. & Karniadakis, G.E. 1993a Direct and large-eddy simulation of axisymmetric wakes. *AIAA Paper* 93-0546.
- Tomboulides, A.G., Orszag, S.A. & Karniadakis, G.E. 1993b Direct and large-eddy simulation of the flow past a sphere. *2nd Int. Conf. on Turbulence Modeling and Experiments*, Florence, Italy.
- Tomboulides, A.G. & Orszag, S.A. 2000 Numerical investigation of transitional and weak turbulent flow past a sphere. *J. Fluid Mech.* **416**, 45-73.

- Tsuji, Y., Morikawa, Y. & Mizuno, O. 1985 Experimental measurement of the Magnus force on a rotating sphere at low Reynolds numbers. *Trans. ASME J. Fluids Eng.* **107**, 484-488.
- Virk, D., Melander, M.V. & Hussain, F. 1994 Dynamics of a polarized vortex ring. *J. Fluid Mech.* **260**, 23-55.
- Wang, Y., Lu, X. & Zhuang, L. 2001 Finite element analysis of viscous flow past a rotating sphere. *J. Hydrodyn.* **13**, no. 2, 80-85.
- Warburton, T.C. & Karniadakis, G.E. 1996 The wake of oscillating cylinder close to a free surface. *Bull. Amer. Phys. Soc.* **41**, 1732.
- Watts, R.G. & Ferrer, R. 1987 The lateral force on a spinning sphere: Aerodynamics of a curveball. *Amer. J. Phys.* **55**, no. 1, 40-44.
- White, F.M. 1994 Fluid Mechanics. 3rd Edition, McGraw-Hill, New York.
- Wieselsberger, C.v. 1922 Weitere Feststellungen über die Gesetze des Flüssigkeits- und Luftwiderstandes. *Physikalische Zeitschrift* **23**, 219-224.
- Williamson, C.H.K. 1996 Vortex dynamics in the cylinder wake. *Ann. Rev. Fluid Mech.* **28**, 477-539.
- Williamson, C.H.K. & Govardhan, R. 1997 Dynamics and forcing of a tethered sphere in a fluid flow. *J. Fluids Struct.* **11**, 293-305.
- Wu, J.S. & Faeth, G.M. 1993 Sphere wakes in still surroundings at intermediate Reynolds numbers. *AIAA J.* **31**, no. 8, 1448-1455.
- Ziada, S. & Staubli, T. (eds.) 2000 Flow-Induced Vibration. A.A. Balkema, Rotterdam.